Synthesis and Modification of TiO_2 and WO_3 Based Nanostructured Materials for Environmental Applications

By

Sapanbir Singh Thind

A thesis submitted in conformity with the requirements for the Degree of
Doctor of Philosophy in Chemistry and Materials Science
Faculty of Science and Environmental Studies
Department of Chemistry
Lakehead University

Abstract

TiO_2 and WO_3 based nanomaterials are highly attractive for various applications encompassing photocatalysis, electrochromic devices, dye sensitized solar cells, hydrogen production, and sensing applications due to their low cost, non-toxicity, high efficiency, chemical inertness and ability to be synthesized in various morphologies. TiO_2 is the most intensely studied photocatalyst and a significant proportion of research focuses on improving its photocatalytic activity, which is innately limited due to its wide band gap and electron/hole recombination kinetics. The doping and co-doping of metals and non-metals into the crystal lattice of TiO_2 have proved to reduce the band gap and decrease the rate of electron/hole recombination. This band gap reduction results in absorptive red shifting, which may be utilized for visible light-driven photocatalysis and dye sensitized solar cells (DSSC). Although WO_3 is a very promising material that has the capacity for absorbing in the visible spectrum, it pales in comparison to TiO_2 in terms of efficacy and thus there are considerable opportunities for the improvement of its activity for various applications through its modification.

During my PhD study, mesoporous N-doped and N,W co-doped TiO_2 photocatalysts were initially prepared with an exclusive anatase phase and high specific surface areas, utilizing a facile, reproducible and inexpensive solution combustion synthesis method. The atomic percentage of N was kept constant, whereas that of W was varied from 0.5% to 3% in order to evaluate the effects of the amount of W on the photocatalytic activities and other properties of the materials. It was observed that the N and W atoms were well incorporated into the titania lattice structure, which led to a significant red shift in the absorption edge of the co-doped TiO_2, and concordantly, a dramatic narrowing of the band gap. Photodegradation studies of rhodamine B (RhB) dye on the various samples revealed that an enhancement of up to 14 fold in the reaction rate was observed with 1.5 at% W doped TiO_2 as compared with commercial Degussa P25.

To enhance the activity of the TiO_2 based materials we introduced a novel UV treatment approach. The UV treated electrodes exhibited a dramatic increase in the donor density of the TiO_2 nanotubes by three orders of magnitude. For the UV treated electrodes the photocurrent was enhanced 15 fold and the photoelectrochemical activity was approximately 6.8 times higher than that of the untreated TiO_2 nanotubes. This novel approach was also employed with the N, W

co-doped mesoporous TiO_2. Following the UV treatment, the photocatalytic activity of the co-doped samples was increased two-fold under UV light and a 12-fold under visible light. The increase in the activity of the TiO_2 nanotubes and N, W co-doped samples may be attributed to the lowering of the band gap due to the formation of Ti^{3+} during the UV treatment process.

Next, WO_3 platelets were grown on W substrate via a hydrothermal method. The WO_3 nanoparticles prepared at 180 °C over one hour heat treatment demonstrated the best photocurrent, and as the duration of the heat treatment was increased, the photocurrent commenced to decrease. The WO_3 prepared at 180 °C over three hours showed minimal photocurrent. To elucidate crystal growth kinetics, for the first time, an electrochemical reduction method was utilized, which revealed that the plate-like structures originated from an arrayed nanosphere layer that resided beneath them. Interestingly, the obtained layer of nanospherical WO_3 demonstrated high photocurrent and photocatalytic activity under UV-Vis light.

To optimize the photocatalytic activity of the WO_3, as well as the electrocatalytic activity of the Pt nanoparticles, so-called bifunctional electrodes were prepared. The Pt nanoparticles that were deposited on one side of the WO_3 electrodes served as an electrocatalyst, while the opposite side, consisting of the WO_3 platelet like structures, was employed as the photocatalyst. The results indicated that the synthesized WO_3 electrodes possessed considerable activity when exposed to visible light, while the deposition of the Pt significantly enhanced the activity of the electrode. An overall enhancement in the catalytic activity was noticed for bifunctional electrodes when electrocatalyst and photocatalyst were activated together, in contrast to the case where photocatalysis and electrocatalysis were employed separately.

Moreover, the platelet WO_3 surfaces were modified with Ta_2O_5, IrO_2 and IrO_2-Ta_2O_5 thin films for energy storage. To the best of our knowledge, no previous study has articulated the utilization of IrO_2-Ta_2O_5 as supercapacitors. Our results revealed that when Ta_2O_5 and IrO_2 were employed concomitantly on the WO_3 surface, they exhibited a synergistic effect, where the capacitance measured for this electrode was much higher than that of the Ta_2O_5 or IrO_2 containing electrodes. These electrodes demonstrated high stability in which the 5000^{th} charge/discharge cycle was identical to that of the initial cycle.

In summary, the photocatalysts and electrocatalysts developed in this PhD study exhibited high activity in the abatement of various pollutants, as well as for energy storage. Our results indicated that the performance of the catalyst was contingent, to a significant degree, on the dimensions, morphologies and electronic structures of the nanostructured materials. The solution combustion method for co-doping TiO_2 and UV treatment approach, developed in this study were shown to be rapid, reproducible and easily amenable to scale-up, thus creating potential opportunities for the fabrication of high-performance TiO_2 and WO_3 nanomaterials in myriad beneficial environmental applications.

This thesis is dedicated to my loving parents *Balwinder Kaur Thind*, *Balbir Singh Thind* and my sister *Amrit* for years of unconditional love, support and encouragement.

Acknowledgements

Foremost, I would like to express my sincere gratitude to my Supervisor Dr. Aicheng Chen for all his hope, efforts and precious time he has put on me. His guidance and immense knowledge in electrochemistry and materials science helped me in all the time of research and writing of this thesis. I could not have imagined having a better advisor and mentor for my Ph.D study. Besides my advisor, I would like to thank the rest of my thesis committee: Dr. Manit Rappon and Dr. Stephen Kinrade for their encouragement and insightful comments. Thanks also to Dr. Greg Spivak, the coordinator of PhD Chemistry and Materials Science program for his great help.

I would like to thank Dr. Guosheng Wu and Dr. Min Tian for guiding me throughout all these years and keeping me on the right track. I would also like to thank all the current and previous members of the Chen research group for providing me an ideal working place. Thanks to Xin Chang, Sharon Chen, Maduraiveeran Govindhan, Asieh Ahmadalinezhad, Xiao Qu, Kai Yan, Pan Ke, Cassandra Ostrom, Matt Simko, Daniel Liba, Walaa Alammari, Kevin Gagnon and Kyle Rozic for their friendship and collaborations. I thank both faculty and the staff members of Department of Chemistry for their support, encouragement and friendship.

I also thank the Canadian Centre for Electron Microscopy at McMaster University for obtaining the TEM images and Surface Interface Ontario/Chemical Engineering & Applied Chemistry at the University of Toronto for carrying out the XPS analysis.

I would also like to thank all the wonderful people I have in my life as friends for their love and support. Thanks to Manish Khatiyan, Preetam Lamba, Harpreet Bhullar, Bhagwant Singh, Jagdeep Singh, Varinder Hayer, Harbinder Hayer, Tristan Fletcher, Shanghuan Feng, Tim Miao and Derek Smith.

My biggest thanks to my ever loving parents and sister. There are no words that can truly express the level of gratitude and appreciation I have for you. I will always appreciate the support that you have given me and the sacrifices you have made to give me the life that I have.

List of Figures

2.1. Depiction of the basic mechanism of photocatalysis **18**

2.2. Planar Ti_3O building-block representation (left) and TiO_6 polyhedra (right) for the TiO_2 phases rutile (a), anatase (b) and brookite (c) [Ti (white); O (red)] **23**

2.3. Graphic of sol-gel chemistry process **18**

2.4. Schematic diagram of a charged and discharged electric double layer capacitor **18**

4.1. XRD patterns of TiO_2, TiO_2:N and the TiO_2:N-W(x%). **73**

4.2. TEM and high resolution TEM images of N doped (a), (c) and N,W co-doped TiO_2 (b), (d), respectively. Inset is respective SAED pattern. **75**

4.3. (a) Nitrogen adsorption-desorption isotherms of the TiO_2:N-W(1.5%) sample, (b) Pore size distribution.. ..... **77**

4.4. (a) UV-visible absorption spectra of TiO_2, TiO_2-N and the TiO_2:N-W(1.5%); (b) Tauc plots of TiO_2, TiO_2:N and TiO_2:N -W(1.5%).. ..... **79**

4.5. XPS spectra of (a) Ti 2p, (b) O 1s, (c) N 1s and (d) W $4d^5$ for TiO_2:N-W(1.5%).. ..... **81**

4.6. (a) Calibration curve for rhodamine B; (b) Relationship between absorbance and concentration at 553 nm.. ..... **84**

4.7. Kinetic curves for the photodegradation of rhodamine B over the TiO_2, N-doped TiO_2 and N,W co-doped TiO_2 samples **85**

4.8. Bar chart showing the effect of W concentration on the rate of the reaction **86**

5.1. SEM images of (A) TiO_2 nanotubes (B) corresponding XRD pattern. Inset in (B) EDS of TiO_2 nanotubes **99**

5.2. (A) Cyclic voltammograms of TiO_2 nanotubes electrode without (a) and with UV irradiation (b, c). Scan rate (mV/s): 20, supporting electrolyte: 0.1 M H_2SO_4. (B) The transient photocurrent-time profiles of the TiO_2 nanotubes with and without the UV pretreatment in methanol. Applied bias (V): 1.4; Insets in Figure 5.2A, the digital images of TiO_2 before (d) and after (e) the UV treatment. (C) Mott-Schottky plot of the TiO_2 nanotubes obtained in 0.1 M H_2SO_4 at 500 Hz without (a) and with (b) the UV pretreatment in methanol. Inset in Figure 5.2C: the Mott-Schotty plot of the TiO_2 nanotubes after the UV pretreatment **101**

5.3. Scanning kinetic curves for photoelectrochemical oxidation of 4-NPh in 0.1 M H_2SO_4 at the TiO_2 nanotubes after (A) and before the UV pretreatment in methanol. Applied bias: 1.4 V. (C) The relationship between ln(C/Co) and time. **103**

5.4. The time effect of the UV pretreatment on the TNW activity under visible light **105**

5.5. Comparison of the TNW sample prior to and following the UV pretreatment with P25 under UV light **106**

5.6. TEM images of N,W co-doped TiO_2 (A) before and (B) after UV pretreatment. **108**

5.7. SAED images of the untreated (a) and UV pretreated (b) sample respectively **109**

5.8. (A) XRD patterns, (B) nitrogen adsorption-desorption isotherms of the unpretreated and UV pretreated TNW **111**

5.9. (A) UV-visible absorption spectra of the unpretreated and UV pretreated TiO_2 (B) respective Tauc plots **112**

5.10. XPS spectra of (a) survey scan, (b) N 1s, (c) O 1s, (d) Ti 2p, (e) W 4d and (f) C 1s for TNW after the UV pretreatment **114**

5.11. Photocatalytic stability tests of the UV pretreated TNW under visible light **116**

5.12. Stability test for TiO_2 nanotubes without (A) and with (B) treatment. Applied potential bias: 1.4 V **118**

6.1. SEM images of (A) WO_3-30 min, (B) WO_3-1h, (C) WO_3-2h and (D) WO_3-3h. Insets are the high resolution SEM images of the respective samples **130**

6.2. XRD patterns of prepared WO_3 samples. **131**

6.3. Cyclic voltammograms of samples under (A) UV irradiation and (B) visible light in 0.5 M H_2SO_4 at 20 mV/s **132**

6.4. (A) Chronopotentiometry curves for the electrochemical reduction (-10 mA) of the various electrodes in 0.5 M H_2SO_4 over 10 min. (B) Images of the electrode depicting the alteration of the electrode during the electrochemical reduction treatment. The electrode was 1×1 cm. **134**

6.5. SEM images of the electrode showing the morphology before (A) and after (B) the electrochemical reduction. **136**

6.6. EDS spectrum comparing WO_3-3h platelets with WO_3 nanospheres. **137**

6.7. (A) Cyclic voltammograms comparing the photocurrent of WO_3-3h plates and the resulting nanospheres. (B) The transient photocurrent-time profiles of the WO_3-3h and WO_3 nanospheres under UV-visible irradiation in 0.5 M H_2SO_4 under 1.0 V of applied potential **138**

6.8. Scanning kinetic curves for the photoelectrochemical oxidation of 4-NP in 0.1 M H_2SO_4 at the WO_3-3h (A) and WO_3 nanospheres (B) under UV irradiation and applied bias of 1 V . **139**

6.9. Figure showing relationship between ln(C/Co) and time for the photoelectrochemical oxidation of 4-NP in 0.1 M H_2SO_4 at the WO_3-3h (blue) and WO_3 nanospheres (red) under UV irradiation and applied bias: 1V. **140**

7.1. SEM images of WO_3 (A and B) and WO_3/Pt (C and D). **150**

7.2. Comparison of the EDS and XRD results of the WO_3 (red) and WO_3/Pt (blue) **152**

7.3. (A) Cyclic voltammograms of the WO_3 electrodes under dark (blue) and under the visible light (red). (B) Comparison of the CVs of WO_3 before and after the deposition of the Pt nanoparticles **154**

7.4. (A) Mott-Schottky plot of the WO_3 (red) and WO_3-Pt (blue) obtained in 0.1 M H_2SO_4 at 500 Hz. (B) Mott-Schottky plot of the WO_3-Pt **156**

7.5. Chronoamperometry results for A) WO_3 (under dark and visible), B) Comparison of WO_3 and WO_3-Pt and C) WO_3-Pt under a dark and visible light. 1.8 V was applied for all these measurements. **158**

7.6. The degradation curves of RhB on WO_3 under EC (A), visible light irradiation (B) and under both EC and visible light (C), WO_3/Pt under EC (D), visible light irradiation (E) and under both EC and visible light (F)..... **160**

7.7. The kinetic curves of the degradation of RhB on WO_3 (A) and on WO_3/Pt (B) **162**

8.1. SEM (A) and high magnification SEM image (B) of prepared WO_3 platelets **174**

8.2. (A) SEM image of WO_3/IrO_2-Ta_2O_5 showing 'mud-crack' type morphology and (B) high magnification image of WO_3/IrO_2-Ta_2O_5 showing presence of IrO_2-Ta_2O_5 in between the WO_3 platelets **175**

8.3. EDS (A) and XRD (B) results of WO_3 and WO_3/IrO_2-Ta_2O_5. ..... **176**

8.4. Cyclic voltammograms for (A) WO_3, (B), WO_3/Ta_2O_5 (C) WO_3/IrO_2 and (D) WO_3/IrO_2-Ta_2O_5 in 0.5 M H_2SO_4 with a sweep rate of 50 mV/sec **179**

8.5. Cyclic voltammograms for WO_3/IrO_2-Ta_2O_5 in 0.5 M H_2SO_4 with different sweep rates... **180**

8.6. (A) Galvanostatic charging/discharging curves of the WO_3/IrO_2-Ta_2O_5 based supercapacitor at different constant currents. (B) Stability test of the WO_3/IrO_2-Ta_2O_5 based supercapacitor **182**

8.7. (A) Electrocatalytic oxidation of rhodamine B at the WO_3/IrO_2-Ta_2O_5. (B) Kinetic relationship between ln(C/Co) and time for WO_3 and WO_3/IrO_2-Ta_2O_5..... **183**

List of Tables

4.1 Textural properties of the samples determined by BET and XRD studies. **78**

4.2 Band gap estimation for prepared nanomaterials..... **80**

4.3 Chemical constitution of the samples determined by XPS.. ..... **82**

4.4 First order kinetic constant and relative coefficient for degradation of rhodamine B over prepared samples..... **86**

5.1 First order kinetic constants and the relative coefficients for degradation of rhodamine B over prepared samples..... **105**

5.2 First order kinetic constants and relative coefficients for the degradation of rhodamine B over the TNW samples prior to and following the UV pretreatment and P25 under UV light. ... **107**

5.3 First order kinetic constants and the relative coefficients for the stability tests.. ..... **117**

7.1 The calculated rate constants for the degradation of the RhB on WO_3 (A) and WO_3/Pt (B) under applied conditions. **163**

8.1 The calculated specific capacitance for different scan rate..... **181**

List of Abbreviations and Symbols

Ar	Argon
C	Concentration
CA	Chronoamperometry
CV	Cyclic Voltammetry
CB	Conduction band
DMFC	Direct methanol fuel cell
DSSC	Dye sensitized solar cell
EC	Electrochemical
EDLS	Electric double layer supercapacitor
EDS	Energy-dispersive X-ray spectroscopy
E_g	Band gap
ES	Electrochemical supercapacitor
ΔE_e	Difference between the equilibrium electrode potentials
F	Faraday constant
I	Current
I_{max}	Maximum current
IL	Ionic liquids
N	Nitrogen
PS	Polystyrene
Q	Charge
RhB	Rhodamine B

SAED	Selected area electron diffraction
sccm	Standard cubic centimeters per minute
SEM	Scanning electron microscopy
T	Temperature
TEM	Transmission electron microscopy
TNW	N,W co-doped TiO_2
UV	Ultraviolet
UV-Vis	Ultraviolet-Visible
VB	Valence band
W	Tungsten
XRD	X-ray diffraction spectroscopy
η_A	Overpotential at the anode
η_C	Overpotential at the cathode
4 NP	4- Nitrophenol

Table of Contents

Abstract ..... **I**

Acknowledgments ..... **V**

List of Figures ..... **VI**

List of Tables ..... **IX**

List of Abbreviations and Symbols ..... **X**

Chapter 1. Introduction **1**

1.1. Nanotechnology and its applications 1

1.2. Environmental catalysis 3

1.2.1. Heterogeneous photocatalysis 4

1.2.1.1 Semiconductor nanomaterials based heterocatalysts 6

1.2.2. Electrocatalysis 8

1.3. Metal oxide nanomaterials in energy storage 9

1.4. Dissertation, Rationale and Scope 11

References 13

Chapter 2. Literature Review **18**

2.1. Introduction 18

2.2. Development of TiO_2 based photocatalyst 19

2.2.1. First generation of TiO_2: Pure TiO_2 nanomaterials 19

2.2.2. Second generation: Metal doped TiO_2 20

2.2.3. Third generation: Non-metal doped TiO_2 21

2.3. Polymorphs of TiO_2 22

2.4. WO_3: Introduction and properties. 24

2.5. Methods used in the preparation of TiO_2 and WO_3 materials. 26

2.5.1. Sol-gel method 26

2.5.2. Sol method (non-hydrolytic sol gel method) 30

2.5.3. Hydrothermal method 30

2.5.4. Solvothermal method 32

2.5.5. Oxidation method 33

2.5.6. Electrodeposition method 34

2.5.7. Chemical vapor deposition 35
2.5.8. Physical vapor method 36
2.5.9. Sonication method 37
2.6. Applications of TiO_2 38
2.6.1. Photocatalytic applications 38
2.6.2. Photocatalytic water splitting 39
2.6.3. Electrochromic devices 40
2.6.4. Hydrogen storage 41
2.6.5. TiO_2 in dye sensitized solar cells (DSSC) 42
2.7. Applications of WO_3 42
2.7.1. Photocatalytic applications 42
2.7.2. Photocatalytic water splitting 43
2.7.3. Electrochromic devices 44
2.7.4. Dye sensitized solar cells 45
2.8 Electrochemical Supercapacitors (ES) 46
2.8.1 Classification of ES 47
2.8.1.1 Electrostatic capacitors or electric double layer supercapacitor (EDLS) 48
2.8.1.2 Faradaic supercapacitors (FS) 49
2.9 Summary and perspectives 50
References 51
Chapter 3. Materials and Methods **62**
3.1. Introduction 62
3.2. Experimental 62
3.2.1. Materials 62
3.2.2. Instruments and electrochemical experiments 63
3.2.3. Fabrication of electrodes 64
3.2.3.1. Synthesis of N-W co-doped TiO_2 64
3.2.3.2. Fabrication of TiO_2 nanotubes 64
3.2.2.3. Fabrication of WO_3 platelet electrodes 65
3.3. UV treatment of TiO_2 nanotubes and N, W co-doped TiO_2 66
3.4. Photocatalytic and electrocatalytic measurements. 66

3.5 Measurement of capacitance 67

References 67

Chapter 4. Synthesis of Mesoporous Nitrogen-Tungsten co-doped TiO_2 Photocatalysts with High Visible Light Activity **68**

4.1. Introduction 68

4.2. Experimental 70

4.2.1. Photocatalyst synthesis 70

4.2.2. Characterization techniques 71

4.2.3. Photocatalytic activity measurements 72

4.3. Results and discussion 73

4.3.1. XRD analysis 73

4.3.2. TEM observation 74

4.3.3. BET surface area and pore structure 76

4.3.4. UV-visible spectroscopic studies 78

4.3.5. XPS analysis 80

4.3.6. Visible-light-induced catalytic activity studies 83

4.4. Conclusions 88

References 89

Chapter 5. Significant Enhancement in the Photocatalytic Activity of TiO_2 Nanotubes and N,W co-doped TiO_2 Nanomaterials **94**

5.1. Introduction 94

5.2. Experimental 96

5.2.1. Materials 96

5.2.2. Photocatalyst synthesis and UV pretreatment 96

5.2.3. Characterization techniques 97

5.2.4. Photocatalytic activity measurements 98

5.3. Results and discussion 99

5.4. Conclusions 119

References 120

Chapter 6. Direct Growth and Photo-Electrochemical Study of WO_3 Nanostructured Materials **127**

6.1. Introduction 127

6.2. Experimental 128
6.3. Characterization techniques 128
6.4. Results and discussion 129
6.5. Conclusions 140
References 141
Chapter 7. WO_3 Based Bifunctional Electrode for Environmental Applications 145
7.1. Introduction 145
7.2. Experimental 147
7.2.1. Materials 147
7.2.2. Photocatalyst synthesis 147
7.2.3. Deposition of Pt nanoparticles on the surface of WO_3 electrode 148
7.2.3. Characterization techniques 148
7.2.5. Photocatalytic activity measurements 149
7.3. Results and discussion 149
7.4. Conclusions 164
References 164
Chapter 8. High Performance WO_3 Supported IrO_2-Ta_2O_5 for Energy Storage Applications. 169
8.1. Introduction 169
8.2. Experimental 171
8.2.1. Materials 171
8.2.2. Synthesis of WO_3 platelets and deposition of IrO_2-Ta_2O_5 171
8.2.3. Characterization techniques 172
8.2.4. Photocatalytic activity measurements 172
8.3. Results and discussion 173
8.4. Conclusions 185
References 186
Chapter 9. Conclusion and Future Prospects 190
9.1. Conclusions 190
9.1.1. Synthesis and characterization of TiO_2 based nanomaterials photocatalysts 190
9.1.2. Synthesis of WO_3 based nanomaterials for environmental applications 192

9.2. Future work 194

Chapter 1: Introduction

Over the last several decades, a number of reports have articulated the growing importance of semiconductor based nanomaterials for energy harvesting and energy storage applications [1-3]. Among all of the studied heterogeneous photocatalysts, semiconductor oxides, particularly TiO_2 and WO_3 based nanomaterials have established their superiority due to their low cost, non-toxicity, high efficiency, chemical inertness and ability to be synthesized in various morphologies [4-7]. Due to these unique attributes, TiO_2 and WO_3 based nanomaterials are highly attractive for various applications including photocatalysis, electrochromic devices, dye sensitized solar cells, hydrogen production, and gas/chemical sensing. In the following sections a brief introduction of this facet of nanotechnology and its applicability to environmental science is provided, which is followed by a brief survey of electrochemical supercapacitors. A detailed review of the properties, methods of synthesis and applications of TiO_2 and WO_3 is presented in the next chapter.

1.1 Nanotechnology and its applications

Nanotechnology comprises a set of fundamentally enabling technologies that may be utilized in the design and precisely controlled fabrication, or self-assembly of extremely small constituents of matter, at the atomic and/or molecular scale, with at least one characteristic dimension that is measured, typically from 1 to 100 nm [8,9]. The first scientist to suggest that in the future materials might be fabricated to nanoscale dimensions was Richard Feynman, who famously quoted in 1959 that “The principles of physics, as far as I can see, do not speak against the possibility of maneuvering things atom by atom. It is not an attempt to violate any laws; it is something, in principle, that can be done but, in practice, it has not been done because we are too

big." [10]. The popularization of nanotechnology was subsequently articulated by K. Eric Drexler in his 1986 book *Engines of Creation*, wherein, for example, he described the "synthesis" of a jet engine in solution via the coordinated efforts of millions of sophisticated autonomous nanorobotic assemblers [11]. The actual term 'nanotechnology' was initially coined by Noiro Taniguichi in 1974, and although still in its nascent stages, great strides have been made in terms of its capabilities [12]. Enormous frontiers and opportunities stand before researchers worldwide, who are addressing various problems and providing their solutions via the synthesis and integration of various classes of unique nanomaterials, which may be employed for the betterment of humankind. The impacts of nanotechnology may be seen in many areas (there are currently over 1,600 products on the market in which it is incorporated), encompassing engine oils, automobile tires, sunscreens, cosmetics, textiles, sports equipment, foodstuffs and myriad other products [13-19]. It would not be an exaggeration to suggest that nanotechnology is the future, as it is currently one of the most potent tools available in the research community. It has been instrumental toward the development of various useful technologies, such as the Scanning Tunnel Microscope (STM), Atomic Force Microscope (AFM) and other ultra-precision systems. It is also contributing increasingly to various facets of medicine, pharmaceuticals and diagnostics, industrial processes, agriculture and the food industry [20, 21].

As aforementioned, it is quite likely that nanotechnology will play a significant role in tackling a wide range of global challenges. Currently, one of the major challenges that confronts human society is the deteriorating environmental conditions that are caused by the anthropogenic contamination of air, water and soil [22, 23]. This technology could be utilized to manufacture nanosensors for the detection of toxic materials and leaks thereof. When contaminants are detected, TiO_2 and other semiconductor based photocatalyst nanomaterials might be used in the

degradation of pollutants via self-cleaning systems. Another area where nanomaterials are initiating considerable paradigm shifts is the energy sector, as there is a direct correlation between energy use and standard of living. As non-renewable sources of energy will inevitably be depleted, the current focus is increasingly on alternative and clean sources of energy, such as solar, wind, hydrogen and fuel cells [24]. Nanotechnology is contributing significantly in these areas, as new nanomaterials for hydrogen storage and generation, as well as photovoltaic/solar cells have been successfully synthesized and are undergoing further optimization through the intensive study of various combinations of different elements. Metallic electrocatalysts have demonstrated superiority when they are incorporated into fuel cells such as direct methanol fuel cell (DMFC) [25]. Nanomembranes have the capacity for being utilized in water purification, desalination and detoxification [26]. Additionally, nanotechnology is contributing to medicine, food processing and storage, the construction industry, health monitoring, diagnostics and agriculture.

1.2 Environmental catalysis

Environmental catalysis refers to catalytic technologies that serve to assist with the reduction of emissions of environmentally unacceptable compounds, as well as the destruction of contaminants that are present in the environment. Over the last two decades the presence of environmental catalysis in the worldwide catalyst market has grown tremendously, as the growing human population, rapid industrial growth and depleting energy resources have imposed a significant negative impact on the environment, resulting in myriad health issues and quality of life degradation. Catalysis can thus assist in the promotion of sustainability, energy, quality of life and health. In today's world, over 90% of all industrial chemicals are produced via the application of catalysis during their synthesis. The Freedonia Group estimated that in 2012, the

global demand for catalysts increased to USD 16.3B, which was nearly double from what it was in 1998 (USD 9.3B). Catalysts are employed primarily in the chemical industry, petrochemicals (refining), polymerization and environmental applications [27]. They facilitate significant increases in the efficiency of reactions, and to reduce the generation of environmentally hazardous bi-products.

The release of industrial waste products into the environment is a major growing concern, however; dedicated environmental catalysts have great potential for being at the forefront of the resolution of this multifaceted issue. Heterogeneous catalysts are employed in wastewater treatment applications as they can be repeatedly utilized and are comparatively very easy to recover via filtration, centrifuge techniques and semipermeable membranes following the completion of reactions as the catalysts exist in a different phase than that of the reaction mixture [28]. They may be activated by applying an external voltage or by photo irradiation.

1.2.1 Heterogeneous photocatalysis

Photocatalysts absorb incident light, which then initiates a sequence of chemical reactions of interest. Typically, photocatalysts are very stable under photonic irradiation and thus, do not undergo photolysis, which makes it possible for them to endure repetitive cycles of photocatalysis without any loss of activity [29].

The pioneering work of Fujishima and Honda in 1972 involved the irradiation of TiO_2 to enable the photocatalytic cleavage of water molecules in the production of hydrogen [30]. Since this initial discovery, an extensive volume of research has been devoted toward the development of photocatalysts and the exploration of new application areas where they might have beneficial effect. Photocatalysts are not restricted solely to oxidative cleavage reactions, as they may also

be employed in various synthesis modes such as reduction, isomerization, substitution, condensation and polymerization reactions. While playing a significant role in synthetic chemistry, photocatalysts also contribute to sustainable chemistry, as their use has a minimal impact on the environment, and the reaction conditions are much milder than they would be otherwise, without the assistance of photocatalysts.

Photodegradation is generally assigned to the total oxidative mineralization of compounds under the influence of a photocatalyst in which complex organic compounds are typically oxidized to very elemental molecules, such as carbon dioxide and water. The rapidly accumulating surge in environmental pollution worldwide necessitates an urgent response in terms of the development of clean and efficacious methods for the thorough eradication of environmental contaminants so as to limit their negative effects on ecosystems. Effective photocatalysts might be utilized to convert contaminants to value added products via photo oxygenation, photooxidative cleavage and other oxidative conversions [31].

Subsequent to irradiation, in a general photocatalytic reaction, activated photocatalysts produce mobile electrons and vacant holes. These electrons and holes then react with surface adsorbed species such as O_2 and H_2O. O_2 reacts with electrons and produces $O_2^{\bullet-}$ species, while H_2O reacts with the holes which results in the formation of $OH^{\bullet}$ free radicals. These active species possess very high oxidizing potencies, and react with the organic contaminants that are present on the catalyst surface. These steps may be summarized as follows.

(a) Absorption of energy

Photocatalyst + $h\nu \rightarrow h^+ + e-$

(b) Generation of active oxygen species

$O_2 + e- \rightarrow O_2^{\bullet-}$

$H_2O + h^+ \rightarrow H^+ + OH^{\bullet}$

(c) Oxidation of dye

Contaminant + $O_2^{\bullet-} \rightarrow$ products

Contaminant + $OH^{\bullet} \rightarrow$ products

New developments in photocatalyst research have led to their utilization in the abatement of air pollution toward potential reductions in the levels of greenhouse gases such as nitrous oxide (N_2O), methane (CH_4) and CO_2.

1.2.1.1 Semiconductor nanomaterials based heterocatalysts

The optimization of all steps in photocatalysis is necessary toward obtaining selectivity in the reactions during the photocatalytic process. There are various factors which affect the activity and selectivity of the electrodes, such as surface area, morphology, porosity, and the surrounding environment, as all of these characteristics contribute to the physical and chemical characteristics of the photocatalytic system. Over the past decade a number of novel synthetic routes and techniques have been developed to facilitate the preparation of photocatalytic materials and have provided a high level of control over synthesis procedures to attain desired photocatalyst compositions, dimensions and morphologies. The capacity for the synthesis of photocatalysts at nanometer scales has spurred a new era in the field of catalysis, as these diminutive particles exhibit much more robust activity as compared to larger molecules and single crystal catalysts [32]. This is because they possess very high surface-area-to-volume ratios due to their nanoscale dimensions. These nanoscopic photocatalysts can enable improved control over atomic level activities, while elucidating their underlying kinetics.

Since the discovery of the photoinduced decomposition of water on TiO_2 electrodes under UV light (Fujishima and Honda, 1972) enormous research efforts have been invested toward the further development of this technology, as well as investigations into a host of new materials which might serve as optimal candidates in this process. Over the last few decades a large number of semiconductors and semiconductor oxides have been studied, which include TiO_2, CdS, SnO_2, WO_3, SiO_2, ZrO_2, ZnO, Nb_2O_3, Fe_2O_3, $SrTiO_3$, CeO_2, Sb_2O_4, and V_2O_5. Further research is focussed on the discovery and investigation of additional new semiconductor based compounds [33].

Fujishima and Honda originally utilized UV light energy to excite TiO_2 VB electrons. Subsequently, however, various efforts have been focussed on enabling these photocatalysts to operate under low energy wavelengths, with the ultimate goal of making them responsive to visible light. The ideal dual aims would be to reduce reaction costs, while establishing techniques to facilitate these photocatalysts to function under exposure to ambient sunlight, which is a vast and unlimited renewable source of energy.

Despite the numerous aforementioned capabilities of nanometric photocatalysts there remain several challenges to be overcome prior to this technology being transitioned to efficient applications in environmental remediation. Foremost is the improvement of their efficiency, by means of decreasing electron hole recombination events, in which excited mobile electrons revert to the valence band to combine with vacant holes. Research efforts toward improving the photocatalytic activity of TiO_2 under visible light or the identification of new materials that have the capacity to convey a high photocatalytic response under exposure to ambient sunlight have led to the development of visible light driven photocatalysts. Further research, however, is

required to ensure that their stability, efficiency, and activity are relatively equivalent to that of UV light driven photocatalysts.

1.2.2 Electrocatalysis

The requirement for efficacious and economical electrocatalytic materials is most conspicuous in large electrolytic processes that require vast amounts of energy, where the cost of electric power is a major factor in the determination of the efficiency and economics of the process [34]. Prime examples include the chlor-alkali industry, aluminium extraction, large scale water electrolysis, large battery systems for load levelling or energy storage and fuel cells. These industrial processes consume thousands of kWh/year of electric power, where the cost of electricity is a major portion of the total production cost. The consumption of energy of an electrolytic cell is proportional to its voltage (V), which is given by an equation of the type

$$V = \Delta E_e - \eta_A + \eta_C - IR \quad (1)$$

where ΔE_e is the difference between the equilibrium electrode potentials for the two electrode reactions, η_A and η_C are the overpotentials at the anode and cathode, respectively (both will increase the numerical value of the negative cell voltage), and the IR term expresses the Ohm's law losses through the electrolyte and other current-carrying cell components. In general, an electrocatalyst may be defined as a catalyst that accelerates the rate of electrochemical reactions. Thus, electrocatalysis is the science of minimizing the overpotential terms.

In the past, electrocatalysis was employed primarily for academic purposes. Recently it has gained considerable importance, as it has facilitated the emergence of new concepts in industrial electrochemical processes. With continual advancements in new technologies, the design and preparation of electrocatalysts is far simpler and may be more easily controlled. The

core concepts that are utilized in tailoring electrocatalysts are controlled surface roughness, atomic topographic profiles, defined catalytic centre sites, atomic rearrangements and phase transitions in the course of the electrochemical reactions [35]. The reaction rates at the surface of the electrocatalyst may be controlled by the electrode surface structure, electrode potential, electrolyte and a number of additional electrochemical variables.

In redox reactions, the storage and consumption of electrons in chemical bonds takes place. For securing the future availability of sustainable energy much focus has been put toward electrochemistry, as redox reactions play an important role in various devices such as fuel cells, batteries, electrolyzers, as well as naturally occurring processes that are related to energy conversion in living systems. Pt and Pd based electrodes have been widely investigated for fuel cell applications, in that these electrodes possess very high surface areas and electrocatalytic activity toward the oxidation of various fuels [36]. The high cost and poisoning of these electrodes are major drawbacks for their application. Their resolution may be realized by using various approaches, such as the formulation of bimetallic or trimetallic alloys, or via the deposition of expensive noble metals on other nanomaterials, which may serve to significantly reduce the volumes required and thus decrease the overall cost of electrode fabrication [37]. Various materials have been utilized as substrate in the past, such as carbon nanotubes, different metal foils, glassy carbon, etc. TiO_2 and WO_3 based materials might be employed to provide a stable and economical substrate for the deposition of precious metal atoms.

1.3 Metal oxide nanomaterials in energy storage

Concurrent with the rapid evolution of portable electronics and hybrid electrical vehicles, there has been an ever increasing demand for high capacity energy storage devices. Hence, two major challenges for electrochemical technologies are the development of new renewable

sources of energy and energy storage materials. Electrochemical supercapacitors have attracted a great deal of interest as they possess improved power and energy densities and much longer life cycles compared with batteries and conventional capacitors [38]. The inherently low energy density of conventional supercapacitors limits the wide applicability of this technology, and hence other materials have been explored for their potential utilization as supercapacitors. Among all of the studied materials in the recent past, transition metal oxides have emerged as being the most suitable due to the variable oxidation states of the metals, which facilitate redox reactions. Metal oxides should have higher surface areas, as supercapacitor properties are directly controlled by the redox reactions that take place at the surface of the electrode. Thus, varying the dimensions and morphologies of identical materials causes differences in their electrochemical performance.

Hydrous RuO_2 has emerged as the most suitable contender for utilization in supercapacitors as the result of its exceptional supercapacitance properties [39]. The limitations for the practical utilization of RuO_2 as a supercapacitor include its very high cost. Various other transition metal oxides have also been investigated to identify eco-friendly and less expensive alternatives for RuO_2, such as NiO, MnO_2, SnO_2, Co_3O_4 and CuO [40-42]. There remains an urgency to develop novel supercapacitor materials to increase efficiency and charge storage, while decreasing the cost of supercapacitor materials. One approach that might be implemented to further reduce the amount of metal oxide required is to deposit precious supercapacitor materials onto a substrate with an extensive surface area. As mentioned previously, TiO_2 and WO_3 provide very stable and affordable alternative to the deposition of noble metals, and thus they might be utilized as substrates for incorporation into supercapacitors.

1.4 Dissertation, Rationale and Scope

The central theme of this dissertation relates to articulating the roles that are played by TiO_2 and WO_3 based nanomaterials in photocatalytic, electrocatalytic and energy storage applications. The primary research objectives are:

1) The fabrication of various TiO_2 based nanomaterials using facile solution combustion and anodization methods.
2) To study the effects of N and W co-doping on the photocatalytic activity, morphology and other physical attributes of TiO_2.
3) To study the synergetic effect of co-doping on TiO_2 activities.
4) The development of methods to enhance the activity of TiO_2 based nanomaterials.
5) Fabrication of WO_3 photocatalysts and their employment in wastewater treatment.
6) Utilization of WO_3 materials as a substrate for use in other applications such as energy storage.

In the ensuing chapters, recent advancements in the development of TiO_2 and WO_3 based materials with different properties and morphologies will be reported along with their potential applications in photocatalysis, electrocatalysis and as energy storage materials.

Chapter 2 will showcase various fabrication methods, properties and applications of TiO_2 and WO_3 materials, followed by an examination of future prospects in this field. In Chapter 3, procedures for the fabrication of reported materials and different characterization techniques used to elucidate morphological, as well as physical and photocatalytic and/or electrocatalytic properties will be discussed. In Chapter 4, a facile method will be reported for the synthesis of N doped TiO_2 and N,W co-doped TiO_2. The morphology, composition and properties of the

samples were characterized by X-ray Diffraction (XRD), Transmission Electron Microscope (TEM), N_2 Adsorption Desorption and X-ray Photoelectron Spectroscopy (XPS). The photodegradation of RhB was employed to evaluate the visible light activity of the samples. A novel UV treatment method to conveniently and efficiently enhance the activity of the TiO_2 nanotubes and N,W co-doped samples is reported in Chapter 5. The effects of UV treatments on TiO_2 nanotube electrodes were characterized by SEM, EDS, CV, potential step chronoamperometry and Mott-Schotty plots. For N,W co-doped samples N_2 adsorption desorption studies, TEM, XRD, XPS and photodegradation studies of RhB were utilized.

Chapter 6 reports on a facile and effective approach for the synthesis of WO_3 nanospheres in conjunction with a study of the WO_3 platelet growth mechanism under hydrothermal conditions via an electrochemical reduction technique. WO_3 platelets with variable dimensions were grown directly on W substrates over different treatment timelines during the hydrothermal process. To the best of our knowledge, the electrochemical treatment method was employed for the first time to investigate the mechanism of WO_3 crystal growth under hydrothermal conditions. The observed WO_3 nanospheres were observed to be well distributed on the substrate, with an average nanoparticle diameter of ~50 nm. These secondary nanospherical WO_3 particles demonstrated a much more robust photocurrent than did their parent platelets. The activities of these samples were also evaluated via 4-nitrophenol (4-NP) oxidation, which showed that these nanospherical particles had a seven-fold photocatalytic enhancement over their parent platelets. In Chapter 7, a WO_3 based bifunctional electrode is described, where Pt is deposited on one side of the electrode, which behaves as an electrocatalyst under applied potential and the other side of the WO_3 was irradiated by visible light. The synergetic effects of both the applied potential and photocatalysis are also reported in terms of their activities on the

electrodes. Chapter 8 reports on the fabrication of WO_3 supported IrO_2-Ta_2O_5 electrodes for supercapacitance applications, for the first time. The various characterization methods indicated that Ta_2O_5 and IrO_2 have a synergetic effect, which induces the electrode to store a much higher charge. The electrode demonstrated very high stability, as was verified by a 5000 cycle stability test.

References

[1] T. Tatsuma, S. Saitoh, Y. Ohko, A. Fujishima. TiO_2-WO_3 Photoelectrochemical anticorrosion system with an energy storage ability, *Chemistry Matererials* 13 (**2001**) 2838-2842

[2] A. I. Hochbaum, P. Yang. Semiconductor nanowires for energy conversion, *Chemical Reviews* 110 (**2010**), 527–546

[3] S. Manzettia, O. Andersena. Toxicological aspects of nanomaterials used in energy harvesting consumer electronics, *Renewable and Sustainable Energy Reviews* 16 (**2012**) 2102–2110

[4] S. Wang, Zi-X. Lin, W-H. Wang, C. L. Kuo, K. C. Hwang, C-C. Hong. Self-regenerating photocatalytic sensor based on dielectrophoretically assembled TiO_2 nanowires for chemical vapor sensing, *Sensors and Actuators B* 194 (**2014**) 1–9

[5] Y. Jiang, Y. Luo, F. Zhang, L. Guo, L. Ni. Equilibrium and kinetic studies of C.I. Basic Blue 41 adsorption onto N,F-codoped flower-like TiO_2 microspheres. *Applied Surface Science* 273 (**2013**) 448–456

[6] F. Hea, J. Li, T. Li, G. Li, Solvothermal synthesis of mesoporous TiO_2: The effect of morphology, size and calcination progress on photocatalytic activity in the degradation of gaseous benzene. *Chemical Engineering Journal* 237 (**2014**) 312–321

[7] C. A. Bignozzi, S. Caramori, V. Cristino, R. Argazzi, L. Meda, A. Tacca. Nanostructured photoelectrodes based on WO_3: applications to photooxidation of aqueous electrolytes, *Chemical Society Reviews* 42 (**2013**) 2228—2246

[8] A. Helland, H. Kastenholz. Development of nanotechnology in light of sustainability, *Journal of Cleaner Production* 16 (**2008**) 885-888

[9] J. J. Ramsden. What is Nanotechnology? *Applied Nanotechnology* (Second Edition) (**2014**) 3–12

[10] R. Fynman. There's plenty of room at the bottom, *Engineering and Science* 23 (**1960**) 22–36.

[11] K. E. Drexler. Engines of creation: The coming era of nanotechnology 1986. *Anchor Double Day New York* (**1986**)

[12] N. Taniguchi. On the basic concept of nanotechnology, *In: Proceedings of International Conference on Production Engineering. Part II. JSPE. Tokyo* (**1974**) p18.

[13] E. Ettefaghi, H. Ahmadi, A. Rashidi, A. Nouralishahi, S. S. Mohtasebi. Preparation and thermal properties of oil-based nanofluid from multi-walled carbonnanotubes and engine oil as nano-lubricant International, *Communications in Heat and Mass Transfer* 46 (2013) 142–147

[14] Z. A. Lewicka, W. W. Yu, B. L. Oliva, E. Q. Contreras, V. L. Colvin. Photochemical behavior of nanoscale TiO_2 and ZnO sunscreen ingredients, *Journal of Photochemistry and Photobiology A: Chemistry* 263 (**2013**) 24–33

[15] C. Botta, J. Labille, M. Auffan, D. Borschnec, H. Miche, M. Cabié, A. Masion, J. Rose, J. Bottero. TiO_2-based nanoparticles released in water from commercialized sunscreens in a

life-cycle perspective: Structures and quantities, *Environmental Pollution* 159 (**2011**) 1543-1550

[16] A. Mihranyan, N. Ferraz, M. Strømme. Current status and future prospects of nanotechnology in cosmetics, *Progress in Materials Science* 57 (**2012**) 875–910

[17] F. Noor-Evans, Nanotechnology innovation for future development in the textile industry. *New Product Development in Textiles* (**2012**) 109–131

[18] Q. Chaudhry. Regulatory frameworks for food nanotechnologies (**2012**) 82–98

[19] M. L. Gulrajani. The use of nanotechnology in the finishing of technical textiles, *Technology & Engineering* (**2013**) 280–308

[20] C. S. S. R. Kumar. Nanotechnology tools in pharmaceutical R&D, *Materials Today* 12 (**2010**) 24–30

[21] B. G. Priestly. Hazards of food contact material: Nanotechnologies and nanomaterials, *Priestly Encyclopedia of Food Safety* (**2014**) 444–448

[22] J. G. Zivin. Pollution and Health, *Encyclopedia of Health Economics* (**2014**) 98–102

[23] L. Liua, L. M. Kauri, M. Mahmud, S. Weichenthal, S. Cakmak, R. Shutt, H. You, E. Thomson, R. Vincent, P. Kumarathasan, G. Broad, R. Dales. Exposure to air pollution near a steel plant and effects on cardiovascular physiology: A randomized crossover study, *International Journal of Hygiene and Environmental Health* 217 (**2014**) 279–286

[24] O. Z. Sharaf, M. F. Orhan. An overview of fuel cell technology: Fundamentals and applications. *Renewable and Sustainable Energy Reviews* 32 (**2014**) 810–853

[25] W. Yuan, B. Zhou, J. Deng, Y. Tang, Z. Zhang, Z. Li. Overview on the developments of vapor-feed direct methanol fuel cells, *International Journal of Hydrogen Energy* 39 (**2014**) 6689-6704

[26] Y.-H. Kim, E.-D. Hwang, W.S. Shin, J.-H. Choi, T.W. Ha, S.J. Choi. Treatments of stainless steel wastewater containing a high concentration of nitrate using reverse osmosis and Nanomembranes, *Desalination* 202 (**2007**) 286–292

[27] J. N. Armor. A history of industrial catalysis, *Catalysis Today* 163 (**2011**) 3–9

[28] I. Fechete, Y. Wang, J. C. Vedrine. The past, present and future of heterogeneous catalysis, *Catalysis Today* 189 (**2012**) 2–27

[29] F. Herrera, A. Lopez, G. Mascolo, P. Albers, J. Kiwi. Catalytic decomposition of the reactive dye UNIBLUE on hematite. Modeling of the reactive surface, *Water Research* 35 (**2001**) 750-760

[30] A. Fujishima, K. Honda. Electrochemical photolysis of water at a semiconductor electrode, *Nature* 238 (**1972**) 37 - 38.

[31] R. Richter, S. Caillol. The potential of photocatalysis against CO_2, CH_4, N_2O, CFCs, tropospheric O_3, BC and other major contributors to climate change, Fighting global warming: *Journal of Photochemistry and Photobiology C: Photochemistry Reviews* 12 (**2011**) 1– 19

[32] N. R. Shiju, V. V. Guliants. Recent developments in catalysis using nanostructured materials, *Applied Catalysis A: General* 356 (**2009**) 1–17

[33] S. S. Thind, M. Tian, A Chen. Direct growth and photo-electrochemical study of WO3 nanostructured materials, *Electrochemistry communications* 43 (**2014**) 13-17

[34] D. Fletcher. Electrochemistry: present and future, *Journal of Applied Electrochemistry* 14 (**1984**) 403-415

[35] C. F. Zinola, M. E.Martins, E. P. Tejera, N. P. Neves Jr. Electrocatalysis: Fundamentals and Applications, *International Journal of Electrochemistry* (**2012**) Article ID 874687, 2 pages

[36] M. Tian, G. Wu, A. Chen. Unique electrochemical catalytic behavior of Pt nanoparticles deposited on TiO_2 nanotubes, *ACS Catalysis* 2 (**2012**) 425−432

[37] Y. Kobayashi, Y. Ishii, H. Yamane, K. Watanabe, H. Koda, H. Kunigami, H. Kunigami. Fabrication of TiO_2/Pt core–shell particles by electroless metal plating, *Colloids and Surfaces A: Physicochemical and Engineering Aspects* 448 (**2014**) 88–92

[38] M. Zhou, T. Tian, X. Li, X. Sun, J. Zhang, Y. Chen, P. Cui, J. Tang, L. Qin. Supercapacitance of chemically converted graphene with composite pores, *Chemical Physics Letters* 581 (**2013**) 64–69

[39] V. D. Patake, C. D. Lokhande. Chemical synthesis of nano-porous ruthenium oxide (RuO_2) thin films for supercapacitor application, *Applied Surface Science* 254 (**2008**) 2820–2824

[40] J. Jiang, A. Kucernak. Electrochemical supercapacitor material based on manganese oxide: preparation and characterization, *Electrochimica Acta* 47 (**2002**) 2381-2386.

[41] P. A. Nelson, J. R. Owen. A high-performance supercapacitor/battery hybrid incorporating templated mesoporous electrodes, *Journal of The Electrochemical Society* 150 (**2003**) A1313-A1317.

[42] D. L. D. Silva, R. G. Delatorre, G. Pattanaik, G. Zangari, W. Figueiredo, R.-P. Blum, H. Niehus, A.A. Pasa. Electrochemical synthesis of vanadium oxide nanofibers, *Journal of The Electrochemical Society* 155 (2**008**) E14-E17.

Chapter 2: Literature Review

2.1 Introduction

Environmental catalysis refers to catalytic technologies that assist with the reduction of emissions of environmentally unacceptable compounds and the destruction of existing pollutants that are present in the environment. These technologies may be roughly divided into two categories including photocatalysts, where light energy is utilized to activate catalysts, and electrocatalysts, which are typically activated via the application of an external potential or current. In photocatalysis, following irradiation with light of suitable wavelength, electrons are excited from the VB to the CB, which triggers a series of reactions at the surface of the photocatalyst [1,2]. These reactions may be summarized in the following figure.

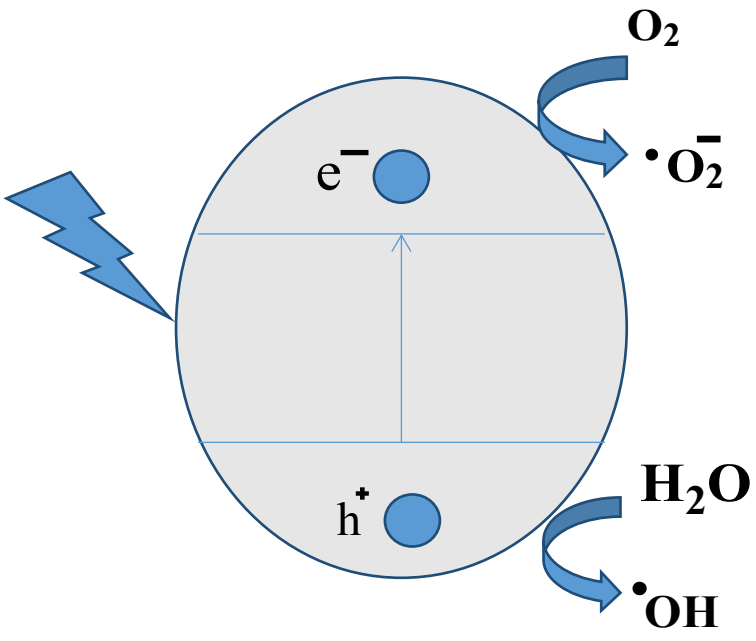

Figure 2.1 Depiction of the basic mechanism of photocatalysis

Over the last two decades metal oxides have been used as key ingredients toward the development of many advanced functional materials and smart devices (electrochromic devices, hydrogen storage, gas sensors, DSSCs) [3]. Due to rapid advancements in nanotechnology, nanomaterials with different morphologies may be fabricated, which has emerged as one of the optimal tools for unlocking the full potential of metal oxides [4, 5]. TiO_2 and WO_3 are unique materials that have been rigorously studied for their chromism, photocatalysis, and sensing capabilities [6-9]. The following sections will present a general review of nanostructured TiO_2 and WO_3, inclusive of their properties, methods of synthesis, and a description of how they might be utilized in unique ways for various applications.

2.2 Development of TiO_2 based photocatalyst

2.2.1 First generation of TiO_2: Pure TiO_2 nanomaterials

First generation nanostructured TiO_2, which is not modified by any means, represents pure TiO_2. Nanostructured TiO_2 has a significantly high surface area due to its diminutive particle size. When particle dimensions are decreased, the band gap becomes wider. This serves to further enhance the redox potential of the holes and electrons that are present in the valence band and conduction bands respectively. Pure TiO_2 may be efficiently used only under UV light, as it requires high energy wavelengths to excite electrons from the valence band to the conduction band [10-11]. Typically, TiO_2 may not be utilized under the visible light, which is a cheaper source of energy, or under ambient sunlight, which is an inexhaustible (relatively speaking) source of energy. Many researchers have employed TiO_2 under UV light to elicit various reactions.

Fox *et al*. used UV irradiated TiO_2 in order to oxidize β-chlorodiethyl sulfide to corresponding sulfoxides, and successively, to sulphones in aerated aqueous, nonaqueous, or mixed solvents [12].

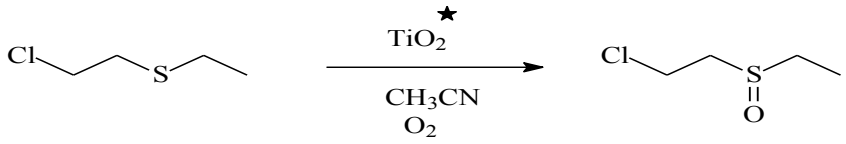

Activated TiO_2 has also been used in isomerization, condensation, substitution, reduction and polymerization reactions [13-16].

A number of studies have been conducted into the decontamination of water from various pollutants using UV irradiated TiO_2, with high efficiency.

2.2.2 Second generation: Metal doped TiO_2

An extensive number of metals have been utilized as dopants, which were incorporated into the crystal structures of TiO_2 nanomaterials (e.g., Fe, Cr, Mo, W, Ru, La, Os, Re, Sn, V, Rh) [17-22]. There are various existing methods by which metal ions may be introduced into the TiO_2 structure. In wet synthesis, TiO_2 nanoparticles are typically fabricated via hydrolysis of a titanium precursor in a mixture of water and other reagents. These reagents normally contain the metal atoms that are needed to be doped into TiO_2. An alternate method for synthesizing metal doped TiO_2 is ion implantation, by which ions of a material are accelerated within an electrical field and impacted into a solid. Apno *et al*. have synthesized a series of Cr and V doped TiO_2 materials using the ion implantation method [23]. The use of CVD was described by Cao *et al*. as an additional method that may be used for doping TiO_2 with Sn [24].

Metal ion doping has a great influence on substrate charge carrier recombination rates and interfacial electron transfer rates. A significant number of factors influence the metal doping

effect, such as the distribution and energy levels of the dopants and electron donor concentrations [25]. Most, but not all, of the metal dopants increase the activity of TiO_2. In some cases, V and Cr doped TiO_2 exhibited reduced activity when compared to that of pure TiO_2 [26, 27]. The explanation as to why some metal dopants demonstrate low activity is primarily due to the promotion of the charge carrier recombination, as new dopant impurity levels in some instances serve as sites for electron hole recombination [25].

2.2.3 Third generation: Non-metal doped TiO_2

The main nonmetal dopants (B, C, Cl, Br, F, S and N) are under study by various research groups [28-30]. Among these, N has emerged as the optimal dopant, which significantly enhances the activity of the doped TiO_2 by increasing its capacity for absorption in the visible portion of the spectrum. The O2p orbital of N has an energy level that is very close to that of the O_2p of O, which constitutes the valence band in TiO_2, thereby facilitating a good interaction [31]. N doped TiO_2 may be synthesized via hydrolysis of titanium tetraisopropoxide (TTIP) in an amine mixture, in conjunction with the post treatment of the TiO_2 sol with amines. The doping of N may also be accomplished using a solution combustion method, by which TTIP in an ethanol solution that contains urea as an N source, is heated to introduce N in the TiO_2 structure during its formation. The synthesis of S doped TiO_2 was achieved by various groups by mixing TTIP with ethanol containing thiourea [32]. The ion implantation of S^- into TiO_2 has also been reported [33].

X. Chen and S. Mao have written a very excellent review article on TiO_2 which gives an insight of every aspect of the TiO_2. They, very well in detail explained various methods of synthesis and the applications of TiO_2 in different applications [25].

2.3 Polymorphs of TiO_2

The three most widely known polymorphs of titanium dioxide are rutile (tetragonal), anatase (tetragonal), and brookite (rhombohedral), which may exist as bulk structures as well as nanoparticles [34, 35]. Structure of Anatase, rutile and brookite phase is shown in Figure 2.2. Anatase and rutile may be visualized as chains of TiO_6 octahedra, where each Ti^{4+} ion is surrounded by an octahedral of six O^{2-} ions. Rutile exists as the most stable form of TiO_2 at high temperatures, in comparison to anatase and brookite which are metastable. Anatase and brookite can, however; be easily transformed to rutile when heated. Anatase is the phase that is normally found in the sol-gel synthesis of TiO_2, but brookite is often observed as a by-product when precipitation is carried out in an acidic medium at low temperature. It is possible to fabricate pure anatase and rutile phases, which has resulted in a great deal of research that is focused on these phases. On the other hand, it is very difficult to synthesize the pure brookite phase without rutile or anatase. This is why brookite is not well studied in terms of exploring its photocatalytic and other properties. Recently, however; there has been much interest among researchers in obtaining pure brookite structures as there are some indications that this phase might poses high photocatalytic properties [36].

The primary difference between anatase and rutile is that the latter phase is more distorted [37]. In anatase, all the Ti-O bonds are not of the same length, as two of the titanium-oxygen bonds are much longer than the others, which induces the O–Ti–O bond angles to deviate more from 90◦ than in rutile. In brookite, although the interatomic distances and O–Ti–O bond angles are similar to those of rutile and anatase, there exist six different Ti–O bonds that range from 1.87 to 2.04 Å in length. In addition, there are also twelve distinct O–Ti–O bond angles that span 77 to 105 Å. In anatase, each octahedron is in contact with eight neighboring octahedrons,

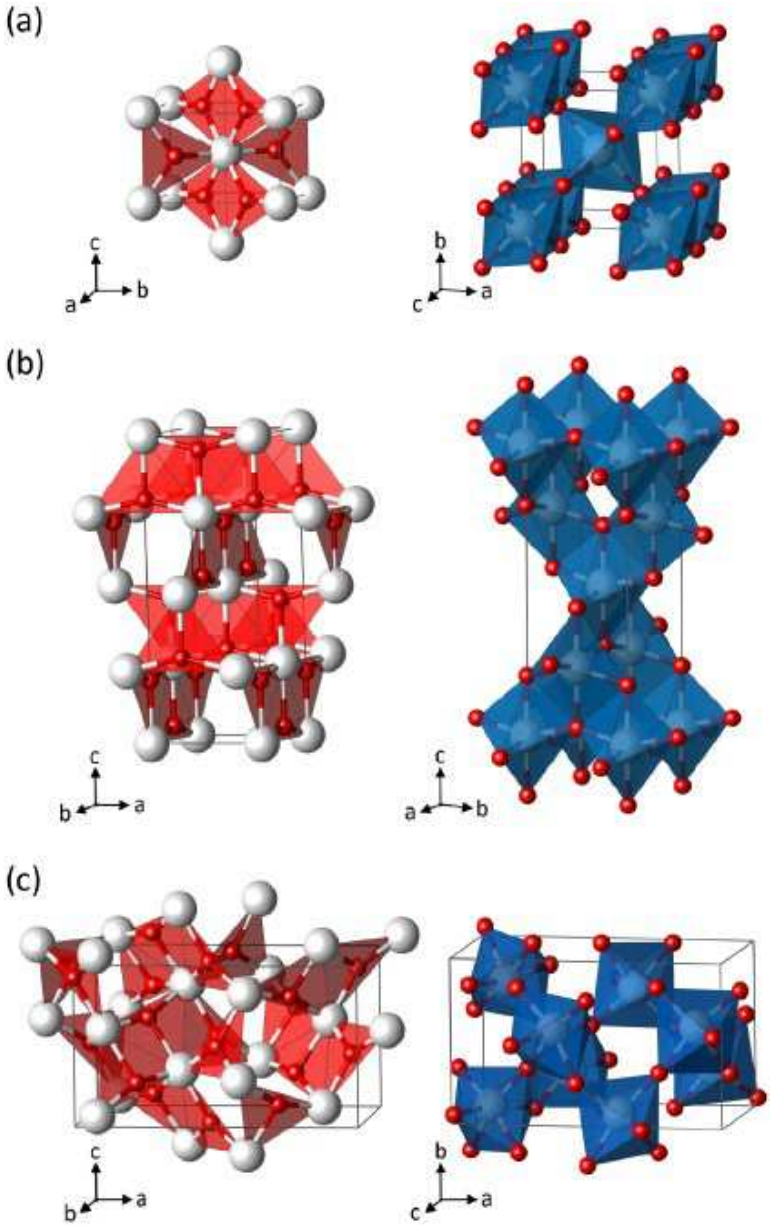

Figure 2.2 Planar Ti_3O building-block representation (left) and TiO_6 polyhedra (right) for the TiO_2 phases rutile (a), anatase (b) and brookite (c) [Ti (white); O (red)] adapted from reference [34] with permission. copyright 2012 IOP science.

four by sharing edge oxygen atoms and four by sharing corner oxygen atoms. In rutile, each octahedron is in contact with 10 neighboring octahedrons, eight of which that share corner oxygen atoms and two that share edge oxygen atoms. Distinct phases of the TiO_2 exhibit different properties and thus have been employed for different applications. Due to its high refractive index, the rutile phase is typically utilized in high-grade, corrosion-protective white coatings and paint, or in plastics, rubber, leather, sunscreens, and paper. The anatase phase has excellent optical and pigment properties due to its electronic structure and is used chiefly as an optical coating and photocatalyst. As mentioned above, brookite has not been much studied as compared to anatase and rutile due to difficulties in synthesis, which has limited its utility.

2.4 WO_3: Introduction and properties.

Tungsten oxide (WO_3) is a semiconductor oxide material with a band-gap of 2.6–3.0 eV that is becoming the focus of much research due to its unique electronic properties [38]. The number of applications of WO_3 is extensive; it may be utilized in (photo) electrochromic "smart" windows, solar energy conversion and storage cells, solar water-splitting cells, a potential catalyst enhancer for fuel cells, photocatalysis, batteries, and gas/chemical sensors [39-42]. WO_3 has the capacity for being synthesized in various nanostructured morphologies, such as nanoparticles, nanoplatelets, nanorods, and nanowires, which impart several unique properties that are not observed in bulk form. The induction of nanocrystallinity significantly alters its surface energies, which allows for the tuning and engineering of its attributes, in that atomic species that are close to the surface have different bond structures than those that are embedded within the bulk [43]. Although the photocatalytic activity and efficacy of WO_3 as a photoanode in DSSC is not comparable to that of TiO_2 and other semiconductor oxides, it has demonstrated its superiority in electrochromism and is being employed in smart windows and EC displays.

The three distinctive crystalline structures that comprise WO_3 includes triclinic, monoclinic, orthorhombic, tetragonal, hexagonal and cubic. The triclinic, monoclinic, orthorhombic, and tetragonal WO_3 phases have the same WO_3 crystals structure, where they are generally formed by corner and edge sharing of WO_6 octahedra, which makes them transform reversibly into one another. They differ only to the extent by which the W atoms are displaced from the center of the WO_6 octahedra. Only triclinic, monoclinic, orthorhombic, tetragonal phases are known for their photocatalytic activity. The crystalline phase of the WO_3 depends to a significant degree on the annealing temperature and the transition from one phase to the other that takes place during annealing and cooling. According to the literature, the phase transformation occurs in the following sequence: monoclinic II (< −43 °C) →triclinic (−43 °C to 17 °C) → monoclinic I (17°C to 330 °C) →orthorhombic (β -WO_3, 330 °C to 740 °C) → tetragonal (α -WO_3,>740 °C) [43-45]

Most of the properties that we are interested in are tailored by the electronic structure of the molecule, and in that sense WO_3 is quite an interesting case. It is a wide-band n-type semiconductor, where the valence band is a 2p orbital of O and the conduction band is empty W 5d orbitals. In the case of WO_3, the band gap is strongly dependant on the crystal phase and the degree of distortion from the ideal cubic phase. In principle, this transition is also accompanied by a change in band gap (E_g), as the occupied levels of the W 5d states change [46]. Amorphous WO_3, which has the most distorted structure, normally possesses a relatively large Eg on the order of ≈3.25 eV, whereas bulk monoclinic WO_3 has been reported to exhibit a typical Eg of ≈2.62 eV at room temperature.

Similar to TiO_2, it is also possible to manipulate the optical properties of WO_3 through doping. The insertion of H, Li, N and Co can induce chromic effects due to changes in the band

gap structure [47-49]. Phase changes in the WO_3 were also reported subsequent to doping, for instance, it is very rare to find cubic WO_3 at room temperature, however; following H intercalation, cubic phase may be observed for the species $H_{0.5}WO_3$, Li_xWO_3, and Na_xWO_3 [50]. WO_3 also undergoes an insulator-to-metal transition after the intercalation of Li, Na, or H, which is due to the position of the energy levels of the dopants. It has been found that the band gap of WO_3 nanowires decreases with N doping, resulting in an increase in conductivity. The conductivity of the electrodes may also be enhanced by the addition of the metal oxides, such as TiO_2, Co_3O_4, MnO_2, LiO and Al_2O_3 [51-53].

2.5 Methods used in the preparation of TiO_2 and WO_3 materials

2.5.1 Sol-gel method

The sol-gel method is likely the most utilized method in the synthesis of TiO_2 nanoparticles, as this technique may be employed to obtain any desired morphology [25]. Typically, a sol is a stable dispersion of colloidal particles (~0.1-1μm) in a liquid, where only Brownian motion suspends the particles. The sol is formed by dissolving metal salts or metal organic compounds. Subsequently, hydrolysis and polymerization takes place in the solution via the removal of the stabilizing components and forms a gel. The gel proceeds to become denser when the removal of the solvent is continued. This step is very critical as it determines the porosity of the gel. Aerogels are very low density materials that are obtained when the solvent is removed under supercritical conditions. Following the complete removal of the solvent the resulting powders are heat-treated to obtain the desired mechanical properties.

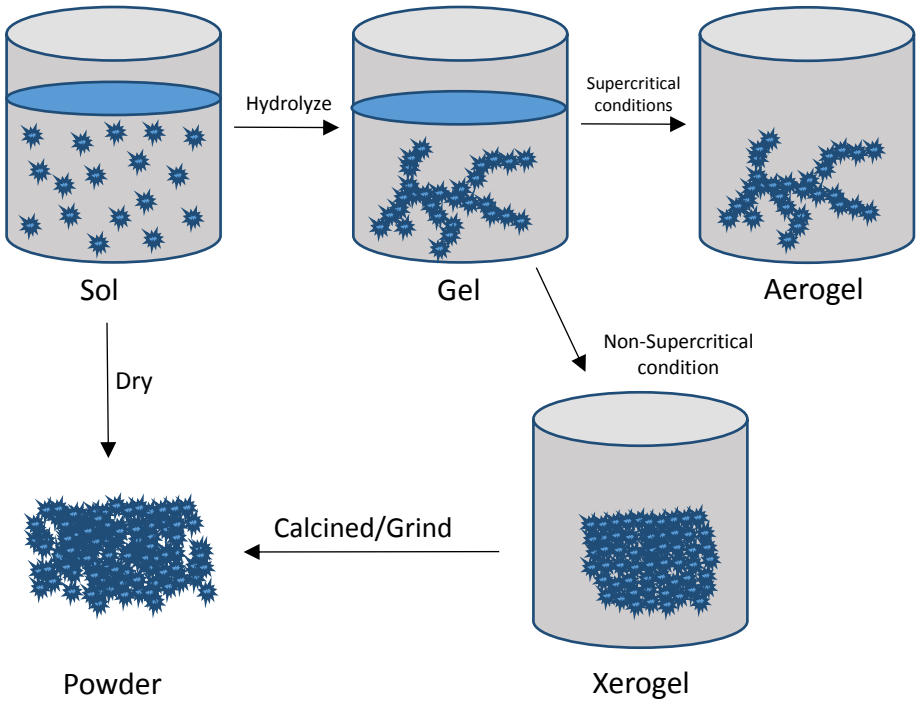

Figure 2.3 Graphic of sol-gel chemistry process

In the case of the synthesis of TiO_2 via the sol-gel method, the process typically undergoes acid-catalyzed hydrolysis of titanium alkoxides followed by condensation. The size and morphology of the particles depends significantly on the hydrolysis rate as Ti-O-Ti bonding is favored at a low hydrolysis rate, which results in the formation of a three dimensional skeleton that is derived from the development of Ti-O-Ti bonds. If the volume of water present in the solution is marginal, the hydrolysis reaction rate is rapid to preferentially form $Ti(OH)_4$, which does not allow for the development of three dimensional polymeric skeletons.

Chemseddine *et. al*. studied the control parameters related to crystal, size, shape and organization of TiO_2 nanocrystals using the sol gel method [25, 54]. In this study the hydrolysis and polycondensation of titanium alkoxide was performed in the presence of tetramethyl

ammonium hydroxide. Briefly, the base was cooled to 2 ^{o}C whereafter the titanium alkoxide dissolved in 2-propanol was introduced dropwise into a three necked flask. During the course of addition, a white precipitate is formed. An aliquot from this solution was then heat-treated at 50-60 ^{o}C for 13 days, or at 90-100 ^{o}C for 6 h. To improve the crystallinity of the prepared samples, a second heat treatment was performed at 175 and 200 ^{o}C for a period of 5h.

The sol-gel method may also be easily employed to synthesize doped and co-doped TiO_2 nanomaterials. J. Li *et al.* synthesized N and W co-doped mesoporous TiO_2 via the hydrolysis of $TiCl_4$ with ammonia in a water solution in the presence of glacial acetic acid and ammonium tungstate, serving as nitrogen and tungsten sources [55]. To avoid the drastic hydrolysis of $TiCl_4$, the $TiCl_4$ solution was introduced very carefully with gentle stirring in an ice bath followed by the addition of the glacial acid and ammonium tungstate. After a 24h aging period, the slurry was rinsed carefully with absolute ethanol three times. The sample was then dried at 353 K for 12 h and calcined at 773 K for 3 h. Various other research groups have contributed in developing TiO_2 based materials with sol-gel method [56-61].

Similar to TiO_2 nanostructures, WO_3 can also be easily synthesized using the sol-gel method. Chan *et al*. synthesized nanostructured WO_3 films utilizing a sol-gel spin coating method. In a typical process, the precursor solutions for WO_3 films were prepared by mixing tungsten hexachloride with anhydrous ethyl alcohol [62]. Silica glass plates (2.5 cm × 2.5 cm) were employed as the substrates. All glass plates were cleaned with detergent soap, alcohol and deionized water prior to coating. The WO_3 coatings were obtained by a spin coating technique and the process was repeated up to seven times in order to obtain a film thickness of ~700 nm. These coatings were then dried at room temperature for 5 min. and annealed in air under 100–

400 °C for 1 h. The gasochromic device was then prepared by sputtering a layer of platinum (Pt) over the WO_3 film. The thickness was estimated to be about 15 nm.

The synthesis of WO_3 conjugated with other semiconductor oxides and metals is gaining interest due to their robust activities. For the photoelectrochemical splitting of water, Liu *et al*. synthesized a mesoporous TiO_2/WO_3 nanohoneycomb at a molar ratio of 3:1, which was prepared by a sol-gel method at room temperature [63]. Briefly, 0.25 g of a triblock copolymer P123 was dissolved in 2.5 g of ethanol and combined with a precursor solution that was prepared by mixing titanium (IV) n-butoxide and WCl_6 at a 3:1 M ratio, and stirring for 2 h. A solution of 300 nm PS(polystyrene) spheres was subsequently spin-coated on a Si wafer to form a mask. Next the Ti and W solution was introduced into the interspaces of the PS spheres via spin coating. The as-prepared sample was aged at 60 °C for 1 day and then annealed at 500 ^{o}C for 4 h. The resulting TiO_2/WO_3 showed a red shift in absorption and high photoelectrochemical activity in water splitting and hydrogen production due to the lowered band gap.

Aqueous solutions of tungstic acid are also widely utilized and are much easier to handle then are precursors containing WCl_6. These are typically obtained by the acidification of aqueous sodium tungstate solutions. Mwakikunga *et al*. reported a new technique for the preparation of a tungstic acid solution, in which the mixing of a Na_2WO_4 solution and HNO_3 was conducted using a microfluidic "Y" connector with a controlled flow rate, rather than mixing the two solutions at once [64]. Micro- and nanotextured tungsten oxide in a randomly aligned flake-like structure was obtained by using this method, with a thickness of 10-30 nm, when the flow rate was slow. The porosity of the prepared structure was contingent on the humidity during the aging process. Enhanced film porosity could be obtained in a more humid environment.

2.5.2. Sol method (non-hydrolytic sol gel method)

The sol method is very similar to that of the sol-gel method; the only difference is that it does not proceed via hydrolysis. In a general reaction, the titanium chloride reacts with the different oxygen donor molecules. Ti-O-Ti bonds are formed via condensation between Ti-Cl and Ti-OR. In this reaction the alkoxide groups may be provided by titanium alkoxides, or can be formed in situ by a reaction titanium chloride with alcohols or ethers [25].

Chang *et. al.* synthesized TiO_2 nanocrystals using the sol method by condensation between $TiCl_4$ and $Ti(OC_3H_7)_4$. Briefly, 0.5 g of $TiCl_4$ and 0.6 g of $Ti(OC_3H_7)_4$ were dissolved in trioctylphosphine oxide at 150 ^oC under a N_2 atmosphere. This mixture was then heated at 320 ^oC for 3 h followed by cooling and the addition of acetone to precipitate the TiO_2 nanocrystals [65].

2.5.3. Hydrothermal method

The hydrothermal method is widely utilized in the synthesis of various nanomaterials. A large number of researchers have employed this method in the preparation of TiO_2 with different morphologies. In this mode of TiO_2 nanoparticle synthesis, the reaction took place in an aqueous solution under controlled temperature and pressure in a Teflon cell that was tightly sealed in a steel pressure vessel. The vapor pressure within the autoclave is controlled by the applied temperature.

Chae *et. al*. synthesized pure anatase phase containing TiO_2 nanoparticles where they regulated the dimensions of the synthesized particles to between 7 - 25 nm by controlling the size and the concentration of the Ti precursor as well as the composition of the solvent system [66]. An acidic ethanol-water solution was employed for the hydrothermal reaction of titanium

alkoxide. In general, TTIP was introduced dropwise to the ethanol and the water solution and the sealed autoclave was subjected to a heat treatment of 240 ^{o}C over 4 h.

Not only spherical nanoparticles but other TiO_2 morphologies have been reported by different investigators. To synthesize TiO_2 nanorods, Zhang *et al.* treated $TiCl_4$ in the presence of acid or inorganic salts at 69.5-149.5 ^{o}C for 12 h [67]. Various surfactants and the composition of the solvents present in the cell influenced the morphology of the nanotubes, thus nanorods with different lengths may be obtained by influencing these parameters.

TiO_2 nanotube structures have garnered much attention in the photocatalytic field as they provide very high surface areas, in that the tubes are hollow. A hydrothermal method was employed by Kasuga *et al*. in the preparation of TiO_2 nanotubes. In general, a 20-110 °C heat treatment over 20 h was applied to the autoclave that contained TiO_2 powders in a 2.5-20 M NaOH solution [68]. Following heat treatment, the samples were rinsed with a dilute aqueous solution of HCl and then water, after which the TiO_2 nanotubes were obtained. Rinsing with HCl and water is critical as they react with Ti-O-Na and Ti-OH, which results in the formation of new Ti-O-Ti bonds. These Ti-O-Na and Ti-OH bonds are formed at the onset of the reaction, where NaOH reacts with the TiO_2 to cleave some of its bonds. Ti-O-Ti bonds or Ti-O-H-O-Ti hydrogen bonds that are generated following the HCl treatment results in a decrease in the distance between the two Ti atoms, thus initiating the folding of the sheets, which results in the formation of the tubes.

Various investigators have also synthesized TiO_2 nanowires using the hydrothermal method. Yoshida *et. al.* used a fine TiO_2 anatase powder as starting material and added this powder (2 g) and 25 ml of a 10 ml NaOH aqueous solution into a Teflon lined stainless steel autoclave. The autoclave was heated at 150 ^{o}C for 72 h and after this process it was washed with

H_2O and then filtered under vacuum. This was followed by stirring the obtained precipitate for 24 h in an aqueous HCl solution at pH 2. This process was repeated three times to ensure that all of the residual Na ions were removed. The samples were then rinsed with distilled water followed by heat treatment in an air atmosphere for 2 h at 200-900 ^{o}C [69].

The hydrothermal treatment is one of the most widely used techniques in the synthesis of the WO_3 nanostructures as it is a very facile and cost-effective, and can be utilized to obtain WO_3 of various morphologies. In most cases, the hydrothermal synthesis of nanostructures involves a tungstic acid solution (H_2WO_4) as the precursor. This solution is then maintained at an elevated temperature (120-300 °C) for a certain period of time, allowing for the nucleation and growth of crystallites. Such synthetic processes generally produce layered $WO_3 \cdot nH_2O$ flakes with lateral dimensions in the range of several tens of nanometers to several micrometers, and thicknesses in the nanometre range.

WO_3 may also be grown by oxidizing the W plates in the presence of an oxidizing agent. Plate-like WO_3 structures were synthesized by Amano *et al.* by using a hydrothermal method. Briefly, a Teflon lined autoclave was employed and tungsten sheets were heated in 8 mL of 1.5 mol L^{-1} nitric acid at 100 °C for 3 h, 140 °C for 2 h, or 180 °C for 1 h, respectively. The films thus obtained were rinsed with pure water and then dried at room temperature (ca. 20 °C). The samples were calcined at 450 °C for 3 h [70].

2.5.4. Solvothermal method

The sole difference between solvothermal and hydrothermal methods is that the former involves only non-aqueous solvents during the synthesis process. The advantage of using the solvothermal method in some cases is that high boiling liquids may be used. Thus the temperature during the heat treatment can be increased significantly, which is not possible when

aqueous solutions are used. As a result of this advantage, the solvothermal method exerts improved control over the size and shape distributions, in contrast to the hydrothermal method.

The solvothermal method has been employed in the synthesis of TiO_2 nanoparticles and nanorods with and without the aid of surfactants. For example, in a typical procedure by Kim *et al.*, TTIP was mixed with toluene at a weight ratio of 1-3:10 and kept at 250 °C for 3 h. Li *et al*. synthesized TiO_2 nanorods by a controlled hydrolysis reaction of $Ti(OC_4H_9)_4$ and linoleic acid [71].

2.5.5. Oxidation method

The oxidation of Ti metal may be accomplished by using various oxidizing materials and/or under applied potentials. TiO_2 nanotubes have been extensively studied in photocatalysis, and as a substrate for the deposition of metals to participate in electrocatalysis. To describe the general synthesis of TiO_2 nanotubes via the anodization method, a Ti plate is rinsed with acetone and water to remove any impurities from the surface and then etched to obtain a rough surface area, which is ideal for the growth of nanotubes. Subsequently, the Ti plate is introduced into a two electrode cell, where the counter electrode is typically a Pt electrode and the solution contains DMSO and HF. The anodization process ensues at applied voltage, which can be anywhere from 10-120 V over different time periods. Following anodization, the electrode is annealed at 450 °C.

TiO_2 nanomaterials may also be synthesized via oxidation without the introduction of an applied potential. TiO_2 nanorods were prepared by the direct oxidation of a titanium metal plate with hydrogen peroxide. Briefly, a clean Ti plate was immersed in a 50 ml, 30 wt% H_2O_2 solution at 353 K for 72 h. The formation of crystalline TiO_2 occurs through a dissolution precipitation mechanism. Inorganic salts such as NaF, NaCl and Na_2SO_4 may be added into the

reaction mixture to control the crystalline phase of TiO_2. The addition of different anions from the inorganic salts assists in the formation of different phases, as SO_4^{2-} and F^- preferentially form the anatase phase, while Cl^- preferably forms the rutile phase [72, 73].

Mukherji *et al*. reported the first use of anodization to produce WO_3 nanostructures. In their experiment, a W foil was used in an oxalic acid electrolyte resulting in the production of a thin nanoporous WO_3 layer on the W foil surface. Following this initial work various other research groups also reported the anodization of WO_3 foils in fluorine containing electrolytes. The presence of fluorine species has a significant effect on the WO_3 growth, and a uniform and thicker layer is obtained, in that it greatly enhances the electrochemical etching and chemical corrosion processes [74].

2.5.6. Electrodeposition method

Electrodeposition, which can also be referred to as electroplating, is a process that is generally employed to deposit a metallic coating by using an electrical current, which reduces the metal atoms on the cathode. The substrate was used as the cathode in a three electrode cell that contained a solution of the metal salt. When a suitable potential was applied, it resulted in the metal ions being attracted toward the cathode and their subsequent deposition. Porous anodic alumina membranes (AAMs) have been utilized extensively as a template for more than 50 years in the fabrication of many types of nanowires and nanotubes. Lei *et al*. fabricated TiO_2 nanowires using an electrodeposition method in which a three compartment cell was used with a saturated calomel reference electrode and a Pt counter electrode. The electrochemical deposition was performed in 100 ml of a 50 mM $TiCl_3$ solution, pH 2.5, at 0 V vs SCE. Following the electrochemical deposition, the sample was heated at 450 °C for 1 h in an argon atmosphere.

2.5.7 Chemical vapor deposition

As its name suggests, for the chemical vapor deposition method, materials are vaporized, which are then allowed to condense onto a substrate to produce a solid phase. This process is typically performed in a vacuum chamber. In CVD, the source material is not pure as it is combined with a volatile precursor that serves as a carrier. This method is primarily used to form coatings in order to alter various properties of the substrates. For example, the deposition of a conductive metal layer onto a non-conductive substrate will alter its electronic properties. Similarly, other properties such as mechanical, thermal, optical, etc. of the substrate can be manipulated and improved by depositing a desired material onto a substrate.

Pradhan *et al*. synthesized TiO_2 nanorods on cobalt-cemented tungsten carbide (WC–Co) substrate. The substrate was initially cleaned via sonication in acetone and water. Argon was subsequently bubbled through the TTIP liquid and maintained in a stainless steel bubbler at 60 ^{o}C, to carry the TTIP vapor to the reactor. The total deposition time for each experiment was 90 min [75].

Houweling *et al*. revealed the CVD synthesis of tungsten oxide (WO_{3-x}) thin films, which consisted of layers with varying oxygen content [76]. In general, the depositions were performed in a vacuum tube reactor on glassy carbon wafers. The reactor vessel was initially evacuated to a high vacuum of 1.0×10^{-7} mbar. The total pressure was then kept constant at various values of between 0.25 to 0.4 mbar as flow of H_2 at 100 Standard cubic centimeters per minute (sccm) and ambient air at between 15 and 30 sccm were admitted. The depositions commenced by passing a constant direct current of 8.0 A through the filaments, which heats them to a temperature of 2160 ^{o}C. Following the deposition, which typically lasts for 30 min the filament was turned off and H_2

flow begun. There are various other examples in the literature where CVD is used in the synthesis of nanostructured WO_3.

2.5.8 Physical vapor method

The major difference between physical vapor deposition and chemical vapor deposition is that the former does not involve any chemical process; rather, deposition is driven by physical forces. In PVD, a pure source material is transitioned into a gas by physical methods such as evaporation, the application of high power electricity, laser ablation, ion implantation and sputtering. This gasified material is then allowed to condense on the substrate to obtain a desired layer. No chemical reactions take place throughout the entire process.

Wu *et al.* described the growth of TiO_2 nanowires using a two-step thermal evaporation method. In the first step, the substrate was covered with a uniform layer using ~0.5 g of Ti powder, and positioned at the high-temperature (HT) zone of a graphite boat [77]. A high frequency dielectric heater was used as the power source and the graphite boat was kept at a high-speed heating ramp of 200 ^{o}C/min up to a temperature of 1050 ^{o}C, where it was held for 30 min. The sample was then removed and cleaned. In the next step, a new source material of ~0.5 g titanium powder and alumina substrate were kept separate and positioned at the graphite boat HT zone and low-temperature (LT) zone, respectively. The heating ramp was 200 °C/min. up to 1050 °C in the HT zone, while the LT zone was heated to 832 ^{o}C, and the temperature was held constant for 30 min.

In the PVD process, the WO_3 material source is in the form of a solid and may be evaporated utilizing many possible techniques. The most important of these are ion bombardment, heating, electron beam, and laser irradiation.

Li *et al.* synthesized WO_3 nanorods using the PVD method. Helically curved tungsten filaments were employed as the target [78]. The tungsten filaments were placed on a steel mesh plate, and a Si wafer was positioned beneath the steel mesh plate at a distance of 2 mm, where it was used as the deposition substrate. The heating was conducted in air, and when heated from the top, the W filaments reached temperatures of 950-1000 ^{o}C, while the temperature of the Si substrate was ~600 ^{o}C. The heating process continued for 1 h. When the chamber cooled to room temperature, the upper surface of the Si substrate was entirely covered with a semi-transparent film, and a layer of green colored oxide powders formed on the surfaces of the tungsten filaments.

There are several additional reports in which PVD method is described for the synthesis of WO_3 nanoparticles.

2.5.9 Sonication method

The sonochemical method has been applied in the preparation of various TiO_2 nanomaterials by different groups. Yu *et al*. applied the sonochemical method to prepare highly photoactive TiO_2 nanoparticles with anatase and brookite phases [79]. Typically, 0.032 mol titanium isopropoxide and 3.2 g of triblock copolymer were dissolved in 20 mL of absolute ethanol. The resulting solution was added dropwise to 100 mL of deionized water under sonication, after which the suspension was heated for 3 h. The suspension was subsequently centrifuged to isolate and collect the particles, which was followed by rinsing and drying at 373 K. The as-prepared sample was calcined at 673 K for 1 h.

2.6 Applications of TiO_2

2.6.1 Photocatalytic applications

TiO_2 is the most extensively investigated heterogeneous photocatalyst as it possesses various unique properties including chemical inertness, high efficiency, non-toxicity, low cost, and the high oxidizing power of generated electrons and holes. Due to these attractive properties it has been widely used as an environmental photocatalyst in the photodegradation of various contaminants. It has the capacity to effectively destroy organic or biological pollutants that are present in wastewater. There are literally thousands of research articles that are published every year as relates to the photocatalytic activities of TiO_2 in the degradation of various types of pollutants, which illustrates its broad versatility.

Pure anatase TiO_2 has a wide band gap of ca. 3.2 eV, which makes its use possible only under UV light. When TiO_2 is exposed to UV light, electron/hole pairs are formed, which can then be utilized for various useful reactions, such as those required for synthetic chemistry. Pichat *et al*. performed the gaseous anaerobic photodegradation of ethanol to acetaldehyde over UV irradiated TiO_2.

$$CH_3CH_2OH \xrightarrow[O_2]{\overset{TiO_2}{hv}} CH_3CHO$$

Similar to the above reaction, various oxidation reactions have been performed on activated TiO_2. For example, the synthesis of sulfones and sulfoxide from sulfides, and the conversion of C=C into C=O. Although the reducing potency of the excited electrons of TiO_2 is significantly lower than that of the oxidizing power of the generated holes, the application of a co-catalyst (Pt, Pd, ZnS etc.) can increase the efficiency of the TiO_2 in reduction reactions. The

presence of hydroquinone, a hole acceptor, also increases the light conversion efficacy of the reduction reactions. Similarly, TiO_2 may also be used in isomerization, condensation, substitutions and polymerization reactions.

The primary focus of TiO_2 applications is in the area environmental decontamination. TiO_2 has been utilized in eradicating myriad species of pollutants from contaminated water and air samples. The eutrophication of water that results from anthropogenic activities initiates the generation of hazardous algae blooms (HAB) comprised of cyanobacteria. These HABs contain and release biological toxins. Cyanobacterial toxins, such as microcystin-LR, can cause skin irritations, liver damage, or affect the nervous system. TiO_2 based photocatalysts have shown promising results in the degradation and detoxification of such biological toxins. Bacterium such as *E. coli* can also be destroyed via TiO_2 photocatalysts.

Industries are the primary sources of hazardous contaminants, as the bulk of the wastewater that they release contains multiple types of harmful chemicals into ambient water resources. TiO_2 has shown its superiority in the complete degradation of most types of hazardous organic wastes, such as phenolic compounds (nitophoenols, amino phenols, chloro phenols, etc.), and organic dyes (rhodamine B, methylene blue, acid orange II).

The doping and co-doping of TiO_2 with metal ions or non-metals enables it to be used as a photocatalyst under visible light or under ambient sunlight toward the photodegradation of contaminants. Recently, Pathakoti *et al.* have utilized N doped and N, F co-doped TiO_2 in the degradation of *E. coli* under simulated solar light and visible light irradiation [80]. Other organic compounds may also be eradicated under visible or ambient sunlight at modified TiO_2.

2.6.2 Photocatalytic water splitting

The discovery, by Fujishima and Honda in 1972, of photocatalytic water splitting on TiO_2 electrodes, led to an enormous amount of research that focused on exploring the properties and applications of TiO_2 for water splitting under photonic irradiation. As the global reserves of fossil fuels are declining very rapidly, there is a critical need for alternative energy sources. The production of H_2 and O_2 occurs due to redox reactions that take place on TiO_2 electrodes following the excitation of electrons from the valence band to the conduction band via the absorption of photonic energy from a light source. Excited electrons react with water molecules and reduce it to release H_2. In similar way vacant electron holes oxidize water molecules to form O_2. The reason that TiO_2 is optimal for water splitting is due to the position of its band gap, as the conduction band should be more negative than the reduction potential of $H+/H_2$. Additional factors that significantly influence photocatalytic water splitting on TiO_2 electrodes are charge separation, mobility, the lifetimes of photogenerated electrons and holes, surface states, surface chemical groups, surface area, and active reaction sites [25]. The activity of TiO_2 electrodes toward photocatalytic water splitting can be further enhanced by depositing metals or metal oxides onto TiO_2 electrodes. These co-catalysts (e.g., Pt, NiO and Mn_2O_3) introduce additional active sites for the evolution of H_2. Fujishima and Honda originally utilized UV light to induce water splitting on TiO_2 electrodes. However, since then efforts have been expended to employ visible light in this process, such that ambient sunlight may be utilized. This can be done by narrowing the band gap via doping of the TiO_2, which creates a new donor level above the valence band.

2.6.3 Electrochromic devices

Electrochromism is the reversible change of color exhibited by various materials that may be induced via the application of an electrical current or a potential difference. TiO_2

nanomaterials have been widely explored as electrochromic devices, such as electrochromic windows and displays. The application of a low voltage to electrochromic windows will cause them to change color, and when this applied voltage is reversed the color will revert back to its original state. Electrochromism of nanocrystalline TiO_2 electrodes in Li^+ containing electrolyte has been reported by various research groups in which the rapid accumulation and Li^+ intercalation within the TiO_2 lattice results in rapid and reversible electrochromatic switching. The dimensions and morphology of the TiO_2 nanoparticles play a critical role in the electrochromic process and it is enhanced when a nanocrystalline morphology is utilized. The rate of the electrochromic process is controlled by the diffusion of the Li^+ ions throughout the TiO_2 lattice. Nanocrystalline TiO_2 electrodes that are modified with viologens may also be efficiently employed as electrochromatic devices. Due to the robust conductivity of TiO_2 and the electron exchange between TiO_2 and the photochromic compound monolayer, these devices respond rapidly to changes in charge, thus exhibiting excellent optical dynamics. Ag-TiO_2 films exhibit multicolored photochromism, which is related to the oxidation and reduction of Ag nanoparticles under UV and visible light irradiation [81].

2.6.4 Hydrogen storage

A significant quantity of research has been dedicated to the utilization of TiO_2 based nanomaterials for H_2 storage. Lim *et al*. showed that TiO_2 nanotubes may be used as a hydrogen storage material as it could reproducibly store up to ~2 wt % H_2 at room temperature. Out of this stored H_2, approximately 75% could be released when the hydrogen pressure was lowered to ambient conditions due to physisorption. Approximately 13% was weakly chemisorbed and could be released at 70 °C as H_2, and approximately 12% was strongly bonded to oxide ions and could only be released at temperatures of above 120 °C as H_2O.

The sorption of hydrogen in the temperature range of -195 to 200 °C between the multilayered walls of nanotubular TiO_2 was studied by Bavykin *et al*. with the results indicating that the hydrogen can intercalate between the layers of TiO_2. The rate of hydrogen sorption is contingent on temperature, and as the temperature was elevated the sorption rate increased with the characteristic time for hydrogen sorption into the TiO_2 nanotubes being several hours at 100 °C. According to the isotherm for hydrogen adsorption at -196 °C, 1.5 hydrogen molecules per Ti atom could be adsorbed at a hydrogen partial pressure of 2 bar [82].

2.6.5 TiO_2 in dye sensitized solar cells (DSSC)

Because of their high energy conversion efficiency, dye-sensitized solar cells (DSSCs) are considered to be an alternative energy source to conventional semiconductor solar cells. TiO_2 with various morphologies have been utilized to fabricate DSSC, as the morphology of the photoanode plays an important role in the determination of electron transport properties. TiO_2 is optimal for use as a photoelectrode material due to its favorable physiochemical properties. Mesoporous TiO_2 produces improved results as a photoanode material in comparison to TiO_2 nanotubes, nanowires and other morphologies, because of their special functionality, where interconnected junctions with open pores in the mesoporous structure speeds up electron transport. Mesoporous TiO_2 also provides a much more extensive surface area as compared to other structures.

2.7 Applications of WO_3

2.7.1 Photocatalytic applications:

Nanostructured WO_3 may provide an optimum surface to volume ratio, and it has a lower band gap as compared to TiO_2, which makes it a promising material for study in photocatalytic

applications. Various research groups have investigated nanostructured WO_3 materials and they have concluded that by using nanostructured WO_3, incident photon to electron conversion efficiency (IPCE) of more than 100% could be achieved. When organic species such as methanol are added into the electrolyte, an IPCE as high as 190% was calculated by researchers. The addition of organic compounds increases the IPCE due to the photo-oxidation kinetics between the WO_3 and the organic species.

Gondal *et al*. studied the deactivation of *E. coli* in culture media with nano WO_3 and concluded that the photocatalytic activity of the WO_3 nanostructured material was so efficient that practically all of the bacteria were eradicated in under five minutes [83].

Recently Hayat *et al*. successfully demonstrated the removal of the carcinogenic dye safranin-O by laser induced photocatalysis on nanocrystalline WO_3 [84]. They further demonstrated a linear relationship between the laser intensity and the degradation of the dye on the WO_3. Their study clearly illustrated that hazardous organic compounds could be eliminated by WO_3 in the presence of a light source. Other groups have successfully used nanostructured WO_3 materials with different morphologies in the abatement of various pollutants in wastewater. An additional advantage of using nanocrystalline WO_3 based photocatalytic devices is that they require less power, as it is easier for the charge carriers to travel to the oxide surface. This translates to mean that if WO_3 films are used in a photoelectrochemical cell, only a very small applied potential is required to generate a relatively higher photocurrent.

2.7.2 Photocatalytic water splitting

Even though WO_3 exhibits good photocatalytic activity when it is irradiated by UV or visible light, it cannot be utilized in photocatalytic water splitting to generate H_2 as it is

thermodynamically unfavourable. This is because WO_3 possesses a more positive conduction band than the H_2/H_2O reduction potential (vs NHE). This shortcoming may be overcome by applying an external potential such that the generated electrons are infused into water molecules, rather than recombining with electron holes. Another strategy for making it possible for WO_3 to photocatalytically split water is to combine it with other metal oxides, which have a more negative CB than that of the H_2/H_2O reduction potential.

The photocatalytic activity of WO_3 may also be enhanced via doping with various metal atoms and non-metals. A few examples of the dopants that have been studied include N, C, Mg, Ni, Au, Cu, Zn, Bi, Ag, Fe and Co. Doping with Ni and Ag were found to be promising for H_2 evolution, while the band positions of WO_3 doped with Fe, Cu and Au shifted downwards, which improved the water oxidation.

2.7.3 Electrochromic devices

WO_3 based electrochromic devices have been widely studied and are commonly used in smart windows and EC displays. Properties such good memory effect, low power consumption, high contrast and long term stability makes WO_3 perfect for this application. A general setup includes WO_3 as an EC layer, an electrolyte for ion storage, and two transparent conductors, which are utilized to establish electrical contacts. For intercalating H^+ ions, the most commonly used electrolytes are H_2SO_4 and $HClO_4$, whereas $LiClO_4$ is used for Li^+. When a voltage is applied, the ions are intercalated, which results in the chromic effect. This process is reversed when the voltage is inverted, in which case the ions are expelled from the WO_3 lattice.

Among amorphous and crystalline WO_3, amorphous films exhibit high efficiency (≈55 $cm^2\ mC^{-1}$ for H^+ intercalation). They also have high a charge density which is ~9 mC cm^{-2} mg^{-1}.

However, the disadvantage of using amorphous WO_3 is that it does not have a high EC stability because of its poor structural and chemical stability. On the other hand, because of its more dense structure and slower dissolution rate, crystalline WO_3 is more stable. The lower energy charge density of the crystalline phase is a negative point. Bulk crystalline WO_3 has a relatively lower charge density of 3 mC cm^{-2} mg^{-1} in comparison to the amorphous form, as well as poor coloration efficiency (≈25 cm^2 mC^{-1} for H^+ intercalation)

Nanostructured WO_3 films have been found to exhibit a much higher charge density, coloration efficiency, and coloration bleach time as compared to bulk amorphous and crystalline WO_3. Recently, researchers have utilized a nanostructured WO_3 film with a high degree of porosity to overcome the drawbacks of crystalline WO_3 for EC applications.

2.7.4 Dye sensitized solar cells

TiO_2 is the most investigated photoanode material for DSSCs, as its efficiency is approximately 11%. For the first time, Zheng *et al*. recently reported that WO_3 nanostructures have the potential to be used as alternative photoelectrode materials in dye-sensitized solar cells. In their experiment they employed commercially available WO_3 nanoparticles (Ø40 nm) as the photoelectrode in DSSC, and investigated the effects of various parameters on the cell performance. The conversion efficiency of the WO_3 nanoparticles in the DSSC was calculated to be 0.75%, which was enhanced to 1.46% via surface modification [85]. The efficiency of WO_3 is very low as compared to that of DSSCs based on other semiconducting metal oxides, such as TiO_2, SnO_2, and ZnO. There is still a need to focus research on increasing the efficiency of WO_3 based photoanodes for DSSCs.

2.8 Electrochemical Supercapacitors (ES)

With the depletion of non-renewable energy resources coupled with rapid increases in energy demands there is a critical need to develop and implement efficient and cleaner sources of energy [86, 87]. The storage of electrical energy may be accomplished either electrostatically in conventional capacitors, or electrochemically in cells or batteries. For capacitors, the electrical energy stored is given by:

$$W = Q\Delta V = C\Delta V^2$$

where ΔV is the electrical potential drop across the capacitor when the electrical charge Q resides on its plates; C is the capacitance of the condenser defined as:

$$C = Q/\Delta V$$

The amount of charge, as well as the capacitance C, is directly proportional to the surface area of the plates.

Supercapacitors (also known as ultracapacitors) and electric double layer capacitors (EDLC), are electrochemical capacitors that can store much higher charges as compared to conventional capacitors. A capacitor stores energy by means of a static charge as opposed to an electrochemical reaction. Supercapacitors store energy using either ion adsorption (electrochemical double layer capacitors) or rapid surface redox reactions (pseudo-capacitors), where the application of a voltage differential on the positive and negative plates charges the capacitor. In recent years ES have attracted much attention due to their high power density and extended longevity [88].

ES are devices similar to batteries, which store a charge. In general ES contains two electrodes which are isolated from each other with an electrolyte. In recent years major

advancements in the development of the ES have been achieved as can be seen by large number of publications dedicated to the technology. There are also a number of excellent review articles such as "A review of electrode materials for electrochemical supercapacitors" by Wang *et al.* which describes the development, functionality, and applications of ES in much detail [89].

ES have long been studied as can be concluded from the fact that the earliest ES patent was filed in 1957. However, they have garnered increasing attention over the last decades due to advancements in material science and nanotechnology, as new materials with unique attributes may be fabricated and utilized as electrode materials. Despite having high power densities and long life cycles, there are some disadvantages of ES that need to be addressed. The chief issues are the high cost of production and low energy density.

Various materials have been studied as candidates for use as efficient electrodes, with the most attractive contenders being carbon particle materials and metal oxides, particularly RuO_2 and MnO_2 [90-91]. Carbon particles have high surface areas for storage, but the physical storage of the charge within the porous electrode layers is limited. These types of capacitors have low specific capacitance and energy density. These issues can be overcome through the addition of active materials on the surface of the carbon electrode.

2.8.1 Classification of ES

According to the type of charging, ES may be classified as two types. One is EDLS, where there is no electrochemical reaction that takes place on the electrode material and the charge is physically accumulated. The other is a Faradaic supercapacitor in which an electrochemical reaction takes place at the electrode surface during charge/discharge [89]. These types are described in more detail below.

2.8.1.1 Electrostatic capacitors or electric double layer supercapacitor (EDLS)

In this type of supercapacitor an electrostatic charge accumulates at the interface. The mechanism of electrode surface charge generation includes surface dissociation, as well as ion adsorption from both the electrolyte and crystal lattice defects. In general, an excess or deficit of electric charge accumulates on the electrode surfaces. In order to maintain the electroneutrality of the system an opposite charge is built up on the electrolytic side. The charge on the electrode is typically generated because of the ion adsorption from both the electrolyte and crystal defects. Thus, there is simply the accumulation of charge taking place that is devoid of an electrochemical reaction. In this type of ES, no charge is transferred across the electrode/electrolyte interface, and no net ion exchanges occur between the electrode and the electrolyte. This implies that the electrolyte concentration remains constant during the charging and discharging processes.

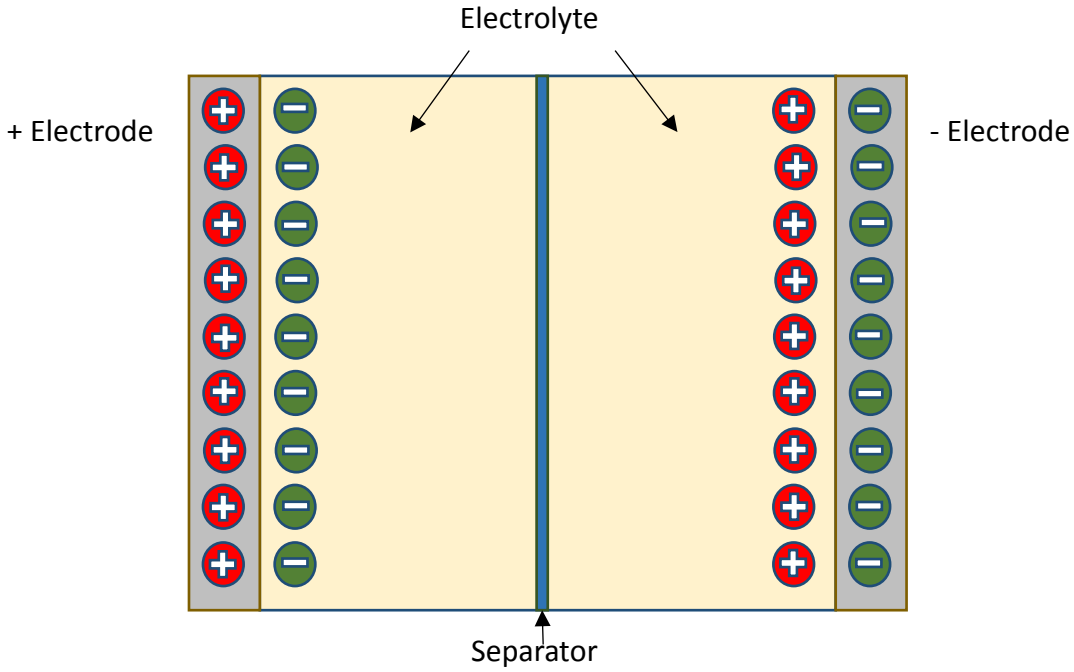

Figure 2.4 Schematic diagram of a charged and discharged electric double layer capacitor

2.8.1.2 Faradaic supercapacitors (FS)

In Faradaic type supercapacitors, when a potential is applied, reversible redox reactions take place on the electrode materials, which results in a flow of charge across the double layer. The material utilized for the fabrication of electrodes for FS typically consists of conducting polymers and several metal oxides, including RuO_2 and MnO_2 [89, 92]. There are three types of reactions which occur on the electrodes including reversible adsorption, redox reactions of transition metal oxides (e.g.RuO_2) and reversible electrochemical doping-dedoping in conductive polymer based electrodes. Because in FS the electrochemical processes are not only occurring in the bulk near the electrode, but also on the surface of the solid electrode, they exhibit far larger capacitance values and energy density than an EDLS. Conway *et al*. reported that the capacitance of FS can be 10-100 fold higher than the electrostatic capacitance of an EDLS. The redox reactions on the FS are typically slower than the physical accumulation of charge on the EDLS with their lower power density [93].

The performance of a supercapacitor depends to a great extent on the type of electrolyte used. The main requirements for an electrolyte is that it should have a wide voltage window, high electrochemical stability, high ionic concentration, low solvated ionic radius, low resistivity, low viscosity, low volatility, low toxicity, low cost and high purity.

The electrolyte could be an aqueous solution of H_2SO_4, KOH, or Na_2SO_4, etc. Aqueous solutions may normally provide higher power than organic electrolytes because they possess a higher ionic concentration [87]. The main issue with the use of aqueous electrolytes is that they provide a very small voltage window. On the other hand, organic electrolytes provide a high voltage window which might attain 3.5 V [87]. The primary organic compounds and organic salts that are typically used currently as electrolytes are acetonitrile, propylene carbonate,

tetramethylammonium tetrafluoroborate etc. Other types of electrolytes that are garnering interest are ionic liquids (IL), which are prepared by melting a salt. They normally remain as a liquid at desired temperatures. The chief advantages of ionic liquids are high chemical stability, thermal stability, low flammability and a wide electrochemical window, which can be in the range of between 2-6 V. Commonly used IL encompass imidazolium, pyrrolidinium and some aliphatic quaternary ammonium salts [87].

The advantages of the ES may be summarized as follows

1. Practically unlimited cycle life; may be cycled millions of time
2. High specific power; low resistance enables high load currents
3. High efficiencies
4. Wide range of operating temperatures
5. Charges in seconds; no end-of-charge termination required
6. Simple charging; draws only what it needs; not subject to overcharge
7. Safe; forgiving if abused
8. Excellent low-temperature charge and discharge performance

Despite all of these positive features there is still a need to further investigate and prepare new electrode materials in ES, as there still remain several issues that need to be addressed in the ES, such as low energy density, high cost and high self-discharging rate.

2.9 Summary and perspectives

TiO_2 and WO_3 have numerous applications in various fields and can be utilized to address practical problems that are related to the environment and energy storage. An array of methods are available for the synthesis of nanoparticles with different morphologies and phases,

which can expand the use of the TiO_2 and WO_3 based nanomaterials. However, some limitations still persist for the broad range use of catalysts. Thus, the further development of nanomaterials based catalysts is needed to 1) increase efficiency, 2) reduce the recombination rate of the electron/hole pairs, 3) increase the stability of the material to extend the operational lifetimes of the materials being employed, 4) make the process of catalysis more affordable through the development of cheaper materials and low cost synthesis techniques such that they can be universally employed and 5) make these techniques environmentally compatible by limiting the use of toxic materials.

References

[1] K. Nakata, A. Fujishima. TiO_2 photocatalysis: Design and applications, *Journal of Photochemistry and Photobiology C: Photochemistry Reviews* 13 (**2012**) 169–189

[2] A. L. Linsebigler, G. Lu, J. T. Yates. Photocatalysis on TiO_2 surfaces: principles, mechanisms, and selected results, *Chemical Reviews* 95 (**1995**) 735–758

[3] K. A. Gesheva T. M. Ivanova, G. Bodurov. Transition metal oxide films: Technology and "Smart Windows" electrochromic device performance, *Progress in Organic Coatings* 74 (2012) 635–639

[4] M. Manoharan. Research on the frontiers of materials science: The impact of nanotechnology on new material development, *Technology in Society* 30 (2008) 401–404

[5] S. Walsh, J. M. Balbus, R. Denison, K. Florini. Nanotechnology: getting it right the first time, *Journal of Cleaner Production* 16 (2008) 1018-1020

[6] J. H. Pan, X.S. Zhao, W. I. Lee. Block copolymer-templated synthesis of highly organized mesoporous TiO_2-based films and their photoelectrochemical applications, *Chemical Engineering Journal 170* (2011) 363–380

[7] M. A. Arvizua, C. A. Triana, B. I. Stefanov, C. G. Granqvist, G. A. Niklasson. Electrochromism in sputter-deposited W–Ti oxide films: Durability enhancement due to Ti, *Solar Energy Materials and Solar Cells* 125 (2014) 184–189

[8] J. Chena, X. Niea, H. Shi, G. Li, T. An. Synthesis of TiO_2 hollow sphere multimer photocatalyst by etching titanium plate and its application to the photocatalytic decomposition of gaseous styrene, *Chemical Engineering Journal* 228 (**2013**) 834–842

[9] P. Su, Y. Peng. Fabrication of a room-temperature H_2S gas sensor based on PPy/WO_3 nanocomposite films by in-situ photopolymerization, *Sensors and Actuators B* 193 (2014) 637–643

[10] T. Sreethawong, S. Laehsalee, S. Chavadej. Use of Pt/N-doped mesoporous-assembled nanocrystalline TiO_2 for photocatalytic H_2 production under visible light irradiation, *Catalysis Communications* 10 (**2009**) 538-543.

[11] M. J. Powell, C. W. Dunnill, I. P. Parkin. N-doped TiO_2 visible light photocatalyst films via a sol–gel route using TMEDA as the nitrogen source, *Journal of Photochemistry and Photobiology A: Chemistry* 281 (**2014**) 27–34

[12] M. A. Fox, A. A. Abdel-Wahab, Y. S. Kim, M. Dulay. Photocatalytic oxidation of multifunctional organic molecules. The effect of an intramolecular aryl thioether group on the semiconductor-mediated oxidation/dehydrogenation of a primary aliphatic alcohol, *Journal of Catalysis* 126 (**1990)** 693-696

[13] J. T. Park, J. H. Koh, J. K. Koh, J. H. Kim. Surface-initiated atom transfer radical polymerization from TiO_2 nanoparticles, *Applied Surface Science* 255 (**2009**) 3739–3744

[14] B. I. Stefanov, Z. Topalian, C. G. Granqvist, L. Österlund. Acetaldehyde adsorption and condensation on anatase TiO_2: Influence of acetaldehyde dimerization, *Journal of Molecular Catalysis A: Chemical* 381 (**2014**) 77–88

[15] J. Zou, B. Zhu, L. Wang, X. Zhang, Z. Mi. Zn- and La-modified TiO_2 photocatalysts for the isomerization of norbornadiene to quadricyclane, *Journal of Molecular Catalysis A: Chemical* 286 (**2008**) 63–69

[16] B. Michalkiewicz, J. Majewska, G. Kadziołka, K. Bubacz, S. Mozia, A. W. Morawski. Reduction of CO_2 by adsorption and reaction on surface of TiO_2-nitrogen modified photocatalyst, *Journal of CO_2 Utilization* 5 (**2014**) 47–52

[17] Z. Mesgari, M. Gharagozlou, A. Khosravi, K. Gharanjig. Spectrophotometric studies of visible light induced photocatalytic degradation of methyl orange using phthalocyanine-modified Fe-doped TiO_2 nanocrystals, *Spectrochimica Acta Part A* 92 (**2012**) 148–153

[18] X. Fan, X. Chen, S. Zhu, Z. Lia, T. Yu, J. Ye, Z. Zou. The structural, physical and photocatalytic properties of the mesoporous Cr-doped TiO_2, *Journal of Molecular Catalysis A: Chemical* 284 (**2008**) 155–160

[19] H. B. Jiang, J. Xing, Z. P. Chen, F. Tian, Q. Cuan, X. Q. Gong, H. G. Yang. Enhancing photocatalytic activity of Sn doped TiO_2 dominated with{1 0 5} facets, *Catalysis Today* 225 (**2014**) 18–23

[20] D. S. Bae, K. S. Han, S. H. Choi. Fabrication and characterization of Ru-doped TiO_2 composite membranes by the sol-gel process, *Materials Letters* 33 (**1997**) 101-105

[21] T. Nguyen, M. Hwang, K. Ryu. High adsorption capacity of V-doped TiO_2 for decolorization of methylene blue, *Applied Surface Science* 258 (**2012**) 7299–7305

[22] Y. Xin, H. Liu. Study on mechanism of photocatalytic performance of La-doped TiO_2/Ti photoelectrodes by theoretical and experimental methods, *Journal of Solid State Chemistry* 184 (**2011**) 3240–3246

[23] M. Anpo. Use of visible light. Second-generation titanium oxide photocatalysts prepared by the application of an advanced metal ion-implantation method, *Pure and Applied Chemistry* 72 (**2000**) 1787-1792

[24] Y. Cao, W. Yang, W. Zhang, G. Liu, P. Yue. Improved photocatalytic activity of Sn^{4+} doped TiO_2 nanoparticulate films prepared by plasma-enhanced chemical vapor deposition, *New Journal of Chemistry* 28 (**2004**) 218-222

[25] X. Chen, S.S. Mao. Titanium dioxide nanomaterials: synthesis, properties, modifications, and applications, *Chemical Reviews* 107 (**2007**) 2891-2959

[26] J. M. Herrmann, J. Disdier, P. Pichat. Effect of chromium doping on the electrical and catalytic properties of powder titania under UV and visible illumination, *Chemistry Physics Letters* 108 (**1984**) 618-622

[27] S. T. Martin, C. L. Morrison, M. R. Hoffmann. Photochemical mechanism of size-quantized vanadium-doped TiO_2 particles. *Journal of Physical Chemistry* 98 (**1994)** 13695.

[28] T. Lindgren, J. M. Mwabora, E. Avendano, J. Jonsson, A. Hoel, C. G. Granqvist, S. E. Lindquist. Photoelectrochemical and optical properties of nitrogen doped titanium dioxide films prepared by reactive DC magnetron sputtering, *Journal of Physical Chemistry B* 107 (**2003)** 5709.

[29] W. Li, Y. Wang, H. Lin, S. I. Shah, C. P. Huang, D. J. Doren, S. A. Rykov, J. G. Chen, M. A. Barteau. Band gap tailoring of Nd^{3+}-doped TiO_2 nanoparticles. *Applied Physics Letter* 83 (**2003)** 4143-4145

[30] R. Asahi, T. Morikawa, T. Ohwaki, K. Aoki, Y. Taga. Visible-light photocatalysis in nitrogen-doped titanium oxides, *Science* 293 (**2001**) 269-271.

[31] G. Wu, J. Wang, D.F. Thomas, A. Chen. Synthesis of F-doped flower-like TiO_2 nanostructures with high photoelectrochemical activity, *Langmuir* 24 (**2008**) 3503-3509.

[32] J. Madarász, A. Brăileanub, G. Pokol. Comprehensive evolved gas analysis of amorphous precursors for S-doped titania by in situ TG–FTIR and TG/DTA–MS: Part 1. Precursor

from thiourea and titanium(IV)-isopropoxide. *Journal of Analytical and Applied Pyrolysis* 82 (2008) 292–297

[33] T. Umebayashi, T. Yamaki, S.Yamamoto, A. Miyashita, S. Tanaka, T. Sumita, K. Asai. Sulfur-doping of rutile-titanium dioxide by ion implantation: Photocurrent spectroscopy and first-principles band calculation studies, *Journal of Applied Physics* 93 (2003) 5156 (5pp)

[34] M. Landmann, E. Rauls, W. G. Schmidt. The electronic structure and optical response of rutile, anatase and brookite TiO_2, *Journal of Physics: Condensed Matter* 24 (**2012**) 195503 (6pp)

[35] W. Yan, B. Chen, S. M. Mahurin, V. Schwartz, D. R. Mullins, A. R. Lupini, S. J. Pennycook, S. Dai, S. H. Overbury. Preparation and comparison of supported gold nanocatalysts on anatase, brookite, rutile, and P25 polymorphs of TiO_2 for catalytic oxidation of CO, *Journal of Physical Chemistry B* 109 (**2005**) 10676-10685

[36] T. Ohno, T. Higo, N.Murakami, H. Saito, Q. Zhang, Y. Yang, T. Tsubota. Photocatalytic reduction of CO_2 over exposed-crystal-face-controlled TiO_2 nanorod having a brookite phase with co-catalyst loading, *Applied Catalysis B: Environmental* 152–153 (**2014**) 309–316

[37] X. Nie, S. Zhuo, G. Maeng, K. Sohlberg. Doping of TiO_2 polymorphs for altered optical and photocatalytic properties, *International Journal of Photoenergy* 2009, Article ID 294042, 22 pages

[38] I. M. Szilágyi, B. Fóriz, O. Rosseler, Á. Szegedi, P. Németh, P. Király, G. Tárkányi, B. Vajna, K. Josepovits, K. László, A. L. Tóth, P. Baranyai, M. Leskelä. WO_3 photocatalysts: Influence of structure and composition, *Journal of Catalysis* 294 (**2012**) 119–127

[39] K. Huang, Q. Pan, F. Yang, S. Ni, X. Wei, D. He. Controllable synthesis of hexagonal WO_3 nanostructures and their application in lithium batteries, *Journal of Physics D: Applied Physics* 41 (**2008**) 155417

[40] E. Llobet, G. Molas, P. Molinàs, J. Calderer, X. Vilanova, J. Brezmes, J. E. Sueiras, X. Correig. Fabrication of highly selective tungsten oxide ammonia sensors, *Journal of The Electrochemical Society* 147 **(2000)** 776-779

[41] S. Jayaraman, T. F. Jaramillo, S. H. Baeck, E. W. McFarland. Synthesis and characterization of Pt−WO_3 as methanol oxidation catalysts for fuel cells, *Journal of Physical Chemistry B* 109 (**2005)** 22958–22966

[42] N. A. Galiote, R. L.T. Parreira, J. M. Rosolen, F. Huguenin. Self-assembled films from WO_3: Electrochromism and lithium ion diffusion, *Electrochemistry Communications* 12 (**2010**) 733–736

[43] J. Z. Ou , M. S. Strano , R. B. Kaner , A. Mitchell, K. Kalantar-zadeh, H. Zheng. Nanostructured Tungsten Oxide – Properties, Synthesis, and Applications, *Advanced. Functional Materials* 21 *(***2011)**, 2175–2196

[44] E. K. H. Salje, S. Rehmann, F. Pobell, D. Morris, K. S. Knight, T. Herrmannsdorfer, M. T. Dove. Crystal structure and paramagnetic behaviour of $WO_{3-}x$, *Journal of Physics: Condensed Matter* 9 (**1997**) 6563-6577

[45] T. Vogt, P. M. Woodward, B. A. Hunter. The high-temperature phases of WO_3, *Journal of Solid State Chemistry* 144 (**1999**) 209-215

[46] M. Gillet, K. Aguir, C. Lemire, E. Gillet, K. Schierbaum. The structure and electrical conductivity of vacuum-annealed WO_3 thin films, *Thin Solid Films* 467 (**2004)** 239-246

[47] P. K. Shen, J. S. Bokhari, A. C. C. Tseung. The performance of electrochromic tungsten trioxide films doped with cobalt or nickel, *Journal of The Electrochemical Society* 138 (**1991**) 2778-2783

[48] I. Porqueras. Efficiency of Li doping on electrochromic WO_3 thin films, *Thin Solid Films* 377-378 (**2000**) 129-133

[49] D. B. Migas, V. L. Shaposhnikov, V. N. Rodin, V. E. Borisenko. Tungsten oxides: Effects of oxygen vacancies and doping on electronic and optical properties of different phases of WO_3, *Journal of Applied Physics* 108 (2010) 093713

[50] A. Hjelm, C. G. Granqvist, J. M. Wills. Electronic structure and optical properties of WO_3, $LiWO_3$, $NaWO_3$, and HWO_3, *Physics Review B* 54 (**1996**) 2436-2445

[51] Dan Su, Jingyu Wang, Yupan Tang, Cheng Liu, Lifei Liu and Xijiang Han. Constructing WO_3/TiO_2 composite structure towards sufficient use of solar energy, *Chemical Communications* 47, (**2011**) 4231–4233

[52] A. K. Chakraborty, M. S. Akter, M. A.Haque, G. M. A. Khan, M. S. Alam. Synthesis of Co_3O_4/WO_3 nanoheterojunction photocatalyst for the decomposition of organic pollutants under visible light irradiation, *Journal of Cluster Science* 24, (**2013**) 701-713

[53] Z. Zou, Y. Liu, H. Li, Y. Liao, C. Xie, Synthesis of $TiO_2/WO_3/MnO_2$ Composites and high-throughput screening for their photoelectrical properties, *Journal of Combinatorial Chemistry* 12 (**2010**) 363–369

[54] A. Chemseddine, T. Moritz. Nanostructuring Titania: Control over nanocrystal structure, size, shape and organization, *European Journal of Inorganic Chemistry* 2 (**1999**), 235-245.

[55] J. Li, J. Xu, W.-L. Dai, H. Li, K. Fan. One-pot synthesis of twist-like helix tungsten–nitrogen-codoped titania photocatalysts with highly improved visible light activity in the abatement of phenol, *Applied Catalysis B: Environmental* 82 (**2008**) 233-243.

[56] Z. Miao, D. Xu, J. Ouyang, G. Guo, X. Zhao, Y. Tang. Electrochemically Induced Sol−Gel Preparation of Single-Crystalline TiO_2 Nanowires, *Nano Letters* 2 (2002) 717-720

[57] T. C. Jagadale, S. P. Takale, R. S. Sonawane, H. M. Joshi, S. I. Patil, B. B. Kale, S. B. Ogale. N-doped TiO_2 nanoparticle based visible light photocatalyst by modified peroxide sol-gel method, *The Journal of Physical Chemistry C* 112 (2008) 14595–14602

[58] H. Zhang, G. Chen. Potent antibacterial activities of Ag/TiO_2 nanocomposite powders synthesized by a one-pot sol-gel method, *Environmental Science and Technology* 43 (2009) 2905–2910

[59] J. C.-S. Wu, C. H. Chen. A visible-light response vanadium-doped titania nanocatalyst by sol–gel method, *Journal of Photochemistry and Photobiology A: Chemistry* 163 (**2004**) 509–515

[60] Y. F. You, C. H. Xu, S. S. Xu, S. Cao, J.P. Wang, Y.B. Huang, S.Q. Shi. Structural characterization and optical property of TiO_2 powders prepared by the sol–gel method, *Ceramics International* 40 (**2014**) 8659–8666

[61] R. Pandeeswari, R.K. Karn, B.G. Jeyaprakash. Ethanol sensing behaviour of sol–gel dip-coated TiO_2 thin films, *Sensors and Actuators B* 194 (**2014**) 470–477

[62] C. Chan, W. Hsu, C. Chang, C. Hsu. Hydrogen incorporation in gasochromic coloration of sol–gel WO_3 thin films, *Sensors and Actuators B* 157 (**2011**) 504– 509

[63] K. Liu, Y. Hsueh, C. Su, T. Perng. Photoelectrochemical application of mesoporous TiO_2/WO_3 nanohoneycomb prepared by sol-gel method, *International Journal of Hydrogen Energy* 38 (2013) 7750-7755

[64] B. W. Mwakikunga, A. Forbes, E. Sideras-Haddad, M. Scriba, E. Manikandan. Self assembly and properties of C:WO_3 nano-platelets and C:VO_2/V_2O_5 triangular capsules produced by laser solution photolysis, *Nanoscale Research Letters* 5 (2010), 389-397

[65] S. Chang, R. Doong. Characterization of Zr-doped TiO_2 nanocrystals prepared by a nonhydrolytic sol-gel method at high temperatures, *Journal of Physical Chemistry B* 110 (**2006**) 20808-20814

[66] S. Y. Chae, M. K. Park, S. K. Lee, T. Y. Kim, S. K. Kim, W. I. Lee. Preparation of size-controlled TiO_2 nanoparticles and derivation of optically transparent photocatalytic films *Chemistry of Materials* 15 (**2003**) 3326-3331

[67] Q. Zhang, L. Gao. Preparation of oxide nanocrystals with tunable morphologies by the moderate hydrothermal method: Insights from rutile TiO_2, *Langmuir* 19 (**2003**) 967-971

[68] T. Kasuga, M. Hiramatsu, A. Hoson, T. Sekino, K. Niihara. Formation of titanium oxide nanotube, *Langmuir* 14 (**1998**) 3160-3163

[69] R. Yoshida, Y. Suzuki, S. Yoshikawa. Syntheses of TiO_2(B) nanowires and TiO_2 anatase nanowires by hydrothermal and post-heat treatments, *Journal of Solid State Chemistry* 178 (**2005**) 2179-2185

[70] F. Amano, M. Tian, B. Ohtani, A. Chen. Photoelectrochemical properties of tungsten trioxide thin film electrodes prepared from facet-controlled rectangular platelets, *Journal of Solid State Electrochemistry* 16 (**2012**) 1965–1973

[71] X. L. Li, Q. Peng, J. X. Yi, X. Wang, Y. D. Li. Near monodisperse TiO_2 nanoparticles and nanorods, *Chemistry-A European Journal* 12 (**2006)** 2383-2391

[72] J. M. Wu, S. Hayakawa, K. Tsuru, A. Osaka. Nanocrystalline titania made from interactions of Ti with hydrogen peroxide solutions containing tantalum chloride, *Crystal Growth and Design* 2 (**2002**) 147-149.

[73] J. M. Wu, S. Hayakawa, K. Tsuru, A. Osaka. Porous titania films prepared from interactions of titanium with hydrogen peroxide solution, *Scripta Materialia* 46 (**2002)**,*46*, 101-106

[74] N. Mukherjee, M. Paulose, O. K. Varghese, G. K. Mor, C. A. Grimes. Fabrication of nanoporous tungsten oxide by galvanostatic anodization, *Journal of Materials Research* 18 (**2003**) 2296-2299

[75] S. K. Pradhan, P. J. Reucroft, F. Yang, A. Dozier. Growth of TiO_2 nanorods by metalorganic chemical vapor deposition, *Journal of Crystal Growth* 256 (**2003**) 83–88

[76] Z. S. Houweling, J. W. Geus, R. E. I. Schropp. Hot-wire chemical vapor deposition of WO_{3x} thin films of various oxygen contents, *Materials Chemistry and Physics* 140 (**2013**) 89-96

[77] J. M. Wu, H. C. Shih, W. Wu, Y. K. Tseng, I-C. Chen. Thermal evaporation growth and the luminescence property of TiO2 nanowires, *Journal of Crystal Growth* 281 (**2005**) 384–390

[78] Y. B. Li, Y. Bando, D. Golberg, K. Kurashima. WO_3 nanorods/nanobelts synthesized via physical vapor deposition process, *Chemical Physics Letters* 367 (**2003**) 214–218

[79] J. C. Yu, L. Zhang, J. Yu. Direct sonochemical preparation and characterization of highly active mesoporous TiO_2 with a bicrystalline framework, *Chemistry of Materials* 14 (**2002**) 4647-4653

[80] K. Pathakoti, S. Morrow, C. Han, M. Pelaez, X. He, D. D. Dionysiou, H. M. Hwang. Photoinactivation of Escherichia coli by sulfur-doped and nitrogen−fluorine-codoped TiO_2 nanoparticles under solar simulated light and visible Light Irradiation, *Environmental Science and Technology* 47 (2013) 9988−9996

[81] M. Ottaviani, S. Panero, S. Morzilli, B. Scrosati, M. Lazzari. The electrochromic characteristics of titanium oxide thin film electrodes, *Solid State Ionics* 20 (**1986**) 197-202

[82] D. V. Bavykin, A. A. Lapkin, P. K. Plucinski, J. M. Friedrich, F. C. Walsh. Reversible storage of molecular hydrogen by sorption into multilayered TiO_2 nanotubes. *Journal of Physical Chemistry B* 109 (**2005**) 19422-19427

[83] M. A. Gondal. Synthesis of nano-WO_3 and its catalytic activity for enhanced antimicrobial process for water purification using laser induced photo-catalysis, *Catalysis Communications* 11 (2009) 214–219.

[84] K. Hayat, M. A. Gondal, M. M. Khaled, Z. H. Yamani, S. Ahmed. Laser induced photocatalytic degradation of hazardous dye (Safranin-O) using self synthesized nanocrystalline WO_3, *Journal of Hazardous Materials* 186 (**2011**) 1226-1233

[85] H. Zheng, Y. Tachibana, K. Kalantar-zadeh. Dye-sensitized solar cells based on WO_3, *Langmuir* 26 (**2010**) 19148-19152

[86] B. E. Conway. Electrochemical supercapacitors, scientific fundamentals and technological applications*; Kluwer Academic/Plenum Press: New York* (**1999**); p 11.

[87] M. Winter, R. J. Brodd. What are batteries, fuel cells, and supercapacitors? *Chemical Rev*iews 104 (2004) 4245-4270

[88] P. Simon and Y. Gogotsi. Materials for electrochemical capacitors, *Nature Matererials* 7 (**2008**) 845-854

[89] G. Wang, L. Zhang, J. Zhang. A review of electrode materials for electrochemical supercapacitors, *Chemical Society Reviews* 41 (**2012**) 797–828

[90] V. D. Patake, C. D. Lokhande, Chemical synthesis of nano-porous ruthenium oxide (RuO_2) thin films for supercapacitor application. *Applied Surface Science* 254 (**2008**) 2820–2824

[91] T. Yousefi, R. Davarkhah, A. N. Golikand, M. H. Mashhadizadeh. Synthesis, characterization, and supercapacitor studies of manganese (IV) oxidenanowires, *Materials Science in Semiconductor Processing* 16 (**2013**) 868–876

[92] X. Dong, W. Shen, J. Gu, L. Xiong, Y. Zhu, H. Li, J. Shi. MnO_2-embedded-in-mesoporous-carbon-wall structure for use as electrochemical capacitors, *Journal of Physical Chemistry B* 110 (**2006**) 6015-6019

[93] B. E. Conway, V. Birss, J. Wojtowicz. The role and utilization of pseudocapacitance for energy storage by supercapacitors, *Journal of Power Sources* 66 (**1997**) 1-14

Chapter 3: Materials and Methods

3.1 Introduction

An overview of TiO_2 and WO_3 based nanomaterials, synthesis methods and applications is presented in previous chapters. In this chapter, various methods that were employed in this study in the fabrication of nanomaterials are briefly discussed. This chapter also presents the various techniques and instrumentation that were employed to characterize the synthesized materials in this study.

3.2 Experimental

3.2.1 Materials

Titanium (IV) isopropoxide (97%), urea (≥ 99%) and sodium tungstate ($Na_2WO_4.2H_2O$) were purchased from Sigma-Aldrich, and rhodamine B was purchased from BDH, UK.

Titanium plates were obtained from Alfa-Aesar and were cut into 1cm × 1cm squares. Hydrochloric acid (37%) and methanol were purchased from Sigma-Aldrich.

Tungsten plates with a thickness of 0.25 mm were received from Sigma-Aldrich (99.9% trace metals basis) and were cut into 1cm × 1cm squares. Acetone (≥99.5%), Nitric Acid (70%), and H_2SO_4 (99.999%), were purchased from Sigma Aldrich and used as received. Anhydrous Ethyl Alcohol was purchased from Commercial Alcohols, Brampton, Canada. $IrCl_3 \cdot 3H_2O$ was purchased from Pressure Chemical Corp. and $TaCl_5$ was purchased from Aldrich.

The water (18:2 MΩ cm) used for the preparation of the aqueous solutions was purified with a NANOpure® Diamond^{TM} water system.

All solutions were deaerated with ultrapure argon (99.999%) prior to performing and measuring experiments.

3.2.2 Instruments and electrochemical experiments

A transmission electron microscope (JEOL 2010) and scanning electron microscope (Hitachi SU 70) were used to determine the surface morphology and particle size of the samples. The crystalline phase of the synthesized samples was obtained by X-ray diffraction (Phillips PW 1050-3710 Diffractometer with Cu Kα radiation (λ=1.5406 Å). N_2 gas adsorption/desorption studies at liquid nitrogen temperature (77 K) were conducted utilizing a Quantachrome Nova 2200 surface area and pore size analyzer for determination of the Brunauer-Emmett-Teller (BET) surface area of the samples. The UV-Vis absorbance spectrum was obtained using a UV-visible spectrophotometer (Varian, Cary 5E). The surface composition was examined either by Energy dispersive X-ray spectroscopy (Oxford AZtech) or X-ray photoelectron spectroscopy (Omicron EA-125 energy analyzer and a multi-channel detector). All binding energies reported in this work were corrected using the C 1s peak at 284.5 eV as an internal standard. The broad N 1s region of samples was fitted using XPSPEAK41 software.

Electrochemical experiments were performed using a Voltalab 40 Potentiostat (PGZ301) or Solatron SI 1287 electrochemical interface instrument. The fabricated electrodes were used as the working electrode. A Pt coil with a 10 cm^2 surface area was utilized as the auxiliary electrode; an Ag/AgCl electrode was used as the reference electrode. The Pt counter electrode was flame annealed prior to each experiment. All measurements were conducted at room temperature (22 ± 2^oC).

3.2.3 Fabrication of electrodes

3.2.3.1 Synthesis of N-W co-doped TiO_2

Titanium (IV) isopropoxide (TTIP) (Sigma-Aldrich, 97%,) was used as a Ti precursor, urea (Sigma-Aldrich, ≥ 99%) as a nitrogen source and sodium tungstate ($Na_2WO_4.2H_2O$, Sigma-aldrich) as a tungsten source, ethanol as a solvent and acetic acid as an inhibitor to the hydrolysis of the organic precursor; 2 ml of TTIP was added dropwise to a mixture of 20 ml of ethanol and 0.5 ml of acetic acid under vigorous stirring for 30 min. To obtain an equivalent composition of N in all samples, 5 g of urea and a predetermined amount of 0.1 M Na_2WO_4, based on the target composition of W, were added. Initially, the mixed solution was heated on a hot plate and subsequently to facilitate the combustion reaction, the solution was transferred to a preheated (300^oC) furnace. Finally, the synthesized powder was calcinated at 450 ^oC for 3 h.

3.2.3.2 Fabrication of TiO_2 nanotubes

Ti plates (99.2%) were obtained with dimensions of 1.25 cm × 0.80 cm × 0.5 mm. The plates were then cleaned, initially by sonication in acetone to remove all the organic impurities present on the surface, followed by rinsing with pure water (18.2 MΩcm). The electrodes were subsequently etched in a 18% HCl solution at 85 °C for 15 min and rinsed with pure water. The TiO_2 nanotubes were grown electrochemically at 40 V for 8 h in a one compartment two-electrode cell, containing DMSO + 2% HF. An etched Ti plate served as the working electrode and a Pt plate was used as a counter electrode. To obtain the anatase crystal structure the plates were then annealed at 450 °C for 3 h.

3.2.3.3 Fabrication of WO_3 platelet electrodes

To prepare the WO_3 nanomaterials, a facile hydrothermal method was employed, where a commercially available tungsten plate (Sigma-Aldrich, 99.7 %) was cut to obtain a 1 cm^2 area, which was utilized as a substrate. To grow the tungsten oxide onto the substrate, the tungsten plate was introduced into a Teflon-lined autoclave containing 1.5 M HNO_3. To observe the effect of temperature on the crystal growth of the WO_3 on the substrate, various temperatures and time increments were employed for the hydrothermal treatment. Following the hydrothermal treatment, the electrodes were rinsed with ultrapure water several times, heated at 450 °C for 3 h and then utilized for the electrochemical tests.

The WO_3 that contained Pt nanoparticles for the bifunctional electrodes were fabricated using a photoreduction method. In general, a 0.1 mM solution of inorganic precursor $H_2PtCl_6 \cdot 6H_2O$ was formulated in ultrapure water. A desired amount of this solution was added into a 5 mL 50% (v/v) methanol solution and was deaerated for 10 min. with ultrapure argon gas to eliminate any oxygen that was present in the solution; the test tube was then sealed with rubber stopper. The electrode in the Pt solution was subsequently irradiated under UV light for 1 h. The electrodes were then rinsed carefully under pure water and dried at 50 °C in an oven overnight.

0.1 M $IrCl_3.3H_2O$ and 0.1 M $TaCl_5$ solutions were prepared in ethanol and painted on one side of the WO_3 electrode in obtaining WO_3/IrO_2 and WO_3/Ta_2O_5 electrodes. The WO_3/IrO_2-Ta_2O_5 electrode precursor solution was made by combining the 0.1 M $IrCl_3.3H_2O$ and 0.1 M $TaCl_5$ solutions in equal amounts. Following this, the mixture was painted onto the WO_3 electrodes, which were subjected to 3 h calcination at 450 ^oC to oxidize the metal chlorides to metal oxides.

3.3 UV treatment of TiO_2 nanotubes and N,W co-doped TiO_2

In general, for the UV pre-treatment, a TiO_2 sample was initially placed in a quartz tube containing 5 mL of 50% methanol-H_2O (v/v); after bubbling with argon for 10 min, the quartz tube was capped, after which it was irradiated under UV light for various time periods for TNW and 30 min for the TiO_2 nanotubes. Following the treatment, the samples were rinsed with ultrapure water and dried in an oven at 50 °C.

3.4 Photocatalytic and Electrocatalytic measurements.

The photocatalytic activity of the as synthesized samples were evaluated by measuring the photodegradation of RhB (organic dye pollutant) or 4-NP under visible light in the case of photocatalysis or under an applied potential, in case of electrocatalysis. The reactor was a cylindrical pyrex/quartz vessel. In a general experiment, 20 mg of the photocatalyst was suspended in 20 ml of 25 μM aqueous solution of RhB. The depth of the solution in the reactor was ~2 cm. The distance between the surface of the reactor and the light source was kept constant. The light source used in this study consisted of an Oriel system, including a 300 W xenon arc lamp. The lamp was allowed to warm up for half an hour prior to testing. For visible light irradiance, the source light was passed through an optical filter (Edmund Optical Co. GG420) which cut off wavelengths of below 420 nm. Infrared light was removed via a water filter. The wavelength range of the resulting light was between 420-700 nm with the intensity of ~2.50 mW cm^{-2} measured by a Cole-Palmer Radiometer Series 9811 at the point where the light entered the reactor. Samples were collected from the reaction mixture at 20 min increments. The samples was taken out at regular time intervals and the degradation of organic compounds were quantified using a UV-visible spectrometer (Varian, Cary 50).

3.5 Measurement of capacitance

A Solatron SI 1287 electrochemical interface instrument was employed to run the charge-discharge cycles. Specific capacitance (mF/mg) may be estimated via the voltammetric charge (integrated from the CV over the potential range) according to the following equation:

$$C = Q/(\Delta E \times W)$$

where Q is the charge (in mC), ΔE is the operating potential window (in V), and W is the weight of the metal oxides deposited (mg) onto the working electrode.

References

[1] S. S. Thind, G. Wu, A. Chen. Synthesis of mesoporous nitrogen–tungsten co-doped TiO_2 photocatalysts with high visible light activity, *Applied Catalysis B: Environmental* 111–112 (**2012**) 38-45

[2] S. S. Thind, G. Wu, M. Tian, A. Chen. Significant enhancement in the photocatalytic activity of N, W co-doped TiO_2 nanomaterials for promising environmental applications, *Nanotechnology* 23 (**2012**) 475706

[3] M. Tian, S. S. Thind, S. Chen, N. Matyasovzsky, A. Chen. Significant enhancement of the photoelectrochemical activity of TiO_2 nanotubes, *Electrochemistry Communications* 13 (**2011**) 1186-1189

[4] S. S. Thind, M. Tian, A. Chen. Direct growth and photo-electrochemical study of WO_3 nanostructured materials, *Electrochemistry Communications* 43 (**2014**), 13–17

Chapter 4: Synthesis of Mesoporous Nitrogen-Tungsten co-doped TiO_2 Photocatalysts with High Visible Light Activity*

4.1. Introduction

The extensive use of dyes in the textile, cosmetic and plastics industries and their subsequent release via wastewater into the ecosystem is one of the major sources of environmental pollution [1, 2]. Due to the high resistivity of these modern dyes towards chemical and microbiological degradation, they are becoming an increasing threat to aquatic life as a result of their tendency to cause aesthetic pollution and eutrophication [3, 4]. Dyes containing N atoms can undergo reductive anaerobic degradation to produce cancer causing aromatic amines [5]. Hence, it is critical that these dyes undergo sufficient degradation prior to their release into wastewaters in order to protect fragile ecosystems. Heterogeneous photocatalysis has demonstrated superiority toward the abatement of organic pollutants over conventional methods (e.g., occulation, reverse osmosis, activated carbon adsorption, ozonization and chemical oxidation technologies), which have inherent problems in the complete removal of color and for the potential generation of secondary pollution [6]. In recent years, a great effort has been placed on the development of clean and inexpensive heterogeneous photocatalysts for the elimination of myriad pollutants from water.

TiO_2 is one of the most intensely investigated semiconductor photocatalysts which may be utilized for the environmentally compatible treatment of inorganic and organic pollutants due to its chemical inertness, high efficiency, non-toxicity and low cost [7, 8]. However, a significant

*Most of the results presented in this chapter have been published in *Applied Catalysis B: Environmental* **2012**, *111-112*, 38-45.

constraint that prevents its pervasive implementation is that the TiO_2 based photochemical process may only be initiated by UV light, due to its large energy band gap (~3.2 eV for anatase) [9]. Unmodified TiO_2 photocatalysts show negligible response to visible light (which constitutes a significant portion of natural sunlight). The modification of the electronic structure of TiO_2 based materials is thus required to shift the absorption edge to the visible region in order to enhance and expand the utilization of renewable solar energy. A common approach in shifting the absorption edge of TiO_2 to the visible region is to modify its electronic structure by substituting the oxygen in the lattice with anionic dopants such an N, C, S and halogen atoms [10-12]. Among these, N stands out as the most promising candidate due to its comparable ionic radius, which is close to that of O such that N 2p states may effectively merge with O 2p states. This modifies the electronic structure of the valance band, which facilitates the transport of charge carriers. Nonmetal doping also induces oxygen vacancies, which have a significant influence on catalytic activity [13]. Asahi *et al.* [14] prepared N doped TiO_2 via the sputtering method and showed absorption in the visible region due to the formation of the O-Ti-N bond. This hypothesis was supported by the presence of the N1s peak at 397 eV that was observed during the XPS analysis. Following this discovery, it was confirmed by a number of researchers that the N1s peak at 397 eV is responsible for the visible light response, as N substitutes for the O atoms in the lattice structure of TiO_2, causing a modification in its electronic structure [15]. Although N-doped TiO_2 exhibits good visible light induced photocatalytic activity, electron-hole recombination remains a major obstacle that blocks the effective use of TiO_2 photocatalysts which are doped with only non-metals [16, 17]. This deficiency has spurred the development of co-doped TiO_2 which may involve the combination of non-metal and metal elements or two different non-metal elements. Due to the synergistic effect of both dopants, co-doped TiO_2 show

greater visible response than single doped TiO_2 [18, 19]. However, very few studies of N,W co-doped TiO_2 photocatalysts have been reported in the literature. Kubacka *et al.* employed a microemulsion method to fabricate N,W co-doped TiO_2 with over 10% of W [20, 21]. B. Dai and co-workers used a slow hydrolysis approach in an ice-water bath to synthesize twist-like helix tungsten-nitrogen-codoped titania [22]. A two-step method has also been reported, where N-doped TiO_2 nanoparticles were fabricated first using a sol-gel method, and followed by either mechanical alloying with W-doped TiO_2 nanoparticles [23] or dispersing the N-doped TiO_2 powders in a dilute ammonia solution containing tungstic acid [24].

In the present work, a novel and facile solution combustion synthesis method was developed and employed to prepare N,W co-doped TiO_2 nanomaterials that contained various percentages of atomic tungsten dopant levels. The one-step solution combustion method is much less time consuming compared to the sol-gel method and the microemulsion method and it does not involve any expensive or complicated instruments. Our experimental results show that the synthesized N,W co-doped TiO_2 exhibit the photocatalytic active anatase phase exclusively, with a very high surface area and mesoporous structure consisting of particles of between 8-12 nm in size. The fabricated N,W co-doped TiO_2 nanomaterials show marvelous photocatalytic activity under visible light irradiation.

4.2. Experimental Section

4.2.1 Photocatalyst synthesis

To prepare the mesoporous N-doped or N,W co-doped TiO_2, commercially available titanium (IV) isopropoxide (TTIP) (Sigma-Aldrich, 97%,) was used as a Ti precursor, urea (Sigma-Aldrich, $\geq$ 99%) as a nitrogen source and sodium tungstate ($Na_2WO_4.2H_2O$, Sigma-

aldrich) as a tungsten source, ethanol as a solvent and acetic acid as an inhibitor to the hydrolysis of the organic precursor. 2 ml of TTIP was added dropwise to a mixture of 20 ml of ethanol and 0.5 ml of acetic acid under vigorous stirring for 30 min. To obtain an equivalent composition of N in all samples, 5 g of urea and a predetermined amount of 0.1M Na_2WO_4, based on the target composition of W, were added. Initially, the mixed solution was heated on a hot plate, and subsequently, to facilitate the combustion reaction, the solution was transferred to a preheated (300^o C) furnace. Finally, the synthesized powder was calcinated at 450 ^{o} C for 3 h.

4.2.2. Characterization techniques

The crystalline phase of the synthesized samples was obtained by X-ray diffraction (Phillips PW 1050-3710 Diffractometer with Cu Kα radiation (λ=1.5406 Å). For the determination of the Brunauer-Emmett-Teller (BET) surface area of the samples, N_2 gas adsorption/desorption studies at liquid nitrogen temperature (77 K) were conducted utilizing a Quantachrome Nova 2200 surface area and pore size analyzer. The samples were initially degassed at 400 ^{o}C for 3 h under vacuum. Transmission electron microscopy (JEOL 2010) analysis was performed in order to determine the surface morphology and particle size of the samples. The UV-Vis absorbance spectrum was obtained using a UV-visible spectrophotometer (Varian, Cary 5E). The surface composition was examined by X-ray photoelectron spectroscopy (Omicron EA-125 energy analyzer and a multi-channel detector). All binding energies reported in this work were corrected using the C 1s peak at 284.5 eV as an internal standard. The broad N 1s region of the sample was fitted using XPSPEAK41 software.

4.2.3. Photocatalytic activity measurements

The photocatalytic activity of as synthesized powders and Degussa P25 was evaluated by measuring the photodegradation of rhodamine B (organic dye pollutant) under visible light. The reactor is a cylindrical pyrex vessel having internal diameter of 4 cm and 4.5 cm internal height and is open to the air. In a general experiment, 20 mg of the photocatalyst was suspended in 20 ml of 25 μM aqueous solution of RhB. The depth of the solution in the reactor was ~2 cm. The distance between the surface of the reactor and the light source was kept at 3 cm. The Rhodamine solution was prepared using pure water (18.2 MΩ.cm) obtained from a NANOpure® Diamond^{TM} UV ultrapure water purification system. The reaction mixture was sonicated for 30 min in the absence of light in order to obtain a homogeneous suspension and to achieve an adsorption-desorption equilibrium. The light source used in this study consisted of an Oriel system including a 300W xenon arc lamp. The lamp was allowed to warm up for half an hour before testing. For visible light irradiance, the source light was passed through an optical filter (Edmund Optical Co. GG420) which cut off wavelengths of below 420 nm. Infrared light was removed by a water filter. The wavelength range of the resulting light was between 420-700 nm with the intensity of ~2.50 mW cm^{-2} measured by a Cole-Palmer Radiometer Series 9811 at the point where the light entered the reactor. Samples were collected from the reaction mixture at 20 min increments. The samples were centrifuged (Thermo Electron Co., Sorvall Biofuge Stratos Centrifuge) to remove particles from the solution and this particle free solution was used to measure the degradation of RhB using a UV-visible spectrometer (Varian, Cary 50). The solution and the centrifuged particles were then added back to the reactor.

4.3. Results and discussion

4.3.1 XRD analysis

The XRD patterns of the synthesized powders are presented in Figure 4.1. Among the anatase, rutile and brookite phases of TiO_2 only the diffraction peaks of the higher photocatalytic active anatase phase was observed in all samples. Additional peaks from WO_3 due to inhomogeneous doping or from any impurities were not observed, which signifies that all of the tungsten was incorporated into the lattice structure of the TiO_2. This indicates that the solution

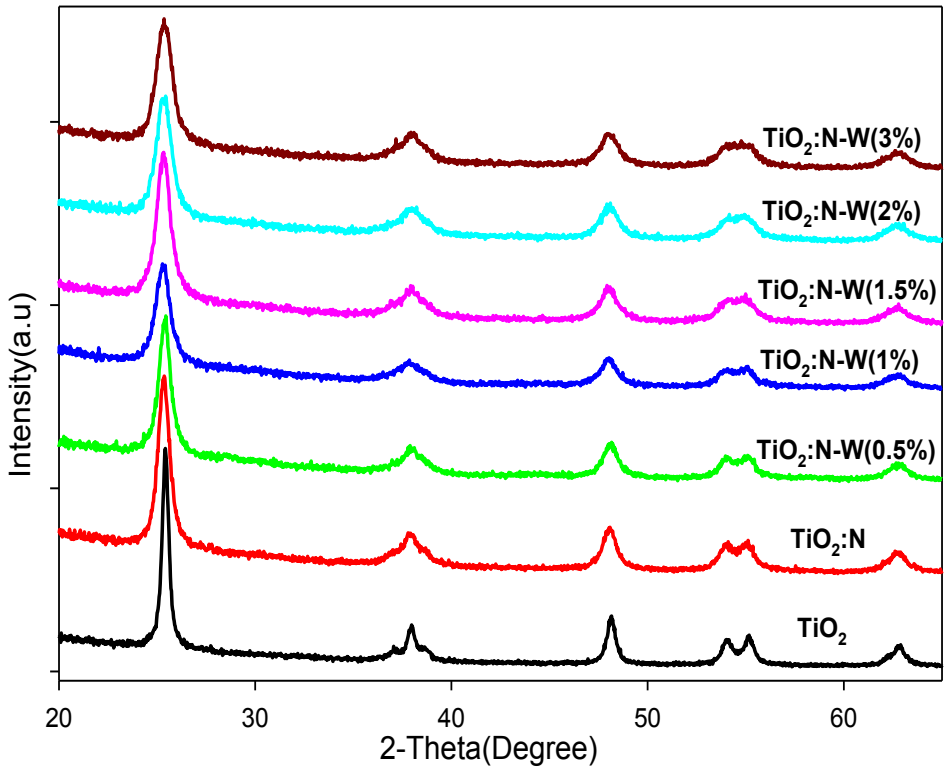

Figure 4.1. XRD patterns of TiO_2, TiO_2:N and the TiO_2:N-W(x%).

combustion approach developed in this study provides a simple and effective method for the doping of certain species of atoms into a TiO_2 lattice. Interestingly, it was observed that concomitant with the increasing W doping level, the (101) peak broadens and its intensity decreases. This may be attributed to the inhibition of crystal growth that is prompted by the metal dopant, which results in the formation of smaller particles [25]. The principal characteristic peak (101) for the anatase phase, located at 25.5^{o}, was studied and used in the determination of the average crystalline size of the samples using the Scherrer equation $d = k\lambda/\beta \cos\theta$, where λ is the X-ray wavelength, β is the full width at half maximum of the (101) peak, θ is the incident angle, and k is a shape factor. The calculated crystalline dimensions of the samples are shown in Table 1. It can be seen that the particle size decreases from 18.80 nm of TiO_2 to 9.00 nm of 3 at% of W doped TiO_2.

4.3.2 TEM Observation

The as-synthesized samples were characterized by TEM. Figure 4.2A and 4.2B depict the TEM micrographs of the N-doped and N,W(1%) co-doped samples, respectively. Both of the samples show a mesoporous structure with irregular pore sizes. The insets in Figure 4.2A and 4.2B are corresponding selected area electron diffraction (SAED) patterns, indicating that the two samples are polycrystalline with an anatase nature. The *d* value for the observed rings (0.351, 0.237, 0.189 and 0.169 nm) in both of the SAED patterns corresponds to the reflections of (101), (004), (200) and (105). Figure 4.2C and 4.2D present the corresponding high resolution TEM (HRTEM) images of N- doped and N,W co-doped TiO_2, respectively. It can be seen that single crystalline TiO_2 particle with 5-8 nm size, which are in concordance with the XRD determination, interconnect with each other to form a porous network. The lattice spacing of the

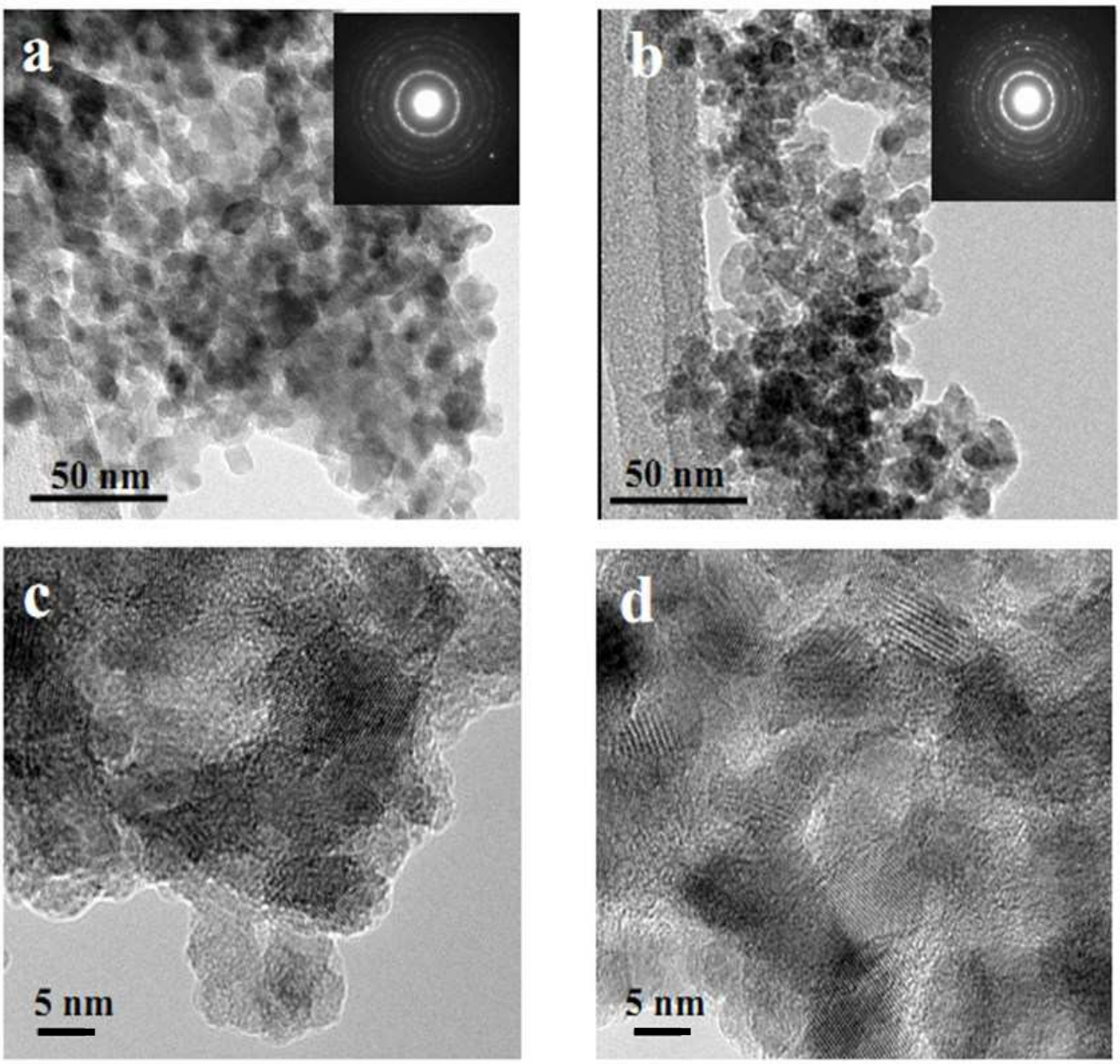

Figure 4.2. TEM and high resolution TEM images of N doped (a), (c) and N,W codoped TiO_2 (b), (d), respectively. Inset is respective SAED pattern.

TiO_2 in the HRTEM images was calculated to be 0.301 nm, which corresponds to the (101) crystal plane of the anatase TiO_2 structure. The pores are visible as bright spots within the darker areas, and the size distribution is relatively narrow with an average diameter of 4-6 nm for both the N-doped and N,W co-doped TiO_2 samples.

4.3.3 BET surface area and pore structure

To examine the surface area, as well as the pore sizes and their distribution, nitrogen adsorption/desorption analysis was performed on all synthesized samples. Each sample showed Type IV N_2 adsorption/desorption isotherms, indicating that mesoporous structures were achieved via this synthesis method; this is consistent with the TEM observations. The isotherm curve for the N,W (1.5%)-TiO_2 sample is presented in Figure 4.3A. The results of the BET analysis on the pure, doped and co-doped samples are displayed in Table 4.1. The specific surface area calculated for the pure TiO_2 is 51 m^2g^{-1}, which is similar to the average value for Degussa P25. However, the surface area increases in correspondence with raised W doping levels. This is ascribed to the small size and mesoporosity that is present in the structure of the samples. The surface area of 1 at% W doping is 147 m^2g^{-1}, which is close to three times that of the un-doped TiO_2 synthesized in this study using the same solution combustion method. N & W co-doping has some impact on the particle size and surface area as observed by comparing the results for W doped TiO_2 from the literature [26], where the surface area for TiO_2-W(2%) is 116 m^2g^{-1} and the particle size is 11.6 nm. With the co-doping of N&W the surface increased to 136 m^2g^{-1} and the particle size decreases to 9.6 nm. Since photocatalytic properties are influenced by surface area and pore size, this enhancement of specific surface area in the co-doped samples signifies the presence of additional available active sites for photocatalysis. The average pore

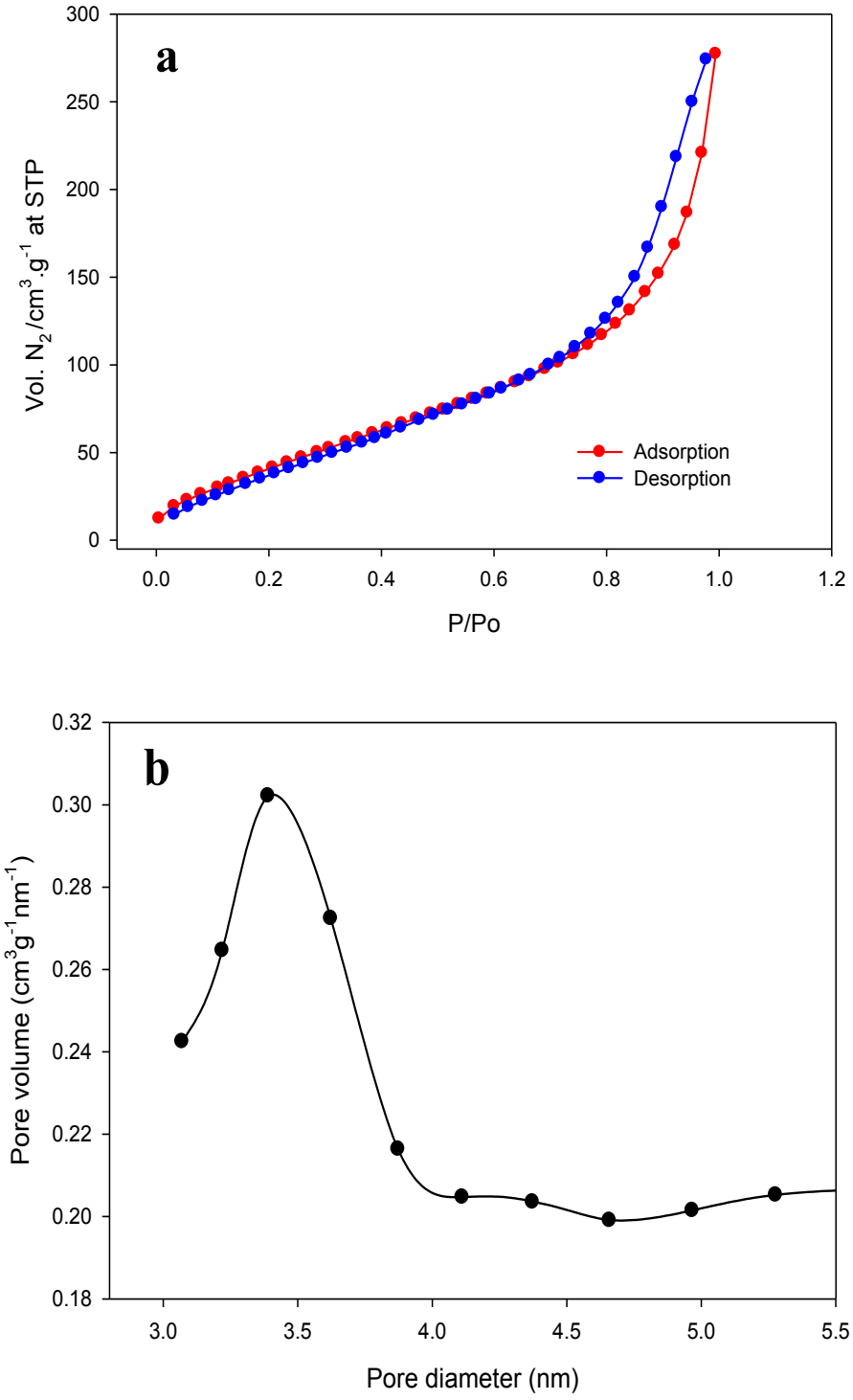

Figure 4.3. (a) Nitrogen adsorption-desorption isotherms of the TiO_2:N-W(1.5%) sample, (b) Pore size distribution.

diameter for the co-doped samples shown in Figure 4.3B, which was calculated from the desorption branch of the N_2 isotherms by the Barret-Jayner-Halenda (BJH) method, is ~3.5 nm, which further validates the existence of a mesoporous structure. This finding is also consistent with the HRTEM observation. The pore sizes were observed to increase slightly with higher W doping levels.

Table 4.1: Textural properties of the samples determined by BET and XRD studies.

Sample	Surface Area (m^2/g)	Pore size (nm)	Pore volume (cm^3/g)	Crystallite size(nm)
TiO_2	52	3.6	0.220	18.80
TiO_2:N	122	3.6	0.235	11.68
TiO_2:N-W(0.5%	128	3.7	0.260	11.82
TiO_2:N-W(1%)	147	3.6	0.290	10.34
TiO_2:N-W(1.5%	146	4.5	0.305	10.74
TiO_2:N-W(2%)	136	4.6	0.311	9.62
TiO_2:N-W(3%)	137	6.0	0.352	9.00

4.3.4 UV-visible spectroscopic studies

The optical properties of materials are very sensitive to, and are heavily influenced by their inherent microstructures and hence electronic structural changes. UV-visible absorbance experiments were carried out, and the resulting spectra are shown in Figure 4.4A. It is seen that pure TiO_2 shows absorbance only in the UV region; the absorbance shifts to longer wavelengths with N doping and N,W co-doping. The corresponding Tauc plots are presented in Figure 4.4B. By assuming TiO_2 to be an indirect semiconductor, the band gap energy of pure TiO_2, N doped and N,W(1.5%) co-doped TiO_2 are 3.08, 2.79, and 2.64 eV, respectively. The absorbance edge in the N doped and N,W co-doped powders was significantly shifted to the visible region. Table 2

presents the calculated band gap for the samples. This red shift is attributed to the presence of nitrogen and tungsten in the lattice structure of the TiO_2. This modification serves to alter the electronic band structure.

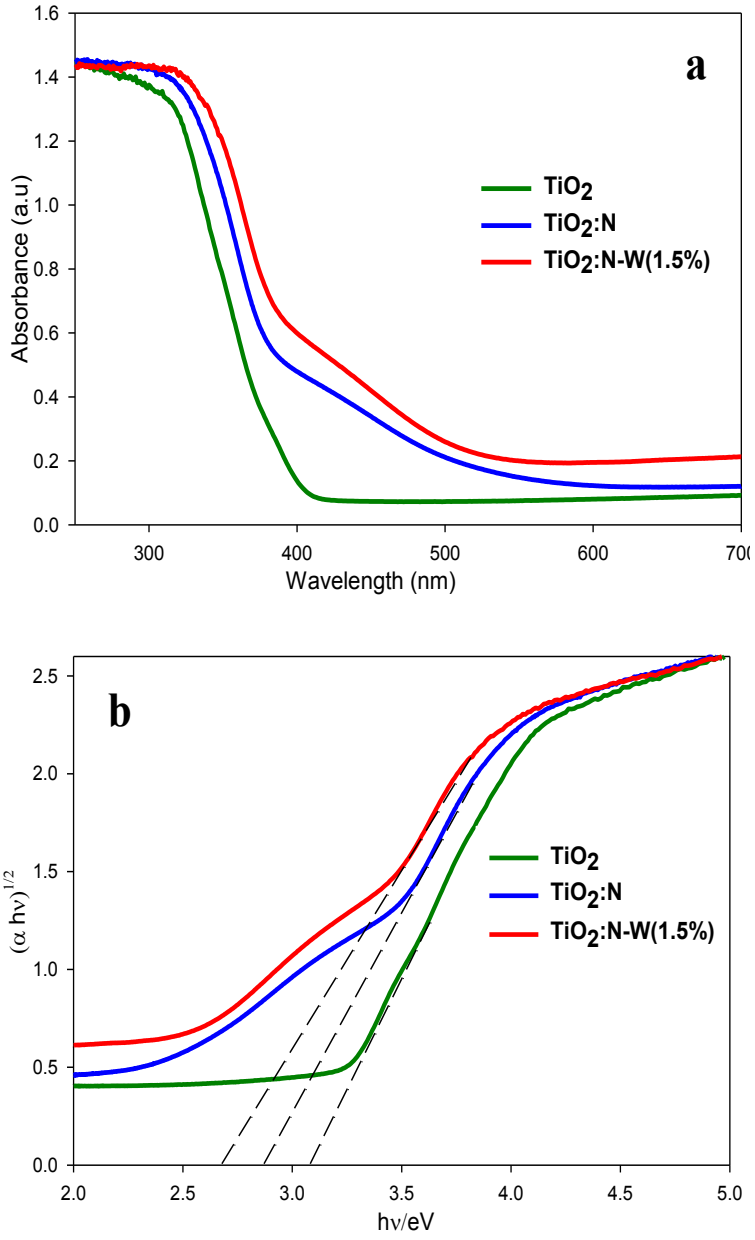

Figure 4.4 (a) UV-visible absorption spectra of TiO_2, TiO_2-N and the TiO_2:N-W(1.5%); (b) Tauc plots of TiO_2, TiO_2:N and TiO_2:N -W(1.5%).

Table 4.2.: Band gap estimation for prepared nanomaterials

Sample	Estimated Band gap (eV)
TiO_2	3.08
TiO_2:N	2.88
TiO_2:N-W(0.5%)	2.82
TiO_2:N-W(1%)	2.87
TiO_2:N-W(1.5%)	2.68
TiO_2:N-W(2%)	2.67

4.3.5 XPS analysis

All of the samples were analyzed by XPS to investigate the chemical components, their electronic state, and atomic concentration. The XPS spectra of TiO_2-N,W(1.5%) are presented in Figure 4.5. As seen in Figure 4.5A, the peaks for Ti $2p_{3/2}$ and Ti $2p_{1/2}$ are centered at 458.69 and 464.38 eV. This clearly shows the presence of a Ti (IV) oxidation state in all samples. The O1s XPS spectra shown in Figure 4.5B reveal a well-defined peak at 530.01 eV with a small shoulder centered at 531.52 eV. The peak at 530 eV is characteristic of the oxides of transition metals. The small peak centered at 531.52 eV could be attributed to the presence of hydroxyl groups or adsorbed water molecules on the surface [27]. A controversy still exists as to which peak corresponds to the doped N in the TiO_2**.** Asahi *et al.* and other researchers assign the peak at 397 eV to anionic doping in which O atoms are substituted by N atoms, and the peak at 399 eV and 402 eV to the molecularly chemisorbed N [14, 28]. This is altercated by Sato *et al*, who postulates

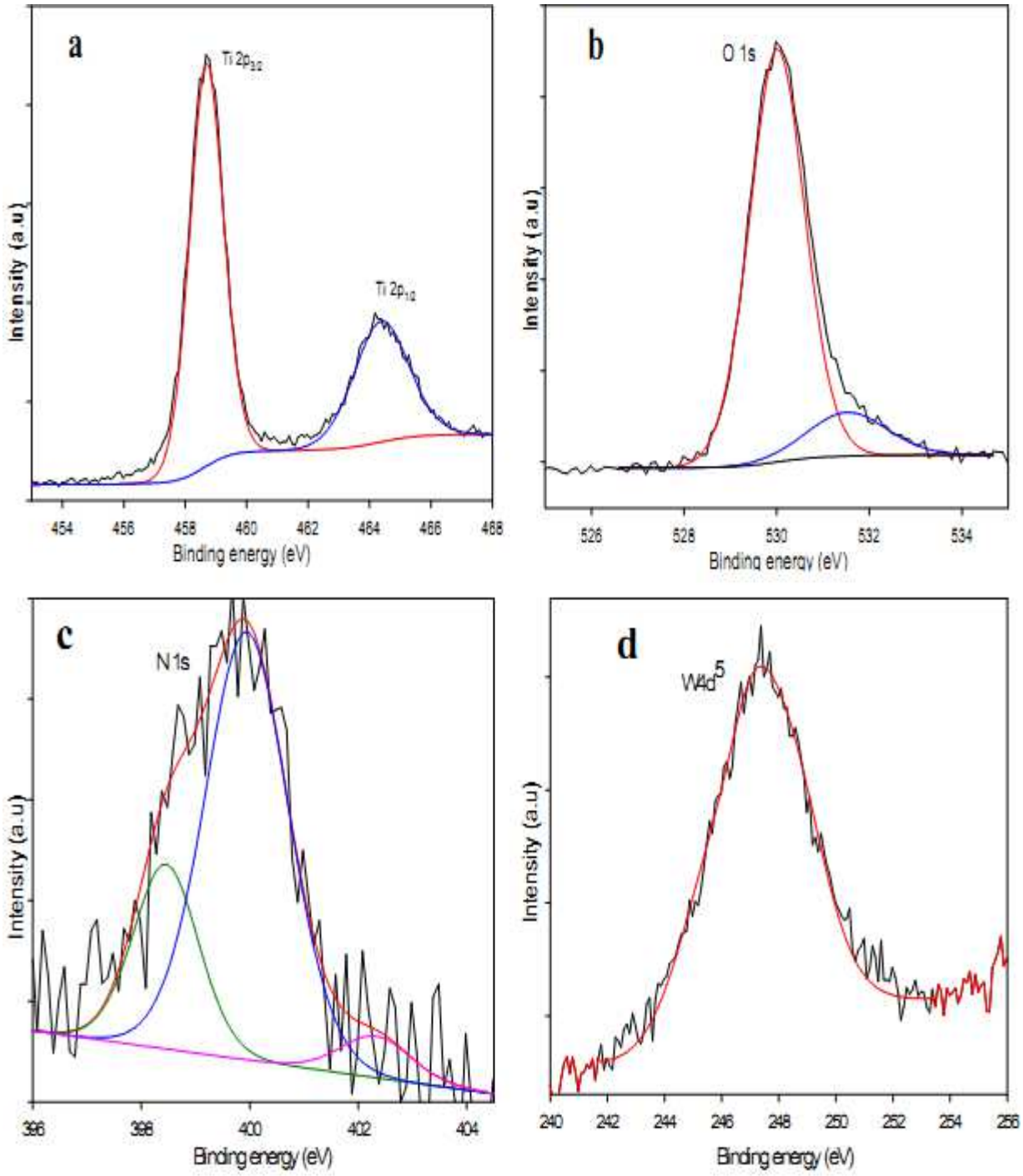

Figure 4.5. XPS spectra of (a) Ti 2p, (b) O 1s, (c) N 1s and (d) W $4d^5$ for TiO_2:N-W(1.5%).

that the peak at 399 eV is due to the interstitial doping of N into the crystal structure of TiO_2 and not chemisorption; an interpretation that is supported by many others [29-32]. Contrary to the above results some authors have attributed the peak at 399 eV to substitution nitrogen doping [33, 34]. As shown in Figure 4.5C, a broad peak extending from 397.5 to 402.5 eV is observed for all the N containing samples. These were fitted via a curve-fitting procedure to give three very distinct peaks centered at 397.93, 399.79 and 402.72 eV. The peaks at 397.93 eV and 399.79 eV may be assigned to substitutional doping in the form of N-Ti-O and interstitial doping as Ti-N-O, respectively. The peak located above 400 eV might be attributed to chemisorbed N containing compounds [35]. For tungsten, as shown in Figure 4.5D, only one strong peak at 247.06 eV is observed. This peak may be assigned to the W dopant within the TiO_2 structure as there was no WO_3 detected in the XRD studies. The value is ~0.5 eV lower than the values obtained by other researchers for the W_{4d} in W doped TiO_2 [36], indicating that the presence of N in the lattice has some significant effect on the surrounding electronic structure. The atomic percentages of nitrogen and tungsten were calculated from their respective peak areas and the results are shown in Table 4.3. The doping percentage level of nitrogen was almost constant as the amount of urea used in all of these experiments was the same. The tungsten doping level was

Table 4.3: Chemical constitution of the samples determined by XPS.

Sample	At wt% of N	At wt% of W
TiO_2	n/a	n/a
TiO_2:N	0.61	n/a
TiO_2:N-W(0.5%)	0.62	0.56
TiO_2:N-W(1%)	0.58	1.11
TiO_2:N-W(1.5%)	0.57	1.68
TiO_2:N-W(2%)	0.40	2.07
TiO_2:N-W(3%)	0.66	2.78

also observed to be consistent with the amount of tungsten solution added during the synthesis of the samples.

4.3.6. Visible-light-induced catalytic activity studies

We tested our as-synthesized samples under UV light, showing that they exhibit very similar photocatalytic activity as P25. The photodegradation reaction of RhB under visible light (λ>420) irradiation was thus used to evaluate and compare the photocatalytic activity of un-doped, N-doped and N,W co-doped TiO_2 and commercial Degussa P25. The irradiation time was 2 h and a sample was collected from the reaction mixture at 20 min intervals to measure the absorbance of RhB using a Cary 50 UV-visible spectrometer. Calibration measurements were performed to correlate the concentration between the dynamic range of 2.5- 25 μM and the absorbance of RhB, as illustrated in Figure 4.6. The linear regression equation was calculated to be A= 0.098c-0.129 with a correlation coefficient of 0.999. Figure 4.7 presents the kinetic curves for the photodegradation of Rhodamine B over P25 and the N-doped TiO_2 and N,W co-doped TiO_2 samples. The kinetics curves for the photodegradation of the dye on the un-doped TiO_2 synthesized in this study and P25 are almost the same. In contrast, the photodegradation of the dye on the N-doped TiO_2 is much more rapid than that on P25, and the speed of degradation is further dramatically improved by increasing the amount of W dopant in the samples until 1.5 at% doping level of W was achieved. Beyond this level a continuous decrease in photocatalytic activity is observed, which indicates that there exists a maximum doping level. Based on the modeling analysis by G. L. Puma [37, 38], the differences in the dye degradation kinetics may be caused by different optical characteristics of each catalyst in suspension if the materials have different particle sizes. In this study, all the samples were prepared using the same method under

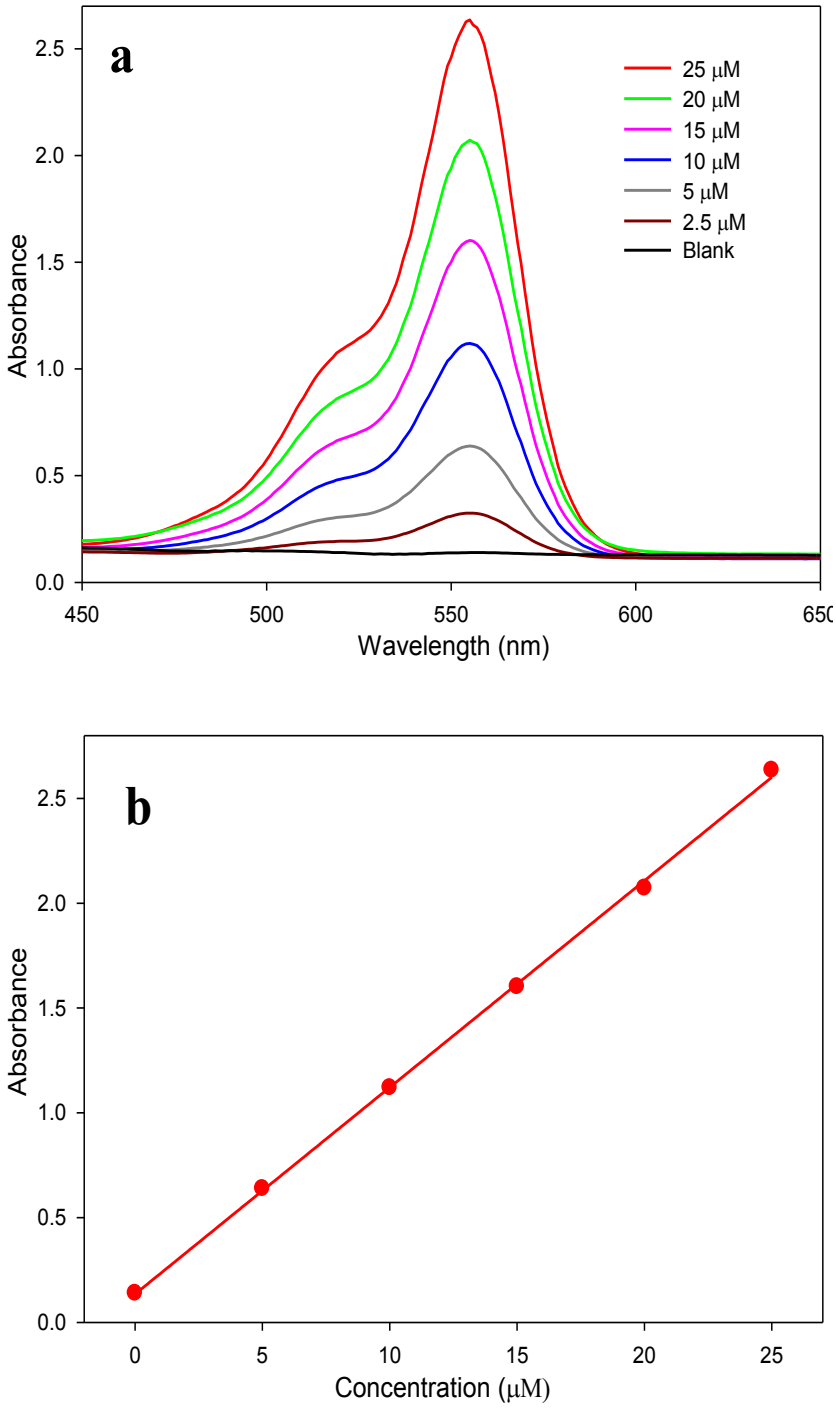

Figure 4.6. (a) Calibration curve for Rhodamine B; (b) Relationship between absorbance and concentration at 553 nm

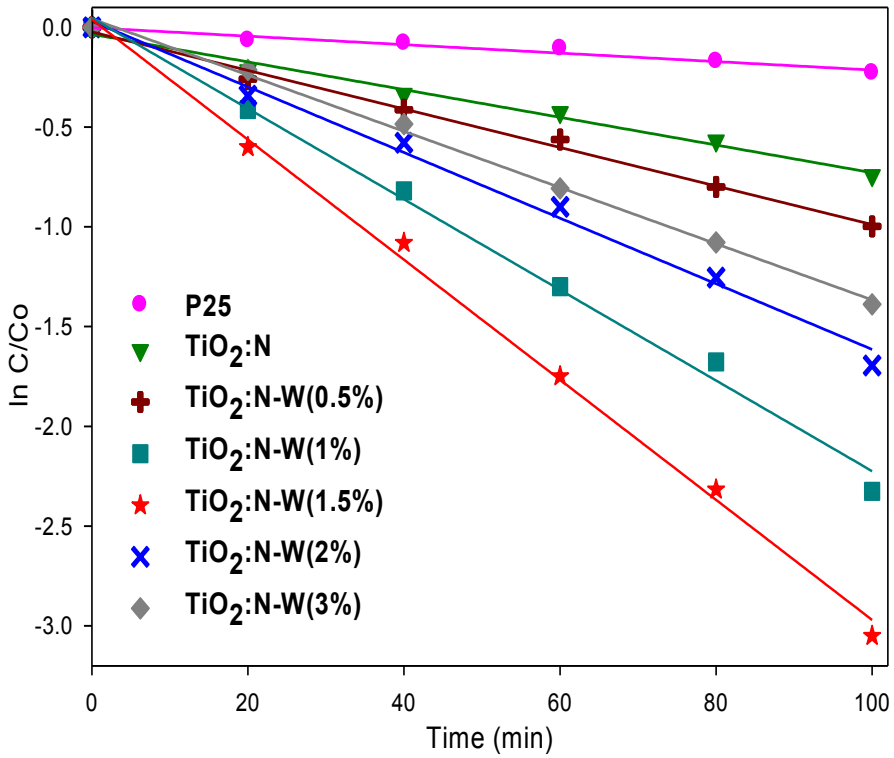

Figure 4.7. Kinetic curves for the photodegradation of Rhodamine B over the TiO_2, N-doped TiO_2 and N,W co-doped TiO_2 samples.

similar conditions. As shown in Table 4.1, the synthesized N,W-codoped TiO_2 catalysts possess similar BET surface area and particle size. The difference observed in the photocatalytic activity can be attributed to the level of the doped W. On one hand, doping can reduce the band gap energy of materials, and therefore may harvest more visible light, which is favorable for photocatalytic efficiency, whereas on the other hand, impurities that are added to the semiconductor lattice due to doping might result in the formation of defects which act as recombination centres. In this co-doping system, the physically larger atomic W occupies more volume than atomic Ti. Hence, a high doping level will produce a significant defect

concentration. The detailed kinetics of the reaction is presented in Table 4.4 and is depicted on Figure 4.8.

Table 4.4: First order kinetic constant and relative coefficient for degradation of Rhodamine B over prepared samples.

Sample	Rate constant(min^{-1})	R^2
P25	2.12×10^{-3}	0.962
TiO_2:N	6.94×10^{-3}	0.986
TiO_2:N-W(0.5%)	9.65×10^{-3}	0.994
TiO_2:N-W(1%)	2.27×10^{-2}	0.994
TiO_2:N-W(1.5%)	3.01×10^{-2}	0.997
TiO_2:N-W(2%)	1.64×10^{-2}	0.991
TiO_2:N-W(3%)	1.40×10^{-2}	0.997

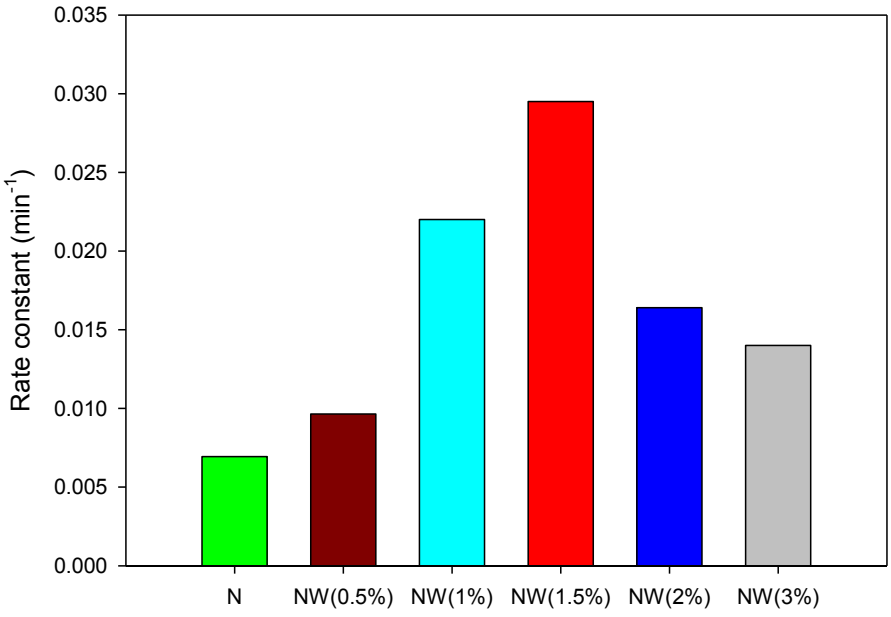

Figure 4.8. Bar chart showing the effect of W concentration on the rate of the reaction.

The kinetic calculations reveal that the rate of photodegradation of RhB on the TiO_2-N,W(1.5%) is approximately 14 times higher than that on the P25, demonstrating that the co-doped samples enable a significant enhancement in the visible light induced photocatalytic activity.

The photodegradation of organic dyes on the surface of a TiO_2 based photocatalyst is generally initiated by the irradiation of the reaction mixture with a light source which excites and transitions the electrons from the valence band to the conduction band. The energy inherent to visible light is not adequate to excite an electron of pure TiO_2 due to the wide band gap of ~3.08 eV, which results in poor photocatalytic activity. The significantly enhanced visible light activity of the prepared N,W co-doped TiO_2 is explained by the fact that doping with nitrogen, which replaces the oxygen atoms resident within the TiO_2 lattice structure creates an impurity level that is just above that of the valence band. The simultaneous doping with tungsten introduces an impurity level that is just below the conduction band; thereby narrowing the band gap and leading to the augmented visible light response of these solution combustion synthesized photocatalysts. Consequently, when these co-doped TiO_2 are irradiated, the electrons may be promoted from the valence band to the impurity level introduced by the doping of the metal atom, or from the lower to higher impurity level. Subsequently, these electrons are captured by the adsorbed O_2 to give $O_2^{\bullet-}$, and the water molecules adsorbed on the surface of the catalyst react with the hole(+) vacancies to give $OH^{\bullet}$. Finally, these active oxygen species attack the dye radical cations and decompose them. The proposed sequential mechanism is as follows.

(a) Absorption of energy

$$TiO_2 + h\nu \rightarrow h^+ + e- \qquad (1)$$

(b) Generation of active oxygen species

$$O_2 + e- \rightarrow O_2^{\bullet-} \qquad (2)$$

$H_2O + h^+ \rightarrow H^+ + OH^{\bullet}$ (3)

(c) Oxidation of dye

$RhB + O_2^{\bullet-} \rightarrow$ products (4)

$RhB + OH^{\bullet} \rightarrow$ products (5)

The slight activity of pure TiO_2 as observed in Figure 7 may be attributed to a photosensitized process whereby RhB absorbs visible light, which results in an intramolecular $\pi \rightarrow \pi^*$ transition. The photoelectrons in π^* are injected into the conduction band of the TiO_2 from where the same series of reactions ensue, as shown below.

(a) $RhB + h\nu \rightarrow RhB^*$

(b) $RhB^* + TiO_2 \rightarrow RhB^{\bullet+} + TiO_2$ (e)

(c) TiO_2 (e) $+ O_2 \rightarrow TiO_2 + O_2^{\bullet-}$

(d) $RhB^{\bullet+} + O_2^{\bullet-} \rightarrow$ products

4.4. Conclusions

We have successfully prepared mesoporous N-doped and N,W co-doped TiO_2 photocatalysts with an exclusive anatase phase and a high specific surface area utilizing a facile, reproducible and inexpensive solution combustion synthesis. The atomic percentage of N was kept constant, whereas that of W was varied. The textural, morphological and chemical composition studies with the prepared samples were done using various characterization techniques. XPS analysis showed that the N and W atoms were well incorporated into the lattice structure of the titania by this combustion preparation method, thus leading to a significant red shift in the absorption edge of the co-doped TiO_2, and concordantly, a dramatic narrowing of the

band gap was observed. This narrowing of the band gap serves to induce high visible light response photocatalytic activities in the co-doped samples in comparison to those of P25 and therefore, may be beneficially utilized in green chemistry. Photodegradation studies of Rhodamine B dye on the different samples revealed that an enhancement factor of up to 14 times in the reaction rate was observed with the 1.5 at% W doped sample in contrast to commercial Degussa P25. The novel combustion process developed in this study is rapid and reproducible, and can be easily scaled-up, thus opening a door to fabricate high-performance TiO_2 photocatalysts for promising environmental applications.

References

[1] W. C. Tincher. Processing wastewater from carpet mills, *Textile Chemist and Colorist* 21 (**1989**) 33-35.

[2] P. K. Malik. Use of activated carbons prepared from sawdust and rice-husk for adsorption of acid dyes: a case study of Acid Yellow 36, *Dyes and Pigments* 56 (**2003**) 239-249.

[3] H. Fu, C. Pan, W. Yao, Y. Zhu. Visible-light-induced degradation of rhodamine B by nanosized Bi_2WO_6, *The Journal of Physical Chemistry B* 109 (**2005**) 22432-22439.

[4] Y. Xu, C. H. Langford. UV- or Visible-light-induced degradation of X_3B on TiO_2 nanoparticles: The Influence of Adsorption, *Langmuir* 17 (**2001**) 897-902.

[5] S. Horikoshi, F. Hojo, H. Hidaka, N. Serpone. Environmental remediation by an integrated microwave/UV illumination technique. 8. fate of carboxylic acids, aldehydes,

alkoxycarbonyl and phenolic substrates in a microwave radiation field in the presence of TiO_2 particles under UV irradiation, *Environmental Science & Technology* 38 (**2004**) 2198-2208.

[6] F. Herrera, A. Lopez, G. Mascolo, P. Albers, J. Kiwi. Catalytic decomposition of the reactive dye UNIBLUE a on hematite. Modeling of the reactive surface, *Water Research* 35 (**2001**) 750-760.

[7] M. Tian, G. Wu, B. Adams, J. Wen, A. Chen. Kinetics of Photoelectrocatalytic degradation of nitrophenols on nanostructured TiO_2 electrodes, *The Journal of Physical Chemistry C* 112 (**2007**) 825-831.

[8] G. Wu, T. Nishikawa, B. Ohtani, A. Chen. Synthesis and characterization of carbon-doped TiO_2 nanostructures with enhanced visible light response, *Chemistry of Materials* 19 (**2007**) 4530-4537.

[9] T. Sreethawong, S. Laehsalee, S. Chavadej. Use of Pt/N-doped mesoporous-assembled nanocrystalline TiO_2 for photocatalytic H_2 production under visible light irradiation, *Catalysis Communications* 10 (**2009**) 538-543.

[10] A. Ghicov, J. M. Macak, H. Tsuchiya, J. Kunze, V. Haeublein, L. Frey, P. Schmuki. Ion implantation and annealing for an efficient N-doping of TiO_2 nanotubes, *Nano Letters* 6 (**2006**) 1080-1082.

[11] S.U.M. Khan, M. Al-Shahry, W. B. Ingler. Efficient photochemical water splitting by a chemically modified n-TiO_2, *Science* 297 (**2002**) 2243-2245.

[12] G. Wu, J. Wang, D.F. Thomas, A. Chen. Synthesis of F-doped flower-like TiO_2 nanostructures with high photoelectrochemical activity, *Langmuir* 24 (**2008**) 3503-3509.

[13] T. Ihara, M. Miyoshi, Y. Iriyama, O. Matsumoto, S. Sugihara. Visible-light-active titanium oxide photocatalyst realized by an oxygen-deficient structure and by nitrogen doping, *Applied Catalysis B: Environmental* 42 (**2003**) 403-409.

[14] R. Asahi, T. Morikawa, T. Ohwaki, K. Aoki, Y. Taga. Visible-light photocatalysis in nitrogen-doped titanium oxides, *Science* 293 (**2001**) 269-271.

[15] Y. Ma, J. Zhang, B. Tian, F. Chen, L. Wang. Synthesis and characterization of thermally stable Sm, N co-doped TiO_2 with highly visible light activity, *Journal of Hazardous Materials* 182 (**2010**) 386-393.

[16] G. Wu, J. Wen, J. Wang, D.F. Thomas, A. Chen. A facile approach to synthesize N and B co-doped TiO_2 nanomaterials with superior visible-light response, *Materials Letters* 64 (**2010**) 1728-1731.

[17] T. Lindgren, J. M. Mwabora, E. Avendaño, J. Jonsson, A. Hoel, C.-G. Granqvist, S.-E. Lindquist. Photoelectrochemical and optical properties of nitrogen doped titanium dioxide films prepared by reactive DC magnetron sputtering, *The Journal of Physical Chemistry B* 107 (**2003**) 5709-5716.

[18] K. Song, J. Zhou, J. Bao, Y. Feng. Photocatalytic activity of (copper, nitrogen)-codoped titanium dioxide nanoparticles, *Journal of the American Ceramic Society* 91 (**2008**) 1369-1371.

[19] E. A. Reyes-Garcia, Y. Sun, D. Raftery. Solid-state characterization of the nuclear and electronic environments in a boron−fluoride co-doped TiO_2 visible-light photocatalyst, *The Journal of Physical Chemistry C* 111 (**2007**) 17146-17154.

[20] A. Kubacka, B. Bachiller-Baeza, G. Colón, M. Fernández-García. Doping level effect on sunlight-driven W,N-co-doped TiO_2-anatase photo-catalysts for aromatic hydrocarbon partial oxidation, *Applied Catalysis B: Environmental* 93 (**2010**) 274-281.

[21] A. Kubacka, G. Colón, M. Fernández-García. N- and/or W-(co)doped TiO_2-anatase catalysts: Effect of the calcination treatment on photoactivity, *Applied Catalysis B: Environmental* 95 (**2010**) 238-244.

[22] B. Gao, Y. Ma, Y. Cao, W. Yang, J. Yao. Great enhancement of photocatalytic activity of nitrogen-doped titania by coupling with tungsten oxide, *The Journal of Physical Chemistry B* 110 (**2006**) 14391-14397.

[23] Y. Shen, T. Xiong, T. Li, K. Yang. Tungsten and nitrogen co-doped TiO_2 nano-powders with strong visible light response, *Applied Catalysis B: Environmental* 83 (**2008**) 177-185.

[24] J. Li, J. Xu, W.-L. Dai, H. Li, K. Fan. One-pot synthesis of twist-like helix tungsten–nitrogen-codoped titania photocatalysts with highly improved visible light activity in the abatement of phenol, *Applied Catalysis B: Environmental* 82 (**2008**) 233-243.

[25] Y.-H. Zhang, A. Reller. Nanocrystalline iron-doped mesoporous titania and its phase transition, *Journal of Materials Chemistry* 11 (**2001**) 2537-2541.

[26] A. Kubacka, G. Colón, M. Fernández-García. Cationic (V, Mo, Nb, W) doping of TiO_2–anatase: A real alternative for visible light-driven photocatalysts, *Catalysis Today* 143 (**2009**) 286-292.

[27] J. A. Rengifo-Herrera, E. Mielczarski, J. Mielczarski, N. C. Castillo, J. Kiwi, C. Pulgarin. Escherichia coli inactivation by N, S co-doped commercial TiO_2 powders under UV and visible light, *Applied Catalysis B: Environmental* 84 (**2008**) 448-456.

[28] N. C. Saha, H. G. Tompkins. Titanium nitride oxidation chemistry: An X-ray photoelectron spectroscopy study, *Journal of Applied Physics* 72 (**1992**) 3072-3079.

[29] S. Sato, R. Nakamura, S. Abe. Visible-light sensitization of TiO_2 photocatalysts by wet-method N doping, *Applied Catalysis A: General* 284 (**2005**) 131-137.

[30] Y. Wang, C. Feng, M. Zhang, J. Yang, Z. Zhang. Visible light active N-doped TiO_2 prepared from different precursors: Origin of the visible light absorption and photoactivity, *Applied Catalysis B: Environmental* 104 (**2011**) 268-274.

[31] O. Diwald, T. L. Thompson, E. G. Goralski, S. D. Walck, J. T. Yates. The effect of nitrogen ion implantation on the photoactivity of TiO_2 rutile single crystals, *The Journal of Physical Chemistry B* 108 (**2003**) 52-57.

[32] G. Wu, S. Nigro, J.Wen, A. Chen, One-step synthesis of N- and F-codoped mesoporous TiO_2 photocatalysts with high visible light activity, *Nanotechnology* 21 (**2010)** pp8.

[33] H. Li, J. Li, Y. Huo. Highly Active TiO_2N Photocatalysts prepared by treating TiO_2 precursors in NH_3/ethanol fluid under supercritical conditions, *The Journal of Physical Chemistry B* 110 (**2006**) 1559-1565.

[34] H. Irie, Y. Watanabe, K. Hashimoto. Nitrogen-concentration dependence on photocatalytic activity of $TiO_{2-x}N_x$ Powders, *The Journal of Physical Chemistry B* 107 (**2003**) 5483-5486.

[35] X. Yang, C. Cao, L. Erickson, K. Hohn, R. Maghirang, K. Klabunde. Photo-catalytic degradation of rhodamine B on C-, S-, N-, and Fe-doped TiO_2 under visible-light irradiation, *Applied Catalysis B: Environmental* 91 (**2009**) 657-662.

[36] A. Kubacka, M. Fernández-García, G. Colón. Nanostructured Ti–M mixed-metal oxides: Toward a visible light-driven photocatalyst, *Journal of Catalysis* 254 (**2008**) 272-284.

[37] G. Li Puma, A. Brucato. Dimensionless analysis of slurry photocatalytic reactors using two-flux and six-flux radiation absorption–scattering models, *Catalysis Today* 122 (**2007**) 78-90.

[38] G. Li Puma. Modeling of thin-film slurry photocatalytic reactors affected by radiation scattering, *Environmental Science & Technology* 37 (**2003**) 5783-5791.

Chapter 5: Significant Enhancement in the Photocatalytic Activity of TiO_2 Nanotubes and N,W co-doped TiO_2 Nanomaterials*

5.1 Introduction

Environmental pollution is becoming an increasingly serious threat to fragile ecosystems worldwide. Every year millions of tons of untreated organic waste are discarded into natural water systems. Thus, there is an urgent need to develop effective methods for the degradation of pollutants in wastewater prior to its discharge. Photocatalysis provides a clean and cost effective method for the oxidation of organic pollutants that is facilitated by highly oxidizing free radicals $O_2^{\bullet-}$ and $OH^{\bullet}$, which are produced by photogenerated electrons and holes [1, 2]. In past decade, various metal oxide semiconductors have been studied for the abatement of organic pollutants from wastewater [3-5]. Titanium dioxide (TiO_2) has been widely investigated as a photocatalyst [6-9] due to its biological and chemical inertness, cost effectiveness, corrosion resistance and the strong oxidizing power of its photogenerated holes [10-17]. When TiO_2 is irradiated with near UV light ($\lambda < 400$ nm), the ensemble of electrons are excited from the valence band to the conduction band, generating electron–hole pairs that initiate subsequent surface catalytic reactions. These electron–hole pairs have an innate tendency to recombine, which cumulatively diminishes photocatalytic efficiency. Despite inherently promising features, the major barrier in the efficient use of TiO_2 is that it possesses a very wide band gap of ~3.2 eV [18, 19]. Thus, in order to populate the conduction band with electrons in carrying out the photocatalytic process, only UV light may be employed for its activation [20, 21]. Hence, unmodified TiO_2 is devoid of visible light response and exhibits low efficiency under irradiation by ambient sunlight, which

* Most of the results presented in this chapter have been published in *Electrochemistry Communications* **2011**, *13*, 1186-1189 and *Nanotechnology* **2012**, *23*, 475706 (8pp)

provides a continuous source of renewable energy. For the most part, sunlight contains radiation in the visible region of the spectra, with ~5% in the UV domain [22]. Thus a modification of the electronic structure is required to shift the absorbance edge of TiO_2 into the visible regions to enable its utility under visible light and sunlight. This may be attained via anionic doping (e.g., with N, C, S and halogens) or through doping with metal ions [23-26]. Doping with N has proven to be very efficacious as recent studies show that it favors the creation of oxygen vacancies [27-29]. Exclusive doping with non-metals, in order to replace O from the TiO_2 lattice, has been shown to be ineffectual. There are still a number of restrictions that impede the improvement of the photocatalyst, as electron-hole recombination remains a major obstacle [30, 31]. Co-doping with metal atoms provides a way forward in the suppression of electron-hole recombination, as metals with changing valence may serve as electron trapping sites [32,33].

TiO_2 nanotubes have been synthesized via various approaches, including using a template of nanoporous alumina [34], sol-gel processes [35], seeded growth method [36], hydrothermal techniques [37] and the anodization of titanium in a fluoride-based electrolyte [38, 39]. The anodization of titanium offers superior control over the nanotube dimensions in comparison to other approaches. However, TiO_2 nanotubes prepared in a fluoride-based electrolyte (e.g. DMSO + HF) exhibits relatively low activity [40-42].

In the present work, we report, for the first time, a facile and effective approach for the enhancement of the photocatalytic activity of TiO_2 and N,W co-doped TiO_2. The TiO_2 nanotubes prepared by the electrochemical oxidation of titanium in DMSO with 2% HF and N,W co-doped TiO_2 prepared with solution combustion method were treated in a methanol solution under UV light irradiation. The treated TiO_2 nanotubes showed considerable enhancements in both photocurrent for water splitting and photocatalytic activity towards wastewater treatment. The

effect of the pretreatment time was also determined for N,W co-doped TiO_2. The efficiency of the UV pretreatment was systemically assessed using the photochemical degradation of RhB under irradiation of both UV and visible light. To decipher the origin of the substantial improvement in the photocatalytic activity, the N,W co-doped TiO_2 samples prior to and following the UV pretreatment were examined using various surface analytical methods. The stability of the UV pretreated N,W co-doped TiO_2 was further tested.

5 2. Experimental

5.2.1 Materials

For synthesizing N,W co-doped TiO_2, Titanium (IV) isopropoxide (TTIP) (97%), urea (≥ 99%), sodium tungstate ($Na_2WO_4.2H_2O$) and acetic acid were purchased from Sigma-Aldrich and used as received for the synthesis of the N, W co-doped TiO_2. For electrochemical tests on TiO_2 nanotubes, solutions were prepared using sulfuric acid (Aldrich, 99.999%), and pure water purified by a Nanopure water system (18.2 MΩ cm). All solutions were deaerated with ultra-pure argon (99.999%) prior to performing and measuring experiments.

Rhodamine B (BDH, UK) was employed as a model of typical organic dye pollutant in the evaluation of the photocatalytic activity of the N,W co-doped TiO_2. 4-Nitro Phenol was used for measuring the photocatalytic activity of the TiO_2 nanotubes.

5.2.2 Photocatalyst synthesis and UV pretreatment

The N,W co-doped TiO_2 photocatalysts were prepared by a facile solution combustion method, where 2 ml of Ti precursor TTIP was added under vigorous stirring into a mixture that consisted of 20 ml ethanol and 0.5 ml acetic acid. Acetic acid acts as an inhibitor of the hydrolysis of the Ti organic precursor. The solution was stirred vigorously for 30 min in order to

obtain a homogenous mixture. Predetermined amounts of urea and 0.1 M sodium tungstate solution were added to obtain 0.5 at% and 1.0 at% of N and W, respectively. The solution was initially heated on a hot plate and subsequently transferred to a preheated furnace (300 ^{o}C) to facilitate the combustion reaction. Finally, the synthesized powder was calcinated at 450 ^{o}C for 3 h.

The TiO_2 nanotubes were grown electrochemically at 40 V for 8 h in a one compartment two-electrode cell containing DMSO + 2% HF [7, 42] first. To obtain the anatase crystal structure, the plates were then annealed at 450 °C for 3h. For the UV pre-treatment, a TiO_2 sample was placed in a quartz tube containing 5 mL of 50% methanol-H_2O (v/v) first; after bubbling with Ar for 10 min, the quartz tube was then capped; and finally it was irradiated under UV light for 30 min.

5.2.3. Characterization techniques

The synthesized N,W co-doped TiO_2 nanomaterials were characterized by X-ray diffraction (Phillips PW 1050-3710 Diffractometer with Cu Kα radiation (λ=1.5406 Å). Transmission electron microscopy (JEOL 2010) analysis was performed in order to determine the surface morphology and particle size of the samples. The N,W co-doped TiO_2 photocatalysts were initially degassed at 400 ^{o}C for 3 h under vacuum and then used for the determination of the surface area by a N_2 gas adsorption/desorption method at liquid nitrogen temperature (77 K), utilizing a Quantachrome Nova 2200 surface area and pore size analyzer. The optical properties of the samples were investigated by measuring the UV-vis absorbance spectrum using a spectrophotometer (Varian, Cary 5E). Corresponding Tauc plots were plotted to estimate the band gap energy of the N,W co-doped TiO_2 photocatalysts before and after the UV pretreatment.

Surface composition was examined via X-ray photoelectron spectroscopy (Omicron EA-125 energy analyzer and a multi-channel detector).

The synthesized TiO_2 nanotubes were characterized by scanning electron microscopy (SEM) (JEOL 5900LV), X-ray diffraction (XRD) (Philips PW 1050-3710 Diffractometer with Cu Kα radiation). A three-electrode cell system was employed for the electrochemical studies. A Pt coil with a 10 cm^2 surface area was used as the auxiliary electrode; a saturated calomel electrode (SCE) was used as the reference electrode. Mott-Schottky plots were measured with Voltalab 40 Potentiostat (PGZ301) at a fixed frequency (500 Hz) [43]. The amplitude of modulation potential for the electrochemical impedance measurements was 10 mV. The potential range for capacitance measurement was varied from -400 mV to 1400 mV vs. SCE. A Dymax Cure Spot 50 (main line of emission, 365 nm) with an intensity of ~2 mW cm^{-2} was used for the irradiation of the TiO_2 nanotubes.

5.2.4. Photocatalytic activity measurements

Photodegradation experiments were performed using a model organic pollutant (Rhodamine B) to evaluate the photocatalytic activity of the N,W co-doped TiO_2 photocatalysts prior to and following the UV pretreatment under UV, visible and ambient sunlight in an open cylindrical pyrex glass vessel. In a typical trial, 20 mg of the sample was suspended in 60 ml of 25 μM Rhodamine B aqueous solution. To attain a homogenous mixture and adsorption-desorption isotherm, the reaction mixture was initially sonicated for 30 min in the dark. The reaction mixture was then exposed to the various light sources. An Oriel system equipped with a 300 W xenon arc lamp was employed in this study as the source of the UV and visible light.

5.3 Results and Discussion

The structure and morphology of the TiO_2 nanotubes were characterized by SEM. As shown in Figure 5.1A, the self-organized nanotubes consist of pored arrays with uniform diameters of ca. 70 nm and lengths of ca. 1μm. It is evident that the lumens of the pores are open

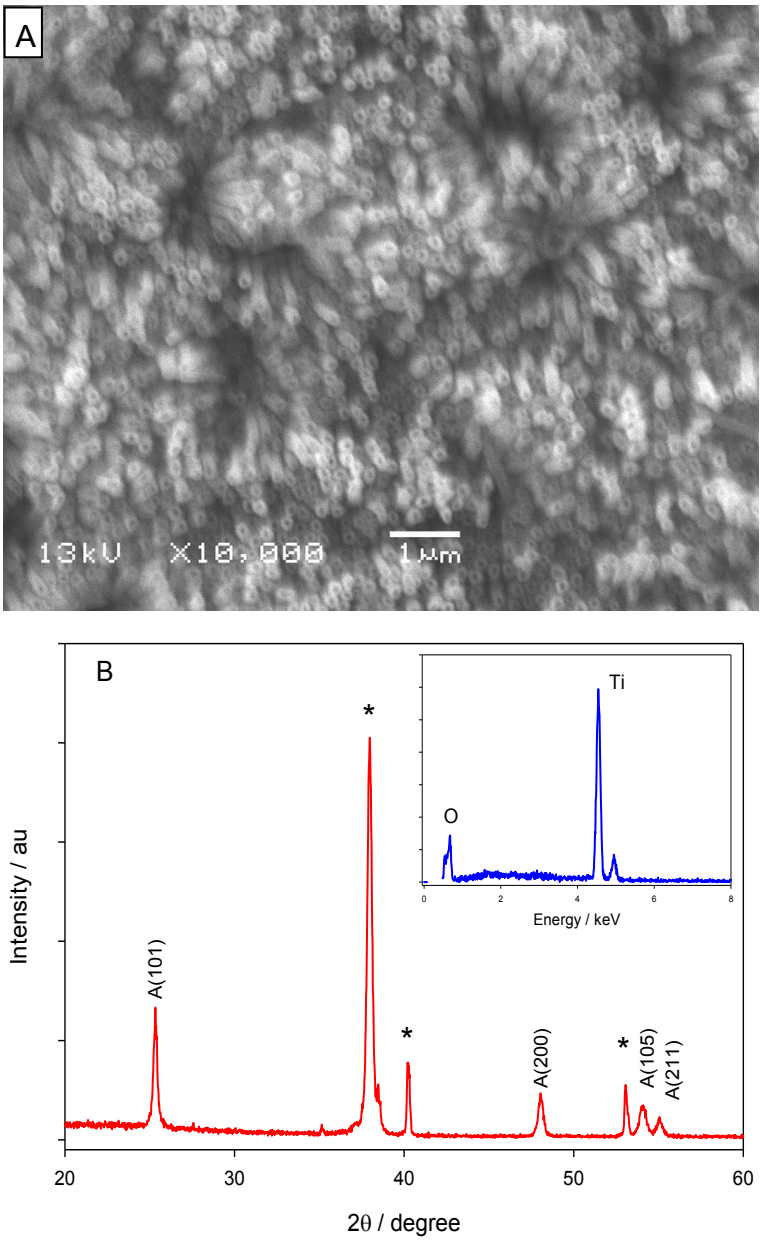

Figure 5.1. SEM images of (A) TiO_2 nanotubes (B) corresponding XRD pattern. Inset in (B) EDS of TiO_2 nanotubes.

at the top of the layer. The EDS of the nanotubes (inset in Figure 5.1B) displays strong oxygen and titanium peaks, which confirms the composition of the formed nanotube arrays. Figure 5.1B presents the corresponding XRD patterns of the prepared TiO_2 nanotubes. Except for the peaks (marked with stars) derived from the Ti substrate, all of the diffraction peaks are attributed to those of the tetragonal anatase TiO_2, revealing that the formed TiO_2 nanotubes exist in the anatase phase.

Figure 5.2A shows the cyclic voltammograms of the synthesized TiO_2 nanotube electrode recorded in a 0.1 M H_2SO_4 solution in the dark (a) and under UV irradiation (b & c). TiO_2 is a semiconductor; it has low electrocatalytic activity [44]. No notable current was observed in the potential range from 0.0 to 1.5V without UV irradiation (Curve a). Under UV illumination, a small photocurrent arose (Curve b). In contrast, the photocurrent of the TiO_2 nanotubes that underwent the UV pretreatment in methanol (Curve c) increased continuously in the investigated potential range and reached 5.2 mA cm^{-2} at 1.5 V vs. SCE, which is ca. 15 times higher than that of the TiO_2 nanotubes without the pretreatment. In addition, the color of the TiO_2 nanotube electrode was dramatically affected by the UV irradiation in methanol. As seen from the insets in Figure 5.2A, the color of the electrode (gray (d)) changed into dark blue (e), indicating change in the structure of the TiO_2 caused by the pre-treatment.

We further investigated the photocurrent transients at the applied electrode potential of 1.4 V vs. SCE by switching the UV light on and off. The duration of light pulses was set at 180 s, followed by dark current measurements for 60 s. As depicted in Figure 5.2B, the response of the photocurrent under UV irradiation is very rapid, and the photocurrents for the unpretreated TiO_2 nanotubes and the TiO_2 nanotubes with the UV pretreatment are 0.32 (curve b) and 4.78 (curve a) mA cm^{-2}, respectively.

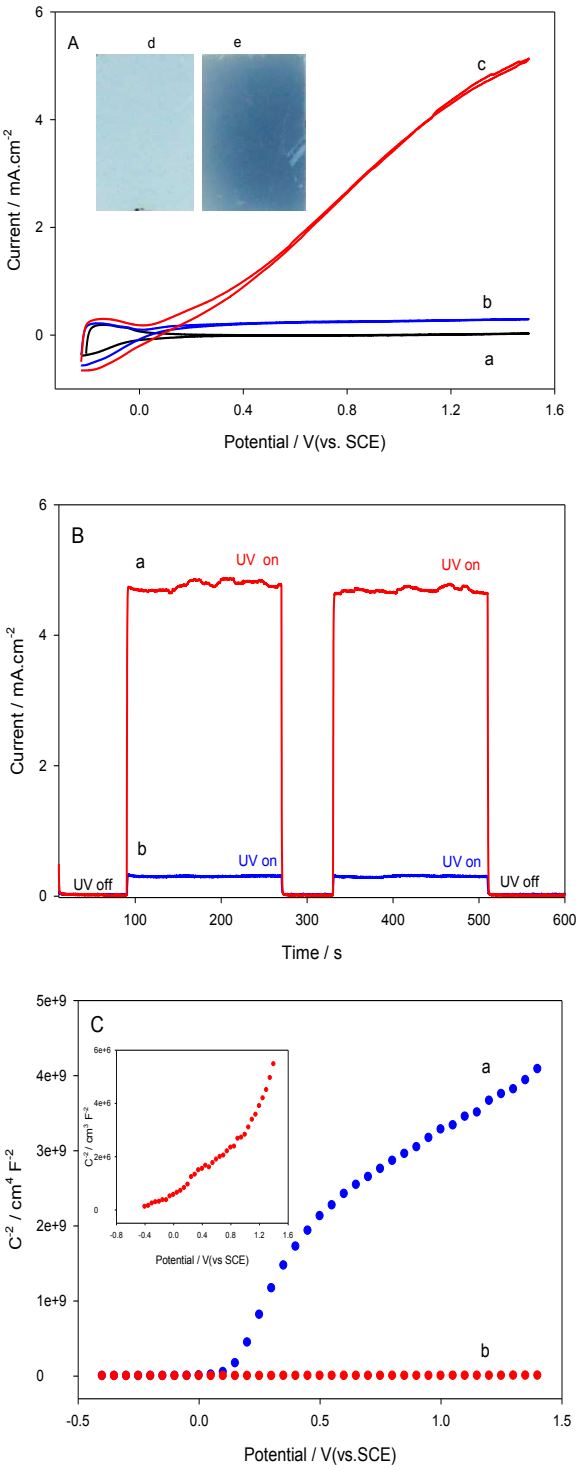

Figure 5.2. (A) Cyclic voltammograms of TiO_2 nanotubes electrode without (a) and with UV irradiation (b, c). Scan rate (mV/s): 20, supporting electrolyte: 0.1 M H_2SO_4. (B) The transient photocurrent-time profiles of the TiO_2 nanotubes with and without the UV pretreatment in methanol. Applied bias (V): 1.4; Insets in Figure 2A, the digital images of TiO_2 before (d) and after (e) the UV treatment. (C) Mott-Schottky plot of the TiO_2 nanotubes obtained in 0.1 M H_2SO_4 at 500 Hz without (a) and with (b) the UV pretreatment in methanol. Inset in Figure 2C: the Mott-Schottky plot of the TiO_2 nanotubes after the UV pretreatment.

The steady-state photocurrent of the TiO_2 nanotubes with the pretreatment is ca. 15 times higher than that of the unpretreated TiO_2 nanotubes, which is consistent with the observation in the cyclic voltammetric study shown in Figure 5.2A.

To further characterize the electronic properties of the TiO_2 nanotubes that were pretreated with methanol and UV light, the Mott-Schottky measurement was carried out in a 0.1M H_2SO_4 solution. The Mott-Schottky plot can be employed to estimate the donor density (N_D) [43]:

$$\frac{1}{C^2} = \frac{2}{\varepsilon\varepsilon_0 e N_D}\left(E - E_{fb} - \frac{kT}{e}\right)$$

where C is the capacitance of the space charge layer [$F \cdot m^{-2}$]; ε is the average value of the semiconductor dielectric constant (~120 for TiO_2); ε_0 is the permittivity of the free space charge (8.854×10^{-12} $F \cdot m^{-1}$); and e is the absolute value of the electron charge (1.602×10^{-19} C). The donor density is dependent on the dopant level and plays a key role in the determination of electronic conductivity. Figure 5.2C presents the Mott-Schottky plot for the as-synthesized TiO_2 nanotubes (a) and the UV pretreated TiO_2 nanotubes (b). For clarification, curve b is also enlarged and presented in Figure 5.2C as the insert. A sigmoidal plot was observed in the investigated potential range, which is typical for n-type semiconductors. There is a good linear relationship between C^{-2} and the potential in the range of 0 and 0.40 V vs. SCE for the non-pretreated TiO_2 nanotubes and the UV pretreated TiO_2 nanotubes. It is interesting to note that the donor density of the nanotubes that underwent the UV pretreatment ($1.1 \times 10^{21} cm^{-3}$) is almost 1000 times larger than that of the TiO_2 nanotubes without the pretreatment ($3.0 \times 10^{18} cm^{-3}$).

To further investigate the enhanced photocatalytic activity of the TiO_2 nanotubes with the pretreatment, we examined the photoelectrocatalytic oxidation of 4-nitrophenol (4-NPh).

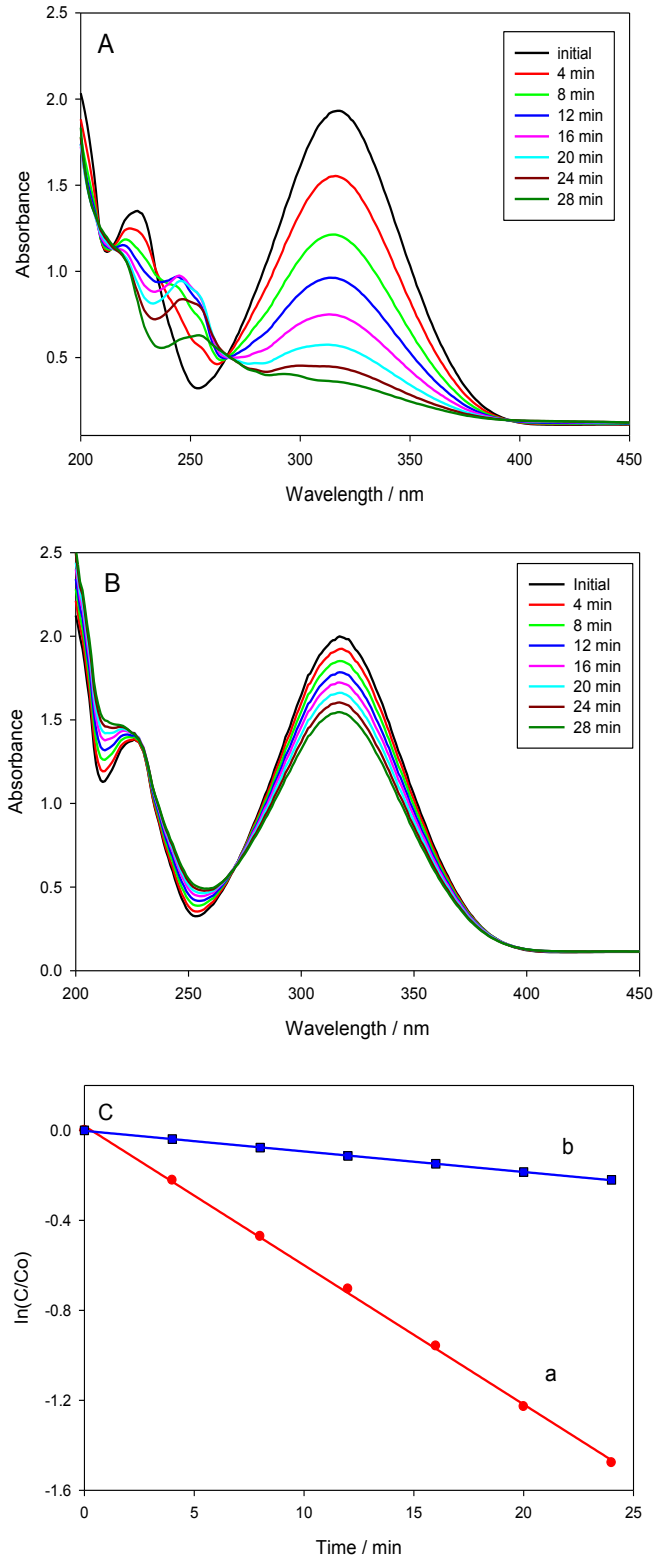

Figure 5.3. Scanning kinetic curves for photoelectrochemical oxidation of 4-NPh in 0.1 M H_2SO_4 at the TiO_2 nanotubes after (A) and before the UV pretreatment in methanol. Applied bias: 1.4 V. (C) The relationship between ln(C/Co) and time.

Figure 5.3A shows the time dependence of the spectral absorbances of 0.2 mM 4-NPh in 0.1 M H_2SO_4 taken at four-minute intervals during the photodegradative process. The absorbance of 4-NPh at 317 nm decreased with time and approached 0.37 after 28 min of photoelectrocatalytic degradation. This corresponds to over 80% removal of the 4-NPh from the solution. For comparison, the photoelectrochemical oxidation of 4-NPh was also carried out (Figure 5.3B) using native unpretreated TiO_2 nanotubes; ca. 20% removal of the NPh from solution was observed. As shown in Figure 5.3C, the photocatalytic oxidation of 4-NPh at the as-prepared TiO_2 nanotubes (Curve b) and TiO_2 nanotubes after the UV pretreatment (Curve a) can be fitted based on first-order kinetics. The rate constants for oxidation of 4-NPh at the TiO_2 nanotubes with and without the UV pretreatment was found to be 9.0×10^{-3} and 6.2×10^{-2} min^{-1}, respectively. It is apparent that the oxidation of 4NPh at pretreated TiO_2 nanotubes is 6.8 times more rapid than that of TiO_2 nanotubes without pretreatment, indicating a significant enhancement of photocatalytic activity by the pretreatment in methanol solution under UV irradiation.

The effect of the UV pretreatment on the photocatalytic properties of the N,W co-doped TiO_2 (TNW) was initially evaluated under visible light using the photodegradation of Rhodamine B (RhB). Figure 5.4 presents the kinetic plots of the photodegradation of RhB using the fabricated TNW before and after the UV pre-treatment for 30, 60 and 90 min under visible light, showing that the UV pretreatment had a significant impact on the improvement of the TNW activity. The linear relationship of $\ln C/C_o$ vs. time reveals that the photodegradation of RhB on TNW follows the pseudo first order kinetics. The rate constants and relative coefficients for the degradation are listed in Table 5.1. For the as-synthesized TNW, the rate constant was determined to be 8.96×10^{-3} min^{-1}, which was significantly increased to 4.60×10^{-2} min^{-1} following 30 min of UV treatment. When the TNW sample was treated for an additional 30 min,

the rate constant was further increased to 1.19×10^{-1} min^{-1}, which is over 12 fold higher in comparison to the untreated TNW. Upon further increasing the UV treatment time to 90 min, no increase of the rate constant was observed, indicating that 60 min is the optimal duration for the UV pretreatment.

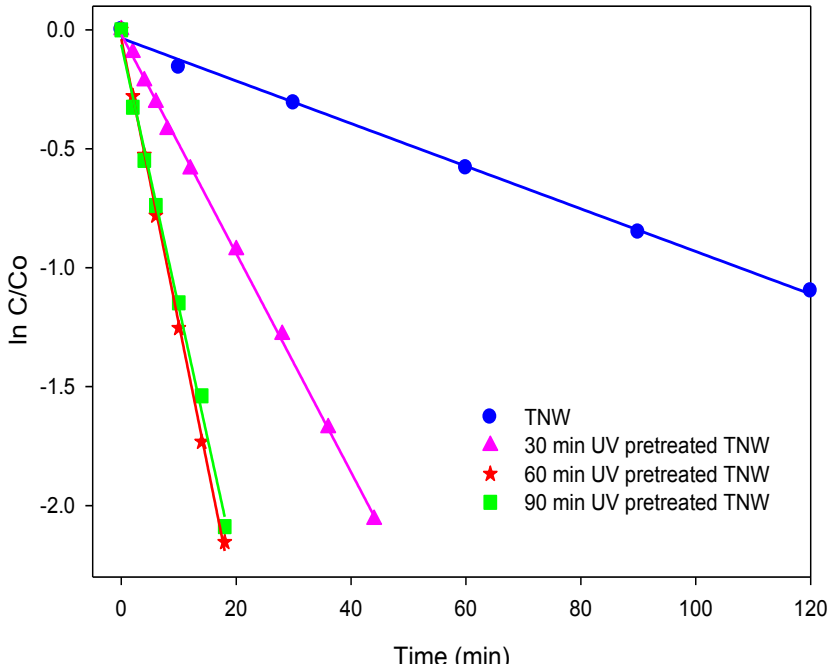

Figure 5.4. The time effect of the UV pretreatment on the TNW activity under the visible light.

Table 5.1: First order kinetic constants and the relative coefficients for degradation of Rhodamine B over prepared samples.

Sample	Rate constant (min^{-1})	R^2
TNW before treatment	8.96×10^{-3}	0.999
TNW 30 min. UV pretreated	4.60×10^{-2}	0.999
TNW 60 min. UV pretreated	1.192×10^{-1}	0.999
TNW 90 min. UV pretreated	1.11×10^{-1}	0.995

The impact of the UV pretreatment of TNW on the photocatalytic activity was also investigated under UV irradiation. Figure 5.5 displays the kinetic plots of the photodegradation of RhB on TNW prior to and following one-hour of UV pretreatment. For comparison, the kinetic plot using P25 (Degussa), one of the best commercially available TiO_2 nanoparticles, was also included in Figure 5.5. The rate constants and the relative coefficients for the degradation under UV irradiation are listed in Table 5.2.

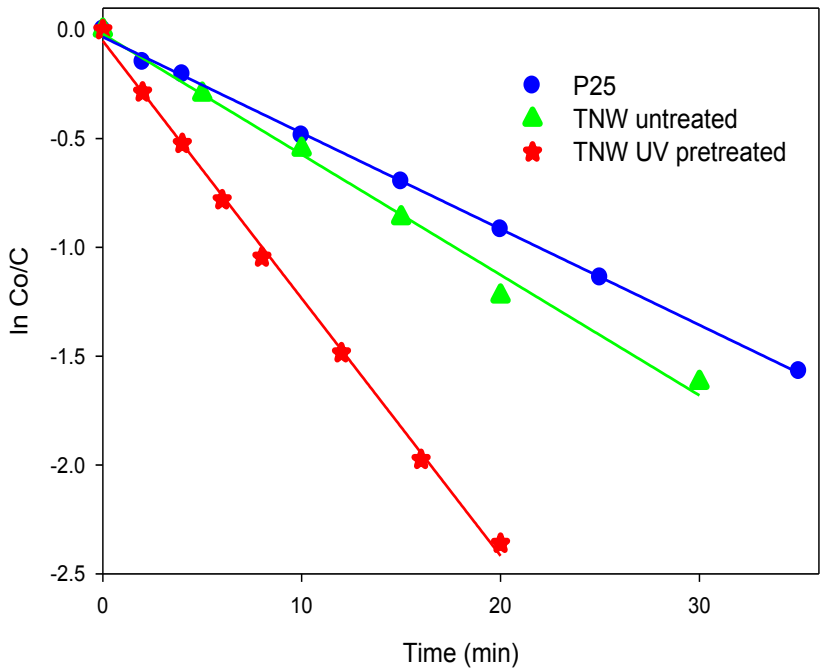

Figure 5.5. Comparison of the TNW sample prior to and following the UV pretreatment with P25 under UV light.

Table 5.2. First order kinetic constants and relative coefficients for the degradation of Rhodamine B over the TNW samples prior to and following the UV pretreatment and P25 under UV light.

Sample	**Rate constant (min-1)**	**R^2**
P25	4.50×10^{-2}	0.998
TNW before treatment	5.53×10^{-2}	0.992
TNW after treatment	1.18×10^{-1}	0.998

The as-synthesized TNW exhibited a slightly higher photocatalytic activity than the P25. The UV pretreatment greatly enhanced the photocatalytic activity of TNW; the rate constant of photodegradation of RhB on the UV pretreated TNW was 2.1 times higher in comparison to the unpretreated TNW, and over 2.6 times higher than that on the P25.

To decipher the origin of the significant enhancement in photocatalytic activity imparted by the UV pretreatment, various surface analytical techniques were employed to characterize the N,W co-doped TiO_2 sample before and subsequent to the UV pretreatment. TEM images of the as-synthesized and UV pretreated TNW samples are presented in Figure 5.6A and 5.6B, respectively. The TNW sample was comprised of spherical nanoparticles that possessed a highly mesoporous structure with irregular pore sizes. No notable difference was observed in the TEM images that were taken before and after the UV pretreatment. In addition, as shown in Figure 5.7, the selected area electron diffraction (SAED) patterns of the TNW samples prior to and following the UV pretreatment are very similar, revealing that both are polycrystalline in nature.

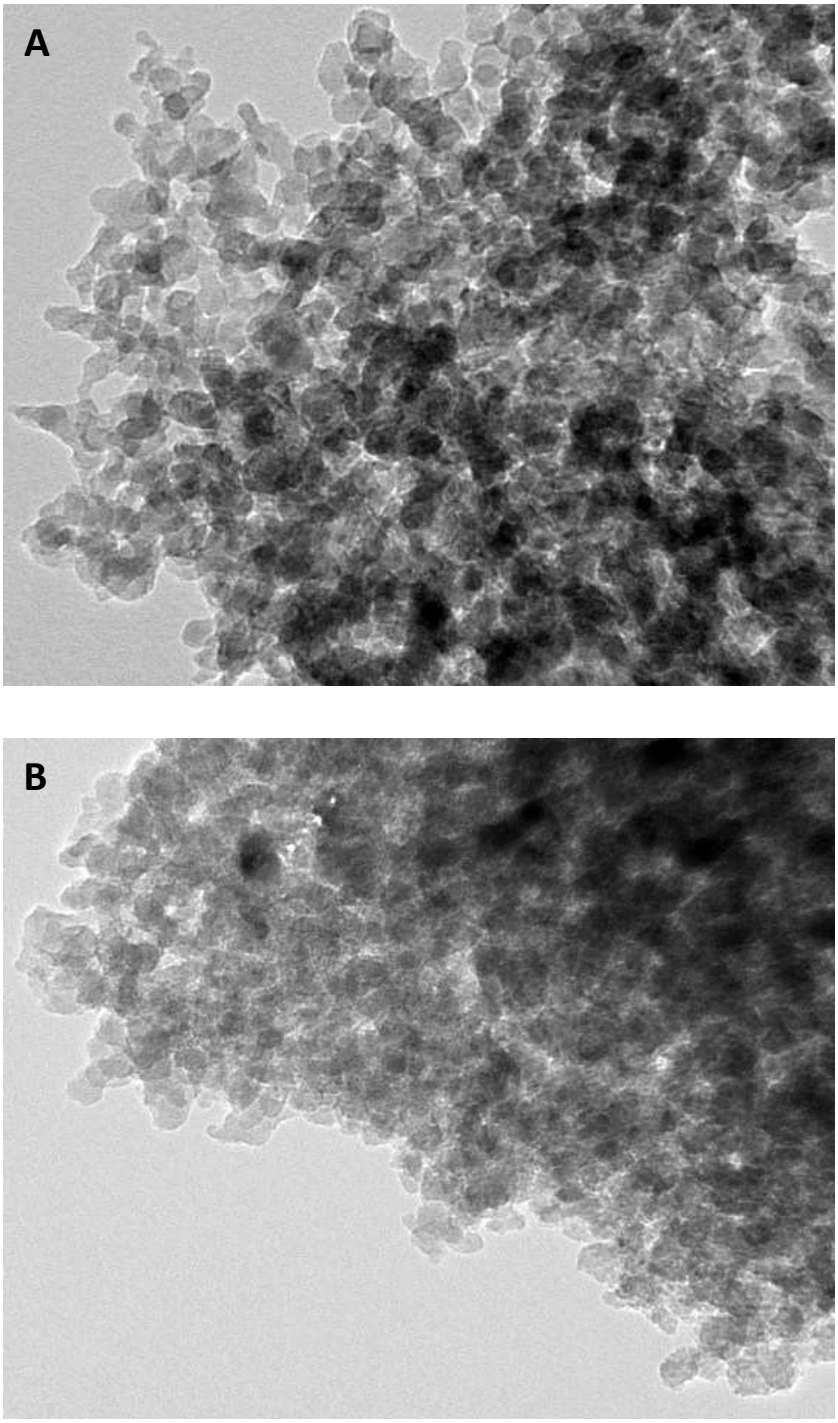

Figure 5.6. TEM images of N,W co-doped TiO_2 (A) before and (B) after UV pretreatment.

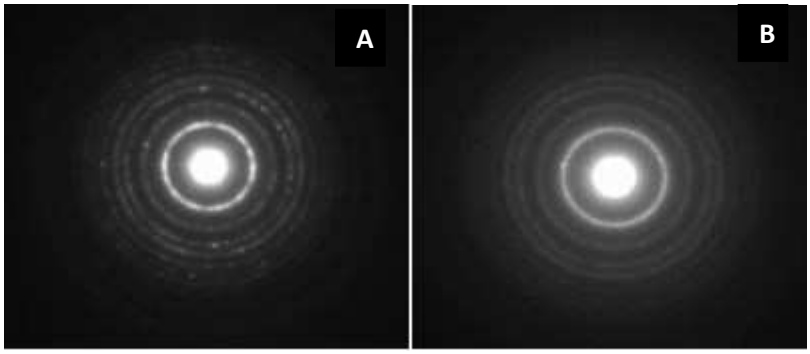

Figure 5.7. SAED images of the Untreated (a) and UV pretreated (b) sample respectively.

It is well known that anatase TiO_2 exhibits more robust photocatalytic properties than the other phases of TiO_2, i.e. rutile and brookite. To examine any alterations in the crystalline structure that might be caused by the one-hour UV pretreatment, the TNW samples were characterized by XRD, with the results shown in Figure 5.8A. The XRD pattern depicts only anatase phase peaks and is devoid of those associated with WO_3, showing that there was no alteration in the crystalline structure following the UV pretreatment in comparison with the as-synthesized TNW sample. The crystalline dimensions of the samples were calculated using the Scherrer equation:

$$d = k\lambda/\beta \cos\theta$$

where λ is the X-ray wavelength, β is the full width at half maximum of the (101) peak, θ is the incident angle, and k is a shape factor based on one of the characteristic peaks of the anatase phase, located at 25.5°. The nanoparticle size calculated from the XRD pattern was in good agreement with the TEM images as we can see that the average particle size is ~10 nm. The crystalline size was slightly decreased from 10.0 to 9.4 nm after the UV pretreatment.

The highly mesoporous structure of the UV pretreated and unpretreated TNW samples was further verified as they exhibited isotherms of type IV for N_2 adsorption-desorption as shown in Figure 5.8B. The UV pretreatment had some positive impact on the surface area. For the as-synthesized TNW, the specific surface area was measured to be 127.0 m^2g^{-1}, which was increased to 138.0 m^2g^{-1} subsequent to the UV pretreatment. This may be attributed to the removal of impurities, which partially blocked the mesoporous structure of the synthesized N,W co-doped TiO_2 nanomaterials. As a large surface area contributes considerably to the photocatalytic properties of heterogeneous photocatalysts [45], the increase in the surface area following the UV pretreatment is expected to play a critical role in enhancing the photocatalytic properties of the N,W co-doped TiO_2, since additional active sites are made available for the photodegradation of RhB. This increase in the specific surface area may be attributed to the removal of impurities, such as residual carbon species, from the surfaces of the co-doped TiO_2 nanoparticles, resulting in a higher degree of photocatalyst exposure.

As shown in Figure 5.4 and 5.5, the response of TNW to visible light was dramatically enhanced by the UV pretreatment. To examine whether the band gap energy was modified, the UV-vis diffuse reflectance spectra of the UV pretreated and unpretreated TNW were recorded. As shown in Figure 5.9A, an enhanced visible light absorbance with a red shift was facilitated by the UV pretreatment. Figure 5.9B presents the corresponding Tauc plots, revealing that the band gap energy of TNW was reduced from 2.85 to 2.65 eV as a consequence of the UV pretreatment. The UV pretreatment was carried out in a 50% methanol solution. Under intense UV irradiation, atomic hydrogen is produced, which may reduce Ti^{4+} to Ti^{3+} [46]. It has been shown that the formation of Ti^{3+} as an isolated state between the band gap results in broad visible light absorption [47].

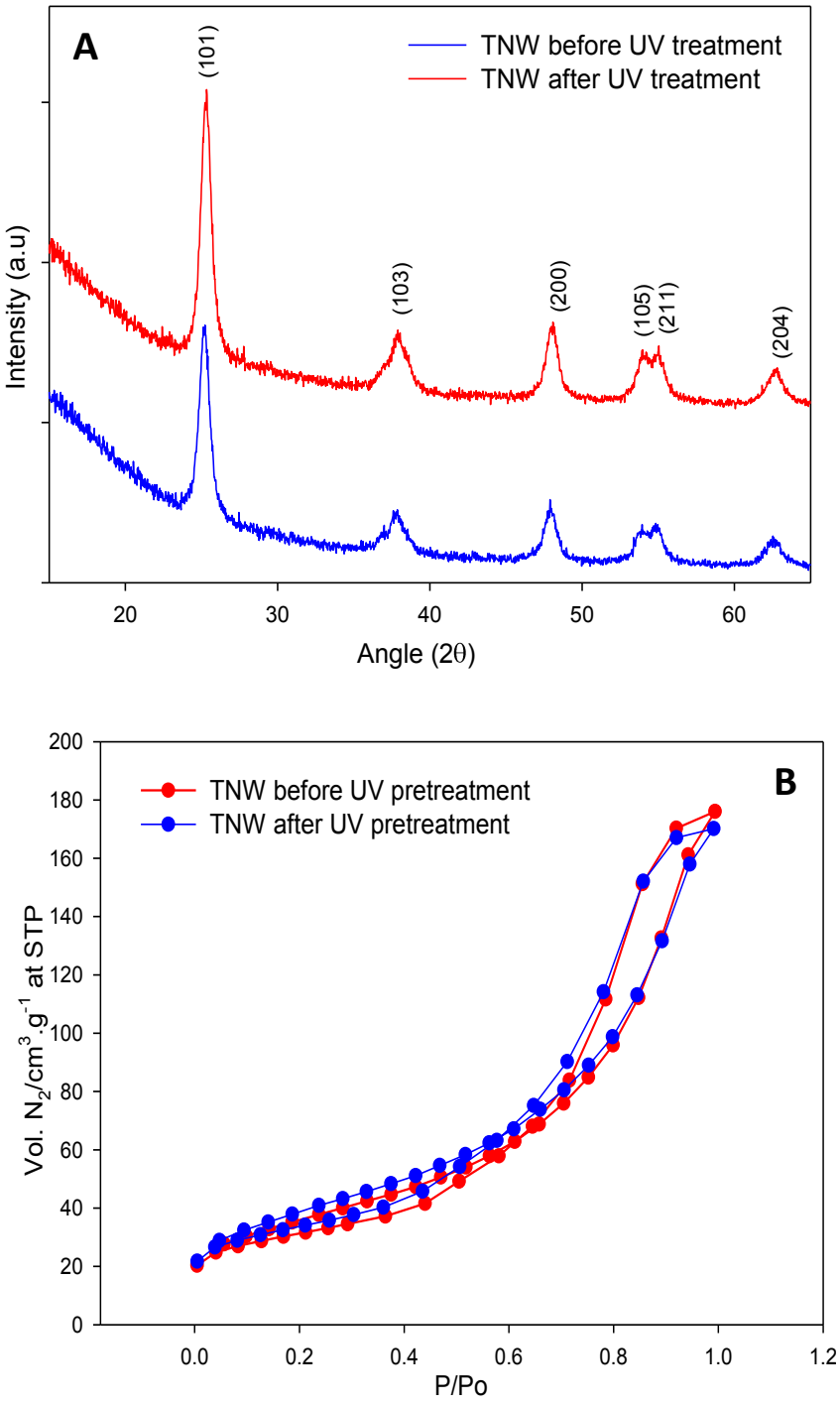

Figure 5.8. (A) XRD patterns and (B) Nitrogen adsorption-desorption isotherms of the unpretreated and UV pretreated TNW.

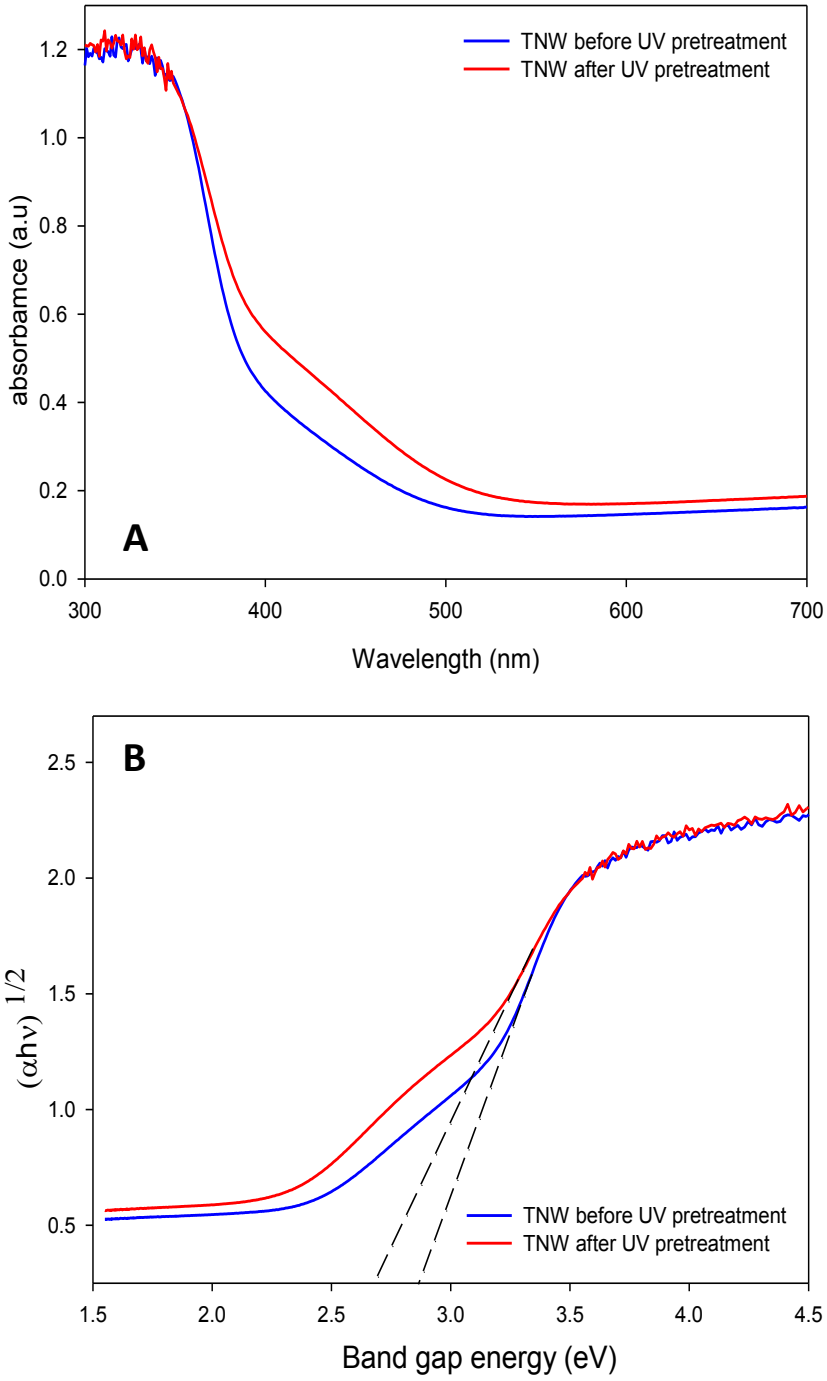

Figure 5.9. (A) UV-visible absorption spectra of the unpretreated and UV pretreated TiO_2 (B) Respective Tauc plots.

To further investigate the chemical composition and electronic state of the samples prior to and following the UV pretreatment, they were analyzed by X-ray photoelectron spectroscopy (XPS). Figure 5.10A displays the survey scan of the sample after the UV pretreatment. In addition to the characteristic peaks of Ti, O, N and W, a carbon peak originating from the combustion process was observed. The intensity of the N and W peaks was weak because of their low atomic %. A high-resolution spectrum of the N 1s peak was recorded as presented in Figure 5.10B, showing a broad peak ranging between 395 to 403 eV. The broad peak was fitted, resulting in the generation of two distinct peaks at 397.91 and 400.02 eV. According to the literature [48-51], three different peaks at ~397, ~399 and ~402 eV are typically obtained for N that is present in TiO_2. The peaks at 397 and 399 eV are due to the substitutional and interstitial doping of N, which creates an O-Ti-N and Ti-N-O type of bonding, respectively, and the peak at a greater value than 400 eV is due to the presence of the adsorption of N containing species on the surface of the TiO_2. No N 1s peak appeared at the range higher than 400 eV, revealing that all N was well incorporated within the crystalline structure of the mesoporous TNW samples synthesized in this study, and that no N containing impurity was present. For oxygen, a very strong O 1s peak coupled with a small shoulder was observed in Figure 5.10C, and when fitted, resulted in giving an intense peak centered at 530.07 eV, and a small peak at 531.78 eV. The ratio of the intensities of these was ca. 90:10. The strong peak at 530.07 eV is characteristic of the Ti oxide peak and the peak at 531.78 eV is likely due to the presence of O containing species, such as hydroxyl groups or water molecules that are adsorbed on the surface of sample [52]. As presented in Figure 5.10D, Ti present as Ti(IV) was confirmed by XPS analysis as it gave two peaks for $2p_{3/2}$ and Ti $2p_{1/2}$ centered at 458.74 and 464.46 eV, respectively. The value for $2p_{3/2}$ was decreased slightly from the value noted in the literature, which is 459.05 eV. The reason for

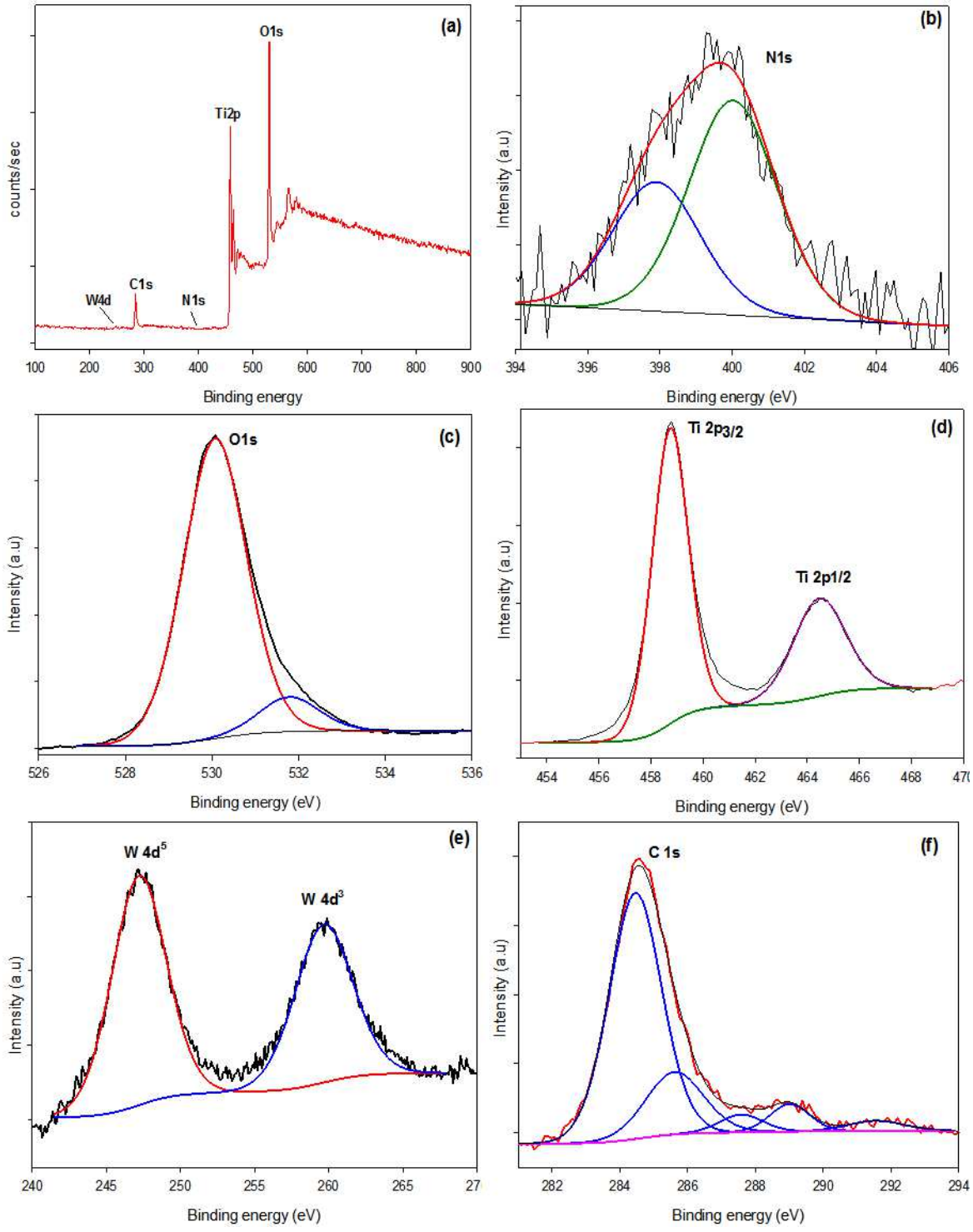

Figure 5.10. XPS spectra of (a) survey scan, (b) N 1s, (c) O 1s, (d) Ti 2p and (e) W 4d (f) C 1s - for TNW after the UV pretreatment

this decrease is because N is less electronegative than O, resulting in new electronic interactions between Ti and its surroundings, and hence increasing the electron density on the Ti as a consequence of N doping [53]. The XPS results of TiO_2 nanotubes shows that after the 30 min UV treatment, there is an increase in the amount of the Ti^{3+} present in the sample and it increases further when the sample is treated for 1 hour. In untreated sample the 3.11 % of the titanium is present as Ti^{3+} and for one hour treatred sample 5.91 % titanium is present in Ti^{3+} oxidation state. This gives an insight to the increase in the enhancement of the activity. For tungsten, two peaks centered at 247.12 and 259.57 eV were observed, which demonstrated that W is present as W(VI) [54]. It is interesting to note that no difference in the peak positions and the intensity of the peaks for the N, Ti, and W were observed in the XPS analysis following the UV pretreatment.

In the XPS analysis, the only other significant difference following the UV treatment was observed in the amount of O and C present. The C1s and O1s XPS prior to the UV treatment are presented as Figure 5.10E and F. The XPS result for carbon shows one strong and two weak peaks between 282 - 293 eV. The XPS curve was fitted to give several peaks, indicating that different states of C were present as impurities. According to the literature [55], the doped C is present at 281 eV, which was not found in the TNW sample. The peaks at 289, 286 and 284.46 correspond to C=O, C-O and C-C bonds, showing that all of the carbon present was in a "free state" in the form of an adsorbed impurity. After the one-hour UV pretreatment, the amount of C decreased by approximately 2%, whereas that of O increased by ~2%. Since carbon is a good conductor, carbon species might be acting as recombination sites that trap electrons and hence, tend to reduce its photocatalytic activity. The removal of carbon impurities by the UV pretreatment would decrease the recombination rate of the photogenerated electron-hole pairs

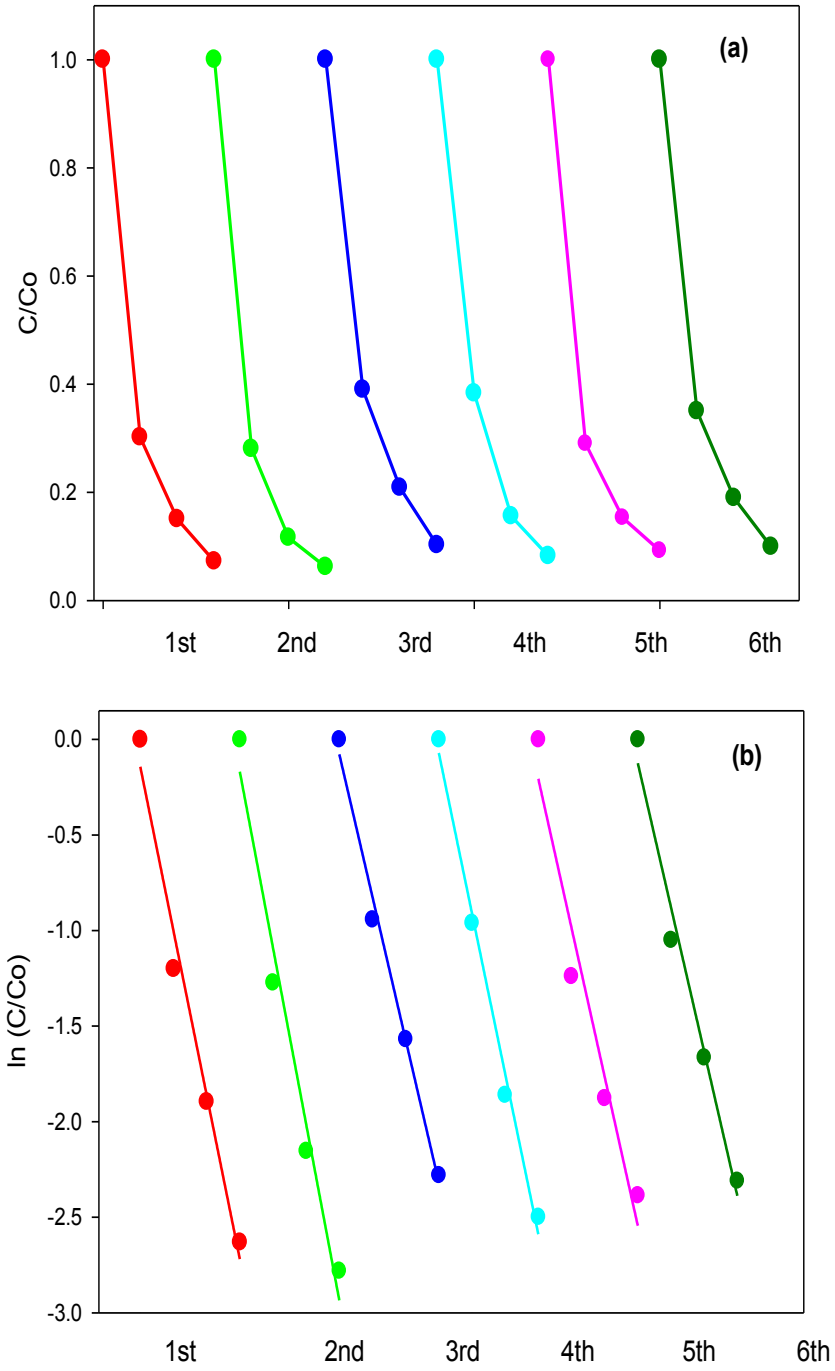

Figure 5.11. Photocatalytic stability tests of the UV pretreated TNW under visible light.

during the photodegradation of RhB, leading to an enhancement in activity. The other possible reasons for the enhancement of photocatalytic activity might be the creation of surface oxygen vacancies, which favors dissociative water adsorption resulting in the formation of hydroxyl groups [56]. It has also been reported that UV treatment increases the wettability of the TiO_2 [57], which would facilitate the water adsorption and OH radical formation.

To investigate the photocatalytic stability of the UV pretreated TNW, six cycles of the photodegradation of RhB were conducted under visible light. The readings were taken at specific predetermined time intervals. The RhB concentration changes for each run are displayed in Figure 5.11A; and they were fitted using first-order kinetics, as shown in Figure 5.11B. The calculated rate constants and relative coefficients are listed in Table 5.3, showing that the photocatalytic activity of the UV pretreated TNW remains virtually constant even after six cycles, which affirms that the UV pretreatment introduces a lastingly high photocatalytic activity in the sample.

Table 5.3. First order kinetics constants and the correlation coefficients for the stability tests.

Cycle	Rate constant(min^{-1})	R^2
1^{st} run	2.15×10^{-1}	0.982
2^{nd} run	2.31×10^{-1}	0.976
3^{rd} run	1.86×10^{-1}	0.992
4^{th} run	2.10×10^{-1}	0.992
5^{th} run	1.95×10^{-1}	0.955
6^{th} run	1.89×10^{-1}	0.982

We further tested the stability of both native TiO_2 nanotubes and the pretreated TiO_2 nanotubes in a 0.1M H_2SO_4 solution. The photocurrent transients were recorded at an applied electrode potential of 1.4 V vs. SCE by switching the UV light on and off. The duration of light

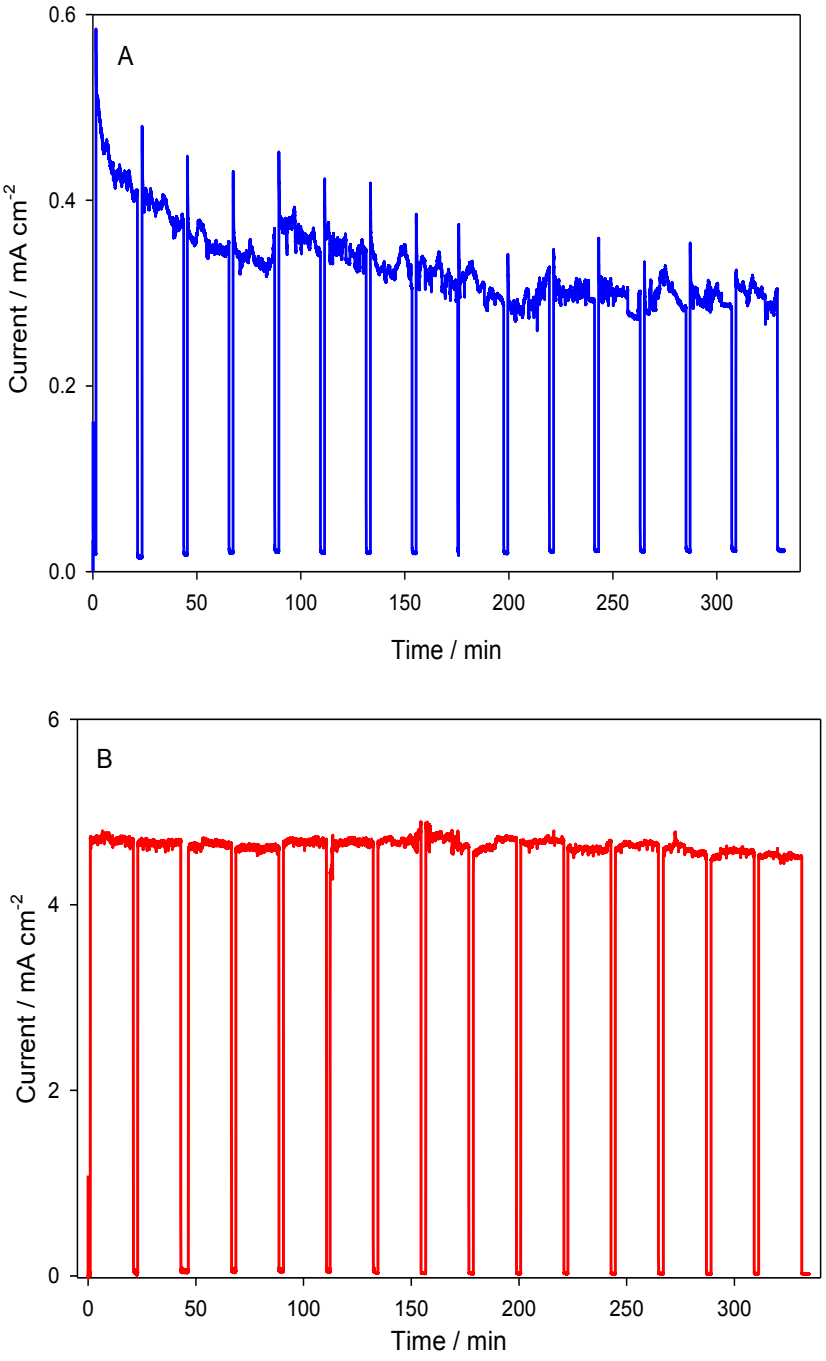

Figure 5.12. Stability test for TiO_2 nanotubes without (A) and with (B) treatment. Applied potential bias: 1.4 V.

pulses was set at 20 min, followed by dark current measurements for 2 min. As seen in Figure 5.14A, for the as-synthesized TiO_2 nanotubes, the photocurrent decreases with the increase of the testing time; and the relative standard error for the photocurrent is ca. 10%. In contrast, for the UV pretreated TiO_2 nanotubes, as shown in Figure 5.14B, there is almost no change in photocurrent; and the relative standard error for the photocurrent is ca. 1%, indicating the remarkable stability of the UV pretreated TiO_2 electrode.

5. 4. Conclusion

In summary, we have demonstrated a facile and effective UV pretreatment method toward the significant enhancement of the photocatalytic activity of TiO_2 nanotubes and mesoporous N,W co-doped TiO_2 under both UV and visible light. The time effect for the UV pretreatment was studied and it was observed that the best results were obtained when the TNW samples were treated for one hour under intense UV light exposure. The as-synthesized TNW exhibited a slightly higher UV photocatalytic activity than P25; the photodegradation of RhB on the UV pretreated TNW was greatly enhanced, over 2.6 times higher than that on the P25. For the visible light activity, the UV pretreatment resulted in an extraordinary >12 fold improvement in photocatalytic activity as compared to unpretreated TNW. Compared with TiO_2 nanotubes without the UV pretreatment, the TiO_2 nanotubes pretreated in a methanol solution under UV light irradiation exhibited substantial enhancements in both photocurrent and activity. The pretreatment also initiates an increase in the donor density of the TiO_2 nanotubes by almost 3 orders of magnitude. This significant enhancement of the photoelectrochemical performance may be attributed to the inhibition of charge recombination of photoinduced electrons and holes, creation of oxygen vacancies [58,59], improvement in conductivity [60], and the promotion of interfacial charge-transfer kinetics at TiO_2 nanotubes. The facile and effective approach proposed

in this study opens many opportunities to develop highly active TiO_2 photocatalysts for the pressing energy and environmental applications, ranging from water splitting, solar energy, and air purification to wastewater treatment. This significant augmentation in photocatalytic activity subsequent to the UV pretreatment may be attributed to the following synergetic factors: (i) the increase of the specific surface area; (ii) the reduction of the band gap energy due to the formation of Ti^{3+} and (iii) the partial removal of carbon impurities. Aside from the significant enhancement in both UV and visible photocatalytic activity, the UV pretreated mesoporous N,W co-doped TiO_2 exhibited high photocatalytic stability, which is very promising for energy and environmental applications.

References

[1] G. Riegel, J. R. Bolton. Photocatalytic efficiency variability in TiO_2 particles, *The Journal of Physical Chemistry* 99 (**1995**) 4215-4224.

[2] C. D. Jaeger, A. J. Bard. Spin trapping and electron spin resonance detection of radical intermediates in the photodecomposition of water at titanium dioxide particulate systems, *The Journal of Physical Chemistry* 83 (**1979**) 3146-3152.

[3] A. M. Ali, E. A. C. Emanuelsson, D. A. Patterson. Photocatalysis with nanostructured zinc oxide thin films: The relationship between morphology and photocatalytic activity under oxygen limited and oxygen rich conditions and evidence for a Mars Van Krevelen mechanism, *Applied Catalysis B: Environmental* 97 (**2010**) 168-181.

[4] M. Tian, G. Wu, B. Adams, J. Wen, A. Chen. Kinetics of Photoelectrocatalytic Degradation of Nitrophenols on Nanostructured TiO_2 Electrodes, *The Journal of Physical Chemistry C* 112 (**2007**) 825-831.

[5] M. Qamar, M. Muneer. A comparative photocatalytic activity of titanium dioxide and zinc oxide by investigating the degradation of vanillin, *Desalination* 249 (**2009**) 535-540.

[6] A. Fujishima, K. Honda. Electrochemical photolysis of water at a semiconductor electrode, *Nature* 238 (**1972**) 37 - 38.

[7] M. Tian, J. Wen, D. MacDonald, R.M. Asmussen, A. Chen. A novel approach for lignin modification and degradation, *Electrochemistry Communications* 12 (**2010**) 527-530.

[8] S. Bauer, A. Pittrof, H. Tsuchiya, P. Schmuki. Size-effects in TiO_2 nanotubes: Diameter dependent anatase/rutile stabilization, *Electrochemistry Communications* 13 (**2011**) 538-541.

[9] M. Tian, M. Malig, S. Chen, A. Chen. Synthesis and electrochemical study of TiO_2-supported PdAu nanoparticles, *Electrochemistry Communications* 13 (**2011**) 370-373.

[10] B. O'Reegan, M. Gratzel. A low-cost, high-efficiency solar cell based on dye-sensitized colloidal TiO_2 films, *Nature* 353 (**1991**) 737 - 740.

[11] A. Hagfeldt, M. Grätzel. Molecular Photovoltaics, *Accounts of Chemical Research* 33 (**2000**) 269-277.

[12] F. Amano, T. Yasumoto, O.-O. Prieto-Mahaney, S. Uchida, T. Shibayama, B. Ohtani. Photocatalytic activity of octahedral single-crystalline mesoparticles of anatase titanium(iv) oxide, *Chemical Communications* (**2009**) 2311-2313.

[13] J. Zhu, J. Yang, Z.-F. Bian, J. Ren, Y.-M. Liu, Y. Cao, H.-X. Li, H.-Y. He, K.-N. Fan. Nanocrystalline anatase TiO_2 photocatalysts prepared via a facile low temperature nonhydrolytic sol–gel reaction of $TiCl_4$ and benzyl alcohol, *Applied Catalysis B: Environmental* 76 (**2007**) 82-91.

[14] C-C Wang, C. C Kei, T. P. Perng. Fabrication of TiO_2 nanotubes by atomic layer deposition and their photocatalytic and photoelectrochemical applications, *Nanotechnology* 22 (**2011**) 365702.

[15] D. Wang, H. Zhao, N. Wu, M. A. E. Khakani, D. Ma. Tuning the charge-transfer property of PbS-quantum dot/TiO_2-nanobelt nanohybrids via quantum confinement, *The Journal of Physical Chemistry Letters* 1 (**2010**) 1030-1035.

[16] J. H. Im, S. J. Yang, C. H. Yun, C. R. Park. Simple fabrication of carbon/TiO_2 composite nanotubes showing dual functions with adsorption and photocatalytic decomposition of Rhodamine B, *Nanotechnology* 23 (**2012**) 035604.

[17] H. Li, S. G. Sunoi, A. K. Sunoi. Development of titanium-dioxide-based aerogel catalyst with tunable nanoporosity and photocatalytic activity, *Nanotechnology* 23 (**2012**) 294012.

[18] X. Chen, S. S. Mao. Titanium Dioxide Nanomaterials: Synthesis, Properties, Modifications, and Applications, *Chemical Reviews* 107 (**2007**) 2891-2959.

[19] G. Wu, S. Nigro, J. Wen, A. Chen. One-step synthesis of N- and F-codoped mesoporous TiO_2 photocatalysts with high visible light activity, *Nanotechnology* 21 (**2010**) 085701.

[20] M. Tian, S.S. Thind, S. Chen, N. Matyasovzsky, A. Chen. Significant enhancement of the photoelectrochemical activity of TiO_2 nanotubes, *Electrochemistry Communications* 13 (**2011**) 1186-1189.

[21] F. Amano, O.-O. Prieto-Mahaney, Y. Terada, T. Yasumoto, T. Shibayama, B. Ohtani. Decahedral single-crystalline particles of anatase titanium(IV) oxide with high photocatalytic activity, *Chemistry of Materials* 21 (**2009**) 2601-2603.

[22] T. Sreethawong, S. Laehsalee, S. Chavadej. Use of Pt/N-doped mesoporous-assembled nanocrystalline TiO_2 for photocatalytic H_2 production under visible light irradiation, *Catalysis Communications* 10 (**2009**) 538-543.

[23] R. Asahi, T. Morikawa, T. Ohwaki, K. Aoki, Y. Taga. Visible-light photocatalysis in nitrogen-doped titanium oxides, *Science* 293 (**2001**) 269-271.

[24] H. Kim, W. Choi. Effects of surface fluorination of TiO_2 on photocatalytic oxidation of gaseous acetaldehyde, *Applied Catalysis B: Environmental* 69 (**2007**) 127-132.

[25] G. Wu, J. Wang, D.F. Thomas, A. Chen. Synthesis of F-doped flower-like TiO_2 nanostructures with high photoelectrochemical activity, *Langmuir* 24 (**2008**) 3503-3509.

[26] H. Irie, Y. Watanabe, K. Hashimoto. Nitrogen-concentration dependence on photocatalytic activity of $TiO_{2-x}N_x$ powders, *The Journal of Physical Chemistry B* 107 (**2003**) 5483-5486.

[27] T. Ihara, M. Miyoshi, Y. Iriyama, O. Matsumoto, S. Sugihara. Visible-light-active titanium oxide photocatalyst realized by an oxygen-deficient structure and by nitrogen doping, *Applied Catalysis B: Environmental* 42 (**2003**) 403-409.

[28] C. Di Valentin, G. Pacchioni, A. Selloni, S. Livraghi, E. Giamello. Characterization of paramagnetic species in N-doped TiO_2 powders by EPR spectroscopy and DFT calculations, *The Journal of Physical Chemistry B* 109 (**2005**) 11414-11419.

[29] S. Livraghi, M.C. Paganini, E. Giamello, A. Selloni, C. Di Valentin, G. Pacchioni. Origin of photoactivity of nitrogen-doped titanium dioxide under visible light, *Journal of the American Chemical Society* 128 (**2006**) 15666-15671.

[30] G. Wu, J. Wen, J. Wang, D.F. Thomas, A. Chen. A facile approach to synthesize N and B co-doped TiO_2 nanomaterials with superior visible-light response, *Materials Letters* 64 (**2010**) 1728-1731.

[31] T. Lindgren, J.M. Mwabora, E. Avendaño, J. Jonsson, A. Hoel, C.-G. Granqvist, S.-E. Lindquist. Photoelectrochemical and optical properties of nitrogen doped titanium dioxide films prepared by reactive DC magnetron sputtering, *The Journal of Physical Chemistry B* 107 (**2003**) 5709-5716.

[32] M. Miyauchi, A. Nakajima, K. Hashimoto, T. Watanabe. A highly hydrophilic thin film under 1 $\mu W/cm^2$ UV illumination, *Advanced Materials* 12 (**2000**) 1923-1927.

[33] J. Li, J. Xu, W.-L. Dai, H. Li, K. Fan. One-pot synthesis of twist-like helix tungsten–nitrogen-codoped titania photocatalysts with highly improved visible light activity in the abatement of phenol, *Applied Catalysis B: Environmental* 82 (**2008**) 233-243.

[34] H. Imai, Y. Takei, K. Shimizu, M. Matsuda, H. Hirashima. Direct preparation of anatase TiO_2 nanotubes in porous alumina membranes, *Journal of Materials Chemistry* 9 (**1999**) 2971-2972.

[35] J. H. Jung, H. Kobayashi, K. J. C. van Bommel, S. Shinkai, T. Shimizu. Creation of Novel Helical Ribbon and Double-Layered Nanotube TiO_2 Structures Using an Organogel Template, *Chemistry of Materials* 14 (**2002**) 1445-1447.

[36] Z.R. Tian, J.A. Voigt, J. Liu, B. McKenzie, H. Xu. Large Oriented Arrays and Continuous Films of TiO_2-Based Nanotubes, *Journal of the American Chemical Society* 125 (**2003**) 12384-12385.

[37] X. Peng, A. Chen. Aligned TiO_2 nanorod arrays synthesized by oxidizing titanium with acetone, *Journal of Materials Chemistry* 14 (**2004**) 2542-2548.

[38] Y. Ji, K.-C. Lin, H. Zheng, J. Zhu, A.C.S. Samia. Fabrication of double-walled TiO_2 nanotubes with bamboo morphology via one-step alternating voltage anodization, *Electrochemistry Communications* 13 (**2011**) 1013-1015.

[39] A. Mazare, I. Paramasivam, K. Lee, P. Schmuki. Improved water-splitting behaviour of flame annealed TiO_2 nanotubes, *Electrochemistry Communications* 13 (**2011**) 1030-1034.

[40] Z. Liu, X. Zhang, S. Nishimoto, M. Jin, D.A. Tryk, T. Murakami, A. Fujishima. Highly ordered TiO_2 nanotube arrays with controllable length for photoelectrocatalytic degradation of phenol, *The Journal of Physical Chemistry C* 112 (**2007**) 253-259.

[41] Y. Liu, J. Li, B. Zhou, J. Bai, Q. Zheng, J. Zhang, W. Cai. Comparison of photoelectrochemical properties of TiO_2-nanotube-array photoanode prepared by anodization in different electrolyte, *Environmental Chemistry Letters* 7 (**2009**) 363-368.

[42] O. K. Varghese, M. Paulose, T. J. LaTempa, C. A. Grimes. High-Rate Solar Photocatalytic Conversion of CO_2 and Water Vapor to Hydrocarbon Fuels, *Nano Letters* 9 (**2009**) 731-737.

[43] S. Licht. Semiconductor electrodes and Photoelectrochemistry, *Encyclopedia of Electrochemistry* 6 (**2002**).

[44] S. Liu, A. Chen. Coadsorption of horseradish peroxidase with thionine on TiO_2 nanotubes for biosensing, *Langmuir* 21 (**2005**) 8409-8413.

[45] Z. Zhang, C.-C. Wang, R. Zakaria, J.Y. Ying. Role of particle size in nanocrystalline TiO_2-based photocatalysts, *The Journal of Physical Chemistry B* 102 (**1998**) 10871-10878.

[46] X. Chen, L. Liu, P.Y. Yu, S.S. Mao. Increasing solar absorption for photocatalysis with black hydrogenated titanium dioxide nanocrystals, *Science* 331 (**2011**) 746-750.

[47] M. Liu, X. Qiu, M. Miyauchi, K. Hashimoto. Cu(II) Oxide amorphous nanoclusters grafted Ti^{3+} self-doped TiO_2: An efficient visible light photocatalyst, *Chemistry of Materials* 23 (**2011**) 5282-5286.

[48] C. Feng, Y. Wang, Z. Jin, J. Zhang, S. Zhang, Z. Wu, Z. Zhang. Photoactive centers responsible for visible-light photoactivity of N-doped TiO_2, *New Journal of Chemistry* 32 (**2008**) 1038-1047.

[49] J. L. Gole, J.D. Stout, C. Burda, Y. Lou, X. Chen. Highly efficient formation of visible light tunable $TiO_{2-x}N_x$ photocatalysts and their transformation at the nanoscale, *The Journal of Physical Chemistry B* 108 (**2003**) 1230-1240.

[50] S. Sato, R. Nakamura, S. Abe. Visible-light sensitization of TiO_2 photocatalysts by wet-method N doping, *Applied Catalysis A: General* 284 (**2005**) 131-137.

[51] X. Yang, C. Cao, L. Erickson, K. Hohn, R. Maghirang, K. Klabunde. Photo-catalytic degradation of Rhodamine B on C-, S-, N-, and Fe-doped TiO_2 under visible-light irradiation, *Applied Catalysis B: Environmental* 91 (**2009**) 657-662.

[52] J. A. Rengifo-Herrera, E. Mielczarski, J. Mielczarski, N.C. Castillo, J. Kiwi, C. Pulgarin. Escherichia coli inactivation by N, S co-doped commercial TiO_2 powders under UV and visible light, *Applied Catalysis B: Environmental* 84 (**2008**) 448-456.

[53] Y. Ma, J. Zhang, B. Tian, F. Chen, L. Wang. Synthesis and characterization of thermally stable Sm,N co-doped TiO_2 with highly visible light activity, *Journal of Hazardous Materials* 182 (**2010**) 386-393.

[54] A. Kubacka, G. Colón, M. Fernández-García. Cationic (V, Mo, Nb, W) doping of TiO_2–anatase: A real alternative for visible light-driven photocatalysts, *Catalysis Today* 143 (**2009**) 286-292.

[55] W. C. Peisheng Liu, M. Fang, Z. Li, H. Zeng, J. Hu, X. Luo, W. Jing. Room temperature synthesized rutile TiO_2 nanoparticles induced by laser ablation in liquid and their photocatalytic activity, *Nanotechnology* 20 (**2009**) 285707.

[56] J.-M. Wu, B. Huang. Enhanced Ability of Nanostructured Titania Film to Assist Photodegradation of Rhodamine B in Water Through Natural Aging, *Journal of the American Ceramic Society* 90 (**2007**) 283-286.

[57] K. H. R. Wang, A. Fujishima, M. Chikuni, E. Kojima, A. Kitamura, M. Shimohigoshi, T. Watanabe. Light-induced amphiphilic surfaces, *Nature* 388 (**1997**) 431-432.

[58] A. Janotti, J. B. Varley, P. Rinke, N. Umezawa, G. Kresse, C. G. Van de Walle. Hybrid functional studies of the oxygen vacancy in TiO_2, *Physical Review B* 81 (**2010**) 085212.

[59] R. Schaub, E. Wahlström, A. Rønnau, E. Lægsgaard, I. Stensgaard, F. Besenbacher. Oxygen-mediated diffusion of oxygen vacancies on the TiO_2(110) surface, *Science* 299 (**2003**) 377-379.

[60] I. Cesar, K. Sivula, A. Kay, R. Zboril, M. Grätzel. Influence of feature size, film thickness, and silicon doping on the performance of nanostructured hematite photoanodes for solar water splitting, *The Journal of Physical Chemistry C* 113 (**2008**) 772-782.

Chapter 6: Direct Growth and Photo-Electrochemical Study of WO_3 Nanostructured Materials*

6.1. Introduction

A wide array of metal oxides have undergone investigation to elucidate their catalytic properties, which include, but are not limited to TiO_2, ZnO, SnO_2, Bi_2WO_6, $BiVO_4$, Bi_2MoO_6, and $CaIn_2O_4$ [1-5]. Tungsten oxide (WO_3) is a semiconductor oxide material with a band-gap of 2.6–3.0 eV and it is becoming the focus of research attention due to its unique electronic properties [6-10]. WO_3 has many applications, which encompass photochromism, electrochromism, thermochromic gas sensors, batteries, photoelectric sensors, water splitting and other photocatalytic behavior [11-19]. WO_3 nanostructured materials are expected to play significant roles toward future technological advances. Many different shapes of nanostructured WO_3, like nanowires, nanorods and nanobelts have been prepared by various methods, including sputtering [20], pulsed laser deposition [21], electrosynthesis [22], sol–gel [23] and hydrothermal methods [24].

In the present study, WO_3 platelets were fabricated using a facile hydrothermal method. The effect of treatment time during synthesis on the morphology and dimensions of the formed platelets was investigated and it was found that as the treatment duration was increased, the photo-activity of the sample decreased drastically. Nanospherical WO_3 was obtained by removing the top platelets via a facile electrochemical cathodic treatment. To the best of our knowledge, the electrochemical treatment method was employed for the first time, to investigate the mechanism of WO_3 crystal growth under the hydrothermal condition. The observed WO_3

* Most of the results presented in this chapter have been published in *Electrochemistry communications*, **2014,** 43, 13-17

nanospheres are well distributed on the substrate with an average particle size of ~50 nm. These secondary nanospherical WO_3 particles demonstrated a much more robust photocurrent than their parent platelets. The photocatalytic activities of these samples were also evaluated via 4-NP oxidation, which showed that these nanospherical particles had a 7-fold enhancement.

6.2. Experimental

To prepare the WO_3 nanomaterials, a facile hydrothermal method was employed, where a commercially available tungsten plate (Sigma-Aldrich, 99.7 %) was cut to obtain a $1cm^2$ area, which was utilized as a substrate. The tungsten plates were then sonicated several times in acetone to remove all the organic impurities present on the surface followed by sonication in water. To grow the tungsten oxide on the substrate, the substrate was put in the Teflon lined autoclave with 80% of its volume filled with 1.5 M HNO_3. To observe the effect of temperature on the crystal growth of the WO_3 on the substrate, various temperatures and time increments were employed for the hydrothermal treatment. Following hydrothermal treatment, the electrodes were rinsed with ultrapure water several times, heated at 450 °C for 3 h and then used for the electrochemical tests.

6.3. Characterization techniques

The synthesized materials were then characterized by X-ray diffraction (Phillips PW 1050-3710 Diffractometer with Cu Kα radiation (λ=1.5406 Å) and scanning electron microscopy (Hitachi SU 70). For electrochemical characterization, a three-electrode cell system was employed, where a Pt coil with a 10 cm^2 surface area was used as the auxiliary electrode, whereas an Ag/AgCl electrode was used as the reference electrode. All of the electrochemical studies were performed with a Voltalab 40 Potentiostat (PGZ301). The photocatalytic activity of

the as synthesized WO_3 was evaluated by measuring the photodegradation of 0.1 mM 4-NP under UV-Visible light. An Oriel system containing 300W xenon arc lamp was utilized in this study as the light source. The UV-Vis absorbance spectra were recorded using a UV-visible spectrophotometer (Varian, Cary 5E).

6.4. Results and Discussion

It is known that the photocatalytic activity of a material depends, to a significant degree, on its morphology and the dimensions of its constituent elements. To investigate the influence of the treatment duration, the Teflon autoclaves that contained W plates in 1.5 M HNO_3 were subjected to treatment over different time intervals at 180 °C. Figure 6.1 A, B, C and D depict low resolution images, whereas the insets show the associated high resolution images of the samples treated for 30 min, 1h, 2h and 3h respectively. These images reveal that platelet-like structures were obtained. It can be seen that the treatment duration has significant effect on the morphology of the synthesized samples. As we lengthened the duration of the heat treatment, the dimensions of the platelets increased and wide and thick platelets were formed when samples were prepared for 3 h. The thickness of the WO_3 platelets were calculated to be ca. 60 nm, 75 nm, 100-120 nm and 200-300 nm for the 30 min, 1h, 2h and 3h time treated electrodes respectively. It can be concluded that the longer the reaction vessel goes heat treatment the thicker the obtained WO_3 is. Another interesting point to note is that the in the beginning of the platelet growth the process is slow and there is not much difference in the thickness of the WO_3 platelets grown for 30 min and 1 hour. If the reaction vessel is treated in heat for more than 1h, the platelet growth is rapid and bulky platelets are obtained.

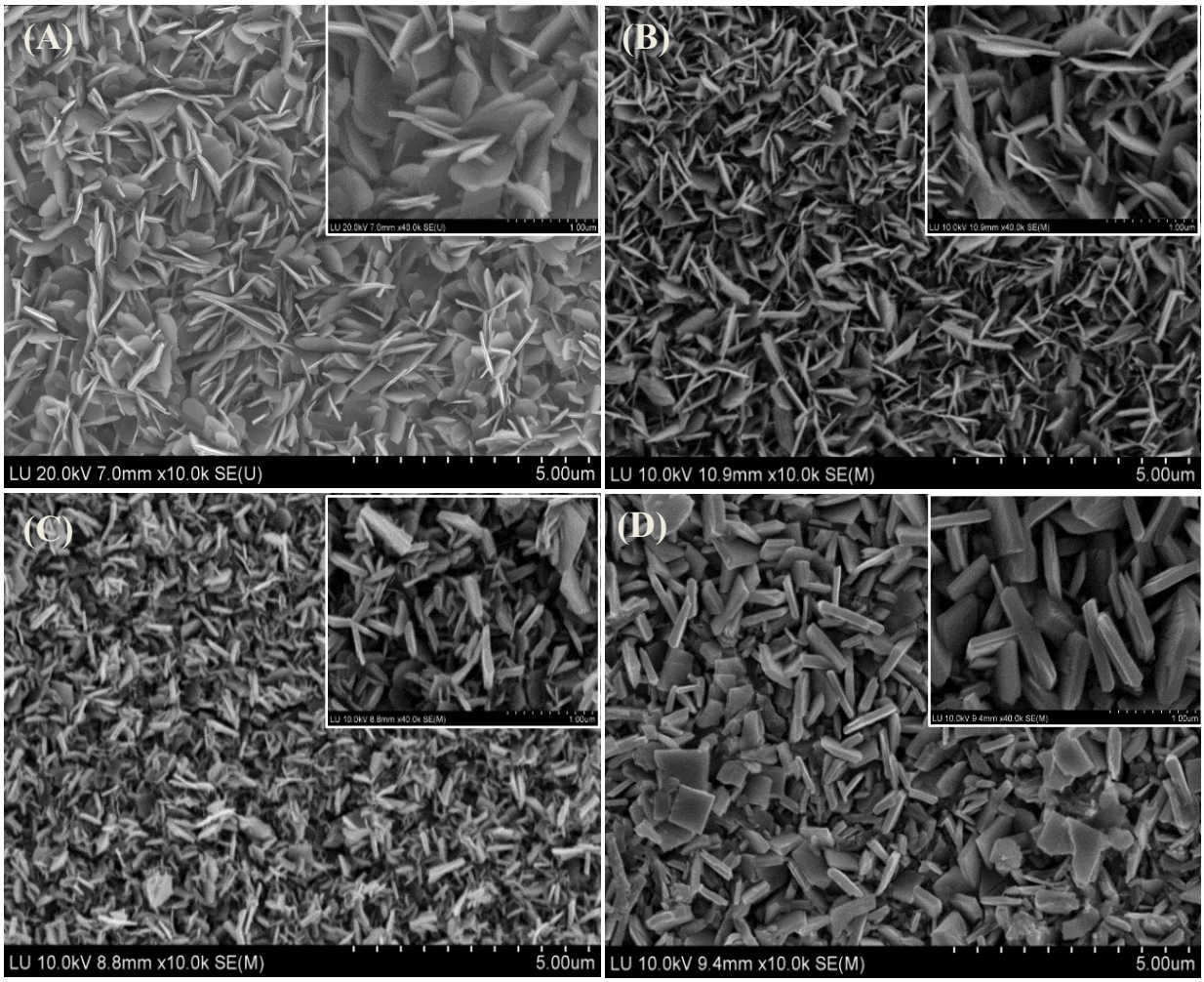

Figure 6.1. SEM images of (A) WO_3-30 min (B) WO_3-1h (C) WO_3-2h (D) WO_3-3h. Insets are the high resolution SEM images of the respective sample.

To discover the crystalline phase, all of the samples were analyzed by XRD, which are shown in Figure 6.2. In general, all of the samples exhibited two characteristic peaks of WO_3 at 23.5^o and 33.7^o. According to the database (ICDD), the peak at 23.5^o corresponds to the [002], [020] and [200] planes and the weak peak at 33.7^o corresponds to the [021] and [201] plane. All the other peaks associated with WO_3 are very weak in nature. The strong peaks at 40.26^o, 58.28^o, 73.20^o and 87.02^o are derived from the tungsten substrate. The noticeable decrease of the peak centered at 58.28^o indicates the increase of the thickness of the WO_3 layer on the W substrate.

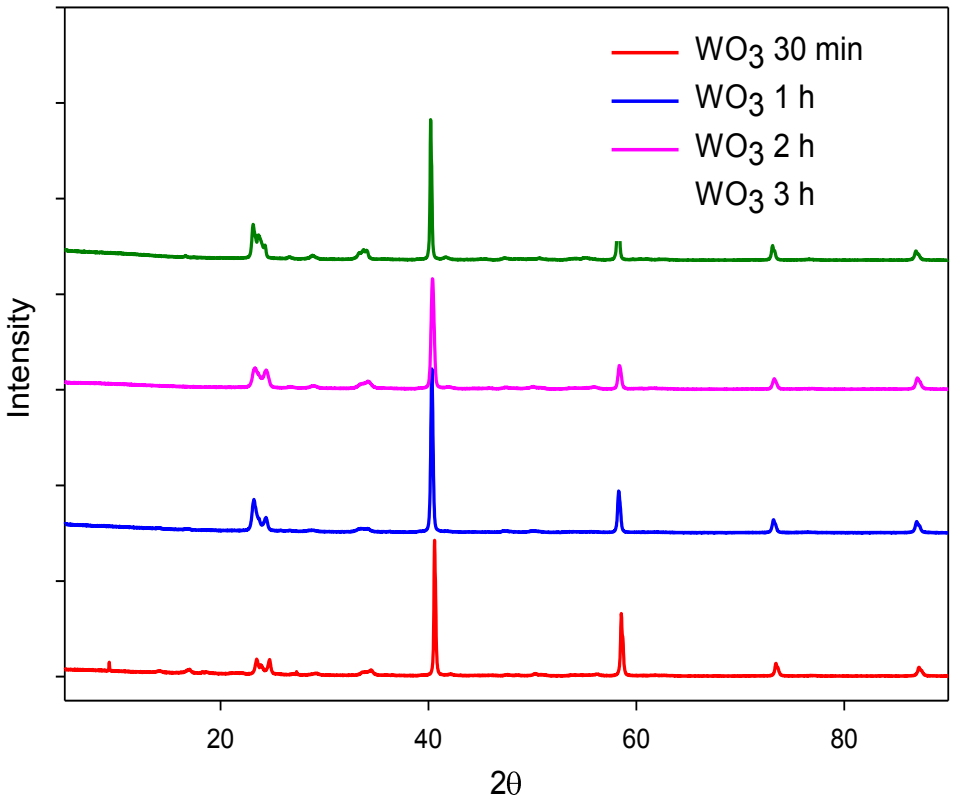

Figure 6.2. XRD pattern of prepared WO_3samples.

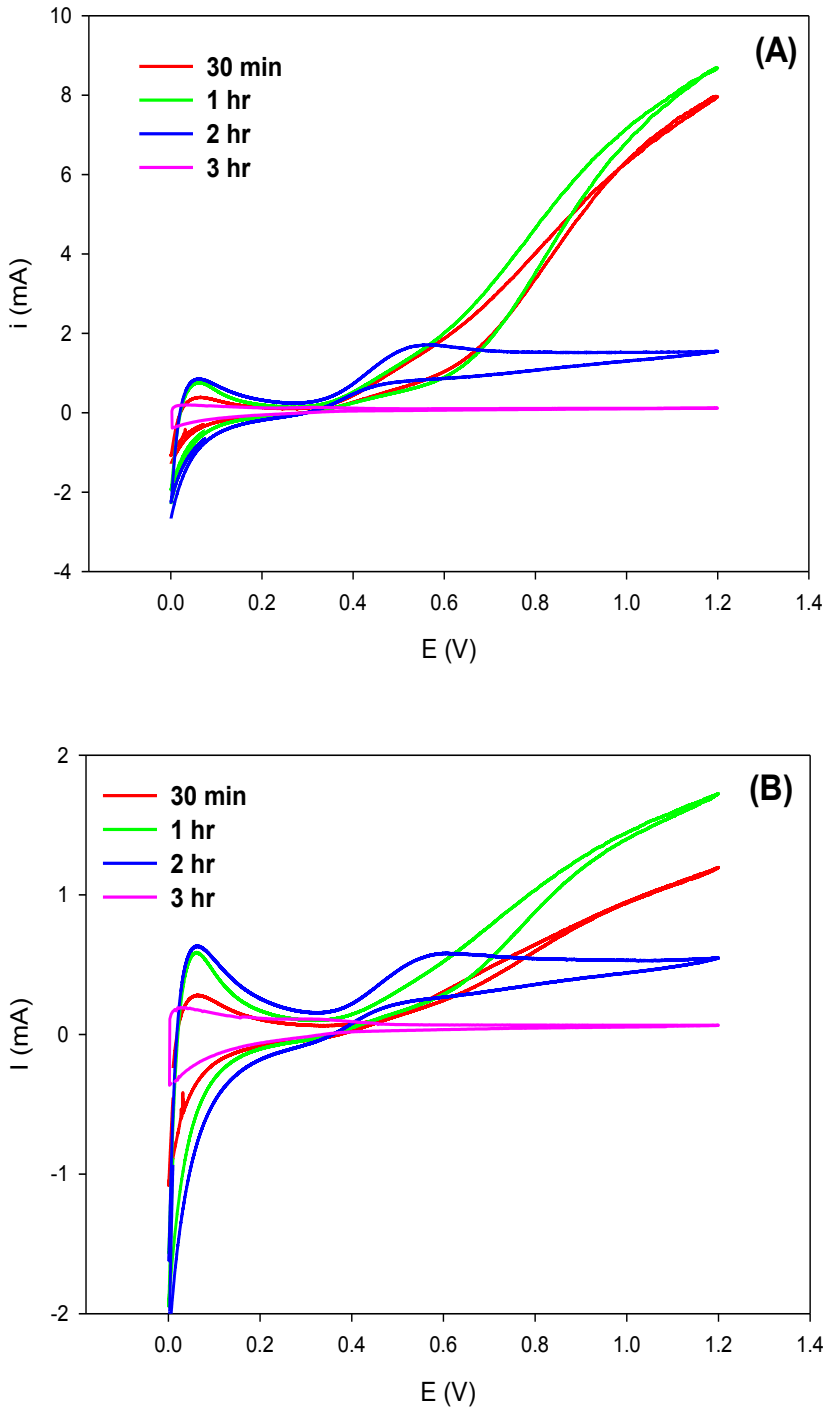

Figure 6.3. Cyclic voltammograms of samples under (A) UV irradiation and (B) visible light in 0.5 M H_2SO_4 at 20 mV/s.

Figure 6.3A represents cyclic voltammograms of the synthesized electrodes, showing that the electrode prepared over one-hour treatment exhibited the highest photocurrent under the UV- Visible light, followed by the electrode prepared over 30-minute treatment. The values of the photocurrents observed under UV-Visible light at a potential of 1.2V for the electrodes were 7.4, 8.2, 1.4 and 0.112 mA/cm^2 treated for 30 min, 1h, 2h and 3h electrodes, respectively. As we observed, following even a brief (30 min) treatment period the synthesized electrode exhibited a very high photocurrent, which indicated that this hydrothermal method was very effective and the crystal growth began as soon as the Teflon autoclave was inserted into the furnace. As the duration of the heat treatment was further increased to two hours, the photocurrent decreased. For the electrode treated for three hours, the photocurrent decreased significantly to a very low value of 112 μA/cm^2. This considerable decrease in photoelectrochemical activity might be attributed to the significant increase of the thickness of WO_3 layer. After one-hour treatment, the dimensions of the formed WO_3 platelets increased rapidly, whereas for the three-hour heat-treated electrode, they attained a very thick and bulky platelet structure. The cyclic voltammograms shown in Figure 6.3B are the results when only visible light was shine on the electrode during the electrochemical experiment. These results are also consistent with the results obtained when UV-Vis light was used. The maximum current at 1.2 V was calculated to be 1.7 mA, 1.2 mA, 0.4 and only 0.15 mA/cm^2 treated for 30 min, 1h, 2h and 3h electrodes, respectively. Such a low visible light response is big hindrance in using these electrodes under the cheaper source of the energy and thus only UV light can be used to excite the electrodes.

To study the mechanism of WO_3 crystal growth under the hydrothermal condition, all the electrodes were electrochemically treated via the application of -10 mA/cm^2 current for 650 s

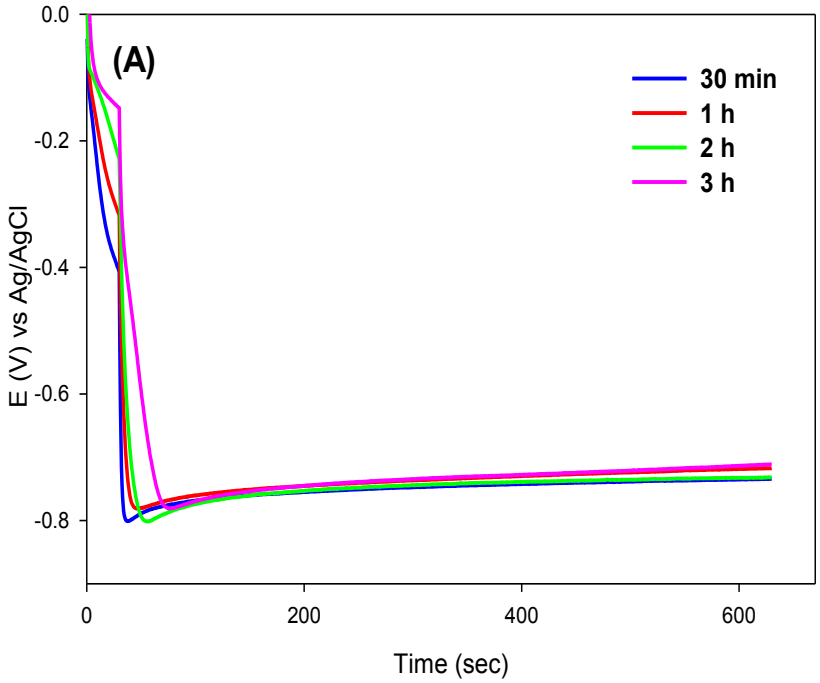

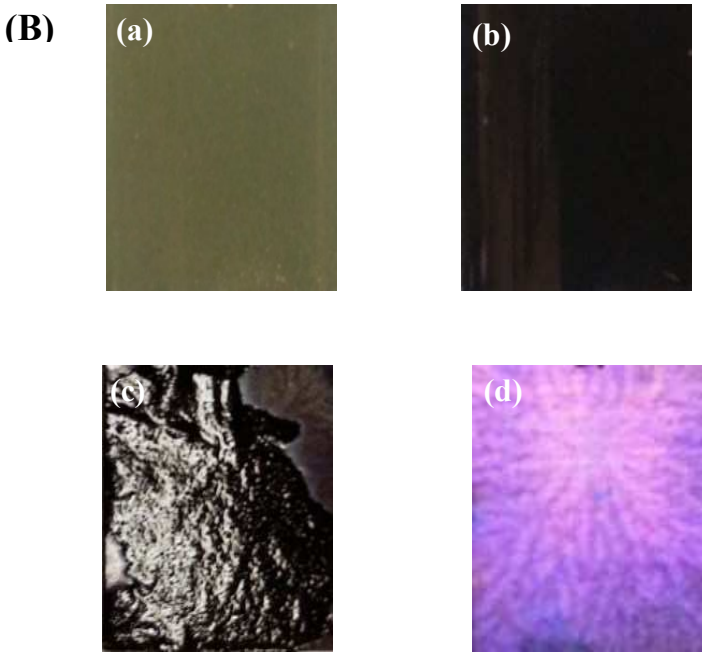

Figure 6.4. (A) Chronopotentiometry curves for the electrochemical reduction (-10 mA) of the various electrodes in 0.5 M H_2SO_4 over 10 min. (B) Images of the electrode depicting the alteration of the electrode during the electrochemical reduction treatment. The electrode was 1×1 cm.

and the chronopotentiometric results are shown in Figure 6.4A. Although the overall change trends of E vs. t plots were similar, the decrease of the electrode potential during the first 20 s was slower with the hydrothermal treatment time increased from 30 min to 3 h, which can be attributed to the increase of the WO_3 layer. Interestingly, as can be seen in Figure 6.4B, the electrochemical treatment had a significant effect on the color and morphology of the electrode. Shortly following the application of the current, the color of the electrodes was altered from yellowish green (picture a) to black (picture b) likely due to the hydrogenation of the WO_3 [25]. Vigorous gas evolution occurred at both the working and the counter electrodes, which weakened the attachment of the WO_3 platelets to the W plate and resulted in the formation of the WO_3 flakes (picture c). It is worth noting that the WO_3 electrodes that were prepared under two-hour and three-hour treatments, underwent this transformation easily due to their large plate dimensions, and were more susceptible to shed their external layer as compared to the electrodes, which were prepared over 30 min and 1 h. Subsequently, the formed WO_3 flakes were detached from the electrode surface, resulting in the color change to bluish-purple (picture d).

To investigate further, SEM and EDS were utilized to characterize the electrodes. The SEM image of the electrode following the electrochemical treatment is shown as Figure 6.5, revealing that beneath the WO_3 platelets, a layer of spherical WO_3 particles was present. This indicated that the WO_3 platelets were grown on these nanospheres, thus the mechanism of the crystal growth in the preparation of the WO_3 platelets may be explained. At the initial stage, a large population of crystal nuclei aggregate into clusters and when these crystals grow, the nanoparticles are generated. These nanoparticles then develop in variable planes and recrystallize to form platelet-like structures. The EDS results also show that these nanospheres are comprised of WO_3 with a perfect 1:3 ratio. The only difference in the EDS spectra of the WO_3 platelets and the nanospheres is that the later had

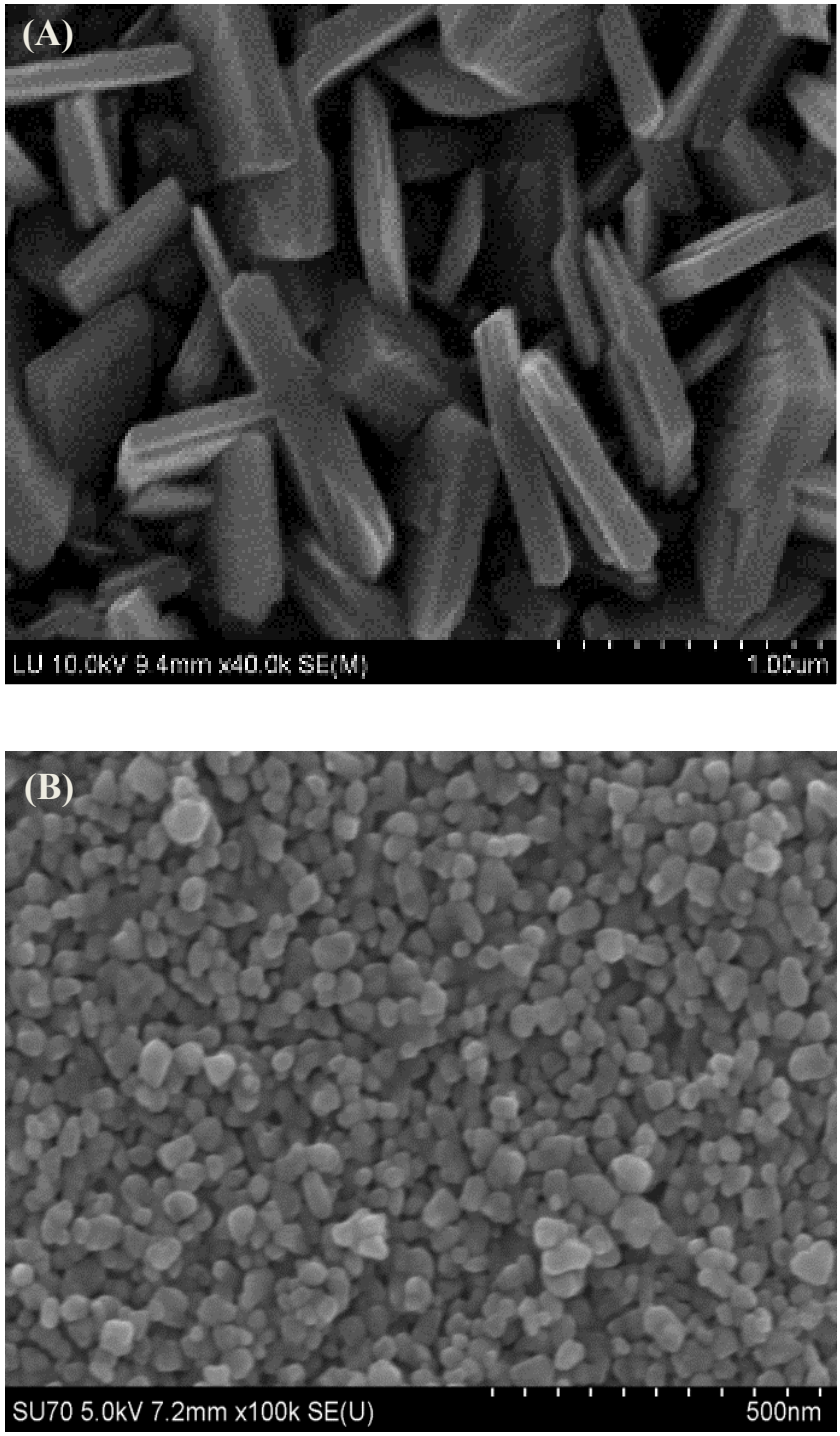

Figure 6.5. SEM images of the electrode showing the morphology before (A) and after (B) the electrochemical reduction

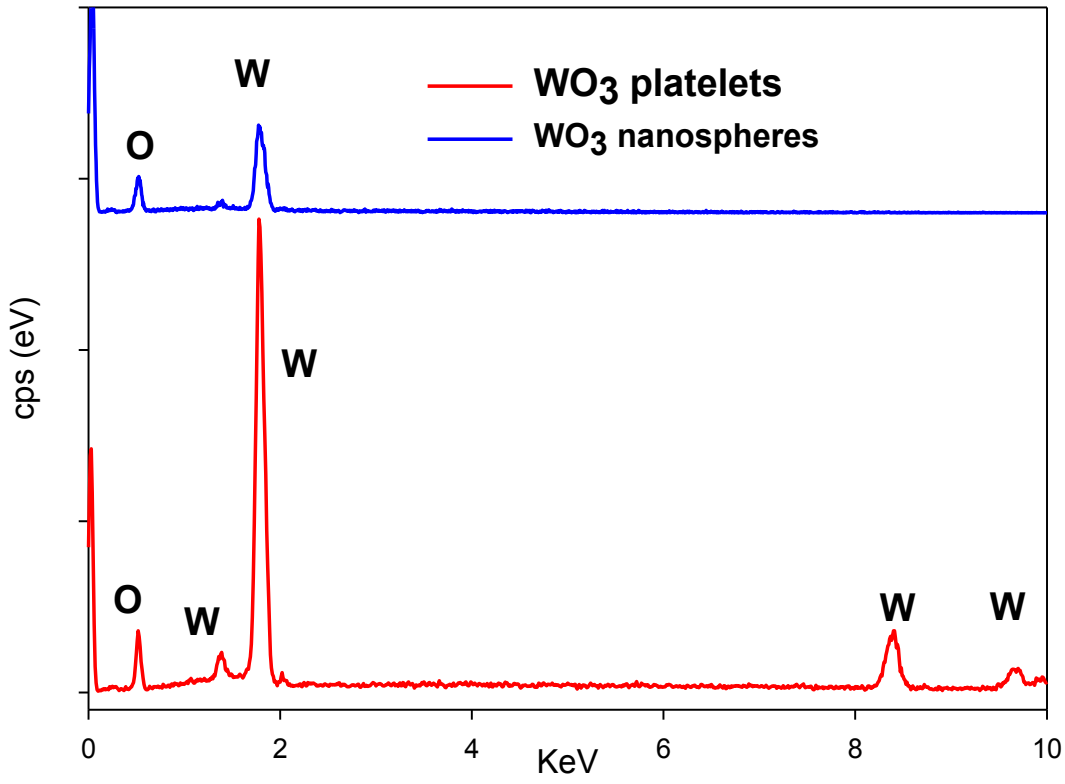

Figure 6.6. EDS spectrum comparing WO_3-3h platelets with WO_3 nanospheres.

less intense peaks, which was due to a lower amount of WO_3 within the nanospheres in comparison to the fully grown WO_3 platelets.

Figure 6.7A depicts the CV of the WO_3 electrode under UV-Visible light prior to and following treatment. It may be seen that the photocurrent was pretty low for the WO_3 platelets, 112 $\mu A/cm^2$ during the UV-Visible irradiation under 1.2 V. Following the electrochemical treatment, the resulting nanospheres exhibited a far higher photocurrent, which was ca. 2.6 mA/cm^2 at 1.2 V. These results were further verified by chronoamperometric tests, which were run at an applied potential of 1.0 V under the irradiation and presented in Figure 6.7B.

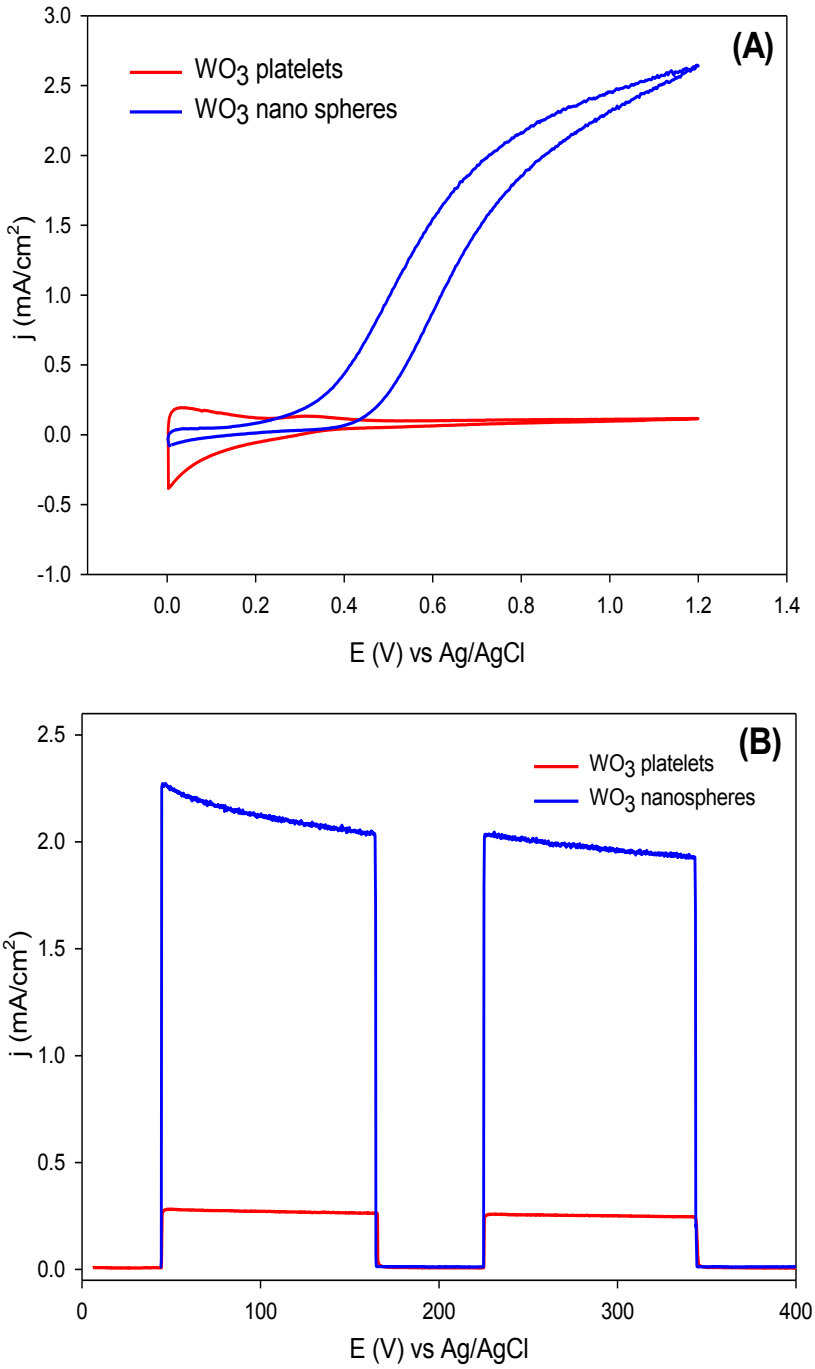

Figure 6.7 (A) Cyclic voltammograms comparing the photocurrent of WO_3-3h plates and the resulting nanospheres. (B) The transient photocurrent-time profiles of the WO_3-3h and WO_3 nanospheres under UV-visible irradiation in 0.5 M H_2SO_4 under 1.0 V of applied potential.

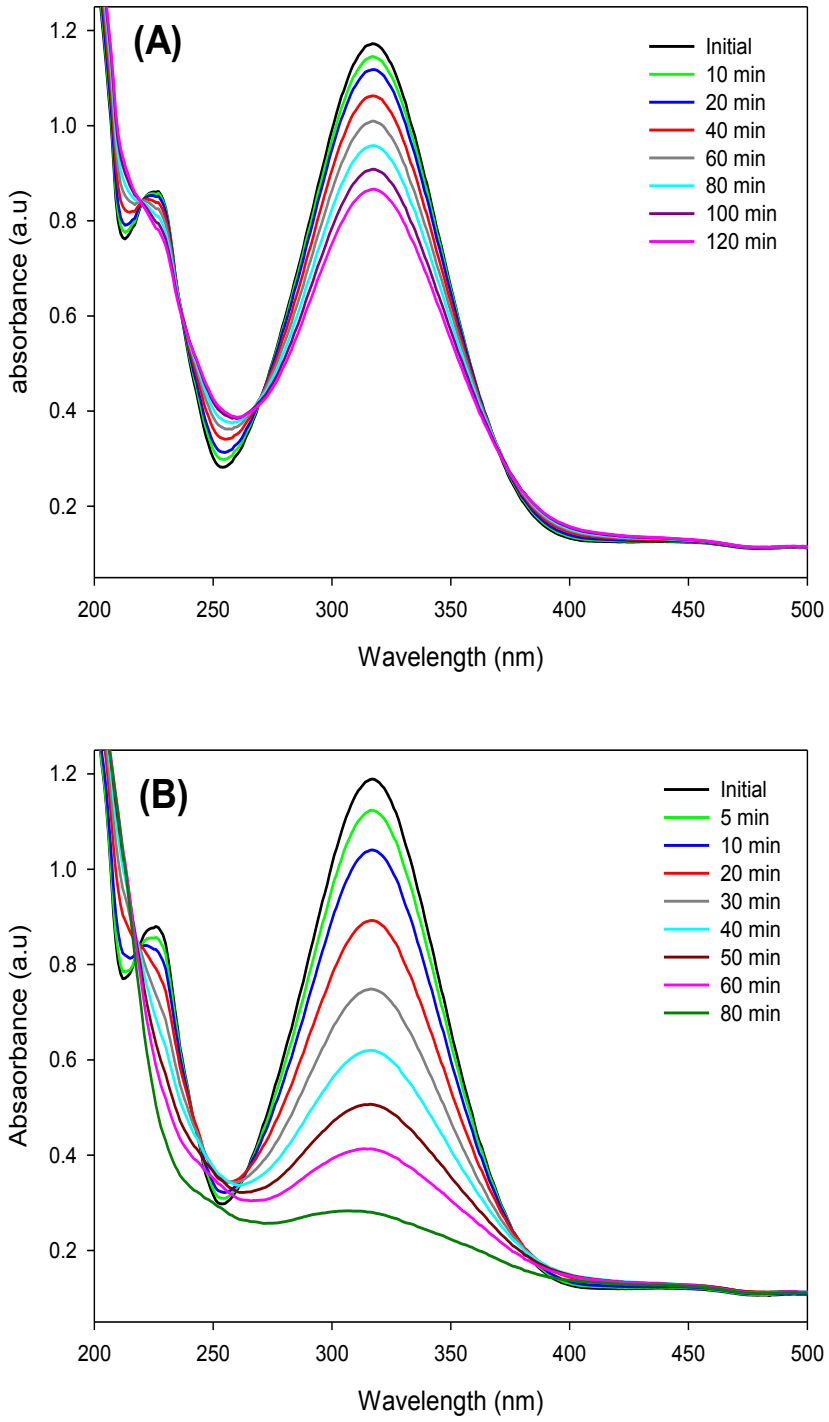

Figure 6.8. Scanning kinetic curves for the photoelectrochemical oxidation of 4-NP in 0.1 M H_2SO_4 at the WO_3-3h (A) and WO_3 nanospheres (B) under UV irradiation and applied bias: 1 V.

To elucidate whether these highly UV-Visible light responsive spherical nanoparticles possessed valuable photocatalytic activity, the electrode was utilized for the oxidation of 4-nitrophenol (4-NP), which is a priority organic pollutant. Figures 6.8A and 6.8B present the photocatalytic activity of the WO_3 platelets and spherical nanoparticles respectively, where it can be seen that the WO_3 nanospheres had a much higher (ca. 7 times) photocatalytic activity than the WO_3 platelets. Figure 6.9 presents the kinetic curves of the respective electrodes.

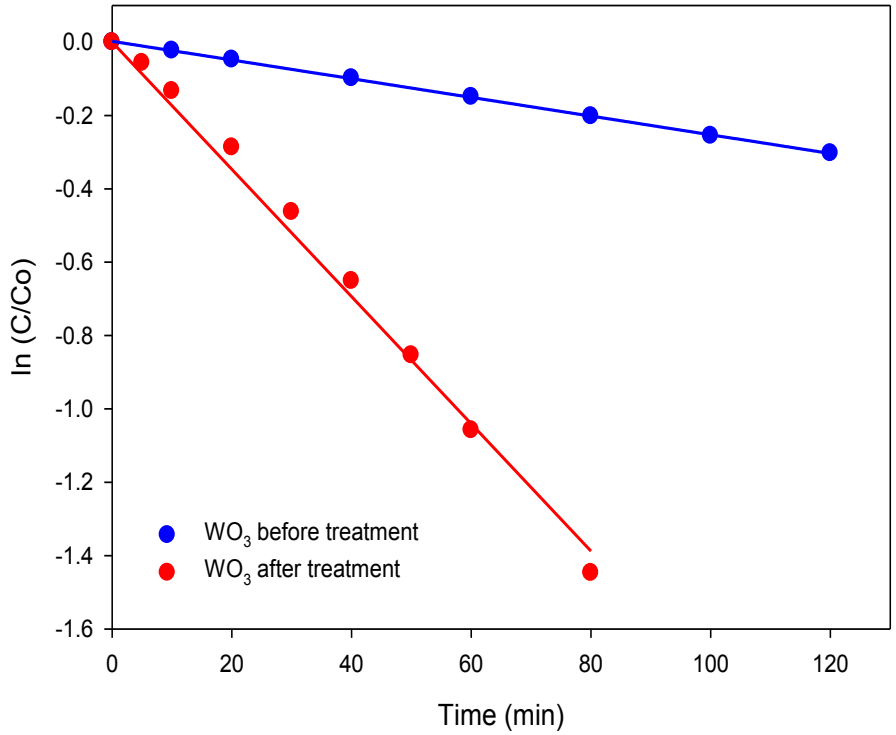

Figure 6.9. Figure showing relationship between ln(C/Co) and time for the photoelectrochemical oxidation of 4-NP in 0.1 M H_2SO_4 at the WO_3-3h (blue) and WO_3 nanospheres (red) under UV irradiation and applied bias: 1V.

6.5. Conclusions

In summary, we have successfully prepared WO_3 nanospheres with a facile electrochemical reduction approach, through the removal of the external layer of WO_3 platelets,

which were grown on the W substrate by a hydrothermal method. The time interval of the hydrothermal treatment had a significant impact on the dimensions of the formed WO_3 platelets and their photoelectrochemical activity. The electrochemically treated electrode consisted of spherical nanoparticles, which exhibited higher photocurrent and photocatalytic activity towards the degradation of 4-NP as compared to their parent WO_3 platelets. The electrochemical treatment described in this communication not only provides insights in the growth of the WO_3 nanostructures under the hydrothermal condition, but also offers a facile approach toward the preparation of high-performance WO_3 nanospheres for myriad energy and environmental applications.

References

[1] M. Tian, S. S Thind, M. Simko, F. Gao, A. Chen. Quantitative structure–reactivity study of electrochemical oxidation of phenolic compounds at the SnO_2–based electrode, *Journal of Physical Chemistry A* 116 (**2012**) 2927-2934

[2] S. S Thind, G. Wu, M. Tian, A. Chen. Significant enhancement in the photocatalytic activity of N, W co-doped TiO_2 nanomaterials for promising environmental applications, *Nanotechnology* 23 (**2012**) 475706 (8pp)

[3] J. Sun, C. Sun, S. K. Batabyal, P. D. Tran, S. Pramana, L. H. Wong, S. G. Mhaisalkar. Morphology and stoichiometry control of hierarchical $CuInSe_2/SnO_2$ nanostructures by directed electrochemical assembly for solar energy harvesting, *Electrochemistry Communications* 15 (**2012**) 18-21

[4] G. Zhao; S. Liu, Q. Lu. Fabrication of electrospun Bi_2WO_6 microbelts with enhanced visible photocatalytic degradation activity, *Journal of Alloys and Compounds* 578 (**2013**) 12-16

[5] G. Lei. Preparation of novel visible-light-driven In_2O_3–$CaIn_2O_4$ composite photocatalyst by sol–gel method, *Journal of Sol-Gel Science and Technology* 44 (**2007**) 263-268

[6] C. D. Valentin, F. Wang, G. Pacchioni. Tungsten oxide in catalysis and photocatalysis: hints from DFT, *Topics in Catalysis* 56 (**2013**) 1404-1419

[7] O. Lavi, G.L. Frey, A. Siegmann, Y. Ein-Eli. Enhanced tungstate electrochromism via formation of transparent conductive networks, *Electrochemistry Communications* 10 (**2008**) 1210-1213

[8] L. M. Bertus, C. Faure, A. Danine, C. Labrugere, G. Campet, A. Rougier, A. Duta. Synthesis and characterization of WO_3 thin films by surfactant assisted spray pyrolysis for electrochromic applications, *Matererials Chemistry and Physics* 140 (**2013**) 49-59

[9] S. Han, J. Li, X. Chen, Y. Huang, C. Liu, Y. Yang, W. Li. Enhancing photoelectrochemical activity of nanocrystalline WO_3 electrodes by surface tuning with Fe(Ⅲ), *International Journal of Hydrogen Energy* 37 (**2012**) 16810-16816

[10] J. Z. Ou, R. A. Rani, S. Balendhran, A. S. Zoolfakar, M. R. Field, S. Zhuiykov, A. P. O'Mullane, K. Kalanta-zadeh. Anodic formation of a thick three-dimensional nanoporous WO_3 film and its photocatalytic property *Electrochemistry Communications* 27 (**2013**) 128–132

[11] C.G. Granqvist. Electrochromic tungsten oxide films: Review of progress 1993–1998, *Solar Energy Materials and Solar Cells* 60 (**2000**) 201-262.

[12] C. M. White, D. T. Gillaspie, E. Whitney, S.-H. Lee, A.C. Dillon. Flexible electrochromic devices based on crystalline WO_3 nanostructures produced with hot-wire chemical vapor deposition, *Thin Solid Films* 517 (**2009**) 3596-3599

[13] X. He, R. F. Boehm. Direct solar water splitting cell using water, WO_3, Pt, and polymer electrolyte membrane, *Energy* 34 (2009) 1454-145

[14] M. Shibuya, M. Miyauchi. You have full text access to this content site-selective deposition of metal nanoparticles on aligned WO_3 nanotrees for super-hydrophilic thin films, *Advanced Mater*ials 21 (**2009**) 1373-1376

[15] A. C. Dillon, A. H. Mahan, R. Deshpande, P. A. Parilla, K. M. Jones, S. H. Lee. Metal oxide nano-particles for improved electrochromic and lithium-ion battery technologies, *Thin Solid Films* 516 (**2008**) 794-797.

[16] A. Hauch, A. Georg, U. Opara Kraovec, B. Orel. Photovoltaically self-charging battery, *Journal of The Electrochemical Society* 149 (**2002**) A1208-A1211.

[17] K. Ito, T. Ohgami. Hydrogen detection based on coloration of anodic tungsten oxide film, *Applied Physics Letters* 60 (**1992**) 938-940.

[18] M. Bendahan, R. Boulmani, J. L. Seguin, K. Aguir. Characterization of ozone sensors based on WO_3 reactively sputtered films: influence of O_2 concentration in the sputtering gas, and working temperature, *Sensors and Actuators B: Chemical* 100 (**2004**) 320-324

[19] K. Wang, P. Zeng, J. Zhai, Q. Liu. Electrochromic films with a stacked structure of WO_3 nanosheets, *Electrochemistry Communications* 26 (**2013**) 5-9

[20] E. L. Miller, B. Marsen, B. Cole, M. Lum. Low-temperature reactively sputtered tungsten oxide films for dolar-powered water splitting applications, *Electrochemical and Solid-State Letters* 9 (**2006**) G248-G250

[21] H. Kawasaki, J. Namba, K Iwatsuji, Y. Suda, K. Wada, K. Ebihara, T. Ohshima. NO_x gas sensing properties of tungsten oxide thin films synthesized by pulsed laser deposition method, *Applied Surface Science* 197 (**2002**) 547-551

[22] C. C. Liao, F. R. Chen, J. J. Kai. Electrochromic properties of nanocomposite WO_3 films, *Solar Energy Materials and Solar Cells* 91 (**2007**) 1282-1288

[23] W. Cheng, E. Baudrin, B Dunn, J. I. Zink. *Journal of Materials Chemistry* 11 (**2000**) 92-97

[24] F. Amano, M. Tian, B. Ohtani, A. Chen. Photoelectrochemical properties of tungsten trioxide thin film electrodes prepared from facet-controlled rectangular platelets, *Journal of Solid State Electrochemistry* 16 (**2012**) 1965–1973

[25] J. Li, Y. Liu, Z. Zhu, G. Zhang, T. Zou, Z. Zou, S. Zhang, D. Zeng, C. Xie. *Scientific Reports* 3 (**2013**) 1-6

Chapter 7: WO_3 Based Bifunctional Electrode for Environmental Applications

7.1 Introduction

Over the last several decades considerable attention has been focused on the development of technologies that may be utilized in the eradication of pollutants from the environment, which are anthropogenically generated [1]. Traditional wastewater treatment techniques are activated via electrosorption, chemical oxidation and biological digestion [2-4]. Heterogeneous photocatalysis is a promising alternative technique for the elimination of organic pollutants in wastewater [5, 6]. Heterogeneous photocatalysts function by absorbing incident light, which results in the activation of materials that then initiate a sequence of chemical reactions of interest. Various semiconductor based metal oxides, such as TiO_2, CdS, SnO_2, WO_3, SiO_2, ZrO_2, ZnO, Nb_2O_3, Fe_2O_3, $SrTiO_3$, CeO_2, Sb_2O_4, V_2O_5, α-C_3N_4 have been studied by different research groups over the last few decades [7-12]. Among these investigated materials, TiO_2, WO_3 and ZnO have shown the best results [13-16]. TiO_2 is the most extensively studied of these materials due to its stability, non-toxicity and high inertness. However, it has the drawback of being activated only by UV light, due to its large band gap. Thus TiO_2 will require structural and electronic modifications to facilitate its activation via ambient sunlight [17-19]. This visible light response might be achieved by doping the TiO_2 with non-metals, metals or by coupling TiO_2 with WO_3, which has the capacity to absorb visible light [20, 21]. One of the most important aspirations of modern science is to achieve the efficient utilization of solar energy.

WO_3 possesses a far lower band gap (ca. 2.6-3.0 eV), thus it may be employed as a visible light driven photocatalyst due to its unique electronic properties [22-24]. Due to its ability

to absorb in the visible light region and other properties, WO_3 is gaining in popularity for use in photoelectrochromic "smart" windows, solar energy conversion, storage cells and solar water-splitting cells and as a potential catalyst enhancer for fuel cells, photocatalysis, batteries and gas/chemical sensors [25-28].

On the other hand, electrocatalysts are very useful in large electrolytic processes that require significant energy. Currently, electrocatalysts are employed in industry in order to cut the costs of manufacturing, by reducing the amount of electric power that is needed for specific processes. Transition metals dominate in electrocatalysis due to the presence of unpaired d electrons and unfilled d orbitals, which form bonds with adsorbates [29]. The fundamental advantages of electrochemical oxidation processes are ease of operation, a wide range of possible treatment conditions and environmental compatibility [30]. The most and efficient electrocatalyst is Pt, which has been intensively studied for its utility in fuel cell and elecrocatalytic applications [31, 32].

In this study, for the first time, WO_3 based bifunctional electrodes have been synthesized, wherein platelet-like structures comprised of WO_3 were synthesized via a hydrothermal method. The WO_3 electrodes possessed a high visible light response. To amalgamate the photocatalytic activity of WO_3 and electrocatalytic activity of Pt nanoparticles, Pt was deposited on one side of the WO_3 electrodes in obtaining a bifunctional electrode. The prepared electrodes were examined using various surface analytical methods. The results indicated that the WO_3 electrode had a very high visible light response, which may be translated to high photocatalytic activity. With the addition of Pt on one side of the electrode, the activity of the electrode was seen to increase significantly on the application of a potential. To verify the activity of the prepared electrodes, a number of photodegradation reactions of RhB were performed under various applied conditions.

The bifunctional electrode exhibited greater activity as compared to the WO_3 electrode as photocatalyst and WO_3/Pt as electrocatalyst, under both applied potential and visible light.

7.2 Experimental section

7.2.1 Materials

Tungsten plates, having a thickness of 0.25 mm, were received from Sigma-Aldrich (99.9% trace metals basis) and cut into 1cm × 1cm squares. Acetone (≥99.5%) and Nitric Acid (70%), H_2SO_4 (99.999%) were purchased from Sigma Aldrich and were utilized as received. Rhodamine B (BDH, UK) was employed as a typical model of an organic dye pollutant in the evaluation of the photocatalytic and electrocatalytic activity of the WO_3 based catalyst. The water (18:2 MΩ cm) used in the preparation of the aqueous solutions was purified using a NANOpure® Diamond™ water system.

7.2.2 Photocatalyst synthesis

To prepare the WO_3 photocatalysts, a very facile hydrothermal method was employed, wherein a commercially available tungsten plate (Sigma-Aldrich, 99.7 %,) was cut to obtain a $1cm^2$ area and used as a substrate. The tungsten plates were then sonicated multiple times in acetone to remove all organic impurities that were present on the surface, followed by sonication in water. In order to grow tungsten oxide on the substrate, it was introduced into a Teflon lined autoclave, with 80% of its volume filled with 1.5 M HNO_3. Following the hydrothermal treatment, the electrodes were rinsed with ultrapure water several times and then heated at 450 °C over three hours, and used for the electrochemical tests, as such, after calcination.

7.2.3 Deposition of Pt nanoparticles on the surface of WO_3 electrode

WO_3 electrodes containing Pt nanoparticles were fabricated by using a photoreduction method. In general, a 0.1 mM solution of an inorganic $H_2PtCl_6 \cdot 6H_2O$ precursor was made in ultrapure water. A desired amount of this solution was added into 5 mL of a 50% (v/v) methanol solution, which was deaerated for 10 min with ultrapure argon gas to eliminate any oxygen that was present in the solution; the test tube was then sealed with a rubber stopper. The electrode in the Pt solution was subsequently irradiated under UV light for one hour. The electrodes were then rinsed carefully under the pure water and then dried at 50°C in an oven.

7.2.4 Characterization techniques

The characterization of crystalline phase of the synthesized samples was obtained by X-ray diffraction (Phillips PW 1050-3710 Diffractometer with Cu Kα radiation (λ=1.5406 A^o). Scanning electron microscopy (Hitachi SU 70) analysis was also performed in order to determine the surface morphology and particle size of the samples. The UV-Vis absorbance spectrum was quantified using a UV-visible spectrophotometer (Varian, Cary 5E). For the electrochemical characterization, a three-electrode cell system was employed. A Pt coil with a 10 cm^2 surface area was used as the auxiliary electrode, and an Ag/AgCl electrode was used as the reference electrode.

7.2.5. Photocatalytic activity measurements

The photocatalytic activity of the as synthesized WO_3 was evaluated by measuring the photodegradation of RhB under visible light, and/or 1.8 V applied potential. The RhB solution was prepared using pure water (18.2 MΩ.cm) that was obtained from a NANOpure® Diamond™ UV ultrapure water purification system. An Oriel system, containing a 300W xenon

arc lamp was used in this study as the light source. The lamp was allowed to warm up for half an hour prior to testing. For visible light irradiance, the source light was passed through an optical filter (Edmund Optical Co. GG420), which cut off wavelengths of below 420 nm. Infrared light was removed using a water filter. Samples were collected from the reaction mixture at regular time intervals, and the absorbance of the solution was measured using a UV-visible spectrometer (Varian, Cary 50). Subsequent to taking each reading, the solution was added back to the reaction mixture.

7.3. Results and Discussion

With the aim of optimizing its photoelectrochemical properties, WO_3 was synthesized with different morphologies, such as nanoparticles, platelets, nanorods, and nanowires, which enabled a number of unique properties that are not observed in bulk WO_3. By modifying its crystallinity, the surface energies of WO_3 may be significantly altered, which allows for the tuning of the properties of the material. Much focus has been devoted to rectangular WO_3, $WO_3.H_2O$ and $WO_3.2H_2O$ platelets, as they possess visible light activity. To investigate the morphologies of the prepared WO_3, scanning electron microscopy was utilized, with the results shown in Figure 7.1. The SEM image of the as synthesized WO_3 (Figure 7.1A) reveals that the platelet-like structure was obtained by this hydrothermal method, and that the platelets are well distributed across the WO_3 plate substrate. As was observed from our previous studies, the duration of hydrothermal process had a significant effect on the thickness of the WO_3 platelets. As the hydrothermal vessel was heat treated for longer durations, the thickness of the WO_3 platelets increased, while the activity decreased. The average length of the platelets was observed to be ~1μm, while the width was ~50 nm. The smaller particles resulted in an increase in the surface area of the electrodes, which made available additional active sites for reactions,

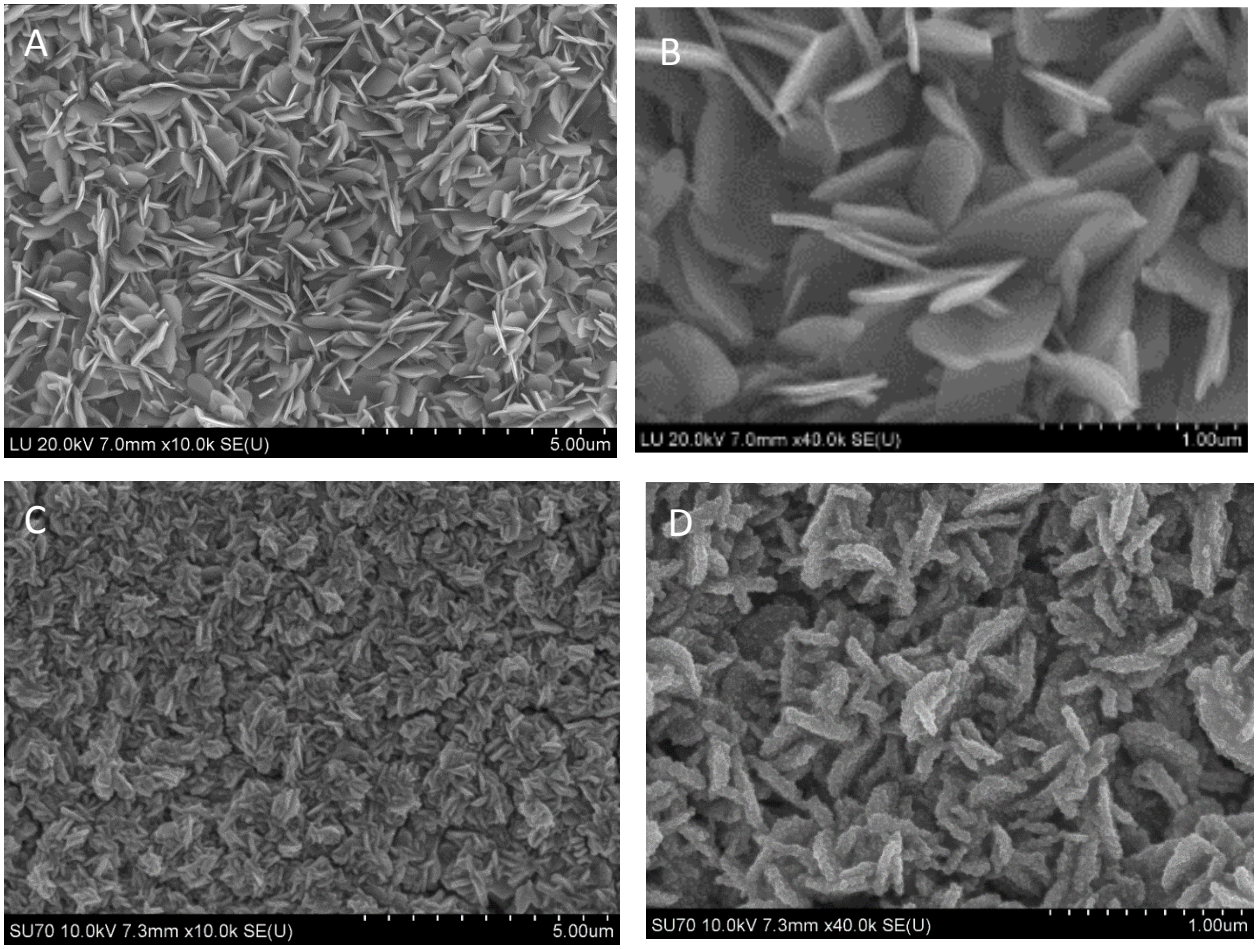

Figure 7.1 SEM images of WO_3 (A and B) and WO_3/Pt (C and D)

there by increasing the photocatalytic activity of the electrodes. SEM was also performed on the electrodes onto which Pt was deposited by a UV reduction method and the result are shown in Figure 7.1C and D. The Pt can be easily seen as the small dots on the WO_3 plates which resulted in a rough surface in comparison to the bare WO_3. The image illustrates that the Pt nanoparticles were very well adhered to the WO_3 plates and that they were very finely distributed. The UV reduction method is very efficient in the deposition of uniform distribution of Pt, as there were no Pt particle aggregates to be seen anywhere on the electrodes. These deposited Pt particles served to further increase the surface area of the electrodes.

To further investigate the composition of the WO_3 electrodes as well as the Pt deposited WO_3, the electrodes were analyzed by EDS, with the results shown in Figure 7.2A. A typical WO_3 spectra was obtained for the WO_3 electrode, as four tungsten peaks at 1.37, 1.76, 8.42 and 9.65 were observed. The peaks were analyzed to calculate the composition of the electrodes and a perfect 1:3 ratio for W:O was observed. For the Pt deposited electrodes, the intensity of the W and O peaks were slightly less than that of the bare WO_3, as Pt covered the platelets. With all the W and O peaks, one strong Pt peak at 2.05, and a weak peak centered at 2.33 was also detected, which showed the presence of Pt on the surface of the electrodes.

To discover the crystalline phase, the samples were analyzed by XRD and are shown in Figure 7.2B. In general, all of the samples showed three very characteristic peaks of WO_3 at 2θ values of 23.5, 40.5 and 33.7. According to the literature, the peak at 23.5 corresponds to the phase [002], [020] and [200], whereas the 40.5 peak is due to the presence of the [222] phase. It is worth noting that even after the deposition of the Pt on the WO_3 plates, no Pt peaks were obtained in the XRD patterns, which is most likely due to the very small amount of Pt that was deposited on the electrodes, which is beyond detection limits of the XRD instruments.

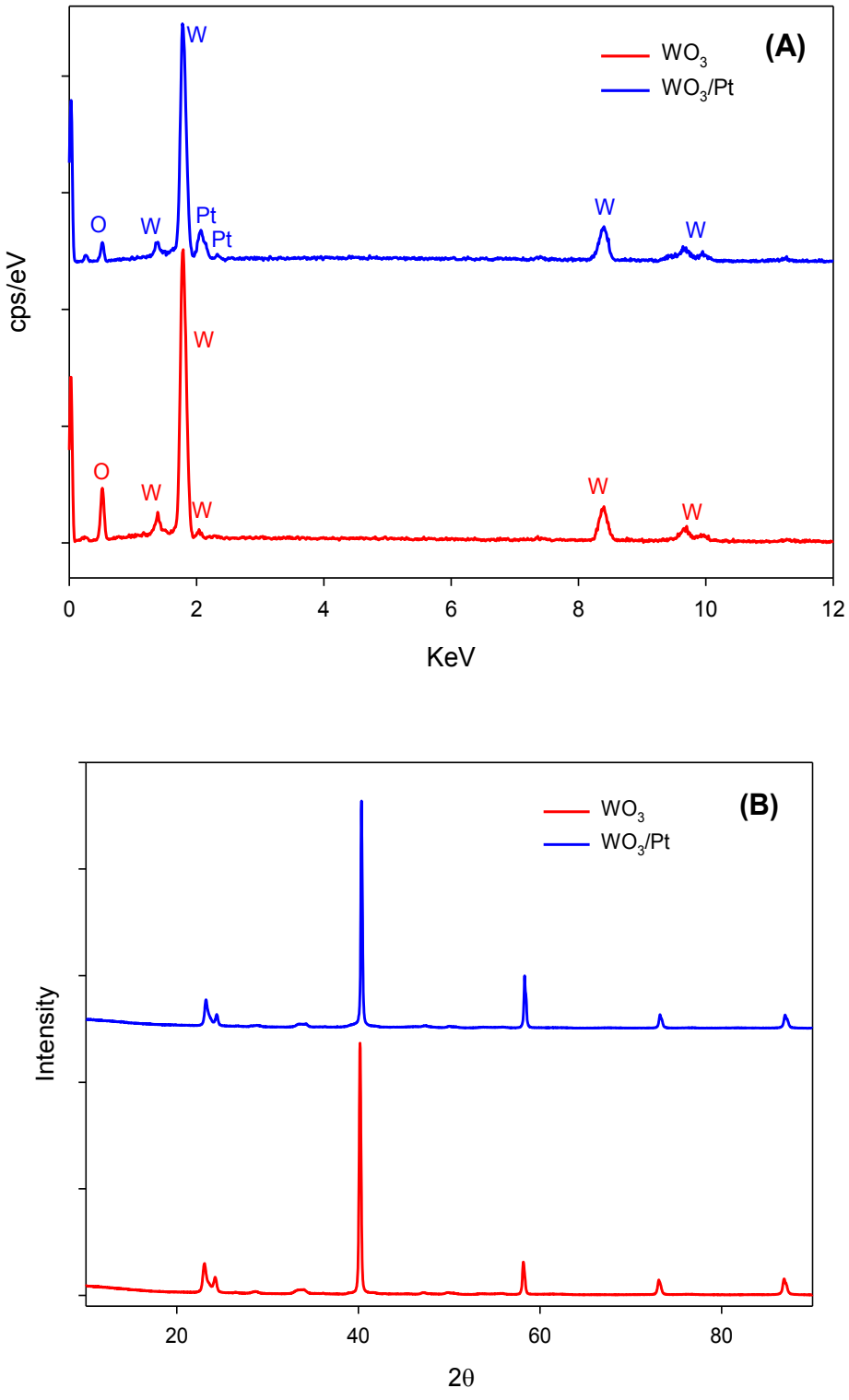

Figure 7.2 Comparison of EDS and XRD results of the WO_3 (red) and WO_3/Pt (blue).

Cyclic voltammograms were run for the prepared samples to investigate the electrochemical behaviours of the electrodes. Figure 7.3A shows the CV's of the WO_3 electrodes between the potential ranges of 0.0 to 1.2 V in 0.5 M H_2SO_4 at 20 mV/sec. It presents a typical CV for WO_3 and it can be seen that the activity of the electrode is very low, as the electrochemical current is in the range of few microamperes. Because of its low band gap, WO_3 typically exhibits good activity under visible light. To analyze the visible response of the fabricated electrodes, a CV was run under visible light irradiation, where after it was concluded that the as-synthesized WO_3 platelets had a very high visible light response, and the photocurrent was 1.47 mA at 1.2 V. Thus these electrodes may be effectively utilized under visible light for photocatalysis.

To further verify that the Pt nanoparticles were well-deposited on the WO_3 platelets, the CV was run and compared to that of the bare WO_3 electrode, and is presented as Figure 7.3B. Pt has a characteristic H_2 adsorption and desorption peak, thus to show these peaks, the CV's were run at between -0.225 to 1.2V. The red curve in the voltammogram depicts the typical hydrogen adsorption/desorption in the potential range of between -0.225 and +0.2 V, which may be used to calculate the active electrochemical surface area of the electrode. It can be concluded from this region that due to the deposition of the Pt nanoparticles on the surface of the WO_3, the capacity of the electrode to adsorb hydrogen increases many fold. It also represents that the surface area of the electrode has increased significantly, as can be seen from the H_2 adsorption-desorption region. As it is well understood that cumulative surface area plays an important role in photocatalysis and electrocatalysis, this increase in area might be significant in enhancing the activity of the prepared bifunctional electrodes. Pure WO_3 electrodes have an almost non-existent level of electrochemical current between the potential range of +0.2 and 1.2. On the other hand,

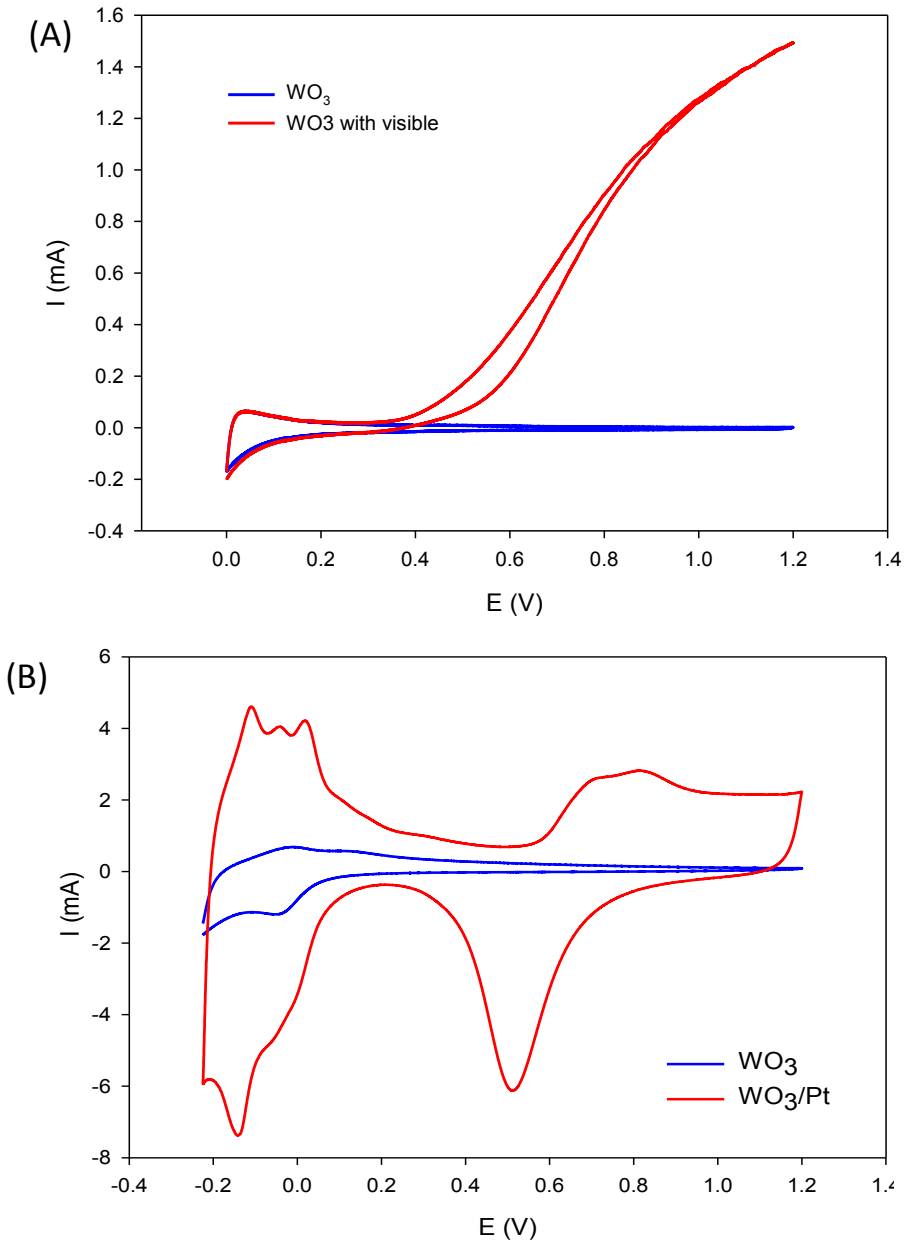

Figure 7.3 (A) Cyclic voltammograms of the WO_3 electrodes under a dark condition (blue) and under visible light (red). (B) Comparison of the CV's of WO_3 prior to and following the deposition of the Pt nanoparticles.

Pt exhibits a high electrochemical current in the positive cycle due to the formation of Pt oxide at =>0.6 V. On the negative potential sweep this oxide gets reduced back to Pt and a very distinct reduction peak is observed that is centered at 0.5V. Several scans were run to evaluate the stability of the deposited nanoparticles on the surface of the WO_3 electrode and the practically overlapping CV's show that the prepared bifunctional electrodes are highly stable. This increase in electrochemical current due to the deposition of Pt may be employed as an effective electrocatalyst.

To further characterize the electronic properties of the WO_3 and WO_3-Pt electrodes, a Mott-Schottky measurement was carried out in a 0.1M H_2SO_4 solution. The Mott-Schottky plot can be employed to estimate donor density (ND):

$$\frac{1}{C^2} = \frac{2}{\varepsilon\varepsilon_0 e N_D}\left(E - E_{fb} - \frac{kT}{e}\right)$$

where C is the capacitance of the space charge layer [$F \cdot m^{-2}$]; ε is the average value of the semiconductor dielectric constant; ε_0 is the permittivity of the free space charge (8.854×10^{-12} $F \cdot m^{-1}$); e is the absolute value of the electron charge (1.602×10^{-19} C); E is the applied potential and E_{fb} is the flat band potential. Dopant levels highly influence the donor density, and hence, the electronic properties of the material. The Mott-Schottky plots for the as-synthesized WO_3 and WO_3-Pt electrodes are presented at Figure 7.4A. For clarification, the Mott Schottky plots for the WO_3-Pt are presented as Figure 7.4B. A sigmoidal plot was observed in the investigated potential range, which is typical for n-type semiconductors. A good linear relationship was

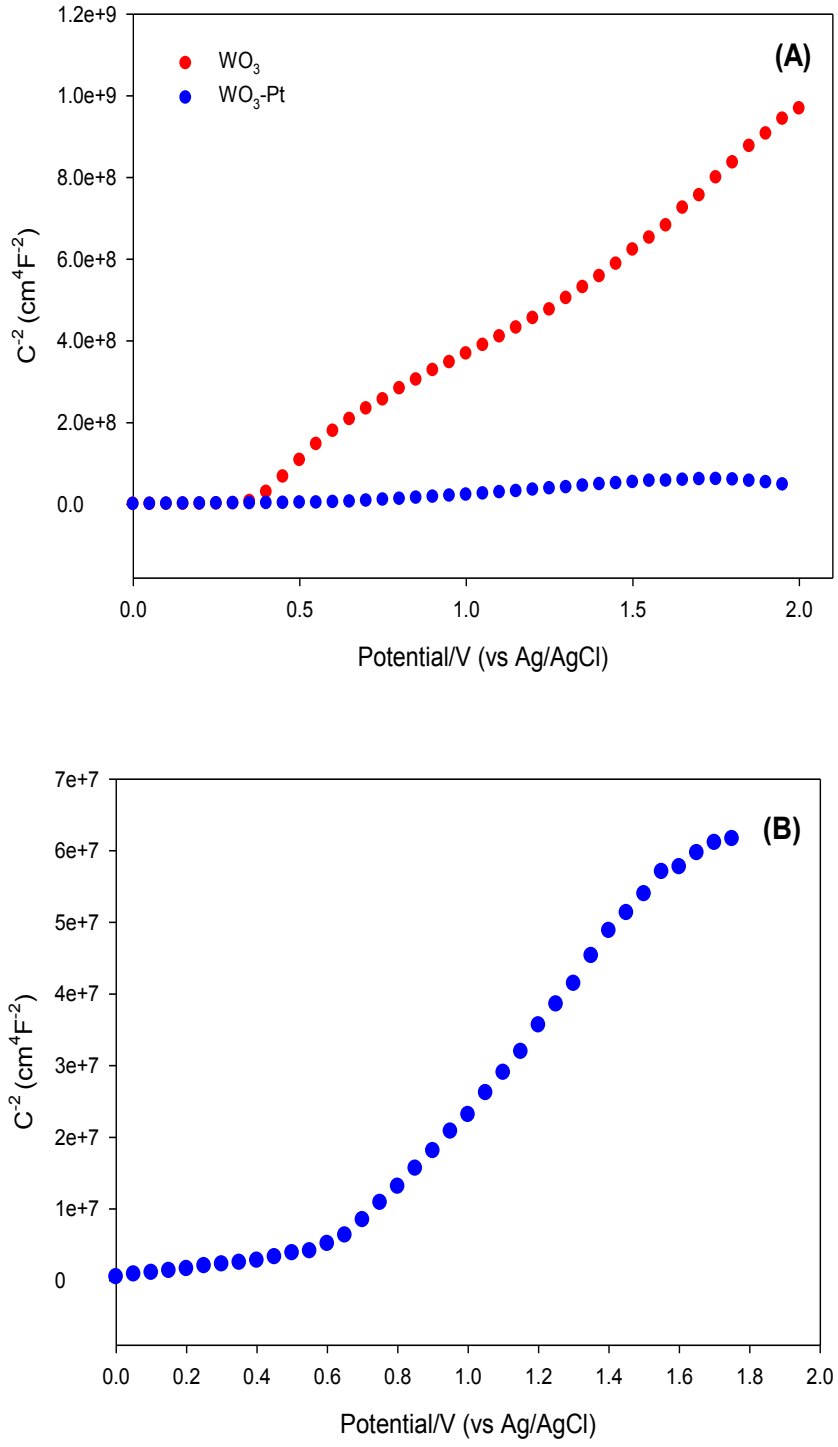

Figure 7.4 (A) Mott-Schottky plot of the WO_3 (red) and WO_3-Pt (blue) obtained in 0.1 M H_2SO_4 at 500 Hz. (B) Mott-Schottky plot of the WO_3-Pt

observed between C^{-2} and the potential, in the range of 0 and 0.40 V vs. Ag/AgCl for the WO_3 and WO_3-Pt electrode. It is interesting to note that the donor density of the WO_3 following the photodeposition of the Pt nanoparticles increased to ten times that of the bare WO_3 electrode. The donor densities were calculated by obtaining the slope of the curve and were 6.0×10^{22} and 6.2×10^{23} for the WO_3 and WO_3-Pt electrode. This increase in the electron donor density of the WO_3-Pt electrodes may contribute to the deposition of the Pt nanoparticles onto the WO_3, which enhances its conductivity. This increase in electron donor density may efficiently be utilized in the electrochemical treatment of the wastewater.

To examine the photocurrent behavior of the prepared WO_3 and the bifunctional WO_3-Pt electrodes, series of chronoamperometry measurements were performed, with the results presented in Figure 7.5. Figure 7.3A shows that the WO_3 electrodes prepared in this study produce a significant amount of visible light induced photocurrent. To verify these results as well as to evaluate the stability of this photocurrent, a potential of 1.8V was applied to the electrode with the results shown in Figure 7.5A. An applied potential of 1.8V was utilized as Pt nanoparticles can only be activated at higher positive potentials. The as-synthesized WO_3 electrodes generated a ca. 1mA electrochemical current under 1.8V of applied potential and when the electrode is exposed to visible light there is an approximate 0.5mA increase in the photocurrent.

Figure 7.5B shows the results obtained when the WO_3-Pt bifunctional electrode was utilized and interestingly a very large increase in the electrochemical current is observed as compared to the WO_3 electrode. This further signifies that with such a small volume of Pt nanoparticle deposition, the electrochemical current was increased ca. 15 times that of the native

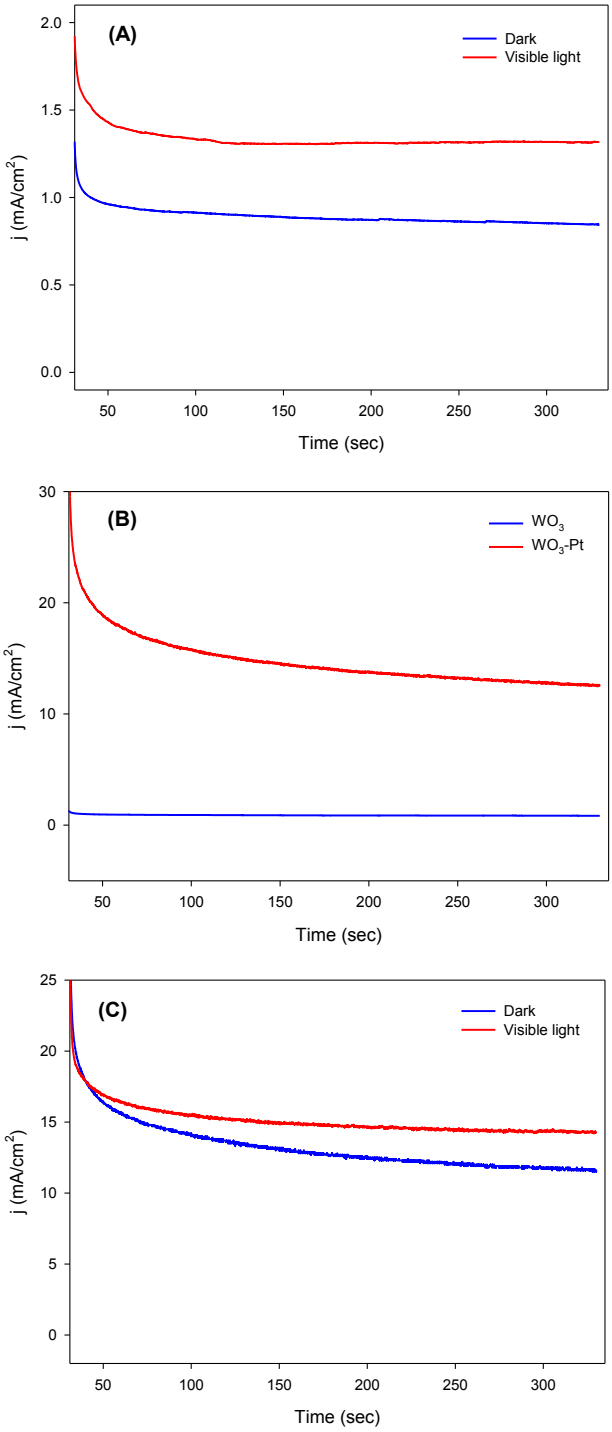

Figure 7.5. Chronoamperometry results for A) WO_3 (under dark and visible), B) Comparison of WO_3 and WO_3-Pt and C) WO_3-Pt under a dark and visible light. 1.8 V was applied for all these measurements.

WO_3 electrode. These results also support the data obtained from the Mott-Schottky plots, as a tenfold increase in the electron donor density was obtained.

The bifunctional electrodes exhibited a very high EC current. To examine whether the prepared electrodes might be employed as a photocatalyst and electrocatalyst simultaneously, chronoamperometric measurements were performed under visible light, with the results shown in the Figure 7.5C. Even under an applied potential of 1.8 V, with such a significant EC current, when the electrode was exposed to visible light during the experiment a further increase in the overall current was observed. This increase was approximately 3 mA, which was much higher in comparison to the visible light response of the WO_3 electrode. This conveys that when the bifunctional electrode was employed simultaneously as a photocatalyst and electrocatalyst, there was a synergistic effect by which the overall activity of the electrode was much higher than that of the monofunctional electrode.

From the above characterization techniques it was clear that we had successfully deposited Pt nanoparticles onto the WO_3 electrodes, and that they were very well distributed across the WO_3 plates and had the typical electrochemical properties of Pt electrodes. To further evaluate the strength of this bifunctional approach, the WO_3 and WO_3/Pt electrodes were tested for the degradation of the Rhodamine B, which is an organic dye pollutant. RhB was selected as the target molecule in this study to represent organic dye pollutants that might be a threat to aquatic ecosystems and to human populations if left untreated in water. These degradation tests were conducted under different applied conditions and are presented in Figure 7.6.

WO_3 is a semiconductor that has poor conductivity, thus it exhibits a very low electrochemical activity by itself. This is indeed the case in our studies as can be seen from

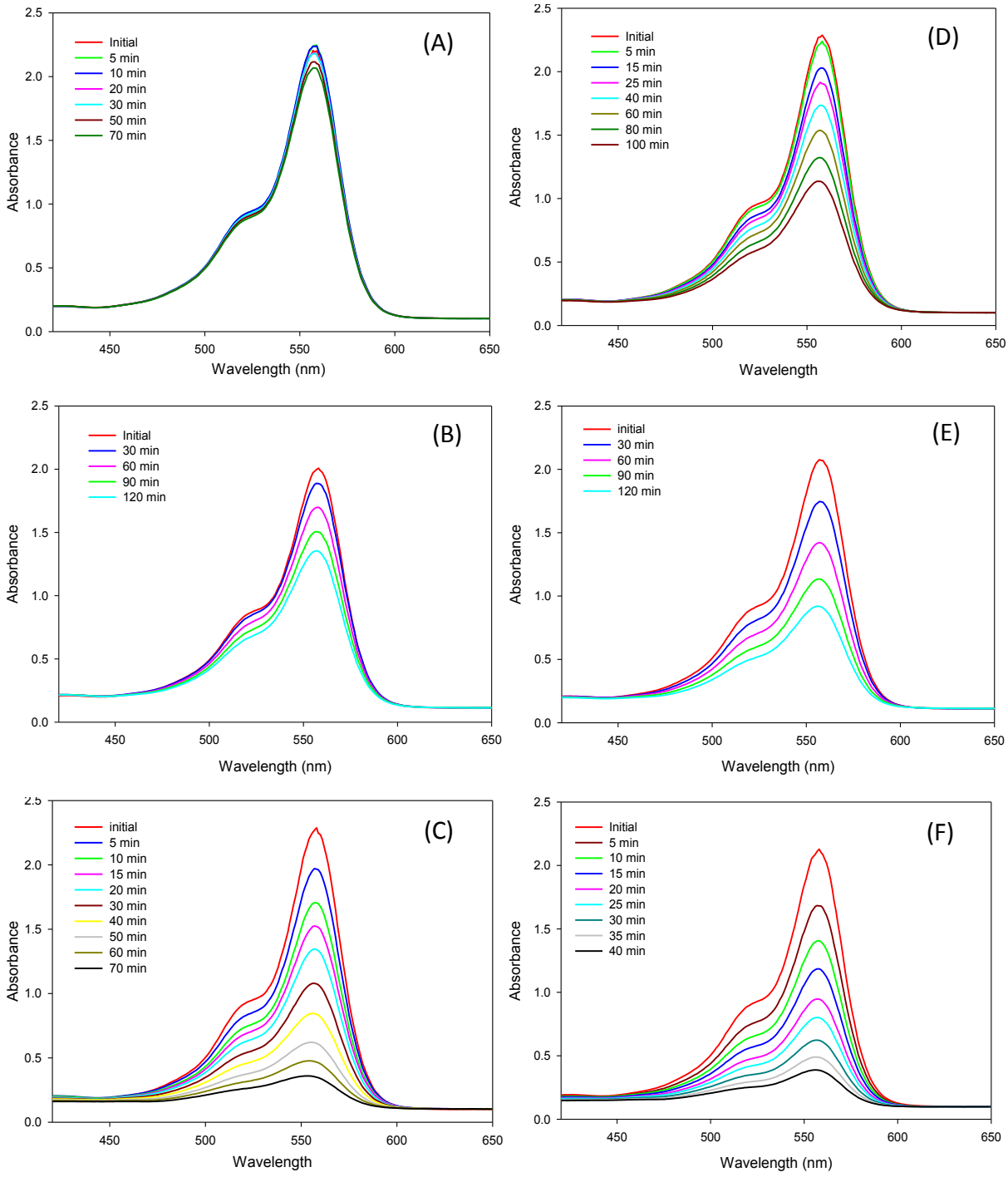

Figure 7.6. The degradation curves of RhB on WO_3 under EC (A), Visible light irradiation (B) and under both EC and visible light (C). WO_3/Pt under EC (D), Visible light irradiation (E) and under both EC and visible light (F)

Figure 7.6A, which presents the absorbance spectroscopy results of the electrochemical degradation of RhB, where WO_3 is employed as an electrocatalyst with a 1.8 V applied potential.

As may be concluded from the Figure, the electrochemical activity of WO_3 was very low and even after 70 min a very insignificant volume of RhB had been oxidized. The rate constant for this reaction was calculated to be 1.05×10^{-3}, which is very low. As expected, the Pt deposited WO_3 electrodes demonstrated a far better electrochemical activity than that of the bare WO_3 electrodes, and it can be seen from Figure 7.6B that within 100 min. approximately half of the RhB has been degraded via this electrode. The electrocatalyst on the WO_3/Pt electrode was ca. 4 times that of the bare WO_3. This is significant, as knowing that even when a very small amount (0.5 mg) of Pt was deposited on the WO_3, it resulted in a considerable increase in electrochemical activity.

As concluded from Figure 7.5A, the prepared WO_3 had a high visible light response. A series of photodegradation experiments were run to verify whether this highly visible light response may be translated to photocatalytic activity. In these experiments, no external potential was applied, and the WO_3 electrode was irradiated only with visible light. WO_3 exhibited good activity under visible light, and in 120 min. ~70% of the RhB was oxidized, and the rate constant of this reaction was 3.27×10^{-3}. Very interestingly, when Pt deposited WO_3 electrode was utilized under the same conditions; the rate of the reaction was twofold compared to that of the bare WO_3. This shows that, even though is not activated by an applied potential, the Pt deposited on the WO_3 is still participating in the reaction via some indirect mechanism. Most probably the excited electrons that travel to the surface from the conduction band are taken up by the Pt, thus reducing the electron/hole recombination rate. This decrease in the recombination rate significantly enhances the activity of the electrode in the visible region.

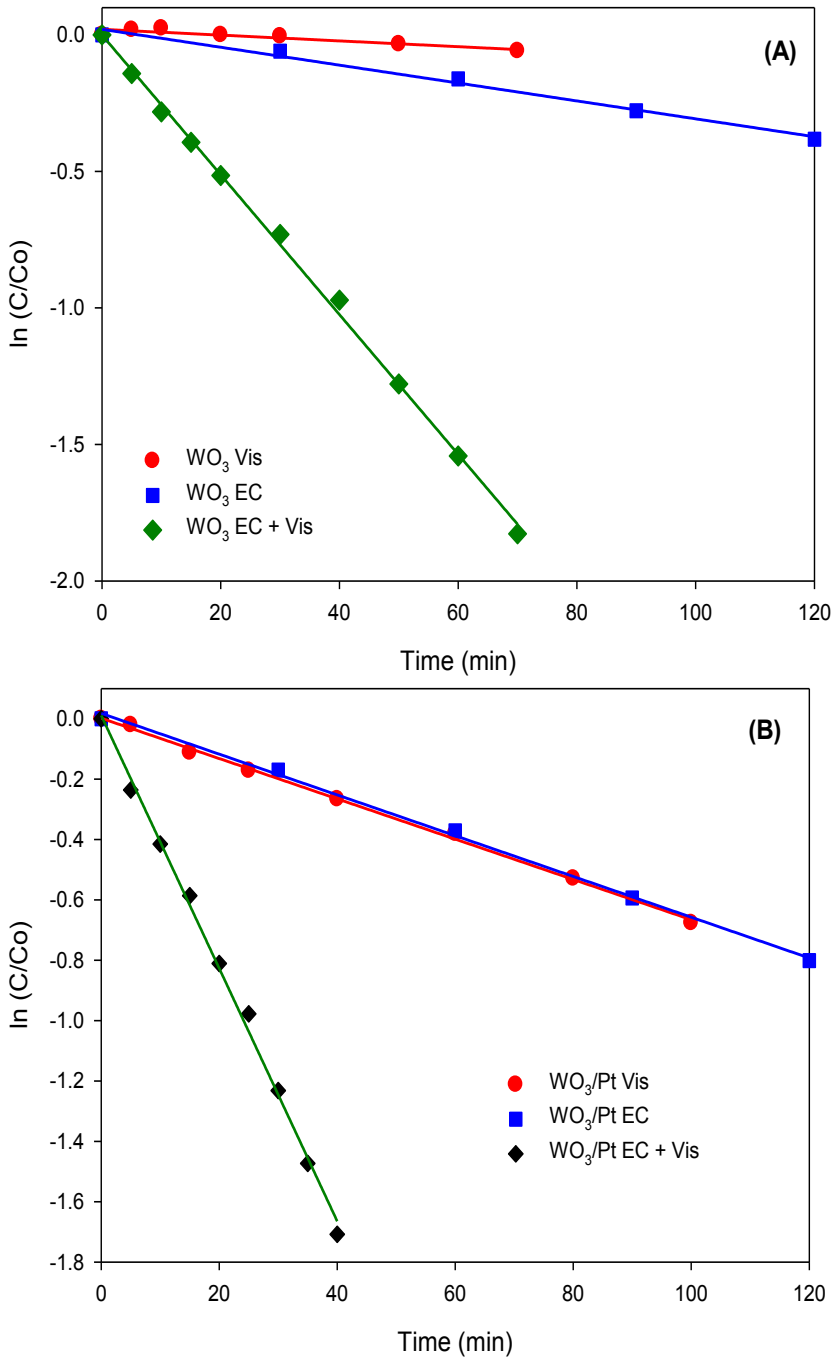

Figure 7.7 The kinetic curves of the degradation of RhB on WO_3 (A) and on WO_3/Pt (B) photodegradation of Rhodamine B over WO_3 and WO_3/Pt electrodes, respectively, under various applied conditions. The rate constant values are given in Table 1, which shows that the WO_3/Pt bifunctional electrodes had higher activity.

A bifunctional electrode was utilized simultaneously under an applied potential and visible light irradiation to investigate whether the aforementioned high electrochemical activity of Pt nanoparticles and the significant photocatalytic activity of the WO_3 can be employed simultaneously to obtain high efficiency in the abatement of RhB, with the results shown in Figure 7.6F. It can be seen that the bifunctional electrode had a much higher activity as compared to when the electrode was used individually for photocatalysis or electrocatalysis. This demonstrates that there is present a synergistic effect, where both the photocatalysis and electrocatalysis collaborate in conveying a high catalytic response. The WO_3/Pt bifunctional electrodes had ca. twofold higher catalytic activity toward the degradation of RhB as compared to when WO_3 electrode is used as bifunctional. Figure 7.7A and B presents the kinetic curves for the photodegradation of Rhodamine B over WO_3 and WO_3/Pt electrode respectively under various applied conditions. The rate constant values are given in the Table 1 and it shows that the WO_3/Pt bifunctional electrodes has higher activity.

Table 7.1. The calculated rate constants for the degradation of the RhB on WO_3 (A) and WO_3/Pt (B) under applied conditions

Sample/condition	Rate constant
WO_3 EC	1.057×10^{-3}
WO_3 Vis	3.277×10^{-3}
WO_3 EC + Vis	2.500×10^{-2}
WO_3/Pt EC	6.677×10^{-3}
WO_3/Pt Vis	6.754×10^{-3}
WO_3/Pt EC + Vis	4.190×10^{-2}

7.4. Conclusion

WO_3 platelet-like structures were successfully synthesized by a very facile hydrothermal method where highly ordered WO_3 platelets were obtained. The WO_3 platelets were well distributed across the W plate and they possessed a very high visible light response under exposure to visible light. The deposition of the Pt nanoparticles on one side of the WO_3 was achieved by a UV reduction method, which resulted in the very uniform deposition of Pt nanoparticles on the WO_3 plates, as may be concluded from the SEM results. The EDS results further verified the presence of the Pt on the electrodes, as well defined Pt peaks were observed in the EDS results. Cyclic voltammograms for the bifunctinal electrodes showed a typical curve for Pt, and had a high hydrogen adsorption/desorption capacity. The RhB degradation tests on the various synthesized electrodes revealed that the bifunctional electrodes, when used under both visible light and applied potential, showed much better activity. The deposition of the Pt enhanced the activity of the bifunctional electrodes by approximately two fold as compared to when a bare WO_3 electrode was used as a bifunctional electrode. This two fold enhancement in the catalytic properties of the WO_3 electrodes via the deposition of a very small amount of Pt might be used in green chemistry for wastewater treatment and in fuel cells.

References

[1] G. Wu, S. S. Thind, J. Wen, K. Yan, A. Chen. A novel nanoporous α-C_3N_4 photocatalyst with superior high visible light activity, *Applied Catalysis B: Environmental* 142–143 (**2013**) 590-597.

[2] J. Yang, Y. Zhao, C. Zhang, Y. Hu, M. Zhou. Electrosorption driven by microbial fuel cells without electric grid energy consumption for simultaneous phenol removal and wastewater treatment, *Electrochemistry Communications* 34 (**2013**) 121-124.

[3] Y. Yavuz, A. Savas Koparal, Ü. Bakir Ögütveren. Phenol removal through chemical oxidation using fenton reagent, *Chemical Engineering & Technology* 30 (**2007**) 583-586.

[4] X. Qiu, Q. Zhong, M. Li, W. Bai, B. Li. Biodegradation of p-nitrophenol by methyl parathion-degrading Ochrobactrum sp. B_2, *International Biodeterioration & Biodegradation* 59 (**2007**) 297-301.

[5] M. C. Ortega-Liébana, E. Sánchez-López, J. Hidalgo-Carrillo, A. Marinas, J. M. Marinas, F. J. Urbano. A comparative study of photocatalytic degradation of 3-chloropyridine under UV and solar light by homogeneous (photo-Fenton) and heterogeneous (TiO_2) photocatalysis, *Applied Catalysis B: Environmental* 127 (**2012**) 316-322.

[6] W. Wilson, A. Manivannan, V. R. Subramanian. Heterogeneous photocatalytic degradation of recalcitrant pollutants over CdS–TiO_2 nanotubes: Boosting effect of TiO_2 nanoparticles at nanotube–CdS interface, *Applied Catalysis A: General* 441–442 (**2012**) 1-9.

[7] P. Praus, L. Svoboda, J. Tokarský, A. Hospodková, V. Klemm. Core/shell CdS/ZnS nanoparticles: Molecular modelling and characterization by photocatalytic decomposition of Methylene Blue, *Applied Surface Science* 292 (**2014**) 813-822.

[8] X. Fu, L. A. Clark, Q. Yang, M. A. Anderson. Enhanced photocatalytic performance of titania-based binary metal oxides: TiO_2/SiO_2 and TiO_2/ZrO_2, *Environmental Science & Technology* 30 (**1996**) 647-653.

[9] C. Zhan, F. Chen, J. Yang, D. Dai, X. Cao, M. Zhong. Visible light responsive sulfated rare earth doped TiO_2@fumed SiO_2 composites with mesoporosity: Enhanced photocatalytic activity for methyl orange degradation, *Journal of Hazardous Materials* 267 (**2014**) 88-97.

[10] J. Nilsson, A. Landa-Cánovas, S. Hansen, A. Andersson. Catalysis and structure of the $SbVO_4/Sb_2O_4$ system for propane ammoxidation, *Catalysis Today* 33 (**1997**) 97-108.

[11] S. Choi, M.-S. Lee, D.-W. Park. Photocatalytic performance of TiO_2/V_2O_5 nanocomposite powder prepared by DC arc plasma, *Current Applied Physics* 14 (**2014**) 433-438.

[12] G. Wu, S. S. Thind, J. Wen K. Yan, A. Chen. A novel nanoporous alpha-C_3N_4 photocatalyst with superior high visible light activity *Applied Catalysis B: Environmental* 142-143 (**2013**) 590-597

[13] H. Zheng, J.Z. Ou, M.S. Strano, R.B. Kaner, A. Mitchell, K. Kalantar-zadeh. Nanostructured Tungsten Oxide – Properties, Synthesis, and Applications, *Advanced Funtional Materials* 21 (**2011**) 2175-2196.

[14] S. S. Thind, G. Wu, M. Tian, A. Chen. Significant enhancement in the photocatalytic activity of N, W co-doped TiO_2 nanomaterials for promising environmental applications, *Nanotechnology* 23 (**2012**) 475706.

[15] F. Amano, M. Tian, B. Ohtani, A. Chen. Photoelectrochemical properties of tungsten trioxide thin film electrodes prepared from facet-controlled rectangular platelets, *Journal of Solid State Electrochemistry* 16 (**2012**) 1965-1973.

[16] M. Rezapour, N. Talebian. Synthesis and investigation of Indium doping and surfactant on the morphological, optical and UV/Vis photocatalytic properties of ZnO nanostructure, *Ceramics International* 40 (**2014**) 3453-3460.

[17] S. S. Thind, G. Wu, A. Chen. Synthesis of mesoporous nitrogen–tungsten co-doped TiO_2 photocatalysts with high visible light activity, *Applied Catalysis B: Environmental* 111–112 (**2012**) 38-45.

[18] G. Wu, J. Wang, D.F. Thomas, A. Chen. Synthesis of F-doped flower-like TiO_2 nanostructures with high photoelectrochemical activity, *Langmuir* 24 (**2008**) 3503-3509.

[19] S.U.M. Khan, M. Al-Shahry, W. B. Ingler. Efficient photochemical water splitting by a chemically modified n-TiO_2, *Science* 297 (**2002**) 2243-2245.

[20] K. Song, J. Zhou, J. Bao, Y. Feng. Photocatalytic activity of (copper, nitrogen)-codoped titanium dioxide nanoparticles, *Journal of the American Ceramic Society* 91 (**2008**) 1369-1371.

[21] E.A. Reyes-Garcia, Y. Sun, D. Raftery. Solid-state characterization of the nuclear and electronic environments in a boron−fluoride co-doped TiO_2 visible-light photocatalyst, *The Journal of Physical Chemistry C* 111 (**2007**) 17146-17154.

[22] M. Gillet, K. Aguir, C. Lemire, E. Gillet, K. Schierbaum. The structure and electrical conductivity of vacuum-annealed WO_3 thin films, *Thin Solid Films* 467 (**2004**) 239-246.

[23] S. K. Gullapalli, R. S. Vemuri, C. V. Ramana. Structural transformation induced changes in the optical properties of nanocrystalline tungsten oxide thin films, *Applied Physics Letters* 96 (**2010**) Article number 171903

[24] Z. S. Houweling, J. W. Geus, R. E. I. Schropp. Hot-wire chemical vapor deposition of WO_{3-x} thin films of various oxygen contents, *Materials Chemistry and Physics* 140 (**2013**) 89-96.

[25] W. J. Li, Z. W. Fu. Nanostructured WO_3 thin film as a new anode material for lithium-ion batteries, *Applied Surface Science* 256 (**2010**) 2447-2452.

[26] J. Rajeswari, B. Viswanathan, T. K. Varadarajan. Tungsten trioxide nanorods as supports for platinum in methanol oxidation, *Materials Chemistry and Physics* 106 (**2007**) 168-174.

[27] M. Sadakane, K. Sasaki, H. Kunioku, B. Ohtani, W. Ueda, R. Abe. Preparation of nano-structured crystalline tungsten(vi) oxide and enhanced photocatalytic activity for decomposition of organic compounds under visible light irradiation, *Chemical Communications* (**2008**) 6552-6554.

[28] M. Shibuya, M. Miyauchi. Site-selective deposition of metal nanoparticles on aligned WO_3 nanotrees for super-hydrophilic thin films, *Advanced Materials* 21 (**2009**) 1373-1376.

[29] D. Pletcher. Electrocatalysis: present and future, *Journal of Applied Electrochemistry* 14 (**1984**) 403-415.

[30] M. Tian, S. S. Thind, M. Simko, F. Gao, A. Chen. Quantitative structure−reactivity study of electrochemical oxidation of phenolic compounds at the SnO_2−based electrode, *Journal of Physical Chemistry A* 116 (**2012**) 2927−2934

[31] M. Tian, G. Wu, A. Chen. Unique electrochemical catalytic behavior of Pt nanoparticles deposited on TiO_2 nanotubes, *ACS Catalysis* 2 (**2012**) 425-432.

[32] M. Shao, A. Peles, K. Shoemaker. Electrocatalysis on platinum nanoparticles: particle Size effect on oxygen reduction reaction activity, *Nano Letters* 11 (**2011**) 3714-3719.

Chapter 8: High Performance WO_3 Supported IrO_2-Ta_2O_5 Electrodes for Energy Storage Applications.

8.1. Introduction

The expeditious growth of industries globally has exacerbated the rapid depletion of fossil fuels, as well as to increase the degradation of the environment via the release of myriad contaminants. An efficient, affordable, sustainable and clean source of energy is thus required to tackle fast growing energy challenges [1]. Electrochemical supercapacitors (ES) are ideal energy storage devices that have attracted much interest due to their high power density, long life cycles as compared to batteries, and higher energy density [2-7]. In ES, capacitance depends heavily upon the electrode material that is used [8-10]. Generally, three types of electrode materials are utilized in ES: 1) carbon materials 2) conductive polymers and 3) metal oxides [11, 12]. Carbon materials have a high surface area, low cost, non-toxicity and high specific power, however; a significant resistivity reduces their performance [13]. Conductive polymers also possess various advantages when employed as an electrode material in ES, but swelling and shrinking via intercalation/deintercalation mechanically degrades the electrodes [14, 15]. Metal oxides, such as RuO_2, IrO_2, MnO_2, NiO, SnO_2, V_2O_5 are most suitable for use as supercapacitors due to the variable oxidation states of the metals, which facilitate redox reactions [16-20]. Thus, they provide the optimal alternative as they exhibit higher energy densities than carbon materials and higher stability than conductive polymer materials [21-23].

Among all the metal oxides, RuO_2 has been extensively studied as a suitable material with significant capacitance [24-26]. The constraint to its wide utilization in supercapacitors is its rarity and high cost, which limits its applications. An additional disadvantage of RuO_2 is its

poisonous nature [27, 28]. As a result, much research has been focused on the exploration of new materials with comparable or superior performance, that are more ecofriendly and less expensive.

Over the last few years a number of researchers have attempted to investigate the properties of IrO_2 so that it might be used as an electrode material in ES, as it shows large pseudocapacitance. IrO_2 belongs to a family of transition metal dioxide compounds that have rutile structures and metal like conductivities [29]. Due to its high conductivity, it is used in industry for electrical, magnetic and electrochemical purposes. Chemically, Iridium oxide is a very stable oxide that has been used in electrode materials, in electrochromic displays and in microsensors for gas sensing [30, 31]. To the best of our knowledge, which was derived from a survey of the literature, no results are present that describe a perfect rectangular shape CV for IrO_2, which translates to uneven charging and discharging.

In this work we have synthesized IrO_2-Ta_2O_5, which was deposited on the surface of WO_3 electrodes. In these electrodes, WO_3 serves as a substrate with IrO_2-Ta_2O_5 as material for storing charge. A substrate comprised of WO_3 (n-type oxide semiconductor) was selected, as it has recently attracted a lot of interest for various applications. It is well known for its excellent electron transport properties and stability against corrosion [32-35]. The prepared electrodes were characterized so as to investigate their structural, surface morphological and electrochemical properties. Further, cyclic voltammetric studies were carried out in order to elucidate the supercapacitive properties of the prepared electrodes. Electrodes comprised of WO_3 and WO_3/ Ta_2O_5 exhibited no supercapacitance. However, WO_3/IrO_2 electrodes showed promising charge storage capabilities. WO_3/IrO_2-Ta_2O_5 electrodes were prepared with a 55:45 ratio of IrO_2 and Ta_2O_5. The results indicated that WO_3/IrO_2-Ta_2O_5 electrodes possessed a high

specific capacitance as compared to WO_3 electrodes that individually contained IrO_2 or Ta_2O_5. This shows that there is a synergetic effect present when IrO_2 and Ta_2O_5 are combined. The shape of the CV is also an ideal rectangle for this electrode, which verifies the superiority of this electrode.

8.2. Experimental section

8.2.1. Materials used

Tungsten plates with a thickness of 0.25 mm were received from Sigma-Aldrich (99.9% trace metals basis), which were cut into 1cm × 1cm squares. Acetone (≥99.5%) and Nitric Acid (70%), H_2SO_4 (99.999%), were purchased from Sigma Aldrich and were used as received. Anhydrous Ethyl Alcohol was purchased from Commercial Alcohols Brampton Canada. $IrCl_3 \cdot 3H_2O$ (Pressure Chemical Corp), and $TaCl_5$ (Aldrich) were utilized in the preparation of the precursor solution. Rhodamine B (BDH, UK) was employed as a model of a typical organic dye pollutant in the evaluation of the photocatalytic and electrocatalytic activity of the WO_3 based catalyst. The water (18:2 MΩ cm) used in the preparation of the aqueous solutions was purified via a NANOpure® Diamond™ water system.

8.2.2. Synthesis of WO_3 platelets and deposition of IrO_2-Ta_2O_5

To prepare the WO_3 a very facile hydrothermal method was employed; commercially available Tungsten plate (Sigma-Aldrich, 99.7 %,) was cut to obtain a $1cm^2$ area, which was employed as a substrate. To grow the tungsten oxide onto the substrate, it was introduced into a Teflon lined autoclave with 80% of its volume filled with 1.5 M HNO_3. Following hydrothermal treatment, the electrodes were rinsed several times with ultrapure water and heated at 450 °C over three hours. Subsequent to calcination, they were utilized as such in electrochemical tests.

Solutions containing 0.1 M $IrCl_3.3H_2O$ and 0.1 M $TaCl_5$ were prepared in ethanol and isopropanol respectively and then painted on one side of the WO_3 electrode to obtain WO_3/IrO_2 and WO_3/Ta_2O_5 electrodes. The WO_3/IrO_2-Ta_2O_5 electrode precursor solution was obtained by mixing 0.1 M $IrCl_3.3H_2O$ and 0.1 M $TaCl_5$ solutions in required amounts, which was then painted onto the WO_3 electrode. Following the painting process, the electrodes were subjected to three hours of calcination at 450 ^oC in order to oxidize the metal chlorides to metal oxides.

8.2.3. Characterization techniques

The crystalline phase of the synthesized samples was obtained by X-ray diffraction (Phillips PW 1050-3710 Diffractometer with Cu Kα radiation (λ=1.5406 A^o). Scanning electron microscopy (Hitachi SU 70) analysis was performed in order to determine the surface morphology and particle size of the samples. A Pt coil with a 10 cm^2 surface area was used as the auxiliary electrode; an Ag/AgCl electrode was used as the reference electrode. Cyclic voltammograms were performed using a Voltalab 40 Potentiostat (PGZ301), and a Solatron SI 1287 electrochemical interface instrument was used to run the charge-discharge cycles. The UV-Vis absorbance spectrum was obtained using a UV-visible spectrophotometer (Varian, Cary 5E).

8.2.4. Photocatalytic activity measurements

The photocatalytic activity of as-synthesized WO_3 was evaluated by measuring the photodegradation of RhB with a 1.8 V applied potential. The RhB solution was prepared using pure water (18.2 MΩ.cm) that was obtained from a NANOpure® Diamond^{TM} UV ultrapure water purification system. Samples were collected from the reaction mixture at regular time intervals and the absorbance of the solution was measured using a UV-visible spectrometer (Varian, Cary 50). After taking each reading, the solution was added back into the reaction mixture.

8.3. Results and Discussion

Highly ordered WO_3 platelets were grown onto a W substrate using a hydrothermal method, after which the various metal chlorides were painted onto them. The composition and morphology of the formed electrodes were characterized via energy dispersive spectroscopy and scanning electron microscopy. Figure 8.1 A and B represents the SEM images of the bare WO_3 electrodes, which showed that very highly ordered WO_3 platelets were present on the electrode. These platelets provided an extensive surface area for the deposition of metal oxides on the surface. Figure 8.2A and B presents the images of the WO_3/IrO_2-Ta_2O_5 deposited electrodes and the coating that was prepared by the painting method displays a typical "cracked-mud" structure, which increased the surface area of the electrodes. The EDS spectra of WO_3 and WO_3/IrO_2-Ta_2O_5 are depicted in Figure 8.3A. A perfect 1:3 ratio for W and O was observed in the EDS spectra of WO_3. For WO_3/IrO_2-Ta_2O_5 electrode no W peak was observed, which reveals that the WO_3 was fully covered by the IrO_2-Ta_2O_5 layer. When the chemical composition in atomic percentages for the WO_3/IrO_2-Ta_2O_5 electrode was calculated by EDS, it gave 59:41 at% results, which was close to our target composition of 55:45%. The further characterization of these electrodes was accomplished by analyzing them with XRD, with the results shown in Figure 8.3B. In general, all of the samples showed three very characteristic peaks of WO_3 at 2θ values 23.5, 40.5 and 33.7. According to the literature, the peak at 23.5 corresponds to the phase [002], [020] and [200] and the peak at value 33.7 is due to the presence of the [201] phase. The peaks that are shown with an asterisk are from the W substrate. Interestingly, there was no difference in the XRD patterns prior to and following the IrO_2-Ta_2O_5 deposition, due to very low deposition volume, which is below the detection limit of the XRD instrument.

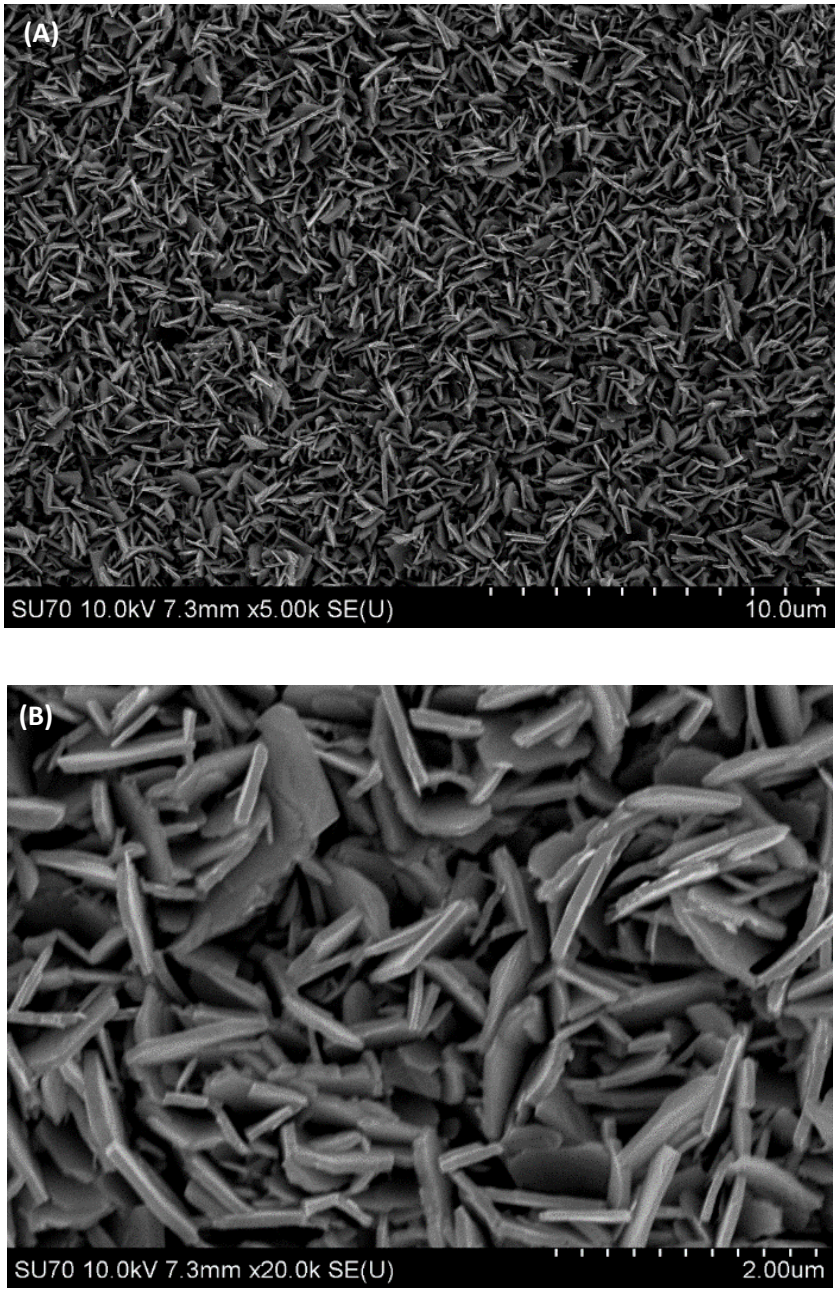

Figure 8.1. SEM (A) and high magnification SEM image (B) of prepared WO_3 platelets

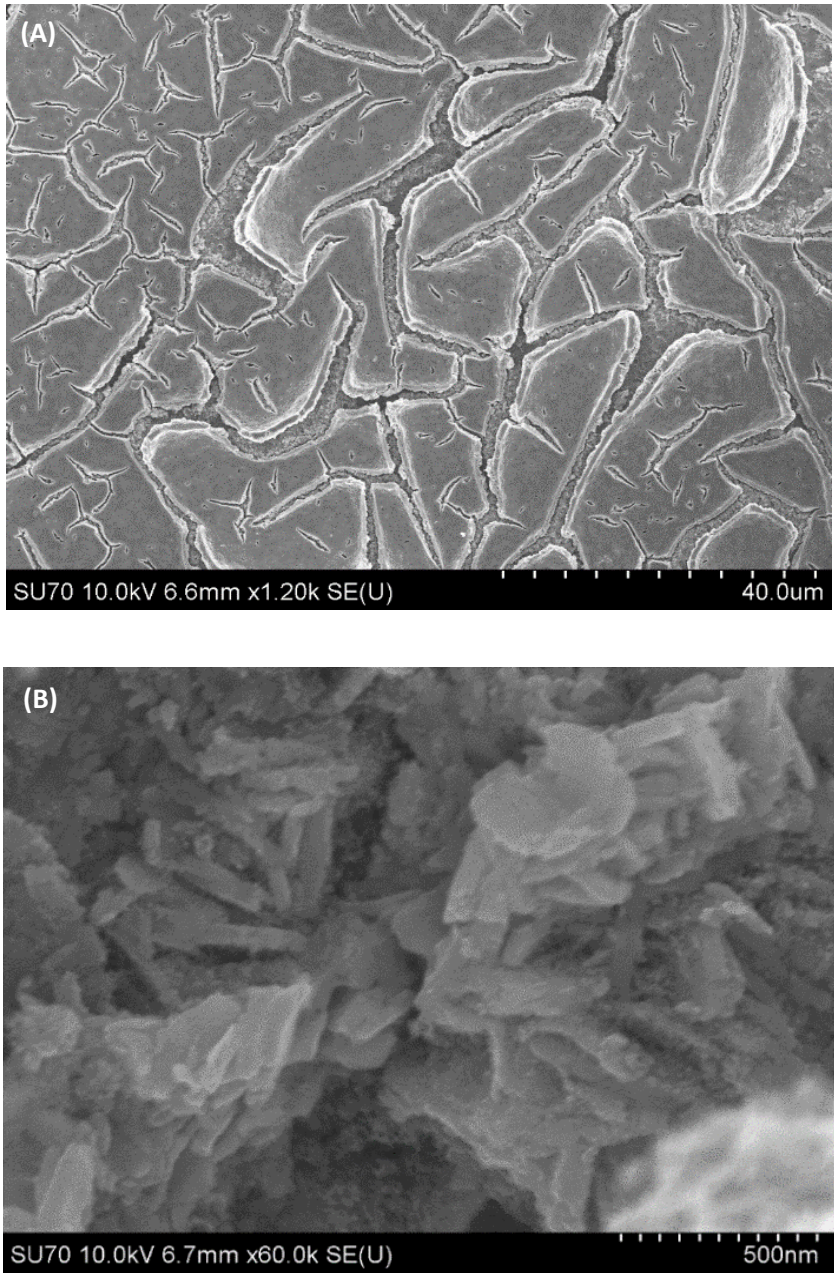

Figure 8.2. (A) SEM image of WO_3/IrO_2-Ta_2O_5 showing 'mud-crack' type morphology and (B) High magnification image of WO_3/IrO_2-Ta_2O_5 showing presence of IrO_2-Ta_2O_5 between the WO_3 platelets.

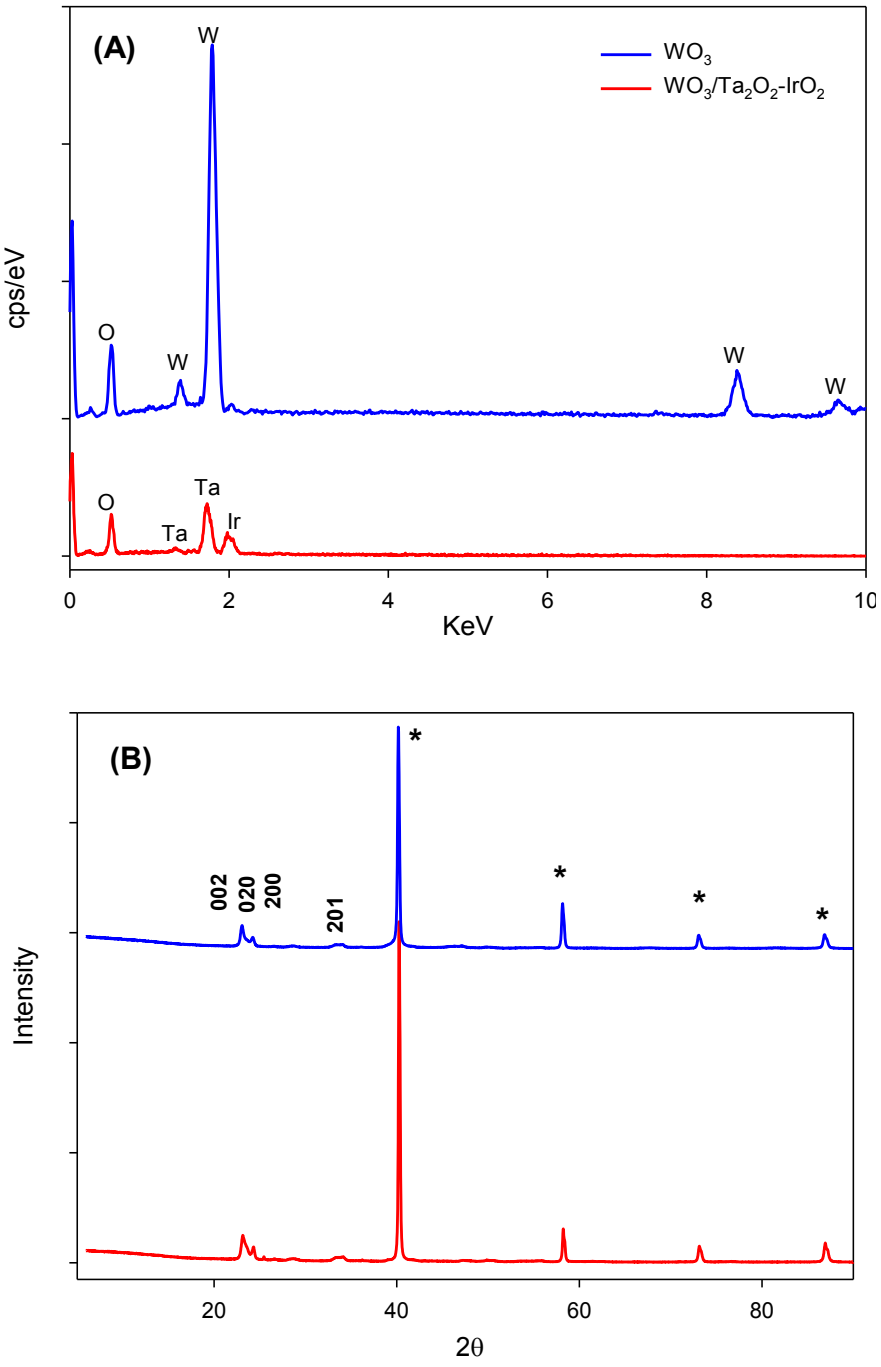

Figure 8.3. EDS (A) and XRD (B) of WO_3 and WO_3/IrO_2-Ta_2O_5.

Figure 8.4 depicts the CVs of the synthesized electrodes recorded in a 0.5 M H_2SO_4 solution at a scan rate of 50 mV s^{-1}. The CV of pure WO_3 consisted of two regions: (I) an initial stage where hydrogen adsorption/desorption proceeds between 0 and 0.35 V; and (II) the double-layer charging region, between 0.35 and 1.2 V. For the WO_3-Ta_2O_5 electrode there was no significant difference between its CV and that of the bare WO_3, which indicates that Ta_2O_5 does not possess supercapacitance properties. It is well known that charge stored in a capacitor may be determined by integrating the CV. The integrated charge for the WO_3/Ta_2O_5 was very small, which is understandable due to the small area under the CV. Figure 8.5A presents the CV for the WO_3/IrO_2 electrode, which reveals that the IrO_2 electrode had a significant amount of charge stored within it. The CV of WO_3/IrO_2 was significantly different than that of WO_3/Ta_2O_5, as we can see that there is an increase in both Region I and Region II. The value of capacitance calculated from the CV was 30.33 mF for the WO_3/IrO_2 electrode. Although the WO_3/IrO_2 showed a high capacitance, the shape of the CV for this electrode is not symmetrical, which demonstrates that charging and discharging is not even with this type of electrode. Surprisingly, when IrO_2 and Ta_2O_5 was deposited together on the WO_3 electrode, the shape of the CV was almost rectangular, indicating that when these two metal oxides are combined, the electrode behaved as a pure capacitor due to a synergetic effect. The capacitance value calculated from the CV was 38.63 mF for the WO_3/IrO_2-Ta_2O_5 electrode. Even though the volume of IrO_2 (which was the main supercapacitance material in this electrode), was reduced by half and replaced by Ta_2O_5 (which is a non-supercapacitor material), a 22% increase in the capacitance was still observed for the bimetallic oxide electrode. This shows that the presence of Ta_2O_5 has a significant role in enhancing the capacitance of the IrO_2 electrode. With the presence of Ta_2O_5

the CV was more symmetrical, which translates to very uniform charging-discharging that occurs in this electrode.

Specific capacitance (mF/mg) may be estimated via the voltammetric charge (integrated from the CV over the potential range) according to the following equation:

$$C = Q/(\Delta E \times W)$$

where Q is the charge (in mC), ΔE is the operating potential window (in V), and W is the weight of the metal oxides deposited (mg) on the working electrode.

The specific capacitance of the various synthesized electrodes was calculated, using Equation (1), and is 3.22 F/g, 81.97 F/g and 124.65 F/g for WO_3/Ta_2O_5, WO_3/IrO_2 and WO_3/IrO_2-Ta_2O_5, respectively. Thus, a high specific capacitance for the bimetallic oxide electrode was observed. $IrCl_3 \times H_2O$ which is most commonly used to obtain IrO_2 is a very expensive material, which hinders its widespread use as an electrode material in supercapacitors. According to Sigma-Aldrich, one gram of 99.9% trace metal basis $IrCl_3 \times H_2O$ costs $256.0, which is very high for the production of electrodes on a large scale. Through this study we have presented a very simple method for reducing the amount of IrO_2 that is required for an efficient electrode, without compromising its activity and capacitance by using bimetallic oxides. $TaCl_5$, which was used with $IrCl_3$ in the fabrication of these bimetallic oxide electrodes, is very cheap as compared to its counterpart, iridium salt. The cost of 1g of 99.8% trace metal basis $TaCl_5$ is only $9.8. Hence, by reducing the volume of IrO_2 via the addition of Ta_2O_5, we not only significantly reduced the cost required for the manufacturing of the electrodes, but also significantly increased the specific capacitance of the electrodes.

In Figure 8.4D the CV of WO_3/IrO_2-Ta_2O_5 at a scan rate of 50 mVs^{-1} is shown, where an ideal rectangular shape was obtained. To investigate the capacitance behaviour of the electrode at different potential sweeps, various CV's were run starting from 20 mVs^{-1} to 100 mVs^{-1} and are

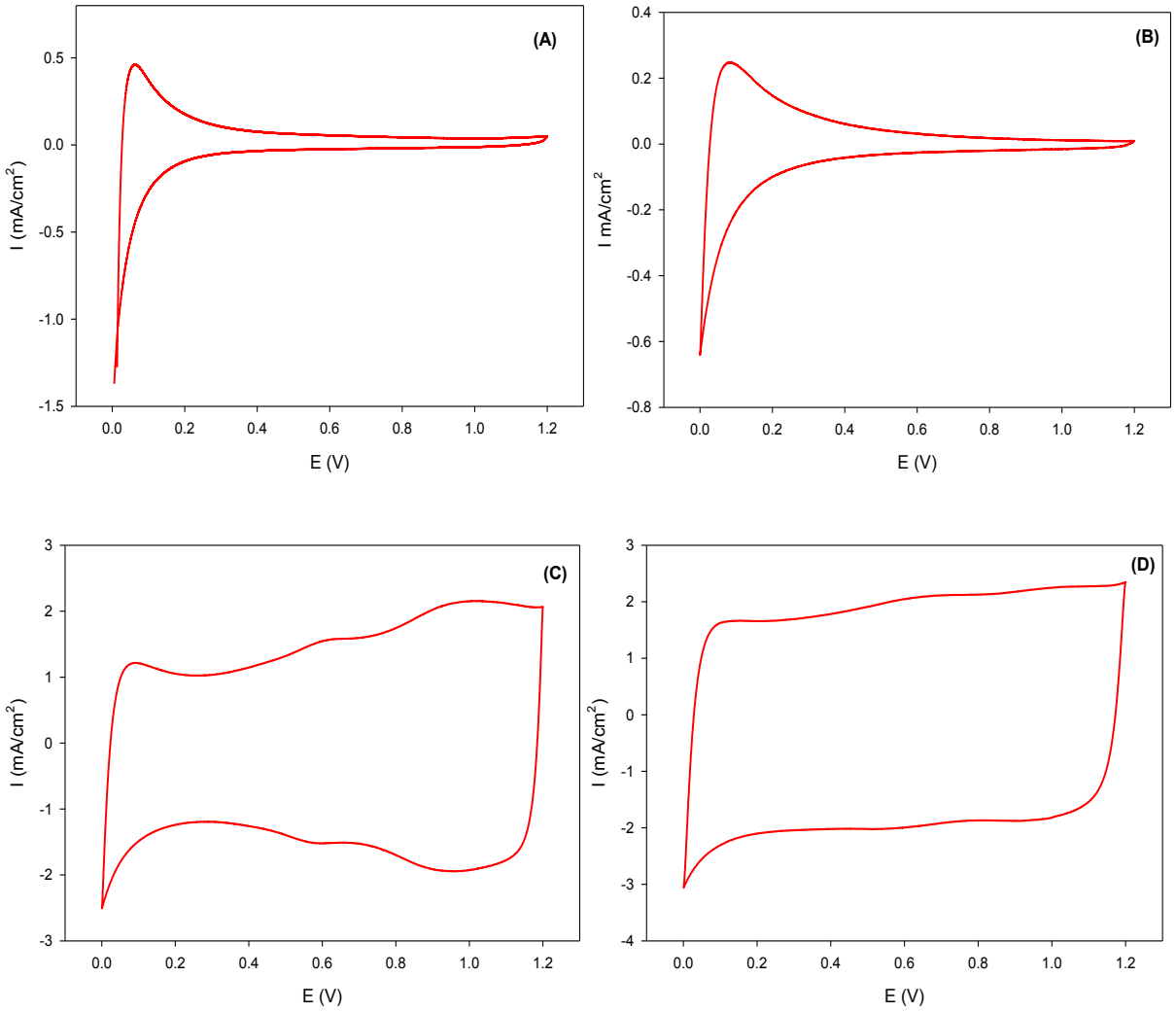

Figure 8.4. Cyclic voltammograms for (A) WO_3, (B) WO_3/Ta_2O_5, (C) WO_3/IrO_2 and (D) WO_3/IrO_2-Ta_2O_5 in 0.5 M H_2SO_4 with a sweep rate of 50 mV/sec.

presented in Figure 8.5. At all of the applied potential sweeps the electrode was found to be very stable, and an ideal rectangular shape was observed for different scan rates, which indicated a good capacitance behaviour and high-rate capability of the electrode. The CV's were very smooth, indicating that there were no faradic reactions proceeding on the electrode. Thus, it was concluded that the WO_3/IrO_2-Ta_2O_5 electrode operates as a pure double layer capacitor.

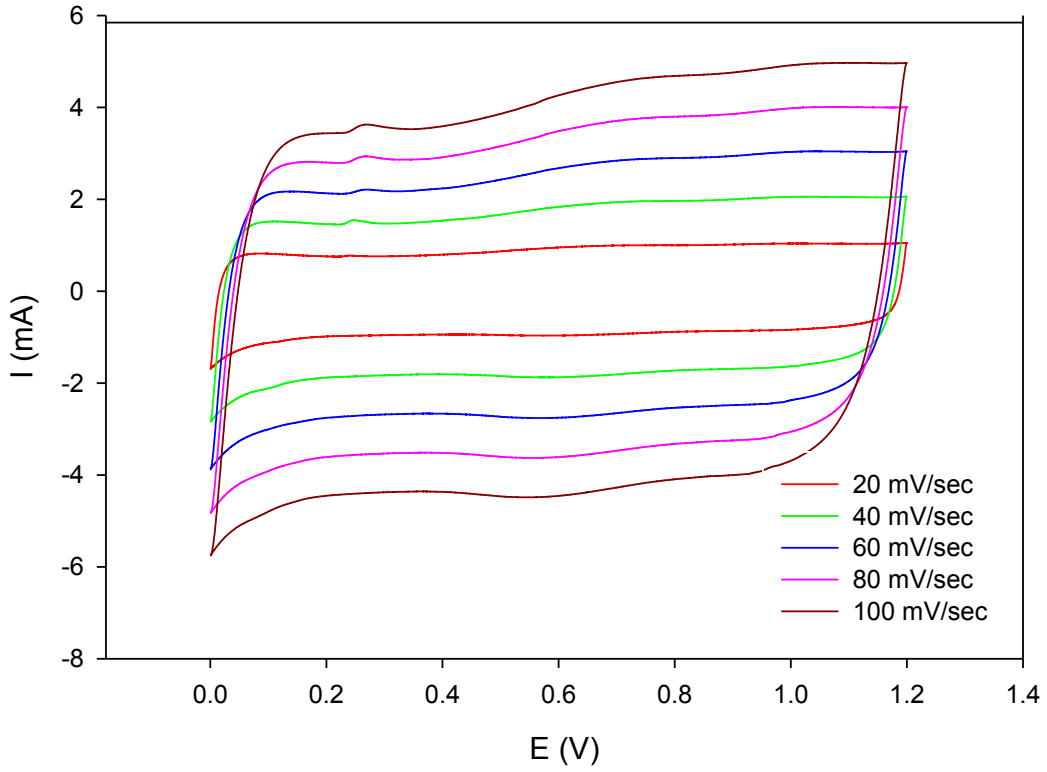

Figure 8.5. Cyclic voltammograms for WO_3/IrO_2-Ta_2O_5 in 0.5 M H_2SO_4 at different sweep rate.

The specific capacitance for each scan was calculated and is given in the **Table 8.1**

Scan Rate mV/sec	Specific capacitance F/g
20	143.8
40	140.45
60	136.58
80	133.54
100	130.99

It can be concluded from Table 1 that the prepared WO_3/IrO_2-Ta_2O_5 electrodes possessed excellent stability as the scan rate was increased from 20 to 100 mV/sec. The small decrease in the specific capacitance might be due to the slow charge transfer when the scan rate was increased.

Cyclic charge discharge is a standard technique that is commonly used to test the performance and cycle life of supercapacitors. In general, a repetitive loop of charging and discharging is called a cycle. Most often, charge and discharge are conducted at constant current until a set voltage is attained. In our study, charge-discharge measurements were performed under galvanostatic conditions at different applied current densities. Constant current charging and discharging curves recorded in a 0.5 M H_2SO_4 solution at 0.25, 0.5, 1.0, 2.0 and 4.0 mA cm^{-2} are shown in Figure 8.6A. It may be concluded that a linear relationship between the potential versus time at various charging and discharging currents was observed. There was no voltage drop at the onset of discharging, which suggests the relatively low equivalent series resistance (ESR) of the electrode and its high electrical conductive behavior.

We tested further the charging/discharging stability of the WO_3/IrO_2-Ta_2O_5 in a 0.5 M H_2SO_4 solution at a current density of 0.5 mA cm^{-2}, with the results are shown in Figure 8.6B. In Figure 8.6B first four, 2497-2500 and 4997-5000th charge-discharge cycles are shown, and it

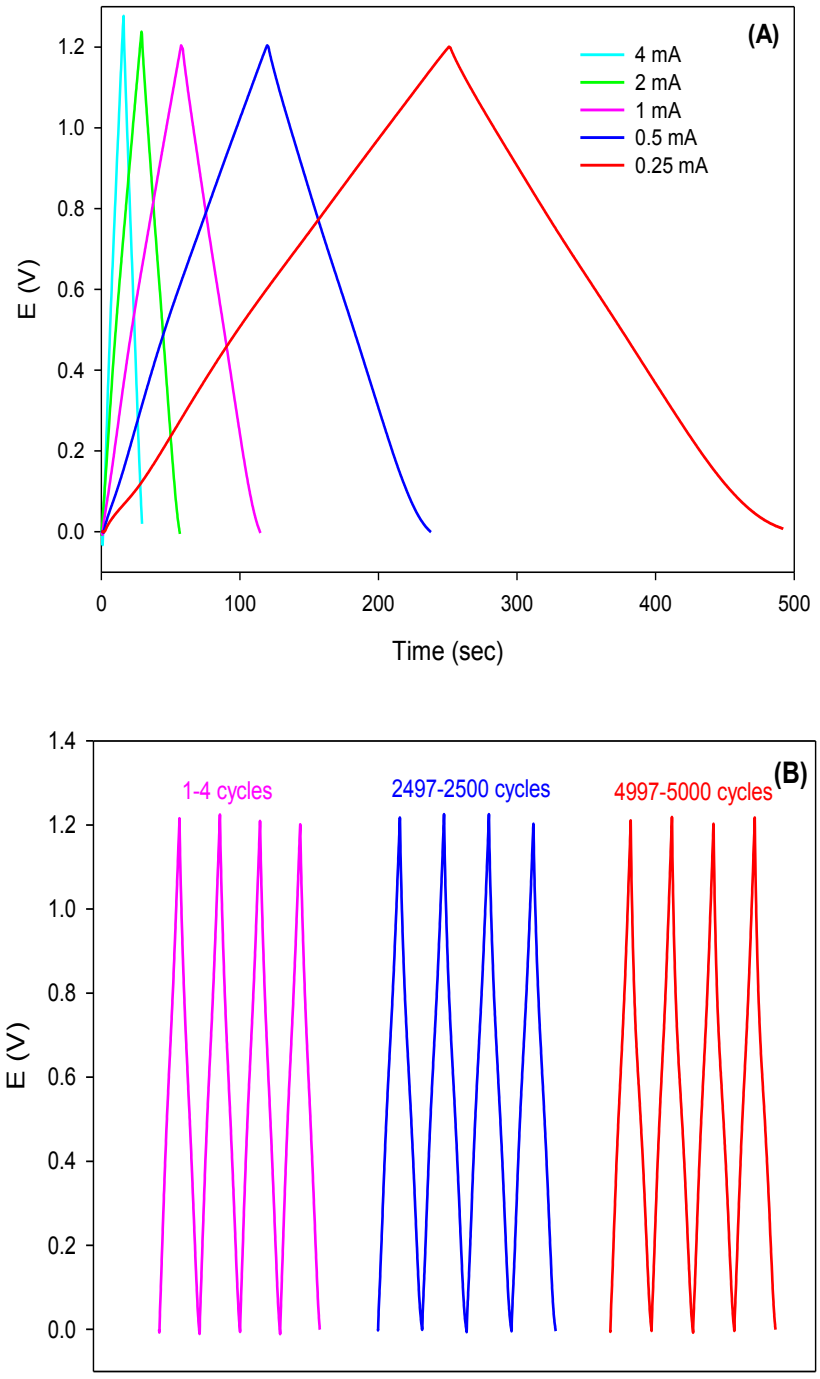

Figure 8.6. (A) Galvanostatic charging/discharging curves of the WO_3/IrO_2-Ta_2O_5 based supercapacitor at different constant currents. (B) Stability test of the WO_3/IrO_2-Ta_2O_5 based supercapacitor

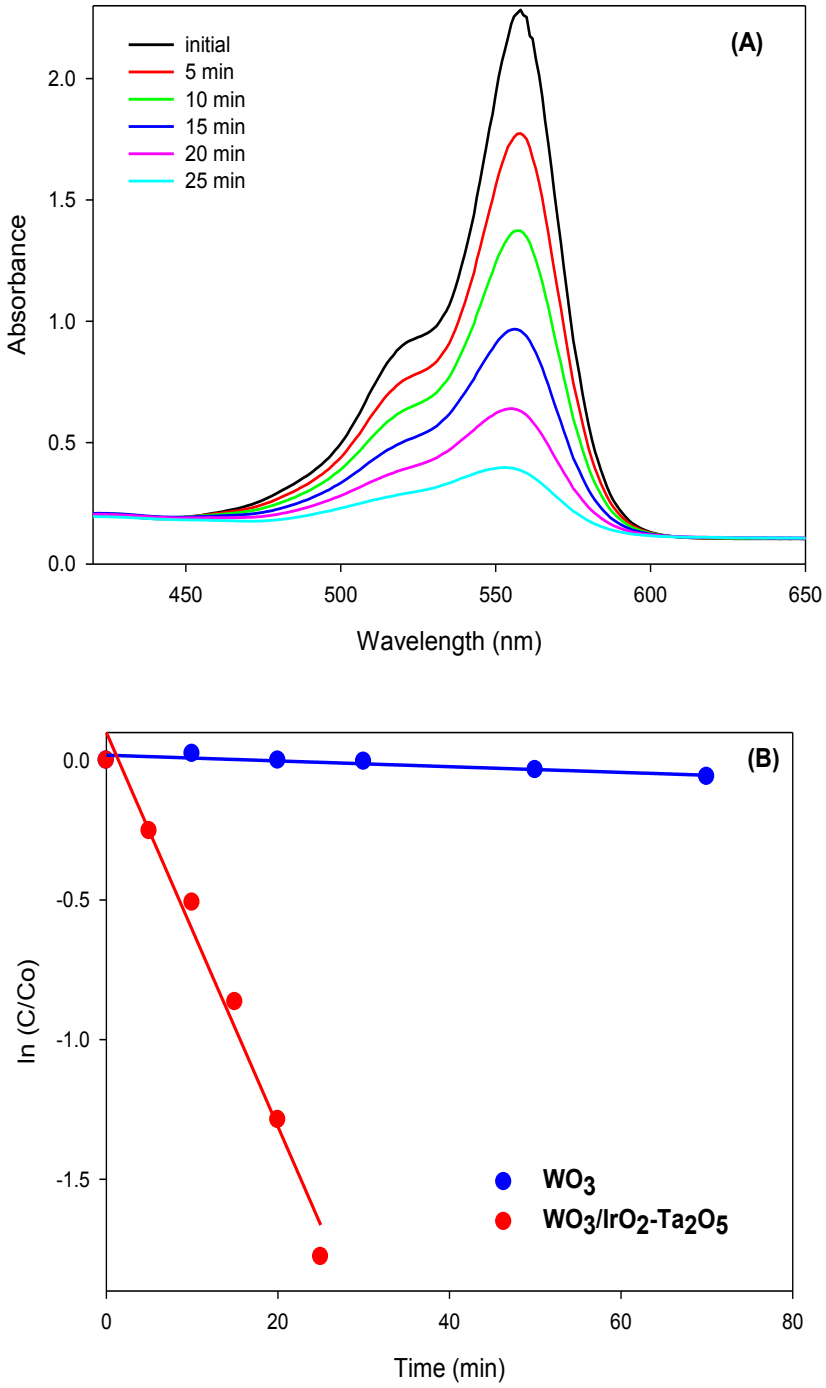

Figure 8.7. (A) Electrocatalytic oxidation of Rhodamine B at the WO_3/IrO_2-Ta_2O_5. (B) Kinetic relationship between ln(C/Co) and time for WO_3 and WO_3/IrO_2-Ta_2O_5

may be concluded that the charge-discharge profiles retained excellent linearity and symmetry following 5,000 cycles, and the specific capacitance remained unchanged. This verified that the prepared WO_3/IrO_2-Ta_2O_5 electrodes were very stable and could be utilized as an electrode material for supercapacitors.

IrO_2 based electrodes have higher conductivity, however; as they are semiconducting, the conductivity of WO_3 is unacceptable. To investigate the impact and electrochemical properties of the IrO_2-Ta_2O_5 that was deposited on the WO_3 electrode, the electrocatalytic degradation of RhB was carried out on WO_3 and WO_3/IrO_2-Ta_2O_5. RhB, which is an organic dye pollutant was selected as a target pollutant for the testing of electrocatalytic activity, with the results for the WO_3/IrO_2-Ta_2O_5 shown in Figure 8.7A. This figure shows the time dependence of the spectral absorbances of 25 μM RhB in 0.1 M H_2SO_4 taken at five-minute intervals during the electrochemical oxidation process. The peak for RhB was centered at 555 nm, and with continuing oxidation, the absorbance of RhB continually decreased over time and approached 0.37 after 25 min. of electrochemical degradation. This represents a 84% decrease in the concentration of RhB over 25 min. To compare this result, its electrochemical oxidation on the WO_3 electrode was also performed, but due to its low conductivity the degradation of RhB was very slow, where an only 11% decrease in the concentration of RhB was observed after 70 min of reaction. Figure 8.7B presents the kinetic curves for the electrochemical degradation of RhB over WO_3 and the WO_3/IrO_2-Ta_2O_5 electrodes, and it can be seen that the results may be fitted, based on first-order kinetics. The rate constants for the oxidation of RhB at the WO_3 and the WO_3/IrO_2-Ta_2O_5 were calculated to be 1.028×10^{-3} and 7.057×10^{-2} min^{-1}, respectively. Thus from the kinetic curves it may be concluded that the oxidation of RhB at the WO_3/IrO_2-Ta_2O_5 electrodes was approximately 70 times higher than at the WO_3 electrodes. The novel electrode

developed in this study possessed high capacitance and very high electrocatalytic properties, which may have strong potential utility for myriad environmental applications.

7.4. Conclusion

In this work we have successfully prepared WO_3/IrO_2-Ta_2O_5 electrodes for their supercapacitance and electrocatalytic properties. WO_3 electrodes were prepared using a very facile hydrothermal method, where platelet-like structures were obtained. A precursor mixture of $IrCl_3.H_2O$ and $TaCl_5$ was painted on one side of the WO_3 electrode and annealed to obtain a WO_3/IrO_2-Ta_2O_5 electrode. WO_3/IrO_2 and WO_3/Ta_2O_5 electrodes were also synthesized for comparative purposes. The SEM images of the electrodes indicated a 'cracked-mud' like structure that was obtained via this deposition method, which increased the surface area of the electrode. The chemical composition of the electrodes calculated for the EDS was very close to the target composition and was well distributed across the WO_3 substrate. The presence of Ta_2O_5 along with IrO_2 significantly enhanced the capacitance of the electrodes due to a synergetic effect. The WO_3/IrO_2 electrode presented a distorted rectangular shape CV, however; the CV of WO_3/IrO_2-Ta_2O_5 showed an ideal rectangular shape, which is optimal for a supercapacitor. The electocatalytic activity of the electrode was also evaluated through the electrochemical degradation of RhB, showing that the WO_3/IrO_2-Ta_2O_5 electrodes were far superior to the parent WO_3 as they have a 70 fold higher activity toward the oxidation of RhB. These electrodes may thus be utilized in a broad range of green and environmental applications.

References

[1] D. Bhattacharjya, M.-S. Kim, T.-S. Bae, J.-S. Yu. High performance supercapacitor prepared from hollow mesoporous carbon capsules with hierarchical nanoarchitecture, *Journal of Power Sources* 244 (**2013**) 799-805.

[2] B. E. Conway. Electrochemical supercapacitors, scientific fundamentals and technological Applications, *Kluwer AcademicéPlenum Press: New York* (**1999**) 11.

[3] P. Simon. Materials for electrochemical capacitors, *Nature Materials* 7 (**2008**) 845-854.

[4] M. Winter, R.J. Brodd. What are batteries, fuel cells, and supercapacitors? *Chemical Reviews* 104 (**2004**) 4245-4270.

[5] E. Faggioli, P. Rena, V. Danel, X. Andrieu, R. Mallant, H. Kahlen. Supercapacitors for the energy management of electric vehicles, *Journal of Power Sources* 84 (**1999**) 261-269.

[6] C. Largeot, C. Portet, J. Chmiola, P.-L. Taberna, Y. Gogotsi, P. Simon. Relation between the ion size and pore size for an electric double-layer capacitor, *Journal of the American Chemical Society* 130 (**2008**) 2730-2731.

[7] S. G. Kandalkar, D. S. Dhawale, C. K. Kim, C. D. Lokhande. Chemical synthesis of cobalt oxide thin film electrode for supercapacitor application, *Synthetic Metals* 160 (**2010**) 1299-1302.

[8] A. S. Arico, P. Bruce, B. Scrosati, J.-M. Tarascon, W. van Schalkwijk. Nanostructured materials for advanced energy conversion and storage devices, *Nature Materials* 4 (**2005**) 366-377.

[9] L. L. Zhang, X. S. Zhao. Carbon-based materials as supercapacitor electrodes, *Chemical Society Reviews* 38 (**2009**) 2520-2531.

[10] M. Mastragostino, C. Arbizzani, F. Soavi. Polymer-based supercapacitors, *Journal of Power Sources* 97–98 (2001) 812-815.

[11] D. Choi, P.N. Kumta. Nanocrystalline TiN derived by a two-step halide approach for electrochemical capacitors, *Journal of The Electrochemical Society* 153 (**2006**) A2298-A2303.

[12] K. Yokoshima, T. Shibutani, M. Hirota, W. Sugimoto, Y. Murakami, Y. Takasu. Electrochemical supercapacitor behavior of nanoparticulate rutile-type $Ru_{1-x}V_xO_2$, *Journal of Power Sources* 160 (**2006**) 1480-1486.

[13] Y. Zhang, H. Feng, X. Wu, L. Wang, A. Zhang, T. Xia, H. Dong, X. Li, L. Zhang. Progress of electrochemical capacitor electrode materials: A review, *International Journal of Hydrogen Energy* 34 (**2009**) 4889-4899.

[14] G. Wang, L. Zhang, J. Zhang. A review of electrode materials for electrochemical supercapacitors, *Chemical Society Reviews* 41 (**2012**) 797-828.

[15] V. Khomenko, E. Frackowiak, F. Béguin. Determination of the specific capacitance of conducting polymer/nanotubes composite electrodes using different cell configurations, *Electrochimica Acta* 50 (**2005**) 2499-2506.

[16] Y. R. Ahn, M. Y. Song, S. M. Jo, C. R. Park, D. Y. Kim. Electrochemical capacitors based on electrodeposited ruthenium oxide on nanofibre substrates, *Nanotechnology* 17 (**2006**).

[17] C.-C. Hu, Y.-H. Huang, K.-H. Chang. Annealing effects on the physicochemical characteristics of hydrous ruthenium and ruthenium–iridium oxides for electrochemical supercapacitors, *Journal of Power Sources* 108 (**2002**) 117-127.

[18] J. Jiang, A. Kucernak. Electrochemical supercapacitor material based on manganese oxide: preparation and characterization, *Electrochimica Acta* 47 (**2002**) 2381-2386.

[19] P. A. Nelson, J. R. Owen. A high-performance supercapacitor/battery hybrid incorporating templated mesoporous electrodes, *Journal of The Electrochemical Society* 150 (**2003**) A1313-A1317.

[20] D. L. D. Silva, R.G. Delatorre, G. Pattanaik, G. Zangari, W. Figueiredo, R.-P. Blum, H. Niehus, A.A. Pasa. Electrochemical synthesis of vanadium oxide nanofibers, *Journal of The Electrochemical Society* 155 (**2008**) E14-E17.

[21] A. Burke. Ultracapacitors: why, how, and where is the technology, *Journal of Power Sources* 91 (**2000**) 37-50.

[22] B. E. Conway. Transition from "supercapacitor" to "battery" behavior in electrochemical energy storage, *Journal of The Electrochemical Society* 138 (**1991**) 1539-1548.

[23] Y. Takasu, Y. Murakami. Design of oxide electrodes with large surface area, *Electrochimica Acta* 45 (**2000**) 4135-4141.

[24] I.-H. Kim, K.-B. Kim. Electrochemical characterization of hydrous ruthenium oxide thin-film electrodes for electrochemical capacitor applications, *Journal of The Electrochemical Society* 153 (**2006**) A383-A389.

[25] Q. X. Jia, S. G. Song, X. D. Wu, J. H. Cho, S. R. Foltyn, A. T. Findikoglu, J. L. Smith. Epitaxial growth of highly conductive RuO_2 thin films on (100) Si, *Applied Physics Letters* 68 (**1996**) 1069-1071.

[26] H. Lee, M. S. Cho, I. H. Kim, J. D. Nam, Y. Lee. RuO_x/polypyrrole nanocomposite electrode for electrochemical capacitors, *Synthetic Metals* 160 (**2010**) 1055-1059.

[27] S. N. Pusawale, P. R. Deshmukh, C. D. Lokhande. Chemical synthesis of nanocrystalline SnO_2 thin films for supercapacitor application, *Applied Surface Science* 257 (**2011**) 9498-9502.

[28] S. K. Meher, G. R. Rao. Ultralayered Co_3O_4 for high-performance supercapacitor applications, *The Journal of Physical Chemistry* C 115 (**2011**) 15646-15654.

[29] Y. M. Chen, J. H. Cai, Y. S. Huang, K. Y. Lee, D. S. Tsai. Preparation and characterization of iridium dioxide–carbon nanotube nanocomposites for supercapacitors, *Nanotechnology* 22 (**2011**) 115706.

[30] Y. M. Chen, Y. S. Huang, K. Y. Lee, D. S. Tsai, K. K. Tiong. Characterization of IrO_2/CNT nanocomposites, *Journal of Materials Science: Materials Electronics* 22 (**2011**) 890-894.

[31] K. Nishio, Y. Watanabe, T. Tsuchiya. Preparation and properties of electrochromic iridium oxide thin film by sol-gel process, *Thin Solid Films* 350 (**1999**) 96-100.

[32] F. Wang, C. Di Valentin, G. Pacchioni. Electronic and structural properties of WO_3: A systematic hybrid DFT study, *The Journal of Physical Chemistry C* 115 (**2011**) 8345-8353.

[33] J. M. Berak, M. J. Sienko. Effect of oxygen-deficiency on electrical transport properties of tungsten trioxide crystals, *Journal of Solid State Chemistry* 2 (**1970**) 109-133.

[34] M. A. Butler, R. D. Nasby, R. K. Quinn. Tungsten trioxide as an electrode for photoelectrolysis of water, *Solid State Communications* 19 (**1976**) 1011-1014.

[35] D. E. Scaife. Oxide semiconductors in photoelectrochemical conversion of solar energy, *Solar Energy* 25 **(1980)** 41-54.

Chapter 9: Concluding Remarks and Future Work

9.1 Conclusions

Following the universal belief that nanomaterials based catalysts are the new and most promising technology to be utilized in the environmental applications, this thesis is dedicated to the development of facile methods to synthesize TiO_2 and WO_3 based nanomaterials, with the aim of evolving a less expensive, efficient, reproducible and environment friendly catalytic process. All of the synthesis methods described herein for the preparation of nanomaterials are very simple and do not involve the utilization of expensive instrumentation. The major findings based on the results of the employed characterization techniques are: i) the solution combustion method that was utilized to synthesize co-doped TiO_2 is very effective in obtaining a highly mesoporous and uniformly doped material; ii) the development of a UV pretreatment approach for the significant enhancement of the photocatalytic activity of TiO_2 based photocatalysts; iii) the development of an electrochemical reduction technique for simultaneously studying the crystal growth mechanism during the hydrothermal method, and synthesizing WO_3 nanospheres and iv) for the first time, Ta_2O_5 and IrO_2 on a WO_3 substrate were studied in conjunction toward the investigation of their supercapacitance properties.

Brief summaries and important conclusions of the work presented are as follows.

9.1.1. Synthesis and characterization of TiO_2 based nanomaterial photocatalysts.

We successfully prepared mesoporous N-doped and N,W co-doped TiO_2 photocatalysts with an exclusive anatase phase and a high specific surface area utilizing a facile, reproducible and inexpensive solution combustion synthesis.

We also studied the synergetic effect of the simultaneous co-doping of metals and non-metals into the TiO_2 structure. XPS analysis showed that the N and W atoms were well incorporated into the lattice structure of the titania by this combustion preparation method. The band gap studies revealed that the co-doping of N and W significantly shifted the absorption edge of the TiO_2 toward the visible region. This narrowing of the band gap served to induce high visible light response photocatalytic activity in the co-doped samples in contrast to those of P25 and therefore, may be beneficially utilized in green chemistry. Photodegradation studies of Rh B dye on the different samples revealed that an enhancement factor of up to 14 times in the reaction rate was observed with the 1.5 at% W doped sample, in comparison to commercial Degussa P25. The novel combustion process developed in this study is rapid and reproducible and may be easily scaled-up, thus opening a door to the fabrication of high-performance TiO_2 photocatalysts for promising environmental applications.

We have developed a facile and effective UV pretreatment method for the significant enhancement of the photocatalytic activity of TiO_2 nanotubes and mesoporous N,W co-doped TiO_2 under both UV and visible light. The time effect for the UV pretreatment was studied and it was observed that the best results were obtained when the TNW samples were treated for one hour under intense UV light exposure. The as-synthesized TNW exhibited a slightly higher UV photocatalytic activity than did the P25; the photodegradation of RhB on the UV pretreated TNW was greatly enhanced over 2.6 times higher than that on the P25. For the visible light activity, the UV pretreatment resulted in an extraordinary >12 fold improvement in photocatalytic activity, as compared to the non-pretreated TNW. Compared with TiO_2 nanotubes without the UV pretreatment, the TiO_2 nanotubes pretreated in a methanol solution under UV light irradiation exhibited substantial enhancements in both photocurrent and activity. The

pretreatment also initiated an increase in the donor density of the TiO_2 nanotubes by almost three orders of magnitude. This significant enhancement of the photoelectrochemical performance may be attributed to the inhibition of charge recombination of photoinduced electrons and electron holes, the creation of oxygen vacancies, an improvement in conductivity, and the promotion of interfacial charge-transfer kinetics at the TiO_2 nanotubes. The facile and effective approach proposed in this study provides many opportunities to develop highly active TiO_2 photocatalysts for pressing energy and environmental applications, ranging from water splitting, solar energy, and air purification, to wastewater treatment. This significant augmentation in photocatalytic activity subsequent to the UV pretreatment may be attributed to the following synergetic factors: (i) the increase of the specific surface area; (ii) the reduction of the band gap energy; (iii) the partial removal of carbon impurities and (iv) formation of Ti^{3+} energy levels in between the TiO_2 band gap. Aside from the considerable enhancement in both UV and visible photocatalytic activity, the UV pretreated mesoporous N, W co-doped TiO_2 exhibited high photocatalytic stability, which is very promising for energy and environmental applications.

9.1.2 Synthesis of WO_3 based nanomaterials for environmental applications

WO_3 is emerging as a frontrunner to be used in photochromism, electrochromism, thermochromic gas sensors, batteries, photoelectric sensors, water splitting, photocatalytic behavior and much more. We have successfully prepared WO_3 nanospheres using a facile electrochemical reduction approach. To the best of our knowledge, for the first time, an electrochemical reduction method has been utilized to synthesize WO_3 nanospheres and to study the mechanism of WO_3 platelet growth during the hydrothermal method. The time interval of the hydrothermal treatment also had a significant impact on the dimensions of the formed WO_3 platelets and their photoelectrochemical activity. The electrochemically treated electrode

consisted of spherical nanoparticles, which exhibited higher photocurrent and photocatalytic activity toward the degradation of 4-NP as compared to their parent WO_3 platelets. This study thus provides a facile approach toward the preparation of high-performance WO_3 nanospheres for myriad energy and environmental applications.

To amalgamate the photocatalytic properties of WO_3 with the electrocatalytic properties of Pt nanoparticles, we synthesized a WO_3 based bifunctional electrode. Platelets of WO_3 were synthesized by a hydrothermal method and possessed a very high visible light response. A uniform layer of Pt was obtained by a photodeposition method on one side of the WO_3 electrode. SEM and EDS results verified the presence of the Pt nanoparticles on the electrodes and that they were well distributed across the surface. Cyclic voltammograms for the bifunctinal electrodes showed a typical curve for Pt and they had a high hydrogen adsorption/desorption capability, demonstrating that Pt is very much active on the surface of the WO_3 electrode surface. The degradation tests of the RhB on the various synthesized electrodes revealed that the bifunctional electrodes, when used under both visible light and applied potential, showed much improved activity. The deposition of the Pt enhanced the activity of the bifunctional electrodes by approximately two fold, as compared to when a bare WO_3 electrode was used as a bifunctional electrode. This two fold enhancement in the catalytic properties of the WO_3 electrodes via the deposition of a very small amount of Pt might be used in green chemistry, for wastewater treatment and in fuel cells.

Supercapacitors are considered as the future of batteries and there is intense research devoted to the development of new electrode materials. In Chapter 8 we successfully demonstrated that bimetallic oxides can be employed as a supercapacitor material, as they work more efficiently due to the synergetic effect. We successfully prepared WO_3/IrO_2-Ta_2O_5

electrodes to evaluate their supercapacitance and electrocatalytic properties. WO_3/IrO_2 and WO_3/Ta_2O_5 electrodes were also synthesized for comparison purposes. The SEM images of the electrodes showed a 'cracked mud' like structure that was obtained by this deposition technique, which increased the surface area of the electrode. The chemical composition of the electrodes calculated for the EDS is very close to the target composition, and is well distributed across the WO_3 substrate. The presence Ta_2O_5 along with IrO_2 significantly enhanced the capacitance of the electrodes due to a synergetic effect. The WO_3/IrO_2 electrode presented a distorted rectangular shape CV, however, the CV of WO_3/IrO_2-Ta_2O_5 showed an ideal rectangular shape which is optimal for a supercapacitor.

9.2. Future Work

As aforementioned, with the growing environmental and energy challenges that confront human society, there is an urgent need to develop more efficient technologies than those that currently exist. During my PhD research, although I successfully prepared highly active TiO_2 and WO_3 based materials for photocatalytic, electrocatalytic and energy storage applications, I strongly believe that this study will contribute in the development of nanomaterials to be used in these applications.

N,W codoped TiO_2 synthesised in this study showed very promising visible light activity, and this visible light response, which is a great tool in the hands of a chemist, can also be utilized in various other applications, such as water splitting, electrochromic devices and dye sensitized solar cells. The redox reaction occurring at the working and counter electrode produces H_2 and O_2 following the excitation of the electrons from the valence band to the conduction band, by absorbing energy from the light source. For this application there is a need to develop a very

dynamic method for the immobilization of the TiO_2 based nanomaterials on the surface of a substrate, to serve as an electrode. The activity of the TiO_2 electrodes toward photocatalytic water splitting can be further enhanced via the deposition of metals or metal oxides on the TiO_2 based electrodes. Metal deposition on the N, W codoped TiO_2 may also be investigated to further augment the electrode for water splitting. Highly active UV pretreated nanotubes might also be attempted in water splitting reactions to generate H_2.

Although N, W co-doping has a considerable effect on the shifting of the absorbance edge of TiO_2, there are still many other possible combinations of the non-metal and metals that need to be studied. A series of experiments might be run by keeping N as a non-metal dopant and employing all possible metal atoms as co-dopants systematically, in order to evaluate which combination exhibits the best activity. Further studies need to be undertaken to learn of the effects of tri-doping on the visible light and photocatalytic activities of TiO_2 based nanomaterials.

DSSCs are the alternative energy source to traditional semiconductor solar cells. TiO_2 is optimal for being used as photoelectrode materials due to its favorable physiochemical properties. Mesoporous TiO_2 gives better results as a photoanode material as compared to the TiO_2 nanotubes, nanowires and other morphologies because of their special functionality, where the interconnected junctions with open pores in the mesoporous structure, accelerates electron transport. The TNW prepared in this study possessed a highly mesoporous structure, thus it can be employed in the DSSCs.

The solution combustion method utilized in this study to effectively synthesize TiO_2 and TNW is a very facile and efficient method, which should be further explored in the synthesis of

additional metal oxides. Research can also be contributed to synthesize nanoparticles with different morphologies using this method.

Researchers have shown that TiO_2 nanotubes may be used as a hydrogen storage material as it could reproducibly store up to approximately 2 wt % H_2 at room temperature. Out of this stored H_2 approximately 75% could be released when the hydrogen pressure was lowered to ambient conditions due to physisorption. Further studies are required to be done in order to examine whether the UV treatment might increase the H_2 storage capacity of the nanotubes. Modified WO_3 electrodes prepared via the hydrothermal method will be studied for the hydrogen storage studies. As we are aware that the photocatalytic activity of the WO_3 may also be enhanced by doping with various metal atoms and non-metals, such as N, C, Mg, Ni, Au, Cu, Zn, Bi, Ag, Fe and Co, doping of the WO_3 during the hydrothermal process is a promising approach to increase the photocatalytic activity of the WO_3 platelets. The efficiency of the WO_3 is very low as compared to that of DSSCs based on other semiconducting metal oxides, such as TiO_2, SnO_2, and ZnO. There is still the requirement of research work that is focused on increasing the efficacy of WO_3 based photoanodes for DSSCs.